

A dissertation submitted in partial fulfillment of the
requirements for the degree of Doctor of Philosophy in the
Dublin City University

**Accelerated integral equation techniques for
solving EM wave propagation and scattering
problems**

Dung Trinh, M.Eng., B.Eng.

Supervisor: Dr. Conor Brennan



School of Electronic Engineering
Dublin City University

April 2014



Dissertation Committee:

Dr. Conor Brennan, supervisor

Prof. Claude Oestges

Prof. Liam Barry

Dr. Noel Murphy

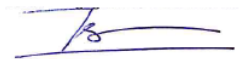


To my family

Declaration

I hereby certify that this material, which is now submit for assessment on the programme of study leading to the award of Doctor of Philosophy is entirely my own work, that I have exercised reasonable care to ensure that the work is original, and does not to the best of my knowledge breach any law of copyright, and has not been taken from the work of others save and to the extent that such work has been cited and acknowledged within the text of my work.

Signed:



ID No.: 58127356. Date: September 11th, 2014

Acknowledgments

First of all, I would like to express my sincere gratitude to my supervisor, Dr. Conor Brennan. This dissertation would not have been possible without his continuous and patient guidance from the beginning of my experience as a master student in the Dublin City University through my preparation and completion of this dissertation.

I also would like to thank my other committee members: Prof. Claude Oestges, Prof. Liam Barry and Dr. Noel Murphy for their valuable comments on the dissertation.

In the RF propagation modeling and simulation group, I would like to acknowledge all former and current members for sharing their knowledge: Marie Mullen, Patrick Bradley and Vinh Pham.

Finally, I would like to express my deepest gratitude to all my family and my girlfriend for their support, encouragement throughout my life.

Contents

| | |
|--|------------|
| Declaration | iii |
| Acknowledgments | iv |
| 1 Introduction | 1 |
| 1.1 EM wave propagation in rural and urban areas | 2 |
| 1.2 EM wave scattering from random rough surfaces | 5 |
| 1.3 Dissertation overview | 7 |
| 1.4 Contribution | 8 |
| 2 Integral Equation Formulations | 10 |
| 2.1 Maxwell's equations and the scattering problem | 10 |
| 2.2 Surface Integral Equations for homogeneous scatterers | 15 |
| 2.2.1 Surface equivalence principle | 15 |
| 2.2.2 Surface Integral Equations for homogeneous scatterers | 16 |
| 2.3 Method of Moments | 19 |
| 2.4 Wave scattering from infinite cylinders | 22 |
| 2.4.1 TM-wave scattering from homogeneous dielectric cylinders [1, 2] . . | 23 |
| 2.4.2 TE-wave scattering from homogeneous dielectric cylinders | 35 |
| 2.5 3D wave scattering problem formulation | 36 |
| 2.5.1 Scattered field in the far zone | 43 |
| 2.6 Conclusions | 45 |
| 3 Improved Tabulated Interaction Method for Electromagnetic Wave Scattering From Lossy Irregular Terrain Profiles | 46 |
| 3.1 Introduction | 46 |
| 3.2 Wave scattering from 1D dielectric surfaces | 48 |
| 3.3 The Improved Tabulated Interaction Method | 50 |
| 3.3.1 Basis function definition | 50 |
| 3.3.2 Derivation of ITIM linear system | 53 |
| 3.4 Derivation of underpinning approximations | 57 |
| 3.4.1 Incident field | 57 |
| 3.4.2 Interaction between groups | 60 |
| 3.4.3 Two-level Improved Tabulated Interaction Method (TL-ITIM) . . . | 62 |

| | | |
|----------|--|-----------|
| 3.5 | Calculation of pathloss and computational complexity | 63 |
| 3.5.1 | Complexity Analysis | 65 |
| 3.6 | Numerical results | 66 |
| 3.6.1 | Rural terrain profile | 67 |
| 3.6.2 | Mountainous terrain profile | 69 |
| 3.7 | Efficient numerical method for computing ITIM basis functions | 71 |
| 3.7.1 | Complexity Analysis of the New FFT Based Method | 75 |
| 3.7.2 | Convergence Analysis | 75 |
| 3.7.3 | Investigation of convergence versus problem size | 78 |
| 3.7.4 | Convergence comparison with Krylov methods | 79 |
| 3.8 | Conclusions | 81 |
| 4 | Fullwave Computation of Path Loss in Urban Areas | 82 |
| 4.1 | Introduction | 82 |
| 4.2 | Description of the algorithm for extracting vertical plane profiles from 3D city map | 83 |
| 4.3 | The Generalized Forward Backward Method (GFBM) | 84 |
| 4.4 | Numerical analysis | 87 |
| 4.4.1 | Accuracy of the forward scattering assumption | 88 |
| 4.4.2 | Comparison with slope diffraction method and measurement data | 88 |
| 4.5 | Conclusion | 90 |
| 5 | Improved Forward Backward Method with Spectral Acceleration for Scattering From Randomly Rough Lossy Surfaces | 96 |
| 5.1 | Introduction | 96 |
| 5.2 | Formulation | 99 |
| 5.2.1 | Forward Backward Method | 101 |
| 5.2.2 | Improved Forward Backward Method | 102 |
| 5.2.3 | Reduction of computational complexity of improvement step | 105 |
| 5.2.4 | Spectral Acceleration of matrix-vector products | 106 |
| 5.2.5 | Scattered wave, Normalised Bistatic Scattering Coefficient, Emissivity and Brightness temperature | 109 |
| 5.2.6 | Absorptivity, Reflectivity and Energy Conservation Check | 111 |
| 5.3 | Results | 112 |
| 5.3.1 | Gaussian Correlation Function | 112 |
| 5.3.2 | Exponential Correlation Function | 115 |
| 5.3.3 | Emissivity and energy conservation | 116 |
| 5.3.4 | Comparison against measurement data | 117 |
| 5.4 | Conclusions | 118 |

| | | |
|----------|--|------------|
| 6 | Block Forward Backward Method with Spectral Acceleration for Scattering from Two Dimensional Dielectric Random Rough Surfaces | 121 |
| 6.1 | Introduction | 121 |
| 6.2 | Block Forward Backward Method with Spectral Acceleration | 122 |
| 6.2.1 | Wave scattering by dielectric surfaces | 122 |
| 6.2.2 | Tapered incident wave | 124 |
| 6.2.3 | Block Forward Backward Method | 125 |
| 6.2.3.1 | A brief review of Forward Backward Method for 2D Random Rough Surface Scattering | 125 |
| 6.2.3.2 | Block Forward Backward Method for 2D Random Rough Surface Scattering | 130 |
| 6.2.4 | Spectral Acceleration (SA) for 2D lossy surface | 131 |
| 6.2.5 | Normalized Bistatic Scattering Coefficient, Emissivity and Brightness Temperature | 138 |
| 6.2.6 | Absorptivity, Reflectivity and Energy Conservation Check | 139 |
| 6.3 | Numerical analysis | 140 |
| 6.3.1 | Comparison against 2D model and measurement data | 140 |
| 6.3.2 | Convergence of the BFBM-SA | 141 |
| 6.3.3 | Emissivity, Reflectivity and Energy Conservation | 149 |
| 6.4 | Conclusion | 149 |
| 7 | Conclusions | 151 |
| | Appendix A | 155 |
| | Appendix B | 158 |
| | Appendix C | 159 |
| | Appendix D | 176 |
| | Publications | 178 |
| | Bibliography | 179 |

Abstract

This dissertation focuses on the development of the robust, efficient and accurate numerical methods of EM wave propagation and scattering from urban, rural areas and random rough surfaces. There are four main contributions of this dissertation.

- The Improved Tabulated Interaction Method (ITIM) is proposed to compute EM wave propagation over lossy terrain profiles using a coupled surface integral equation formulation. The ITIM uses a common set of basis functions in conjunction with a simple matching technique to compress the original system to a reduced system containing considerably smaller number of unknowns and therefore provide a very efficient and accurate method.
- Initial efforts in using the full-wave method to compute EM wave propagation over urban areas. The un-accelerated full-wave method has a massive computational burden. In order to reduce the computational complexity, Generalized Forward Backward Method (GFBM) is applied (note that the conventional Forward Backward Method diverges in this scenario).
- The Improved Forward Backward Method with Spectral Acceleration (FBM-SA) is proposed to solve the problem of 2D wave scattering from random lossy rough surfaces.
- An efficient and accurate iterative method is proposed for computing the 3D wave scattering from 2D dielectric random rough surfaces. The proposed method referred to as the Block Forward Backward Method improves the convergence of the 3D FBM, makes it converge for the case of 2D dielectric surfaces. In addition the Spectral Acceleration is also modified and combined with the BFBM to reduce the computational complexity of the proposed method.

List of Figures

| | | |
|------|---|----|
| 1.1 | Illustration of full 3D ray tracing method. | 3 |
| 1.2 | Illustration of horizontal and vertical ray tracing method. | 4 |
| 1.3 | Illustration of Soil Moisture Active Passive (SMAP) mission, scheduled to launch by NASA in 2014 [3] | 5 |
| 2.1 | Classification of integral equation formulations used in this dissertation . . . | 11 |
| 2.2 | The scattering Problem | 13 |
| 2.3 | (a) Actual problem (b) Equivalent problem | 16 |
| 2.4 | Original Problem | 18 |
| 2.5 | Equivalent exterior problem associated with the homogeneous object in Figure 2.4 | 19 |
| 2.6 | Equivalent interior problem associated with the homogeneous object in Figure 2.4 | 20 |
| 2.7 | An infinite cylinder illuminated by an incident wave (a) Infinite cylinder (b) Cross section of the infinite cylinder | 23 |
| 2.8 | Discretisation of the cylinder contour (a) A cylinder illuminated by an incident wave (b) Cylinder contour is divided into cells | 26 |
| 2.9 | Evaluation of the diagonal elements of impedance matrix | 30 |
| 2.10 | Example of one-dimensional randomly rough surface | 32 |
| 2.11 | Example of two dimensional dielectric rough surface profile illuminated by an incident wave | 37 |
| 2.12 | Near and far field geometry | 44 |
| 3.1 | Wave impinging upon a dielectric surface | 49 |
| 3.2 | A terrain profile (Hjorring - Denmark) is considered to consist of connected identical linear segments. | 51 |
| 3.3 | $K + 1$ direction vectors \hat{e}_k are defined on a reference group and are used to define the set of common basis functions $\phi_0^{(k)}$ and $\phi_1^{(k)}$ | 52 |
| 3.4 | Far Field Approximation of Incidence Field. Circular dots represent centre of Q pulse basis domains while square dot represent centre of group. \hat{x} is unit vector tangent to surface of group. | 57 |
| 3.5 | Incident field on group can be expressed in terms of two plane waves with amplitudes based on linear interpolation. | 59 |

| | | |
|------|---|----|
| 3.6 | Far Field Approximation of interaction between two groups i and j | 60 |
| 3.7 | Near neighbour group j is sub-divided into H sub-groups with $\frac{Q}{H}$ discretisations each. Each scatters its own plane wave to group i | 64 |
| 3.8 | Pathloss generated by proposed method, precise solution and measured data over Hadsund terrain profile. Length of profile: $8km$. (a) Hadsund terrain profile, (b) Pathloss at $144MHz$ with TM^z Polarization. | 68 |
| 3.9 | Pathloss generated by proposed method, precise solution and measured data over Jerslev terrain profile. Length of profile: $5.5km$. (a) Jerslev terrain profile, (b) Pathloss at $435MHz$ with TM^z Polarization. | 69 |
| 3.10 | Pathloss generated by proposed method and precise solution over mountainous terrain profile. Length of profile: $6km$. (a) Wicklow terrain profile, (b) Pathloss at $300MHz$ with TM^z Polarization | 71 |
| 3.11 | Pathloss generated by proposed method and precise solution over mountainous terrain profile. Length of profile: $6km$. (a) Wicklow terrain profile, (b) Pathloss at $300MHz$ with TE^z Polarization | 72 |
| 3.12 | Pathloss generated by proposed method and precise solution over Wicklow terrain profile. Length of profile: $6km$. Operating frequency: $300MHz$. (a) Pathloss generated by TL-TIM with block size of $25m$, (b) Pathloss generated by standard TIM with block size of $25m$, (c) Pathloss generated by standard TIM with block size of $12.5m$ | 73 |
| 3.13 | Spectral Radius of matrix \overline{NM}^{-1} | 79 |
| 3.14 | Comparison of convergence rate between proposed method, GMRES-FFT and block-diagonal preconditioned GMRES-FFT | 80 |
| 4.1 | A example of base station, mobile station and the associated intersection points. | 83 |
| 4.2 | A example of vertical plane profile extraction from the intersection points shown in Figure 4.1. | 84 |
| 4.3 | GFBM Algorithm. | 87 |
| 4.4 | Pathloss generated by proposed method, precise solution over a sample profile (a) Sample profile extracted from Munich city (b) Pathloss at $945MHz$ with TM^z Polarization. | 91 |
| 4.5 | Map of Munich City with 3 Metro routes | 92 |
| 4.6 | (a) Partial map of Munich city and Metro 200 (b) Comparison between measurements, GFBM with forward scattering assumption and Slope Diffraction Method. Route: Metro 200 | 93 |
| 4.7 | (a) Partial map of Munich city and Metro 201 (b) Comparison between measurements, GFBM with forward scattering assumption and Slope Diffraction Method. Route: Metro 201 | 94 |

| | | |
|-----|--|-----|
| 4.8 | (a) Partial map of Munich City and Metro 202 (b) Comparison between measurements, GFBM with forward scattering assumption and Slope Diffraction Method. Route: Metro 202 | 95 |
| 5.1 | Bistatic scattering coefficient of a flat surface. root mean squared height $h_{rms} = 0.0\lambda$ and correlation length: $l_c = 0.5\lambda$. Incident angle: 30° . (a) Flat surface (b) Bistatic scattering coefficients of the surface | 97 |
| 5.2 | Bistatic scattering coefficient of a rough surface. root mean squared height $h_{rms} = 0.1\lambda$ and correlation length: $l_c = 0.5\lambda$. Incident angle: 30° . (a) Rough surface (b) Bistatic scattering coefficients of the surface | 98 |
| 5.3 | Bistatic scattering coefficient of a flat surface. root mean squared height $h_{rms} = 0.5\lambda$ and correlation length: $l_c = 1.0\lambda$. Incident angle: 30° . (a) Rough surface (b) Bistatic scattering coefficients of the surface | 99 |
| 5.4 | One dimensional dielectric rough surface profile $z = f(x)$ illuminated by an incident wave | 100 |
| 5.5 | (a) Eigenvalues of iterative matrix M for random rough surface (b) Eigenvalues associated with dominant value of $\beta_n^{(2)}$, that is the dominant error coefficients after two iterations. | 103 |
| 5.6 | Strong and weak regions in the forward and backward scattering direction (a) Forward Scattering (b) Backward Scattering | 107 |
| 5.7 | Comparison of residual error norm of proposed method (IFBM-SA) and FBM-SA | 113 |
| 5.8 | Comparison of Run Time between IFBM-SA, reference method and FBM-SA | 114 |
| 5.9 | Comparison of averaged TE and TM NBSCs of proposed method and Direct Matrix Inversion (DMI) over 100 realisations. Relative dielectric constant: $\epsilon_r = 20 + 4i$. Autocorrelation function is Gaussian with Gaussian spectrum. $h_{rms} = 2.0\lambda$ and $l_c = 6.0\lambda$ | 119 |
| 6.1 | Two dimensional dielectric rough surface profile $z = f(x, y)$ illuminated by an incident wave | 126 |
| 6.2 | A $8\lambda \times 8\lambda$ surface illuminated by a tapered plane wave with $g = L_x/2 = L_y/2$. 127 | |
| 6.3 | A $8\lambda \times 8\lambda$ surface illuminated by a tapered plane wave with $g = L_x/3 = L_y/3$. 128 | |
| 6.4 | A $8\lambda \times 8\lambda$ surface illuminated by a tapered plane wave with $g = L_x/6 = L_y/6$. 129 | |
| 6.5 | Forward sweep (FS) and backward sweep (BS) of the Forward Backward Method (FBM) | 130 |
| 6.6 | Forward sweep (FS) and backward sweep (BS) of the Block Forward Backward Method (BFBM) | 132 |
| 6.7 | Strong and weak regions in the FS direction | 133 |
| 6.8 | Case 1: Field point is NOT the first point of the block. | 135 |
| 6.9 | Case 2: Field point is the first point of the block. | 137 |

| | | |
|------|---|-----|
| 6.10 | Comparison of the convergence rate of the proposed method (BFBM-SA) and GMRES. | 143 |
| 6.11 | Comparison of run time to achieve the desired residual relative error versus number of unknowns between BFBM-SA and GMRES-SA for the 2D dielectric problem. | 145 |
| 6.12 | Comparison of co-polarisation bistatic scattering coefficients generated by the proposed method and precise solution. Incident angle: 40^0 . Rms height of the surface: $\sigma = 0.05\lambda$. Correlation length of the surface: $l_c = 0.8\lambda$. Size of the surface: $8\lambda \times 8\lambda$. Relative permittivity: $5.46 + 0.37i$. Number of unknowns: 98304. (a) TE Polarization. (b) TM Polarization. | 146 |
| 6.13 | Comparison of co-polarisation bistatic scattering coefficients generated by the proposed method and precise solution. Incident angle: 20^0 . Rms height of the surface: $\sigma = 0.05\lambda$. Correlation length of the surface: $l_c = 0.8\lambda$. Size of the surface: $8\lambda \times 8\lambda$. Relative permittivity: $15.57 + 3.71i$. Number of unknowns: 98304. (a) TE Polarization. (b) TM Polarization.. . . . | 147 |
| 6.14 | Comparison of co-polarisation bistatic scattering coefficients generated by the proposed method and precise solution. Incident angle: 40^0 . Rms height of the surface: $\sigma = 0.15\lambda$. Correlation length of the surface: $l_c = 0.8\lambda$. Size of the surface: $8\lambda \times 8\lambda$. Relative permittivity: $15.57 + 3.71i$. Number of unknowns: 98304. (a) TE Polarization. (b) TM Polarization.. . . . | 148 |
| C-1 | Pathloss generated by ITIM, Hata Okumura model with multiple knife edge diffraction and measured data over Jerslev terrain profile. (a) Jerslev terrain profile, (b) Pathloss at $144MHz$ with TM^z Polarization. | 160 |
| C-2 | Pathloss generated by ITIM, Hata Okumura model with multiple knife edge diffraction and measured data over Jerslev terrain profile. (a) Jerslev terrain profile, (b) Pathloss at $435MHz$ with TM^z Polarization. | 161 |
| C-3 | Pathloss generated by ITIM, Hata Okumura model with multiple knife edge diffraction and measured data over Jerslev terrain profile. (a) Jerslev terrain profile, (b) Pathloss at $970MHz$ with TM^z Polarization. | 162 |
| C-4 | Pathloss generated by ITIM, Hata Okumura model with multiple knife edge diffraction and measured data over Ravnstru terrain profile. (a) Ravnstru terrain profile, (b) Pathloss at $144MHz$ with TM^z Polarization. | 163 |
| C-5 | Pathloss generated by ITIM, Hata Okumura model with multiple knife edge diffraction and measured data over Ravnstru terrain profile. (a) Ravnstru terrain profile, (b) Pathloss at $435MHz$ with TM^z Polarization. | 164 |
| C-6 | Pathloss generated by ITIM, Hata Okumura model with multiple knife edge diffraction and measured data over Ravnstru terrain profile. (a) Ravnstru terrain profile, (b) Pathloss at $970MHz$ with TM^z Polarization. | 165 |

| | | |
|------|---|-----|
| C-7 | Pathloss generated by ITIM, Hata Okumura model with multiple knife edge diffraction and measured data over Mjels terrain profile. (a) Mjels terrain profile, (b) Pathloss at $144MHz$ with TM^z Polarization. | 166 |
| C-8 | Pathloss generated by ITIM, Hata Okumura model with multiple knife edge diffraction and measured data over Mjels terrain profile. (a) Mjels terrain profile, (b) Pathloss at $435MHz$ with TM^z Polarization. | 167 |
| C-9 | Pathloss generated by ITIM, Hata Okumura model with multiple knife edge diffraction and measured data over Mjels terrain profile. (a) Mjels terrain profile, (b) Pathloss at $970MHz$ with TM^z Polarization. | 168 |
| C-10 | Pathloss generated by ITIM, Hata Okumura model with multiple knife edge diffraction and measured data over Hadsund terrain profile. (a) Hadsund terrain profile, (b) Pathloss at $144MHz$ with TM^z Polarization. | 169 |
| C-11 | Pathloss generated by ITIM, Hata Okumura model with multiple knife edge diffraction and measured data over Hadsund terrain profile. (a) Hadsund terrain profile, (b) Pathloss at $435MHz$ with TM^z Polarization. | 170 |
| C-12 | Pathloss generated by ITIM, Hata Okumura model with multiple knife edge diffraction and measured data over Hadsund terrain profile. (a) Hadsund terrain profile, (b) Pathloss at $970MHz$ with TM^z Polarization. | 171 |
| C-13 | Pathloss generated by ITIM, Hata Okumura model with multiple knife edge diffraction and measured data over Hjorringvej terrain profile. (a) Hjorringvej terrain profile, (b) Pathloss at $144MHz$ with TM^z Polarization. . . | 172 |
| C-14 | Pathloss generated by ITIM, Hata Okumura model with multiple knife edge diffraction and measured data over Hjorringvej terrain profile. (a) Hjorringvej terrain profile, (b) Pathloss at $435MHz$ with TM^z Polarization. . . | 173 |
| C-15 | Pathloss generated by ITIM, Hata Okumura model with multiple knife edge diffraction and measured data over Hjorringvej terrain profile. (a) Hjorringvej terrain profile, (b) Pathloss at $970MHz$ with TM^z Polarization. . . | 174 |

List of Tables

| | | |
|-----|--|-----|
| 3.1 | Flowchart of Improved Tabulated Interaction Method. | 56 |
| 3.2 | Computational Complexity and Memory Requirement of the proposed method | 66 |
| 3.3 | Comparison of run time (in seconds) of the proposed method and FBM. Operating Frequency: 435MHz. | 70 |
| 3.4 | Run time (in seconds) for different stages of the proposed method at differ- ent frequency. Terrain profile: Hadsund. | 70 |
| 3.5 | Run time (in seconds) and accuracy of proposed method with SL-ITIM and TL-ITIM at different group size. Terrain profile: Wicklow. Number of discretization points: 62464. | 70 |
| 3.6 | New Iterative Method for Electromagnetic Scattering From Flat Surfaces. . | 75 |
| 3.7 | Total run time (in seconds) and average number of iterations required to generate the basis functions (50 basis functions) for ITIM at different fre- quencies. | 81 |
| 4.1 | Mean (η) and standard deviation (σ) of error between Slope Diffraction Method (SDP), GFBM-FS and measurements | 90 |
| 5.1 | Average run time and number of iterations required to achieve residual error norm 10^{-4} . TM^z polarization. Autocorrelation function: Gaussian. Number of unknowns: 16384. | 115 |
| 5.2 | Average run time and number of iterations required to achieve residual error norm 10^{-4} . TE^z polarization. Autocorrelation function: Gaussian. Number of unknowns: 16384. | 115 |
| 5.3 | Average run time and number of iterations required to achieve residual error norm 10^{-4} . TM^z polarization. Autocorrelation function: Exponential. Number of unknowns: 25600. | 115 |
| 5.4 | Average run time and number of iterations required to achieve residual error norm 10^{-4} . TE^z polarization. Autocorrelation function: Exponential. Number of unknowns: 25600. | 116 |
| 5.5 | Emissivity of surfaces with Gaussian and Exponential Correlation Func- tions. $\sigma = 0.4\lambda$, $l_c = 2.0\lambda$ | 116 |
| 5.6 | Reflectivity, emissivity and energy conservation of rough surfaces. $h_{rms} =$ 0.2λ . $l_c = 1.0\lambda$. $\epsilon_r = 9.09 + 1.43i$ | 117 |

| | | |
|------|--|-----|
| 5.7 | Reflectivity, emissivity and energy conservation of rough surfaces. $h_{rms} = 0.2\lambda$. $l_c = 1.0\lambda$. $\epsilon_r = 15.57 + 3.71i$ | 117 |
| 5.8 | Reflectivity, emissivity and energy conservation of rough surfaces. $h_{rms} = 0.4\lambda$. $l_c = 1.0\lambda$. $\epsilon_r = 15.57 + 3.71i$ | 118 |
| 5.9 | Comparison of brightness temperature between the proposed method and measurement data. Roughness of the surfaces: $\sigma = 0.88cm$. Permittivity: $\epsilon_r = 19.2 + 2.41i$ | 118 |
| 5.10 | Comparison of brightness temperature between the proposed method and measurement data. Roughness of the surfaces: $\sigma = 2.60cm$. Permittivity: $\epsilon_r = 19.2 + 2.41i$ | 120 |
| 6.1 | Comparison of brightness temperature between the proposed method and measurement data. Roughness of the surfaces: $\sigma = 0.88cm$. Permittivity: $\epsilon_r = 19.2 + 2.41i$. Physical temperature: $300K$ | 141 |
| 6.2 | Comparison of brightness temperature between the proposed method and measurement data. Roughness of the surfaces: $\sigma = 2.60cm$. Permittivity: $\epsilon_r = 19.2 + 2.41i$. Physical temperature: $300K$ | 141 |
| 6.3 | Average run time (in seconds) and number of iterations required to achieve residual error norm 10^{-3} . TE Polarization. Size of the surface: $4\lambda \times 4\lambda$. Number of unknowns: 24576. | 144 |
| 6.4 | Average run time (in seconds) and number of iterations required to achieve residual error norm 10^{-3} . TM Polarization. Size of the surface: $4\lambda \times 4\lambda$. Number of unknowns: 24576. | 144 |
| 6.5 | Reflectivity, emissivity and energy conservation of rough surfaces. $h_{rms} = 0.4cm$. $l_c = 8.4cm$. Frequency: $f = 1.5GHz$ | 149 |
| 6.6 | Emissivity and Energy Conservation of rough surfaces. Permittivity: $\epsilon_r = 15.57 + 3.71i$. Incident angle: $\theta_i = 40^\circ$ | 150 |
| 6.7 | Emissivity and Energy Conservation of rough surfaces. Permittivity: $\epsilon_r = 9.09 + 1.43i$. Incident angle: $\theta_i = 40^\circ$ | 150 |
| C-1 | Mean (η) and standard deviation (σ) of error in dB between the ITIM and measurements. | 159 |
| C-2 | Mean (η) and standard deviation (σ) of error in dB between the HT-KED and measurements. | 159 |

1 Introduction

This dissertation focuses on the development of robust, efficient and accurate numerical methods to compute Electromagnetic (EM) wave propagation in urban and rural areas as well as scattering from random rough surfaces.

Electromagnetic wave propagation, underpinning many modern technologies, has revolutionized our daily life via a wide range of applications ranging from wireless communications, radar to medical imaging and remote sensing, etc. Typically an active wireless propagation system involves a transmitter to send the electromagnetic signal and a receiver to determine the transmitted signal and extract the desired information. The successful design of these EM propagation systems depends on the accurate modelling of the wireless channel. For example in order to install a cellular network, pathloss prediction is required for coverage planning. In addition, other physical quantities such as delay spread, angle of arrival and signal correlation which impact on the channel are governed by the propagation of EM waves. EM wave propagation models are necessary to predict these quantities and determine appropriate parameters (location, transmit power, tilt angle) for the base stations. In remote sensing applications, bistatic scattering coefficients are correlated to the root mean square (rms) height, correlation length and dielectric property of the rough surfaces and can be used to sense them. These applications require accurate propagation models to predict the scattering from such surfaces. It is clear that efficient and accurate modelling of electromagnetic wave propagation and scattering from surfaces remains a core requirement of many wireless technologies. A wide range of propagation models has been proposed to solve such scattering problems including empirical models, geometric optics, full-wave methods etc.

In this dissertation, full-wave methods based on the method of moments (MoM) and associated acceleration techniques used to improve their efficiency and performance are investigated. We focus on application of the MoM in two research areas: wave propagation in urban and rural areas and random rough surface scattering. The MoM offers high accuracy, only requires the discretisation of the rough boundary between the scatterer and the background medium and naturally satisfies the radiation condition at infinity through the use of suitable Green's functions. However, it results in a dense set of linear equations which requires computational complexity of $O(N^3)$, where N is the number of basis functions used in the MoM to solve directly. This dissertation introduces several novel techniques to overcome the limitations of the previously proposed methods yielding

more robust, efficient and accurate computational methods for EM wave scattering from surfaces including random rough surfaces and terrain profiles.

1.1 EM wave propagation in rural and urban areas

EM wave scattering from terrain profiles remains a core requirement in many commercial applications such as wireless system planning and has been studied extensively. Two main propagation scenarios under investigation in this dissertation are propagation in rural and urban areas. Many propagation models have been proposed to solve such scattering problems including empirical models, ray tracing models and full-wave methods. The first studies involving empirical models were carried out in the 1980s and included the Hata-Okumura method where measurement was recorded in the form of graphical information in Okumura's report and then generalized into equations by Hata [4, 5]. Due to the extremely low computational complexity, such empirical methods have been studied extensively and many related models have been proposed such as the well-known COST 231 [6], Walfish Ikegami model [7], etc. Despite the fact that the empirical models can be combined with multiple Knife Edge Diffraction (KED) theories such as Bullington [8], Epstein [9], Deygout [10] and Giovanelli [11], their accuracy remains limited. Note that the multiple KED theories are the extensions of the single KED [7] to calculate a total diffraction loss between adjacent edges and can be used to correct the total pathloss of the empirical models in the shadowed regions behind obstructions.

Another popular methods are ray-based methods including ray-tracing and ray launching. These methods identify the dominant rays from the transmitter to the receiver and compute the pathloss at the receiver by evaluating the fields associated with these rays. These dominant rays are those from the transmitter and receiver and based on line of sight, specular diffractions and reflections up to a certain order. Ray-based methods have been shown to provide a better accuracy than the empirical methods [12] and a wide range of ray-based models have been proposed including 2D horizontal models [13, 14, 15], 2D vertical models [16, 17], full 3D models [18, 19, 20, 21] and combination of these models [16]. 2D models, illustrated in Figure 1.2, provide a lower computational complexity than 3D models however they are only valid in certain scenarios. 2D horizontal models are only valid when the transmitter antenna is well below the average height of the buildings [13, 14, 15] while 2D vertical models are only valid when the walls are flat and the transmitter is sufficiently high that roof-top diffraction is the dominant mechanism [16, 17]. Full 3D ray tracing models, illustrated in Figure 1.1, are more general and hence valid in the regions where the 2D models are invalid. The computational burden of the 3D models is considerably higher than that of the 2D models and related to the determination of the rays. To reduce the computational complexity, some simplifications are usually applied, for example transmitted rays through buildings and scattering from trees and other

clutters are assumed small and hence neglected, etc. It is worth to note that these simplifications have also been investigated and it has been shown that in certain scenarios, the contributions from these elements are important [22, 23]. Despite these simplifications, identification of dominant rays still consumes more than 90% of CPU time of ray tracing models [18]. Many approaches have been developed to optimize the computational time required to determine these dominant rays such as the

bounding box method, triangular grid method [18], visibility-based method [24, 21], etc.

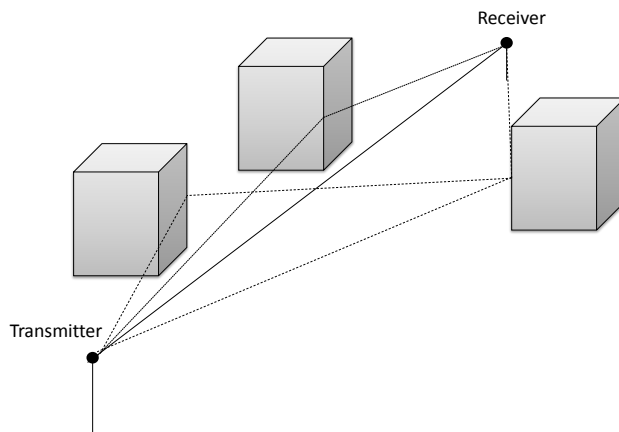


Figure 1.1: Illustration of full 3D ray tracing method.

Recently, full-wave methods such as Parabolic Equation (PE) method and Integral Equation (IE) method have become attractive because they offer high accuracy [25]. The parabolic equation was introduced by Leontovich in the 1940s to compute radiowave propagation around the Earth [26]. Since the 1980s, many numerical solutions have been proposed to solve the parabolic equation and they can be classified into two categories: finite difference method [27] and Fourier Transform based method [28]. The Parabolic Equation method has been extensively studied to model wave propagation in both rural areas and urban areas [29, 30, 31]. But validation against measurement data has not been performed for the case of urban areas.

Integral equation method is an alternative full-wave method. As stated earlier, the discretisation of the integral equations result in a dense set of linear equations which, for large scale problems such as terrain propagation, can only be solved using iterative methods. The integral equation methods have not been applied to the urban scenario due to the large scale of the problem. However they have been studied extensively for computing wave propagation in rural areas ever since the influential paper on the application of integral equation methods by Hviid *et al* [25]. Many techniques have been subsequently

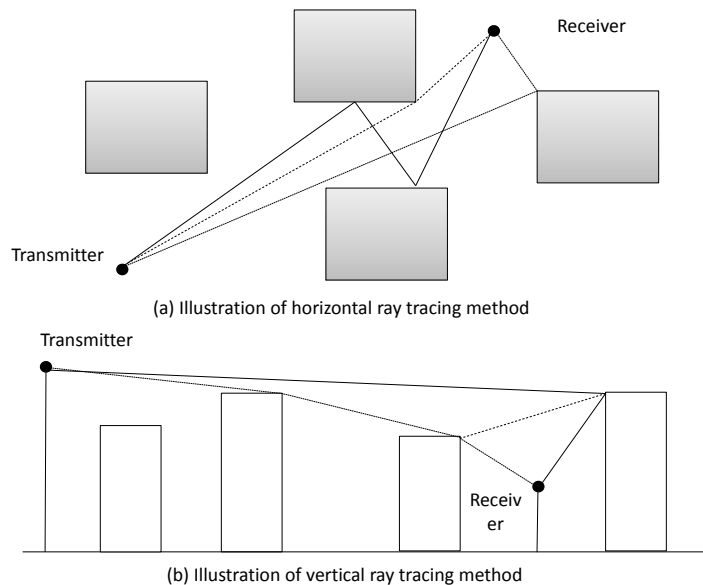


Figure 1.2: Illustration of horizontal and vertical ray tracing method.

proposed to accelerate the integral equation method. Commonly used Krylov-subspace based iterative techniques such as the conjugate gradient (CG) or the Generalized Minimal Residual (GMRES) methods [32, 33] are quite robust but can be very slowly convergent and require the use of effective preconditioners. In response to this limitation, the stationary iterative forward-backward method (FBM) [34, 35] has a very high convergence rate, yielding an accurate solution with considerably fewer iterations. The FBM method is equivalent to the symmetric successive over-relaxation (SSOR) scheme with a unit relaxation factor and zero initial guess vector [33]. However, the FBM requires a matrix-vector multiplication resulting in a $\mathcal{O}(N^2)$ computational complexity for each iteration making the FBM inefficient as the size of problem is increased. Different techniques have been developed to overcome this limitation of the FBM including acceleration methods such as the Forward Backward Method with Spectral Acceleration (FBM-SA) [35, 36, 37, 38], Fast Far Field Approximation (FAFFA) [39, 40, 41, 42], and compression techniques such as the Characteristic Basis Function Method (CBFM) [43, 44], etc. Among these techniques, the CBFM is a recent and interesting method because it is an iteration-free and efficient method [43, 44]. The CBFM constructs a reduced system using primary (PBFs) and secondary basis functions (SBFs) and solves the reduced system directly thereby not suffering from any convergence problems [43, 44]. However the CBFM uses individual basis functions for each block of the terrain profile and generates the reduced matrix using a Galerkin method with testing functions requiring huge computational cost.

1.2 EM wave scattering from random rough surfaces

The computation of EM wave scattering from randomly rough surfaces is also a classic problem with many important applications such as soil moisture estimation [45, 3, 46], sea surface salinity evaluation [47, 48], glacier monitoring, infrastructure defect detection, etc. In this dissertation, we focus on the application of random rough surface scattering to the soil moisture estimation. The distribution of soil moisture allows an improved estimation of land usage, water and energy transfers between land and atmosphere, resulting in more accurate weather prediction [3]. Bistatic scattering coefficients (BSC) and parameters calculated from the BSC such as emissivity, reflectivity of soil surfaces are directly related to their moisture content. These parameters can be used to sense the soil moisture of the surfaces via a microwave remote sensing system as demonstrated in Figure 1.3.

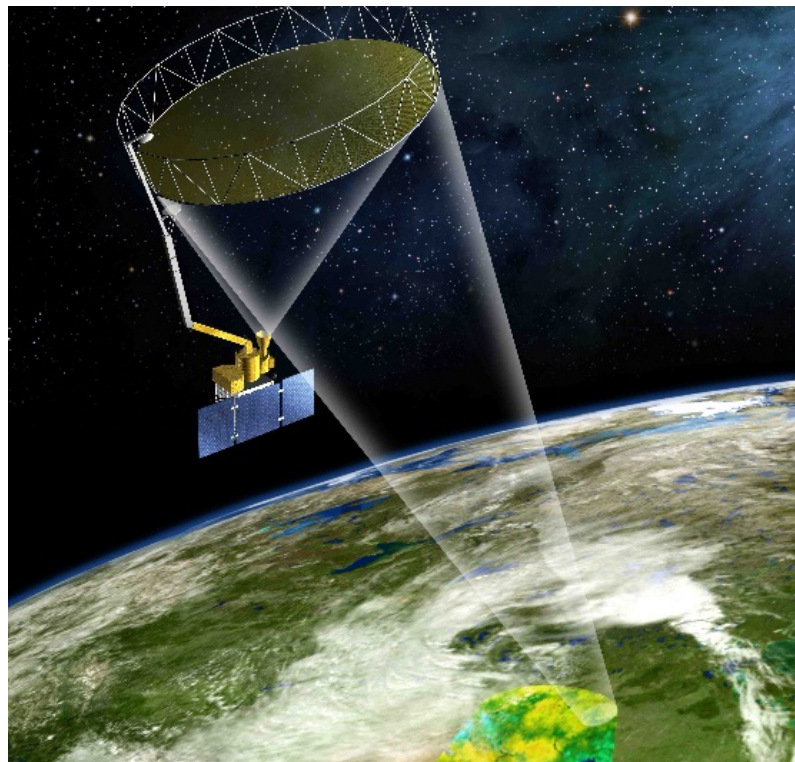


Figure 1.3: Illustration of Soil Moisture Active Passive (SMAP) mission, scheduled to launch by NASA in 2014 [3]

The first studies of random rough surface scattering were conducted in the 1950s and involved the development of analytical theories to compute the scattering from 1D rough surfaces. The theories developed include Kirchoff's approximation (KA) and the small perturbation method (SPM) [49]. Many authors have contributed to the development of these approximate analytical methods [50, 51]. However these analytical approaches are limited by their regime of validity. In the SPM, the perturbation series converge only if the surface heights are much smaller than the incident wavelength and the surface slope

is small while the KA fails to converge in the case of large surface slopes or large incident angles. More recently there has been an interest in full-wave methods, especially those based on the method of moments discretisation of boundary integral equations. The full-wave methods in conjunction with Monte Carlo simulation can be used to compute the scattering from surfaces in the cases where the analytical theories are invalid. However they result in a dense set of linear equations which, for large problems, can only be solved by using iterative methods. Many efficient numerical solutions have been proposed such as the Fast Multipole Method (FMM) [52, 53, 54, 55], the banded matrix iterative approach with canonical grid (BMIA/CAG) [56, 57, 58] for perfectly conducting (PEC) rough surfaces, the physics-based two grid method (PBTG) for dielectric surfaces [59, 60], etc. These methods are based on Krylov-subspace iterative methods such as the conjugate gradient (CG) or Generalized Minimal Residual (GMRES) methods [32, 33] whose computational complexity is dominated by the matrix-vector multiplication. The latter two methods proceed by distinguishing weakly interacting (far) regions from strongly interacting (near) regions for each observation point. The scattered field computation from far regions represents the majority of the computational burden and can be accelerated by using the Fast Fourier Transform (FFT). However, the BMIA/CAG was found to diverge frequently especially when the surfaces become more rough. Another popular technique is the Forward Backward Method (FBM) [34, 35]. The FBM outperforms the Krylov-subspace iterative methods in terms of the convergence rate, achieving similarly accurate results in much fewer iterations. Similar to the BMIA/CAG and PBTG which was accelerated by the FFT, the Spectral Acceleration (SA) was combined to reduce the computational complexity of the FBM from order $\mathcal{O}(N^2)$ to order $\mathcal{O}(N)$ [36, 37, 38, 61]. Recently an interesting technique in this area was introduced by Liu *et al* [62]. Liu *et al* method can be considered as the combination of the BMIA/CAG and the FBM-SA to reduce their respective limitations and enhance their advantages.

With the increasing computational capacities of modern computers and the 2D nature of actual rough surfaces, numerical solutions for the scattering from 2D surfaces, corresponding to the full 3D vector wave problem, have become more attractive. The full 3D vector wave scattering problem brings a great computational challenge even for a medium-sized problem. Several methods have been proposed to reduce the computational complexity such as the Fast Multipole Method (FMM), the Sparse Matrix Canonical Grid (SMCG) method [63, 64, 65, 66] which is an extension of the BMIA/CAG to a full 3D problem, the PBTG [67], the multilevel UV method [68, 69]. The operation of the SMCG is similar to that of the BMIA/CAG, the wave interactions are divided into near field and far field interactions. The near field interactions are computed directly while the far field interactions are accelerated by Fast Fourier Transforms (FFTs). Another interesting technique is the 3D FBM-SA which is an extension of the 2D FBM-SA in computing the wave scattering from 2D rough surfaces. The 3D FBM-SA was firstly developed for PEC surfaces [70] and then extended for impedance surfaces [71]. The 3D FBM-SA inherits the fast convergence

and the extremely low computational complexity from the 2D FBM-SA. However it was found to diverge frequently if applied to compute the wave scattering from 2D dielectric surfaces.

1.3 Dissertation overview

This dissertation proposes efficient and accurate numerical methods for computing EM wave scattering from terrain profiles and random rough surfaces. The remainder of this dissertation comprises six chapters organized as follows:

Chapter 2 describes the general scattering problem and the use of surface integral equations based on electric and magnetic field integral equations (EFIE and MFIE, respectively) in conjunction with the Method of Moments technique to solve the scattering problems numerically. The formulations for both two-dimensional and three-dimensional scattering are derived. These integral equations are extensively applied throughout this dissertation.

Chapters 3 and 4 discuss the numerical methods and acceleration techniques for 2D wave scattering in rural and urban areas. In Chapter 3 an efficient method is proposed for modelling electromagnetic wave propagation over lossy terrain profiles using a coupled surface integral equation formulation. The proposed method, referred to as the Improved Tabulated Interaction Method (ITIM), uses a common set of basis functions in conjunction with a simple matching technique to compress the original system into a reduced system containing a much smaller number of unknowns and therefore provide a very efficient and accurate method. The Tabulated Interaction Method (TIM) [40] is shown to be a particular case of the proposed method where only the lower triangular matrix of the reduced system is retained. Moreover, the Two-level ITIM (TL-ITIM) is applied to improve the accuracy of the ITIM in deep shadow areas. The ITIM is compared with the recently proposed Characteristic Basis Function Method (CBFM) [43, 44] with which it shares several features. It will be shown that the ITIM has an extremely low computational complexity and storage. Moreover, the accuracy of the proposed method is also investigated by comparing the path-loss against a precise solution and measured data.

The ITIM requires the generation of basis functions and tabulated far field patterns in the pre-processing phase. These basis functions are the equivalent electric and magnetic currents on a 1D flat surface illuminated by a plane wave. The calculation of these basis functions can be accelerated by a new FFT based method. The new iterative method is based on a similar implementation to the Conjugate Gradient Fast Fourier Transform (CG-FFT) [72], where the acceleration of the matrix-vector multiplications is achieved using the FFT. However, the iterative method proposed is not based on Krylov subspace expansions and is shown to converge faster than the GMRES-FFT while maintaining the computational complexity and memory usage of those methods. The details of the new FFT method are also described in Chapter 3.

In Chapter 4 the full-wave method, based on integral equation formulations, is proposed to compute electromagnetic scattering in urban areas. The unaccelerated full-wave method has a massive computational burden. In order to reduce the computational complexity, the Generalized Forward Backward Method (GFBM) is developed and applied (note that the conventional Forward Backward Method diverges in this scenario). The results generated by the proposed method show a very good agreement with measurement data.

Chapters 5 and 6 discuss the computation of 2D and 3D wave scattering from random rough surfaces. In Chapter 5 an efficient and accurate iterative method for computing EM scattering from 1D dielectric rough surfaces is introduced. The method is an extension of the Improved Forward Backward Method [73], applying it to the problem of 2D wave scattering from random lossy rough surfaces using a coupled surface integral equation formulation. In addition, a matrix splitting technique is introduced to reduce the number of matrix-vector multiplications required by the correction step and the Spectral Acceleration (SA)[36, 37] is applied to reduce the computational complexity of each matrix-vector product from $\mathcal{O}(N^2)$ to $\mathcal{O}(N)$. The proposed method is called the Improved Forward Backward Method with Spectral Acceleration (IFBM-SA) and is compared to both FBM-SA and a recent technique [62] which is used as a reference method in terms of convergence rate and run time required to achieve a desired relative error norm. The IFBM-SA has a higher convergence rate than the FBM-SA and the reference method. Moreover, the IFBM-SA is more robust than the reference method and has smaller storage requirements meaning that it can readily scale to larger problems. In addition an eigenvalue based analysis is provided to illustrate precisely how the improvement step works.

In Chapter 6 an efficient and accurate iterative method is proposed for computing 3D wave scattering from 2D dielectric random rough surfaces. The proposed method, referred to as the Block Forward Backward Method (BFBM), improves the convergence of the 3D FBM, making it converge for the case of 2D dielectric surfaces. In addition the Spectral Acceleration method is also modified and combined with the BFBM to reduce the computational complexity of the BFBM.

1.4 Contribution

This study constructs efficient and accurate numerical methods of EM wave scattering from surfaces including terrain profiles and random surfaces. The contribution details of this dissertation are described in Chapters 3,4,5 and 6 and are summarized below:

- **Improved Tabulated Interaction Method:** The formulation and application of the ITIM to compute the EM wave propagation over rural areas. Paper accepted for publication by IEEE Transactions on Antenna and Propagation.
- **New Fast Fourier Transform Method:** The formulation and application of a new

FFT method to accelerate the generation of basis functions and far fields patterns of the Improved Tabulated Method (ITIM) described in Chapter 3. Paper published by IEEE Transactions on Antenna and Propagation.

- **Generalized Forward Backward Method (GFBM) for computing wave propagation in urban areas:** Initial efforts in using the full-wave method to compute EM wave propagation in urban areas. The conventional FBM does not converge in the case of urban areas where the buildings have very sharp edges. In order to overcome this limitation of FBM, the Block FBM where the discretisation points are collected into groups has been proposed. The results generated by the proposed method are compared against the measurement data.
- **Improved Forward Backward Method with Spectral Acceleration (IFBM-SA):** An improved analysis which provides a more thorough explanation of the workings of the IFBM is provided, in this case in the context of scattering from lossy dielectrics. In addition, the computational complexity of the optimisation step is reduced from 2.5 matrix-vector products to 1 matrix-vector product (and 0.5 matrix-vector products in several special cases) and then the Spectral Acceleration (SA) is applied to reduce the complexity of the optimization step from $\mathcal{O}(N^2)$ to $\mathcal{O}(N)$. Paper published by IEEE Transactions on Antenna and Propagation.
- **2D Block Forward Backward Method with Spectral Acceleration (BFBM-SA):** The formulation and application of the BFBM to compute the full 3D wave scattering from 2D random rough surfaces. The SA is extended to combine with the BFBM to improve the computational efficiency of the BFBM. The results generated by the proposed method are compared against the measurement data.

2 Integral Equation Formulations

This chapter describes the general electromagnetic (EM) wave scattering problem and the use of surface electric and magnetic field integral equations (EFIE and MFIE, respectively) in conjunction with the Method of Moments technique to solve the problems numerically. In order to simplify the original scattering problems and surface equivalence principle are applied and described in Section 2.2. Then the formulations for both the two-dimensional (2D) scattering problem and three-dimensional (3D) scattering problem are derived in Section 2.4 and Section 2.5 respectively. Note that the 2D problem involves scattering from a 1D surface while the 3D problem involves scattering from a 2D surface. These integral equations are extensively applied throughout this dissertation as shown in Figure 2.1. In particular the surface integral equations for 2D problems are applied to solve the problem of terrain propagation for both rural areas and urban areas and will be discussed in detail in Chapters 3 and 4. They are also applied to solve the problem of wave scattering from 1D random rough surfaces whose details will be discussed in Chapter 5. In addition the surface integral equations for 3D problems are used to solve the scattering from 2D random rough surfaces and will be discussed in detail in Chapter 6.

2.1 Maxwell's equations and the scattering problem

We consider an inhomogeneous scatterer characterized by relative permittivity ϵ_r and permeability μ_r both of which are a function of location. This scatterer is illuminated by a primary source located outside of the scatterer as shown in Figure 2.2. The primary source generates incident electric and magnetic fields \bar{E}^{inc} and \bar{H}^{inc} . Note that these are defined to be the fields that would exist if the source was radiating in the absence of the scatterer, that is in the free space characterized by permittivity ϵ_0 and permeability μ_0 . The illuminated scatterer produces an induced source generating the scattered fields \bar{E}^{scat} and \bar{H}^{scat} . The total fields \bar{E} and \bar{H} in the presence of the scatterer are the superposition of the incident and scattered fields [74]

$$\bar{E} = \bar{E}^{inc} + \bar{E}^{scat}, \quad (2.1)$$

$$\bar{H} = \bar{H}^{inc} + \bar{H}^{scat}. \quad (2.2)$$

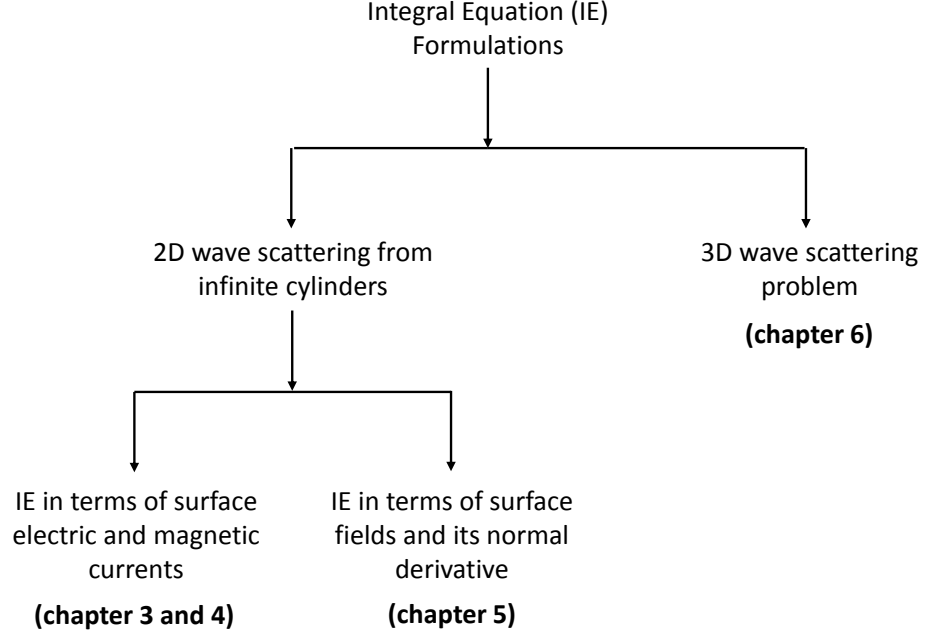


Figure 2.1: Classification of integral equation formulations used in this dissertation

The electric field \bar{E}^{inc} and magnetic field \bar{H}^{inc} in the free-space environment must satisfy the frequency-domain Maxwell's equation

$$\nabla \times \bar{E}^{inc} = -K_i - i\omega\mu_0\bar{H}^{inc}, \quad (2.3)$$

$$\nabla \times \bar{H}^{inc} = J_i + i\omega\epsilon_0\bar{E}^{inc} \quad (2.4)$$

where (J_i, K_i) denote the electric and magnetic source density respectively. The time dependence $e^{j\omega t}$ is assumed and suppressed. In order to determine the scattered fields, the volume equivalence principle is applied. The original problem is converted into an equivalent problem by replacing the scatterer by equivalent induced currents. When the primary sources (J_i, K_i) radiate in the absence of the scatterer, the electric field and magnetic field satisfy

$$\nabla \times \bar{E} = -K_i - i\omega\mu_0\mu_r\bar{H}, \quad (2.5)$$

$$\nabla \times \bar{H} = J_i + i\omega\epsilon_0\epsilon_r\bar{E}. \quad (2.6)$$

Equation (2.3)-(2.6) can be rewritten to produce

$$\nabla \times \bar{E}^s = -i\omega\mu_0\bar{H}^s - \bar{K}, \quad (2.7)$$

$$\nabla \times \bar{H}^s = i\omega\epsilon_0\bar{E}^s + \bar{J} \quad (2.8)$$

where presence of difference between the fields in the free space environment $\bar{E}^{inc}, \bar{H}^{inc}$ and the fields in the scatterer \bar{E}, \bar{H} are referred as the scattered fields

$$\bar{E}^s = \bar{E} - \bar{E}^{inc}, \quad (2.9)$$

$$\bar{H}^s = \bar{H} - \bar{H}^{inc} \quad (2.10)$$

and they can be expressed in terms of volume equivalent induced electric and magnetic current densities \bar{J}, \bar{K} which exist only in the region where $\epsilon_r \neq 1$ and $\mu_r \neq 1$ (only in the inhomogeneous scatterer) radiating in a free-space environment

$$\bar{K} = i\omega\mu_0(\mu_r - 1)\bar{H}, \quad (2.11)$$

$$\bar{J} = i\omega\epsilon_0(\epsilon_r - 1)\bar{E}. \quad (2.12)$$

Although the formulation seems to be simplified, it is still difficult to solve the total electric and magnetic field \bar{E}, \bar{H} because the current densities \bar{J}, \bar{K} are a function of total \bar{E} and \bar{H} fields. The total \bar{E} and \bar{H} fields are obtained by the superposition of the individual current densities \bar{J} and \bar{K} . When only the electric source of current density \bar{J} exists, Maxwell's equation (2.7)-(2.8) is written as

$$\nabla \times \bar{E}^s = -i\omega\mu_0\bar{H}^s, \quad (2.13)$$

$$\nabla \times \bar{H}^s = i\omega\epsilon_0\bar{E}^s + \bar{J}. \quad (2.14)$$

In this case then the magnetic field \bar{H}^s can be expressed in terms of a magnetic vector potential \bar{A}

$$\bar{H}_A^s = \nabla \times \bar{A}. \quad (2.15)$$

Substituting (2.15) into (2.13), we get

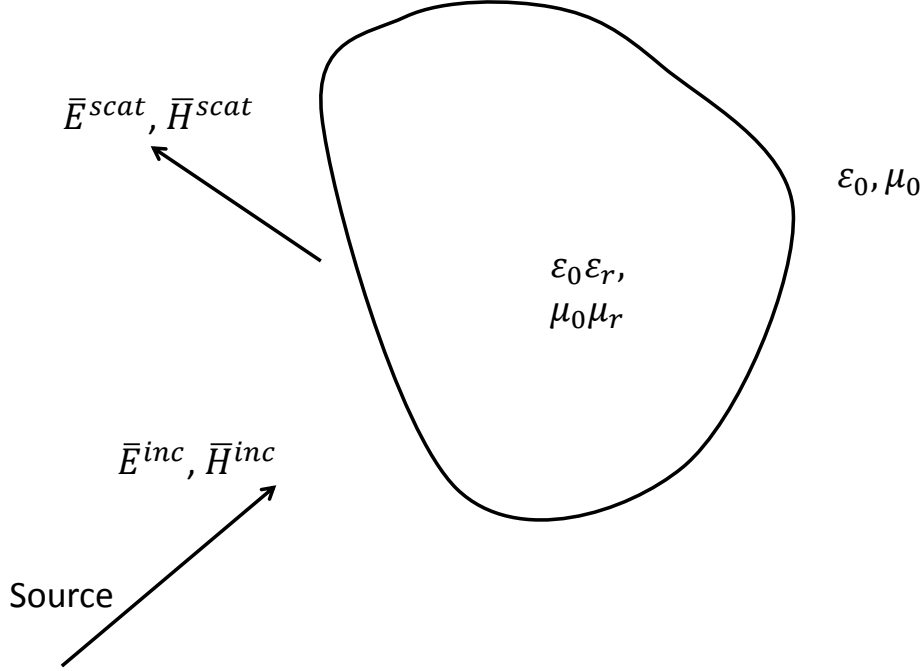


Figure 2.2: The scattering Problem

$$\nabla \times (\bar{E}_A^s + i\omega\mu_0\bar{A}) = 0. \quad (2.16)$$

An arbitrary electric scalar potential ϕ_e where $\nabla \times (\nabla\phi_e) = 0$ is employed to obtain the solution of the electric scattered field

$$\bar{E}_A^s = -i\omega\mu_0\bar{A} - \nabla\phi_e. \quad (2.17)$$

Equation (2.15) and (2.17) are combined with (2.14) and using the vector identity $\nabla \times \nabla \times \bar{A} = \nabla(\nabla \cdot \bar{A}) - \nabla^2\bar{A}$, the magnetic vector potential \bar{A} must satisfy

$$\nabla^2\bar{A} + k_0^2\bar{A} = -\bar{J} + \nabla(\nabla \cdot \bar{A} + i\omega\epsilon_0\phi_e) \quad (2.18)$$

where $k_0 = \omega\sqrt{\mu_0\epsilon_0}$ is the wave number of free-space. The curl of the potential vector \bar{A} has already been defined however its divergence has not been defined. In order to simplify the solution of (2.18), the divergence of \bar{A} is chosen to satisfy $\nabla \cdot \bar{A} = -i\omega\epsilon_0\phi_e$ which simplifies (2.18) to

$$\nabla^2 \bar{A} + k_0^2 \bar{A} = -\bar{J}. \quad (2.19)$$

Now the electric and scattered fields can be expressed in terms of magnetic vector potential \bar{A}

$$\bar{E}_A^s = \frac{\nabla \nabla \cdot \bar{A} + k_0^2 \bar{A}}{i\omega\epsilon_0}, \quad (2.20)$$

$$\bar{H}_A^s = \nabla \times \bar{A} \quad (2.21)$$

where \bar{A} can be written in terms of a convolution of the electric current density \bar{J} and the Greens's function

$$\bar{A}(\bar{r}) = \iiint \bar{J}(\bar{r}') G(\bar{r}, \bar{r}') d\bar{r}' \quad (2.22)$$

where the three-dimensional Green's function is given by

$$G(\bar{r}, \bar{r}') = \frac{e^{-ik_0|\bar{r}-\bar{r}'|}}{4\pi|\bar{r}-\bar{r}'|}. \quad (2.23)$$

When only the magnetic source of current density \bar{K} exists, the Maxwell's equation (2.7)-(2.8) is written as

$$\nabla \times \bar{E}^s = -i\omega\mu_0 \bar{H}^s - \bar{K}, \quad (2.24)$$

$$\nabla \times \bar{H}^s = i\omega\epsilon_0 \bar{E}^s. \quad (2.25)$$

Due to the symmetry of Maxwell's equations, a similar expression of the scattered fields in terms of an electric vector potential \bar{F} can be derived

$$\bar{E}_F^s = -\nabla \times \bar{F}, \quad (2.26)$$

$$\bar{H}_F^s = \frac{\nabla \nabla \cdot \bar{F} + k_0^2 \bar{F}}{i\omega\mu_0} \quad (2.27)$$

where \bar{F} can be written in terms of a convolution of the magnetic current density \bar{K} and the Greens's function

$$\bar{F}(\bar{r}) = \iiint \bar{K}(\bar{r}') G(\bar{r}, \bar{r}') d\bar{r}' = \iiint \bar{K}(\bar{r}') \frac{e^{-ik_0|\bar{r}-\bar{r}'|}}{4\pi|\bar{r}-\bar{r}'|} d\bar{r}'. \quad (2.28)$$

When both the electric and magnetic source of current densities \bar{J} and \bar{K} are present, equation (2.20), (2.26) and (2.21), (2.27) are combined to give

$$\bar{E}^s = \frac{\nabla\nabla \cdot \bar{A} + k_0^2 \bar{A}}{i\omega\epsilon_0} - \nabla \times \bar{F}, \quad (2.29)$$

$$\bar{H}^s = \frac{\nabla\nabla \cdot \bar{F} + k_0^2 \bar{F}}{i\omega\mu_0} + \nabla \times \bar{A} \quad (2.30)$$

2.2 Surface Integral Equations for homogeneous scatterers

2.2.1 Surface equivalence principle

In the previous section, it has been demonstrated that the equivalent electric and magnetic sources existing in the scatterer can be used to replace the inhomogeneous dielectric scatterer. In the case of EM wave scattering from an homogeneous scatterer, the surface equivalence principle can be applied to simplify the problem. By the surface equivalence principle, the dielectric scatterer is replaced with equivalent sources distributed on the surface separating the two environments. The fields outside the surface are obtained by convolving suitable surface electric and magnetic current densities with the free space Greens function. We consider electric and magnetic currents \bar{J}_1 and \bar{K}_1 radiating the field \bar{E}_1 and \bar{H}_1 in a homogeneous environment characterized by the permittivity ϵ_1 and permeability μ_1 . In order to create the equivalent problem, a closed surface is created to separate the space into two different regions as shown in Figure 2.3a. The equivalent sources \bar{J}_s and \bar{K}_s are placed on the surface and radiate into the unbounded space as shown in Figure 2.3b

$$\bar{J}_s = \hat{n} \times (\bar{H}_1 - \bar{H}_2) \quad (2.31)$$

$$\bar{K}_s = -\hat{n} \times (\bar{E}_1 - \bar{E}_2) \quad (2.32)$$

The equivalent sources \bar{J}_s and \bar{K}_s only produce the original fields \bar{E}_1 and \bar{H}_1 outside the surface and only valid in this region. Note that the fields \bar{E}_1 and \bar{H}_1 need to be known on the surface. Since the field inside is not the region of interest, we can assume that they are zero. Then the equivalent sources can be represented in terms of the original fields \bar{E}_1 and \bar{H}_1

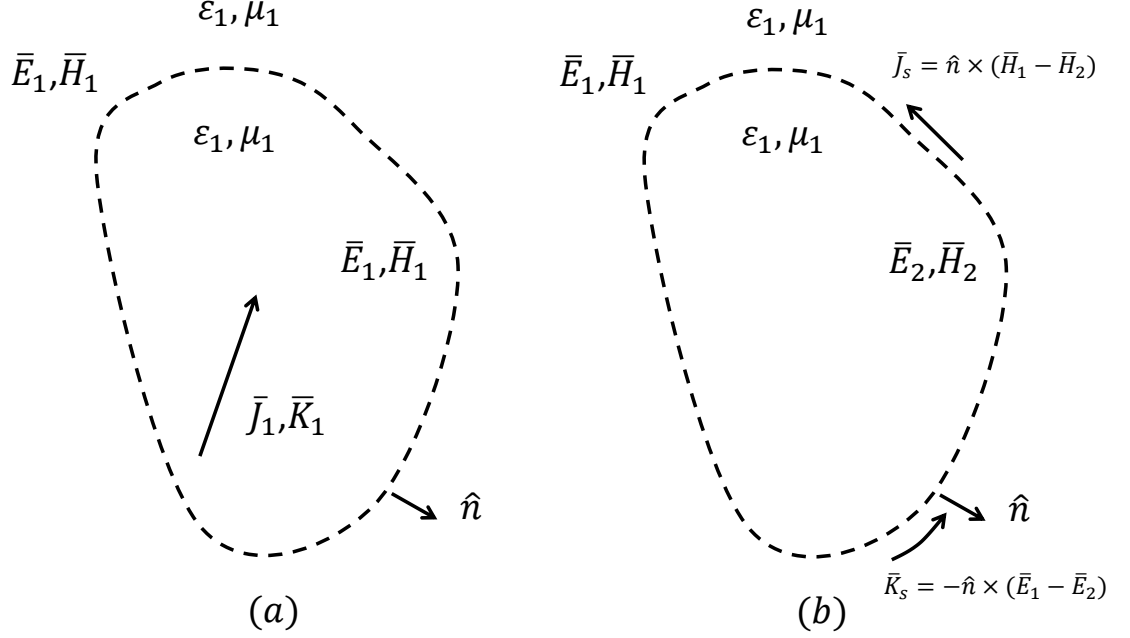


Figure 2.3: (a) Actual problem (b) Equivalent problem

$$\bar{J}_s = \hat{n} \times \bar{H}_1 \quad (2.33)$$

$$\bar{K}_s = -\hat{n} \times \bar{E}_1 \quad (2.34)$$

2.2.2 Surface Integral Equations for homogeneous scatterers

Figure 2.4 shows a dielectric homogeneous body illuminated by an incident EM field. The first region (region 1) is free space characterized by relative permittivity ϵ_0 and permeability μ_0 . The second region (region 2) is a homogeneous scatterer characterized by relative permittivity ϵ_r and permeability μ_r . \bar{E}_1 and \bar{H}_1 denote the electric field and magnetic field in free space (region 1) and \bar{E}_2 and \bar{H}_2 denote the electric field and magnetic field in the scatterer (region 2). Applying the surface equivalent principle [74, 75, 76], we obtain two problems: an equivalent exterior problem and an interior problem as shown in Figure 2.4, Figure 2.5 and Figure 2.6. The electric and magnetic field in region 1, \bar{E}_1 and \bar{H}_1 , generate the equivalent sources \bar{J}_1 and \bar{K}_1 associated with the equivalent exterior problem while the electric and magnetic field in region 2, \bar{E}_2 and \bar{H}_2 , generate the equiv-

alent sources \bar{J}_2 and \bar{K}_2 associated with the equivalent exterior problem. These sources are defined so that

$$\bar{J}_1 = \hat{n} \times \bar{H}_1 \quad (2.35)$$

$$\bar{K}_1 = -\hat{n} \times \bar{E}_1 \quad (2.36)$$

$$\bar{J}_2 = -\hat{n} \times \bar{H}_2 \quad (2.37)$$

$$K_2 = \hat{n} \times \bar{E}_2 \quad (2.38)$$

where \hat{n} is the normal vector pointing into region 1. Applying the boundary condition of continuity of the tangential \bar{E} and \bar{H} field on the surface separating the two regions, we obtain

$$\bar{J}_1 = -\bar{J}_2 \quad (2.39)$$

$$\bar{K}_1 = -\bar{K}_2 \quad (2.40)$$

From equation (2.1), (2.29) and (2.35)-(2.40), we obtain the coupled electric field integral equations (EFIEs)

$$\hat{n} \times \bar{E}^{inc} = -\bar{K}_1 - \hat{n} \times \left\{ \frac{\nabla \nabla \cdot \bar{A}_1 + k_0^2 \bar{A}_1}{i\omega \epsilon_0} - \nabla \times \bar{F}_1 \right\}_{S^+} \quad (2.41)$$

$$0 = \bar{K}_1 - \hat{n} \times \left\{ \frac{\nabla \nabla \cdot \bar{A}_2 + k_1^2 \bar{A}_2}{i\omega \epsilon_0 \epsilon_r} - \nabla \times \bar{F}_2 \right\}_{S^-} \quad (2.42)$$

where

$$\bar{A}_1(\bar{r}) = \iiint \bar{J}_1(\bar{r}') \frac{e^{-ik_0|\bar{r}-\bar{r}'|}}{4\pi|\bar{r}-\bar{r}'|} d\bar{r}' \quad (2.43)$$

$$\bar{F}_1(\bar{r}) = \iiint \bar{K}_1(\bar{r}') \frac{e^{-ik_0|\bar{r}-\bar{r}'|}}{4\pi|\bar{r}-\bar{r}'|} d\bar{r}' \quad (2.44)$$

$$\bar{A}_2(\bar{r}) = \iiint \bar{J}_1(\bar{r}') \frac{e^{-ik_1|\bar{r}-\bar{r}'|}}{4\pi|\bar{r}-\bar{r}'|} d\bar{r}' \quad (2.45)$$

$$\bar{F}_2(\bar{r}) = \iiint \bar{K}_1(\bar{r}') \frac{e^{-ik_1|\bar{r}-\bar{r}'|}}{4\pi|\bar{r}-\bar{r}'|} d\bar{r}' \quad (2.46)$$

Note that the subscript S^+ means that the function in the bracket is evaluated an infinitesimal distance outside the surface of the scatterer. In contrast, the subscript S^- means

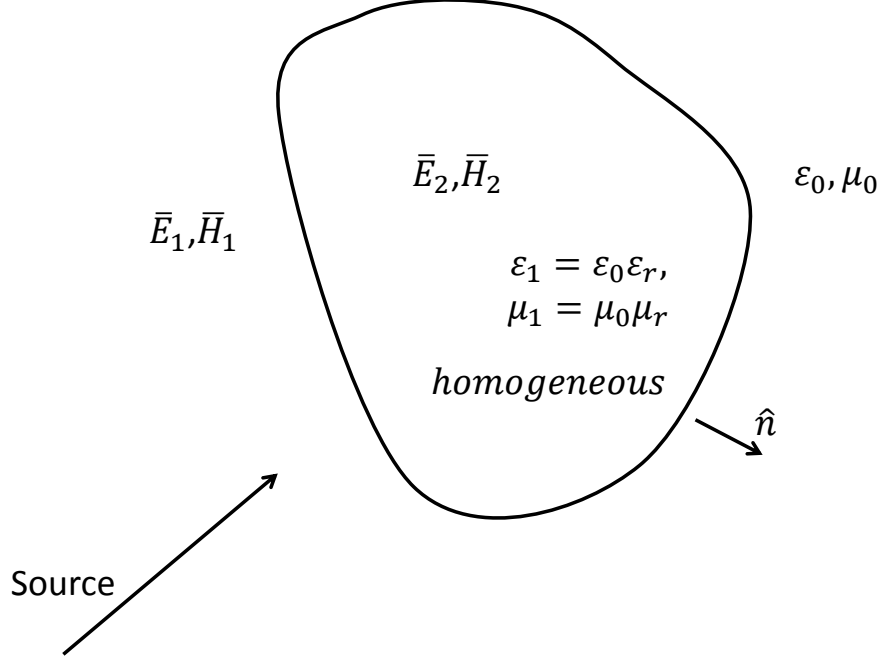


Figure 2.4: Original Problem

that the function in the bracket is evaluated an infinitesimal distance inside the surface of the scatterer. $k_0 = \omega\sqrt{\mu_0\epsilon_0}$ and $k_1 = \omega\sqrt{\mu_1\epsilon_1}$ are the wave numbers in free-space and in the medium respectively where $\epsilon_1 = \epsilon_0\epsilon_r$ and $\mu_1 = \mu_0\mu_r$, $\eta_0 = \sqrt{\mu_0/\epsilon_0}$ and $\eta_1 = \sqrt{\mu_1/\epsilon_1}$ are the intrinsic impedance of free-space and of the medium respectively. Hence $\omega\epsilon_0 = k_0/\eta_0$ and $\omega\epsilon_1 = k_1/\eta_1$. Note that the left hand side (LHS) of equation (2.41) is $\hat{n} \times \bar{E}^{inc}$ which represents the incident field illuminating the outer surface of the scatterer. In contrast the interior surface of the scatterer is not illuminated by any incident field therefore the LHS of equation (2.42) is zero. In the same manner, coupled magnetic field integral equations (MFIEs) are obtained from equation (2.30) and (2.35)-(2.40)

$$\hat{n} \times \bar{H}^{inc} = \bar{J}_1 - \hat{n} \times \left\{ \frac{\nabla \nabla \cdot \bar{F}_1 + k_0^2 \bar{F}_1}{i\omega\mu_0} + \nabla \times \bar{A}_1 \right\}_{S^+} \quad (2.47)$$

$$0 = -\bar{J}_1 - \hat{n} \times \left\{ \frac{\nabla \nabla \cdot \bar{F}_2 + k_1^2 \bar{F}_2}{i\omega\mu_1} + \nabla \times \bar{A}_2 \right\}_{S^-} \quad (2.48)$$

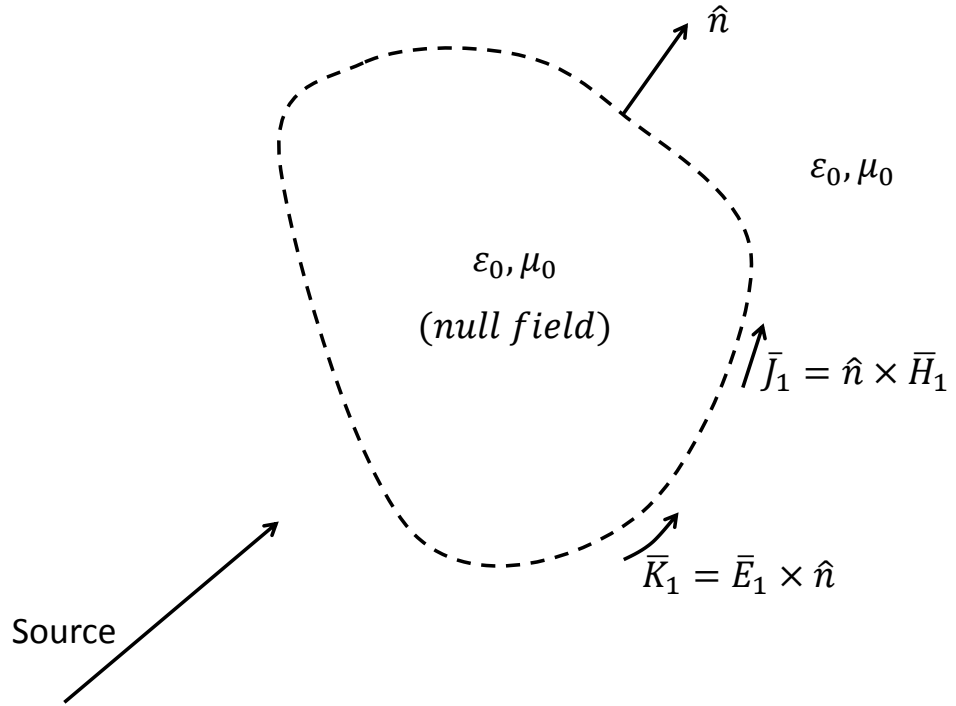


Figure 2.5: Equivalent exterior problem associated with the homogeneous object in Figure 2.4

2.3 Method of Moments

The method of moments (MoM) is a technique used to discretise surface integral equations into systems of linear equations which can be solved numerically. We consider a general linear equation

$$Lf = b \quad (2.49)$$

where f is the unknown continuous function, L is the linear operator acting on f and b is the excitation function.

The MoM constructs an approximation to the unknown function f that is defined using a set of known basis function p_m , $m = 1, \dots, M$.

$$f \simeq \sum_{m=1}^M j_m p_m \quad (2.50)$$

where j_m , $m = 1, \dots, M$ are the to be determined weighted parameters of the basis func-

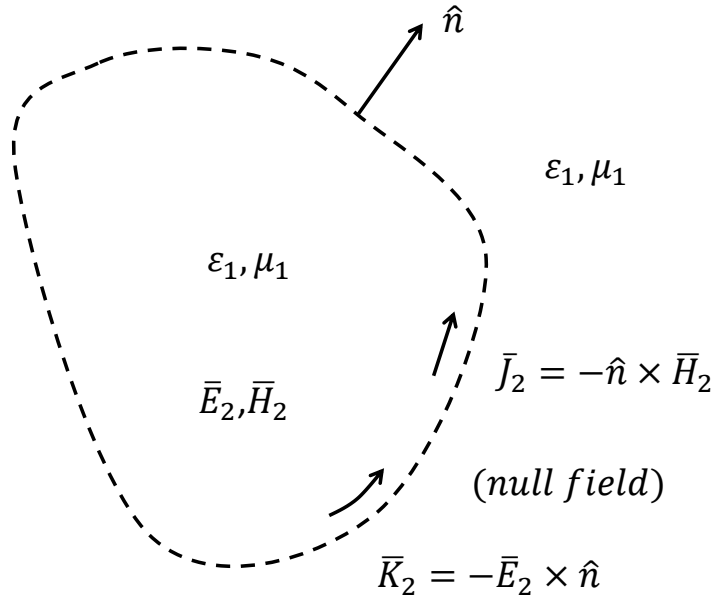


Figure 2.6: Equivalent interior problem associated with the homogeneous object in Figure 2.4

tions. The original problem of identifying the continuous function f reduces to that of identifying the M unknown parameters j_m . Equation (2.50) is substituted into (2.49) to obtain

$$\sum_{m=1}^M j_m L p_m = b \quad (2.51)$$

The residual of the linear equation is given by

$$r_m = \sum_{m=1}^M j_m L p_m - b \quad (2.52)$$

To solve equation (2.51), we minimize equation (2.52) by taking the inner product of both sides with the testing functions $t = \{t_1, t_2, \dots, t_M\}$ to generate a matrix equation. This results in an $M \times M$ system of linear equations where the unknowns are the weighted parameters j_m , $m = 1, \dots, M$

$$\sum_{m=1}^M j_m \langle t_n, Lp_m \rangle = \langle t_n, b \rangle \quad n = 1, 2, \dots, M \quad (2.53)$$

where $\langle \cdot, \cdot \rangle : \mathbb{V} \times \mathbb{V} \rightarrow \mathbb{C}$ represents the Hermitian inner product. Equation (2.53) can be written in the matrix form

$$\overline{\overline{Z}} \overline{x} = \overline{v} \quad (2.54)$$

where

$$\overline{\overline{Z}} = \begin{bmatrix} \langle t_1, Lp_1 \rangle & \langle t_1, Lp_2 \rangle & \cdots & \langle t_1, Lp_M \rangle \\ \langle t_2, Lp_1 \rangle & \langle t_2, Lp_2 \rangle & \cdots & \langle t_2, Lp_M \rangle \\ \vdots & \vdots & \ddots & \vdots \\ \langle t_M, Lp_1 \rangle & \langle t_M, Lp_2 \rangle & \cdots & \langle t_M, Lp_M \rangle \end{bmatrix} \quad (2.55)$$

$$\overline{x} = \begin{bmatrix} j_1 \\ j_2 \\ \vdots \\ j_M \end{bmatrix} \quad (2.56)$$

$$\overline{v} = \begin{bmatrix} \langle t_1, b \rangle \\ \langle t_2, b \rangle \\ \vdots \\ \langle t_M, b \rangle \end{bmatrix} \quad (2.57)$$

The choice of the basis functions has an important role in the numerical solution. The chosen basis function should have the ability to reasonably represent the unknown function throughout its domain while minimizing the required computational costs to evaluate the MoM matrix elements. Basis functions can be divided into two classes. The first class uses the sub-domain functions and requires the subdivision of the scattering surface into non-overlapping segments while the second class involves the entire domain functions and does not require the subdivision of the scattering surface. The most common sub-domain basis functions are the pulse basis functions. Pulse basis functions comprise of a simple approximation over each segment of the scattering surface but they significantly reduce the computation cost of the matrix elements. Piecewise triangular and piecewise sinusoidal basis functions generate smoother representations of the unknown function but also require a higher computational cost to evaluate the matrix elements. Unlike sub-domain basis functions, the entire-domain functions are defined over the entire surface and more suitable for problems where the unknown functions follows a known pattern.

The use of sub-domain basis functions in the MoM requires the subdivision of the scattering surface. There are two main approaches to model these surfaces: wire-grid models and patch models. In the wire-grid model, the surface is modelled as a wire-mesh while in the surface patch model, the surface is partitioned into arbitrary-shaped patches. The wire-grid model has been widely applied in many problems and shown success in those that require the prediction of far-field quantities such as radar cross section (RCS) [77]. However the wire-grid model has many limitations and is not used to compute near field quantities as shown in [78]. These limitations can be overcome by using the surface patch models. Rao, Wilton and Glisson generalized the use of triangular patches for modelling arbitrary shaped objects [77] and developed special basis functions on the triangular patches which has since been referred to as the Rao-Wilton-Glisson (RWG) basis functions. Recently higher order basis functions [79, 80, 81, 82] have received much attention because of their ability to represent the surface fields/currents and model geometries more accurately than the conventional low-order basis functions [83].

Another recent class of basis functions is the Characteristic Basis Function (CBF). The CBF is defined on a large domain of the scatterer. The Characteristic Basis Function Method (CBFM) constructs the reduced system by using primary (PBFs) and secondary basis functions (SBFs) and solves the reduced system directly. The CBFM is similar to the Tabulated Interaction Method and its details will be discussed in Chapter 3.

2.4 Wave scattering from infinite cylinders

In this section, we begin the investigation of numerical techniques for solving the scattering from the two-dimensional problems. Two-dimensional problems are those whose the third dimension is invariant such as an infinite cylinder illuminated by a field that does not vary along the axis of the cylinder [74]. An example of infinite cylinder illuminated by an infinite line source and its cross section are shown in Figure 2.7. Surface integral equations for two-dimensional (2D) problems can be written in terms of electric and magnetic currents and are a special case of 2.41, 2.42 and 2.47, 2.48. This formulation is widely used in the research of wave propagation for both rural areas and urban areas which will be discussed in detail in Chapters 3 and 4. However the surface integral equations for 2D problems are also conveniently expressed in terms of surface field and its normal derivative. This formulation of integral equations in contrast are widely applied to compute the scattering from 1D random rough surfaces, details of which will be discussed in Chapter 5. Both formulations are equivalent and will be investigated in this section.

$$\hat{n} \times \frac{k_0^2 \bar{A}_1}{i\omega\epsilon_0} = ik_0\eta_0 A_z^{(1)} \hat{t} \quad (2.60)$$

$$\hat{n} \times \frac{k_1^2 \bar{A}_2}{i\omega\epsilon_1} = ik_1\eta_1 A_z^{(2)} \hat{t} \quad (2.61)$$

where \hat{t} is the unit vector tangent to the scatterer contour as illustrated in Figure 2.7b. Other components of the EFIE equations (2.58) and (2.59) can be expressed as

$$\hat{n} \times \bar{E}^{inc} = -E_z^{inc} \hat{t} \quad (2.62)$$

$$\bar{K}_1 = -\hat{n} \times \bar{E}_1 = E_z \hat{t} = K_t \hat{t} \quad (2.63)$$

$$\hat{n} \times \nabla \times \bar{F}_1 = - \left\{ \frac{\partial F_y^{(1)}}{\partial x} - \frac{\partial F_x^{(1)}}{\partial y} \right\} \hat{t} \quad (2.64)$$

$$\hat{n} \times \nabla \times \bar{F}_2 = - \left\{ \frac{\partial F_y^{(2)}}{\partial x} - \frac{\partial F_x^{(2)}}{\partial y} \right\} \hat{t} \quad (2.65)$$

Therefore, the EFIE equations (2.58) and (2.59) can be specialized in the case of TM^z -wave polarization

$$E_z^{inc}(t) = K_t(t) + ik_0\eta_0 A_z^{(1)} + \left\{ \frac{\partial F_y^{(1)}}{\partial x} - \frac{\partial F_x^{(1)}}{\partial y} \right\}_{S^+} \quad (2.66)$$

$$0 = K_t(t) - ik_1\eta_1 A_z^{(2)} - \left\{ \frac{\partial F_y^{(2)}}{\partial x} - \frac{\partial F_x^{(2)}}{\partial y} \right\}_{S^-} \quad (2.67)$$

where t is a variable denoting the position around the contour of the cylinder. Note that, in the case of two-dimensional problem, the integration over the z dimension used to compute the magnetic potential A and electric potential F only involves the Green's function and can be performed analytically [74]

$$\int_{z=-\infty}^{z=+\infty} \frac{e^{-ik\sqrt{\rho^2+z^2}}}{4\pi\sqrt{\rho^2+z^2}} dz = G(\bar{\rho}, \bar{\rho}') \quad (2.68)$$

where $G(\bar{\rho}, \bar{\rho}')$ is the two-dimensional Green's function and can be written in the form of a Hankel function of the second kind

$$G_\alpha(\bar{\rho}, \bar{\rho}') = \frac{1}{4i} H_0^2(k_\alpha |\bar{\rho} - \bar{\rho}'|), \quad \alpha = 0, 1 \quad (2.69)$$

From equation (2.68) and (2.43)-(2.46), the magnetic potential A_z and electric potential F_t now can be expressed in the form of the two-dimensional Green's function

$$A_z^{(\alpha)} = \int J_z(t') G_\alpha(\bar{\rho}, \bar{\rho}') dt' \quad (2.70)$$

$$F_t^{(\alpha)} = \int \hat{t}(t') K_t(t') G_\alpha(\bar{\rho}, \bar{\rho}') dt' \quad (2.71)$$

The term $\left\{ \frac{\partial F_y^{(\alpha)}}{\partial x} - \frac{\partial F_x^{(\alpha)}}{\partial y} \right\}$; $\alpha = 0, 1$ can be written in the form of the normal derivative of the Green's function

$$\left\{ \frac{\partial F_y^{(\alpha)}}{\partial x} - \frac{\partial F_x^{(\alpha)}}{\partial y} \right\} = - \int K_t(t') [\hat{n}' \cdot \nabla G_\alpha(\bar{\rho}, \bar{\rho}')] dt' \quad (2.72)$$

Now, the EFIE equations (2.66) and (2.67) can be written in the terms of surface electric current J_z and surface magnetic current K_t

$$E_z^{inc}(t) = K_t(t) + ik_0\eta_0 \int J_z(t') G_0(\bar{\rho}, \bar{\rho}') dt' - \int K_t(t') [\hat{n}' \cdot \nabla G_0(\bar{\rho}, \bar{\rho}')] dt' \quad (2.73)$$

$$0 = K_t(t) - ik_1\eta_1 \int J_z(t') G_1(\bar{\rho}, \bar{\rho}') dt' + \int K_t(t') [\hat{n}' \cdot \nabla G_1(\bar{\rho}, \bar{\rho}')] dt' \quad (2.74)$$

In order to solve the EFIEs, the MoM is applied. The cylinder contour is divided into N cells, each cell has the centre of (x_m, y_m) and a length of ω_m as illustrated in Figure 2.8. The equivalent currents are approximated by a superposition of basis functions

$$J_z(t) = \sum_{n=1}^N j_n p_n(t) \quad (2.75)$$

$$K_t(t) = \sum_{n=1}^N k_n p_n(t) \quad (2.76)$$

where pulse basis functions are used to represent the electric and magnetic current J_z, K_t . These are defined as

$$p_n(t) = \begin{cases} 1 & \text{if } t \in \text{cell } n \\ 0 & \text{otherwise} \end{cases} \quad (2.77)$$

Substituting equations (2.75) and (2.76) into the EFIE equations (2.73), (2.74), we obtain

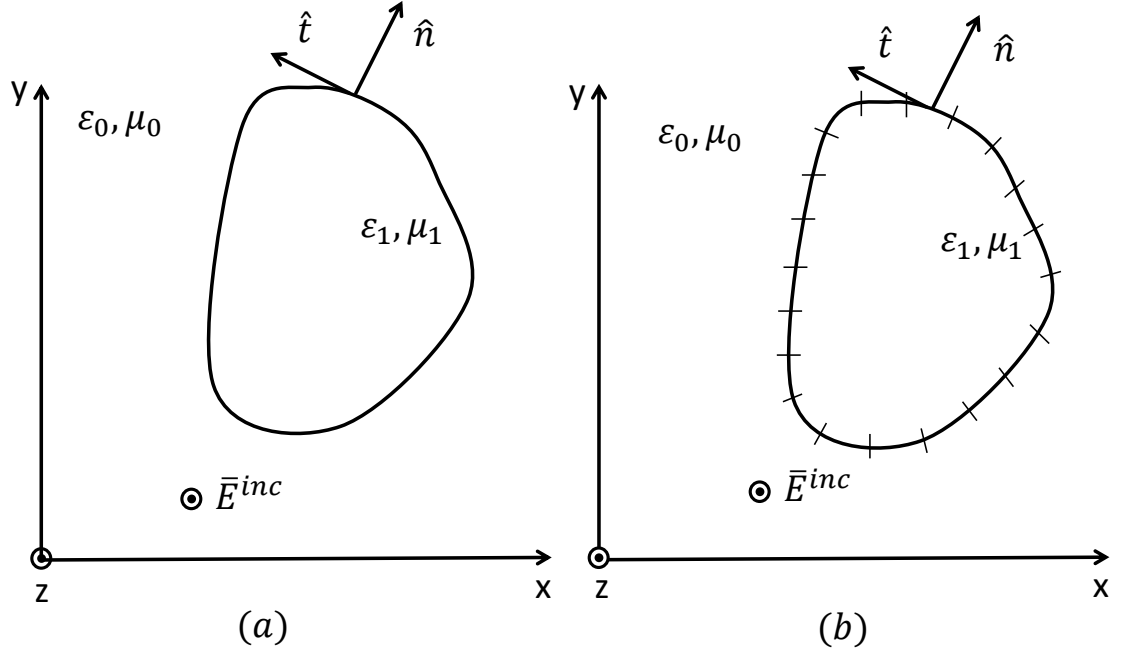


Figure 2.8: Discretisation of the cylinder contour (a) A cylinder illuminated by an incident wave (b) Cylinder contour is divided into cells

$$E_z^{inc}(t) = \sum_{n=1}^N k_n p_n(t) + ik_0 \eta_0 \int \sum_{n=1}^N j_n p_n(t') G_0(\bar{\rho}, \bar{\rho}') dt' - \int \sum_{n=1}^N k_n p_n(t') \frac{\partial}{\partial n'} G_0(\bar{\rho}, \bar{\rho}') dt' \quad (2.78)$$

$$0 = \sum_{n=1}^N k_n p_n(t) - ik_1 \eta_1 \int \sum_{n=1}^N j_n p_n(t') G_1(\bar{\rho}, \bar{\rho}') dt' + \int \sum_{n=1}^N k_n p_n(t') \frac{\partial}{\partial n'} G_1(\bar{\rho}, \bar{\rho}') dt' \quad (2.79)$$

As described in Section 2.3, we take the inner product of both sides of (2.78), (2.79) with every element in the set of testing functions $t \in \{t_1, t_2, \dots, t_N\}$, resulting in

$$\begin{aligned} \langle E_z^{inc}(t), t_m \rangle &= \sum_{n=1}^N k_n \langle p_n(t), t_m \rangle + ik_0 \eta_0 \left\langle \int \sum_{n=1}^N j_n p_n(t') G_0(\bar{\rho}, \bar{\rho}') dt', t_m \right\rangle \\ &\quad - \left\langle \int \sum_{n=1}^N k_n p_n(t') \frac{\partial}{\partial n'} G_0(\bar{\rho}, \bar{\rho}') dt', t_m \right\rangle, \text{ for } m = 1, \dots, N \end{aligned} \quad (2.80)$$

$$\begin{aligned} 0 &= \sum_{n=1}^N k_n \langle p_n(t), t_m \rangle - ik_1 \eta_1 \left\langle \int \sum_{n=1}^N j_n p_n(t') G_1(\bar{\rho}, \bar{\rho}') dt', t_m \right\rangle \\ &\quad + \left\langle \int \sum_{n=1}^N k_n p_n(t') \frac{\partial}{\partial n'} G_1(\bar{\rho}, \bar{\rho}') dt', t_m \right\rangle, \text{ for } m = 1, \dots, N \end{aligned} \quad (2.81)$$

where $\langle \cdot, \cdot \rangle : \mathbb{V} \times \mathbb{V} \rightarrow \mathbb{C}$ represents the Hermitian inner product, $\langle f, g \rangle \equiv \int f(t) g^*(t) dt$. The elements of the testing function t must be chosen to be independent so that the $2N$ equations (2.80) and (2.81) are linearly independent [76]. The testing function is also chosen to minimize the computations required to evaluate the inner products. One of the most commonly used approaches is the method of Galerkin where the basis functions are also used as the testing functions. However this method requires a large amount of computations to evaluate two integrations numerically. Instead using the Dirac delta function as the testing functions helps to reduce the number of integrations. The use of Dirac delta testing functions is equivalent to the point matching technique.

$$t_m(t) = \delta(t - t_m) \quad (2.82)$$

where t_m specifies the point at which the boundary condition is enforced. Then equation (2.80) and 2.81) can be written as, for $m = 1, \dots, N$

$$E_z^{inc}(t_m) = \sum_{n=1}^N \left[k_n + ik_0 \eta_0 \int_{\text{cell } n} j_n G_0(\bar{\rho}_m, \bar{\rho}') dt' - \int_{\text{cell } n} k_n \frac{\partial}{\partial n'} G_0(\bar{\rho}_m, \bar{\rho}') dt' \right] \quad (2.83)$$

$$0 = \sum_{n=1}^N \left[k_n - ik_1 \eta_1 \int_{\text{cell } n} j_n G_1(\bar{\rho}_m, \bar{\rho}') dt' + \int_{\text{cell } n} k_n \frac{\partial}{\partial n'} G_1(\bar{\rho}_m, \bar{\rho}') dt' \right] \quad (2.84)$$

which is equivalent to a discrete system of equations of order $2N \times 2N$

$$\begin{bmatrix}
 Z_{11}^{(a)} & Z_{12}^{(a)} & \cdots & Z_{1N}^{(a)} & Z_{11}^{(b)} & Z_{12}^{(b)} & \cdots & Z_{1N}^{(b)} \\
 Z_{21}^{(a)} & Z_{22}^{(a)} & \cdots & Z_{2N}^{(a)} & Z_{21}^{(b)} & Z_{22}^{(b)} & \cdots & Z_{2N}^{(b)} \\
 \vdots & \vdots & \ddots & \vdots & \vdots & \vdots & \ddots & \vdots \\
 Z_{N1}^{(a)} & Z_{N2}^{(a)} & \cdots & Z_{NN}^{(a)} & Z_{N1}^{(b)} & Z_{N2}^{(b)} & \cdots & Z_{NN}^{(b)} \\
 Z_{11}^{(c)} & Z_{12}^{(c)} & \cdots & Z_{1N}^{(c)} & Z_{11}^{(d)} & Z_{12}^{(d)} & \cdots & Z_{1N}^{(d)} \\
 Z_{21}^{(c)} & Z_{22}^{(c)} & \cdots & Z_{2N}^{(c)} & Z_{21}^{(d)} & Z_{22}^{(d)} & \cdots & Z_{2N}^{(d)} \\
 \vdots & \vdots & \ddots & \vdots & \vdots & \vdots & \ddots & \vdots \\
 Z_{N1}^{(c)} & Z_{N2}^{(c)} & \cdots & Z_{NN}^{(c)} & Z_{N1}^{(d)} & Z_{N2}^{(d)} & \cdots & Z_{NN}^{(d)}
 \end{bmatrix}
 \begin{bmatrix}
 j_1 \\
 j_2 \\
 \vdots \\
 j_N \\
 k_1 \\
 k_2 \\
 \vdots \\
 k_N
 \end{bmatrix}
 =
 \begin{bmatrix}
 e_1^{inc} \\
 e_2^{inc} \\
 \vdots \\
 e_N^{inc} \\
 0 \\
 0 \\
 \vdots \\
 0
 \end{bmatrix}
 \quad (2.85)$$

The above equations can be written in the compact form

$$\begin{bmatrix}
 \overline{\overline{Z}}^{(a)} & \overline{\overline{Z}}^{(b)} \\
 \overline{\overline{Z}}^{(c)} & \overline{\overline{Z}}^{(d)}
 \end{bmatrix}
 \begin{bmatrix}
 \overline{j} \\
 \overline{k}
 \end{bmatrix}
 =
 \begin{bmatrix}
 \overline{e}^{inc} \\
 \overline{0}
 \end{bmatrix}
 \quad (2.86)$$

where $\overline{\overline{Z}}^{(a)}$, $\overline{\overline{Z}}^{(b)}$, $\overline{\overline{Z}}^{(c)}$, $\overline{\overline{Z}}^{(d)}$ are the $N \times N$ impedance matrices whose entries represent the mutual impedance between different cells. \overline{e}^{inc} is the vector containing the incident field at the center of the cells. \overline{j} and \overline{k} are the vectors containing the unknown electric and magnetic currents. The entries of the impedance matrices are given by

$$Z_{mn}^{(a)} = \begin{cases} \frac{k_0 \eta_0}{4} \omega_n H_0^{(2)}(k_0 R_{mn}) & m \neq n \\ \frac{k_0 \eta_0}{4} \int_{\text{cell } m} H_0^{(2)}(k_0 R_{mn}) dt' & m = n \end{cases} \quad (2.87)$$

$$Z_{mn}^{(b)} = \begin{cases} -\frac{k_0}{4i} \omega_n \hat{n}_n \cdot \hat{r}_{mn} H_1^{(2)}(k_0 R_{mn}) & m \neq n \\ \lim_{\overline{\rho}' \rightarrow \overline{\rho}} \left(1 - \int_{\text{cell } m} \frac{\partial}{\partial n'} G_0(\overline{\rho}, \overline{\rho}') dt' \right) & m = n \end{cases} \quad (2.88)$$

$$Z_{mn}^{(c)} = \begin{cases} -\frac{k_1 \eta_1}{4} \omega_n H_0^{(2)}(k_1 R_{mn}) & m \neq n \\ -\frac{k_0 \eta_0}{4} \int_{\text{cell } m} H_0^{(2)}(k_1 R_{mn}) dt' & m = n \end{cases} \quad (2.89)$$

$$Z_{mn}^{(d)} = \begin{cases} \frac{k_1}{4i} \omega_n \hat{n}_n \cdot \hat{r}_{mn} H_1^{(2)}(k_d R_m) & m \neq n \\ \lim_{\overline{\rho}' \rightarrow \overline{\rho}} \left(1 + \int_{\text{cell } m} \frac{\partial}{\partial n'} G_1(\overline{\rho}, \overline{\rho}') dt' \right) & m = n \end{cases} \quad (2.90)$$

where ω_n is the length of the n^{th} cell, \hat{n}_n represents the unit normal vector of the surface at $\overline{\rho}_n$ and \hat{r}_{mn} denotes the unit vector from the source element to a receiving element

$$\hat{r}_{mn} = \frac{\overline{\rho}_m - \overline{\rho}_n}{R_{mn}} \quad (2.91)$$

$$R_{mn} = \sqrt{(x_m - x_n)^2 + (y_m - y_n)^2} \quad (2.92)$$

$H_0^{(2)}$ and $H_1^{(2)}$ are the second-kind Hankel function of order zero and one, respectively. The second-kind Hankel function of first order arises from the partial derivative applied to the Green's function. For the diagonal terms of the impedance matrices where $\bar{\rho}_m \equiv \bar{\rho}_n$, the Hankel function and its derivative are singular and need to be analytically evaluated. The diagonal terms of $\bar{\bar{Z}}^{(a)}$ and $\bar{\bar{Z}}^{(c)}$ impedance matrices can be evaluated using the small argument series expansion of the Hankel functions

$$H_0^{(2)}(x) = 1 - i \left\{ \frac{2}{\pi} \ln \left(\frac{\gamma x}{2} \right) \right\} + \mathcal{O}(x^2) \quad (2.93)$$

where $\gamma = 1.7810724$ is Euler's constant. The diagonal terms of $\bar{\bar{Z}}^{(a)}$ and $\bar{\bar{Z}}^{(c)}$ can then be approximated as

$$Z_{mm}^{(a)} \simeq \frac{k_0 \eta_0 \omega_m}{4} \left\{ 1 - i \frac{2}{\pi} \ln \left(\frac{\gamma k_0 \omega_m}{4e} \right) \right\} \quad (2.94)$$

$$Z_{mm}^{(c)} \simeq -\frac{k_1 \eta_1 \omega_m}{4} \left\{ 1 - i \frac{2}{\pi} \ln \left(\frac{\gamma k_1 \omega_1}{4e} \right) \right\} \quad (2.95)$$

In order to evaluate the diagonal terms of $\bar{\bar{Z}}^{(b)}$ and $\bar{\bar{Z}}^{(d)}$, we use the new coordinate system X and Y which are normal and tangential to the surface as shown in Figure 2.9. We denote Y' as the distance from $\bar{\rho}'$ to the surface and consider the point $\bar{\rho}'$ approaching the surface separating the two media in the direction normal to the surface. Hence $X' = 0$. If $\bar{\rho}'$ approaches the surface from medium 0, Y' is positive and vice versa. [1]

$$|\bar{\rho} - \bar{\rho}'| = \sqrt{X^2 + (0 - Y')^2} \quad (2.96)$$

$$G_\alpha(\bar{\rho}, \bar{\rho}') = \frac{1}{4i} H_0^{(2)}(k_\alpha |\bar{\rho} - \bar{\rho}'|) \quad (2.97)$$

Then the diagonal terms of $\bar{\bar{Z}}^{(b)}$ and $\bar{\bar{Z}}^{(d)}$ can be evaluated by constructing the limit

$$\lim_{\bar{\rho}' \rightarrow \bar{\rho}} \left(\int_{\text{cell } n} \frac{\partial}{\partial n'} G_\alpha(\bar{\rho}, \bar{\rho}') dt' \right) = \lim_{\bar{\rho}' \rightarrow \bar{\rho}} \int_{-a}^a \frac{\partial G_\alpha(\bar{\rho}, \bar{\rho}')}{\partial Y} dX \quad (2.98)$$

Using the small argument series of the Hankel function, we obtain

$$\lim_{\bar{\rho}' \rightarrow \bar{\rho}} G_\alpha(\bar{\rho}, \bar{\rho}') = \frac{1}{4i} - \frac{1}{2\pi} \left[\ln \left(\frac{|\bar{\rho} - \bar{\rho}'|}{2} \right) + \ln \gamma \right] \quad (2.99)$$

The normal derivative of the Green's function with respect to \hat{n}' is given by

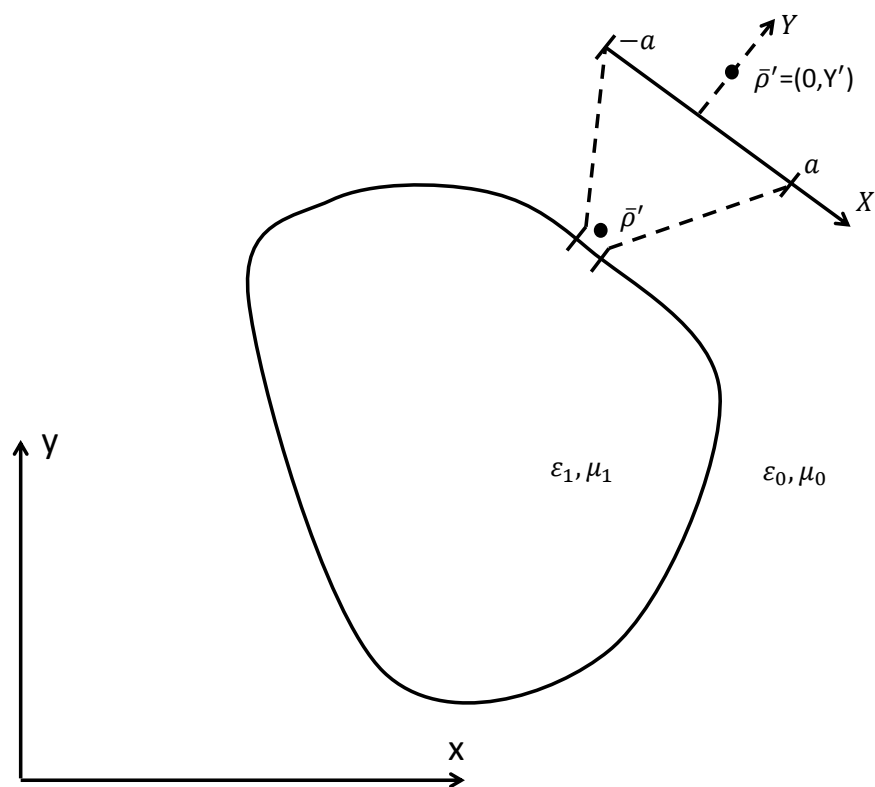


Figure 2.9: Evaluation of the diagonal elements of impedance matrix

$$\lim_{\bar{\rho}' \rightarrow \bar{\rho}} \left(\frac{\partial G_\alpha(\bar{\rho}, \bar{\rho}')}{\partial Y} \right) = \lim_{a \rightarrow 0, |Y'| \rightarrow 0} \left(\frac{1}{2\pi} \frac{Y'}{X^2 + (Y')^2} \right) \quad (2.100)$$

From equation (2.98) and (2.100), we obtain

$$\lim_{\bar{\rho}' \rightarrow \bar{\rho}} \left(\int_{\text{cell } m} \frac{\partial}{\partial n'} G_\alpha(\bar{\rho}, \bar{\rho}') dt' \right) = \lim_{a \rightarrow 0, |Y'| \rightarrow 0} \int_{-a}^a \left(\frac{1}{2\pi} \frac{Y'}{X^2 + (Y')^2} \right) dX \quad (2.101)$$

$$= \lim_{a \rightarrow 0, |Y'| \rightarrow 0} \frac{1}{2\pi} \left[\tan^{-1} \left(\frac{X}{Y'} \right) \right]_{-a}^a \quad (2.102)$$

$$= \lim_{a \rightarrow 0, |Y'| \rightarrow 0} \frac{1}{\pi} \left[\tan^{-1} \left(\frac{a}{Y'} \right) \right] \quad (2.103)$$

$$= \begin{cases} \frac{1}{2} & \text{for } Y' > 0 \\ -\frac{1}{2} & \text{for } Y' < 0 \end{cases} \quad (2.104)$$

Therefore the diagonal elements of $\bar{\bar{Z}}^{(b)}$ and $\bar{\bar{Z}}^{(d)}$ are obtained as

$$Z_{mm}^{(b)} \simeq 1 - \frac{1}{2} = \frac{1}{2} \quad (2.105)$$

$$Z_{mm}^{(d)} \simeq 1 + \left(-\frac{1}{2} \right) = \frac{1}{2} \quad (2.106)$$

In summary the entries of the impedance matrices are given by

$$Z_{mn}^{(a)} = \begin{cases} \frac{k_0 \eta_0}{4} \omega_n H_0^{(2)}(k_0 R_{mn}) & m \neq n \\ \frac{k_0 \eta_0 \omega_m}{4} \left\{ 1 - i \left[\frac{2}{\pi} \ln \left(\frac{\gamma k_0 \omega_m}{4e} \right) \right] \right\} & m = n \end{cases} \quad (2.107)$$

$$Z_{mn}^{(b)} = \begin{cases} -\frac{k_0}{4i} \omega_n \hat{n}_n \cdot \hat{r}_{mn} H_1^{(2)}(k_0 R_{mn}) & m \neq n \\ \frac{1}{2} & m = n \end{cases} \quad (2.108)$$

$$Z_{mn}^{(c)} = \begin{cases} -\frac{k_1 \eta_1}{4} \omega_n H_0^{(2)}(k_d R_{mn}) & m \neq n \\ -\frac{k_1 \eta_1 \omega_m}{4} \left\{ 1 - i \left[\frac{2}{\pi} \ln \left(\frac{\gamma k_1 \omega_m}{4e} \right) \right] \right\} & m = n \end{cases} \quad (2.109)$$

$$Z_{mn}^{(d)} = \begin{cases} \frac{k_1}{4i} \omega_n \hat{n}_n \cdot \hat{r}_{mn} H_1^{(2)}(k_1 R_{mn}) & m \neq n \\ \frac{1}{2} & m = n \end{cases} \quad (2.110)$$

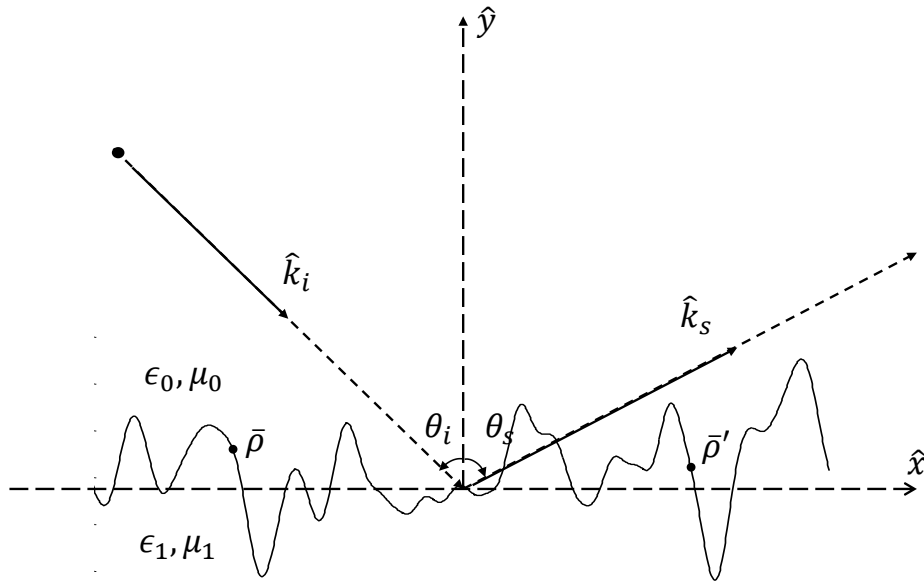


Figure 2.10: Example of one-dimensional randomly rough surface

Electric Field Integral Equation recast in terms of surface field and its normal derivative

In the previous section, the surface integral equations for two-dimensional (2D) problems has been derived in terms of electric and magnetic currents. This formulation of integral equations is widely used in the wave propagation and scattering literature and will be used to model propagation for bot rural and urban areas. The surface integral equations for 2D problems are also conveniently, and equivalently expressed in terms of surface field and its normal derivative. This formulation of the integral equations is widely applied in the random rough surface scattering literature and will be used in Chapter 5. An example of simulation of wave scattering from random rough surfaces is shown in Figure 2.10. The surface is illuminated by an incident wave centered in the direction $\hat{k}_i = \sin\theta_i\hat{x} - \cos\theta_i\hat{y}$ where θ_i denotes the incident angle. The region above the surface is free space with (ϵ_0, μ_0) and the region below the surface is assumed to be a homogeneous dielectric region with (ϵ_1, μ_1) . It is possible to recast the EFIEs in terms of surface field and its normal derivative by using the following relations

$$\bar{E}_1 = E_z \hat{z} = K_t \hat{z} \quad (2.111)$$

$$\bar{H}_1 = -\frac{1}{i\omega\mu} \nabla \times \bar{E}_1 \quad (2.112)$$

$$\bar{J}_1 = \hat{n} \times \bar{H}_1 = -\frac{1}{i\omega\mu} (\hat{n} \times \nabla \times \bar{E}_1) \quad (2.113)$$

$$= \frac{\hat{z}}{i\omega\mu} (\hat{n} \cdot \nabla E_z) \quad (2.114)$$

Using these equations in (2.73) and (2.74) gives, for $\bar{\rho} = x\hat{x} + y\hat{y}$ and $\bar{\rho}' = x'\hat{x} + y'\hat{y}$ on the surface S

$$E_z^{inc}(\bar{\rho}) = \frac{E_z(\bar{\rho})}{2} + \int [\hat{n}' \cdot \nabla E_z(\bar{\rho}')] G_0(\bar{\rho}, \bar{\rho}') dt' - \rlap{-}\int E_z(\bar{\rho}') [\hat{n}' \cdot \nabla G_0(\bar{\rho}, \bar{\rho}')] dt' \quad (2.115)$$

$$0 = \frac{E_z(\bar{\rho})}{2} - \int [\hat{n}' \cdot \nabla E_z(\bar{\rho}')] G_1(\bar{\rho}, \bar{\rho}') dt' + \rlap{-}\int E_z(\bar{\rho}') [\hat{n}' \cdot \nabla G_1(\bar{\rho}, \bar{\rho}')] dt' \quad (2.116)$$

where $\rlap{-}\int$ denotes the Cauchy principal value integral. On the surface S , $y = f(x)$ and $y' = f(x')$ and the tangential vector \hat{t} is defined as

$$\hat{t}(x) = \frac{1}{\sqrt{1 + \left(\frac{df(x)}{dx}\right)^2}} \hat{x} + \frac{\frac{df}{dx}}{\sqrt{1 + \left(\frac{df(x)}{dx}\right)^2}} \hat{y} \quad (2.117)$$

The EFIE (2.115) and (2.116) can be written as

$$E_z^{inc}(\bar{\rho}) = \frac{E_z(\bar{\rho})}{2} + \int \left[\hat{n}' \cdot \nabla E_z(\bar{\rho}') \sqrt{1 + \left(\frac{df(x')}{dx}\right)^2} \right] G_0(\bar{\rho}, \bar{\rho}') dx' - \rlap{-}\int E_z(\bar{\rho}') \left[\sqrt{1 + \left(\frac{df(x')}{dx}\right)^2} \hat{n}' \cdot \nabla G_0(\bar{\rho}, \bar{\rho}') \right] dx' \quad (2.118)$$

$$0 = \frac{E_z(\bar{\rho})}{2} - \int \left[\hat{n}' \cdot \nabla E_z(\bar{\rho}') \sqrt{1 + \left(\frac{df(x')}{dx}\right)^2} \right] G_1(\bar{\rho}, \bar{\rho}') dx' + \rlap{-}\int E_z(\bar{\rho}') \left[\sqrt{1 + \left(\frac{df(x')}{dx}\right)^2} \hat{n}' \cdot \nabla G_1(\bar{\rho}, \bar{\rho}') \right] dx' \quad (2.119)$$

We define the unknowns

$$u(x) = \sqrt{1 + \left(\frac{df(x)}{dx}\right)^2} (\hat{n} \cdot \nabla E_z(\bar{\rho}))_{y=f(x)} \quad (2.120)$$

$$\psi(x) = (E_z(\bar{\rho}))_{y=f(x)} \quad (2.121)$$

The EFIEs (2.118) and (2.119) becomes

$$\psi^{inc}(x) = \frac{\psi(x)}{2} + \int u(x') G_0(\bar{\rho}, \bar{\rho}') dx' - \int \psi(x') \left[\sqrt{1 + \left(\frac{df(x')}{dx}\right)^2} \hat{n}' \cdot \nabla G_0(\bar{\rho}, \bar{\rho}') \right] dx' \quad (2.122)$$

$$0 = \frac{\psi(x)}{2} - \int u(x') G_1(\bar{\rho}, \bar{\rho}') dx' + \int \psi(x') \left[\sqrt{1 + \left(\frac{df(x')}{dx}\right)^2} \hat{n}' \cdot \nabla G_1(\bar{\rho}, \bar{\rho}') \right] dx' \quad (2.123)$$

Then the MoM is applied to solve the integral equation (2.122) and (2.123) by expanding $u(x)$ and $\psi(x)$ into a finite series using pulse basis functions and evaluating equation (2.122) and (2.123) at N different points, resulting in a system of $2N$ linear equations

$$\begin{bmatrix} \bar{Z}^{(a)} & \bar{Z}^{(b)} \\ \bar{Z}^{(c)} & \bar{Z}^{(d)} \end{bmatrix} \begin{bmatrix} \bar{u} \\ \bar{\psi} \end{bmatrix} = \begin{bmatrix} \bar{\psi}^{inc} \\ \bar{0} \end{bmatrix} \quad (2.124)$$

The entries of the impedance matrices are given by

$$Z_{mn}^{(a)} = \begin{cases} \frac{\Delta x}{4i} H_0^{(2)}(k_0 R_{mn}) & m \neq n \\ \frac{\Delta x}{4i} \left\{ 1 - i \left[\frac{2}{\pi} \ln \left(\frac{\gamma k_0 \Delta x}{4e} \right) \right] \right\} & m = n \end{cases} \quad (2.125)$$

$$Z_{mn}^{(b)} = \begin{cases} -\frac{\Delta x}{4i} k_0 \frac{f'(x_n)(x_m - x_n) - [f(x_m) - f(x_n)]}{R_{mn}} H_1^{(2)}(k_0 R_m) & m \neq n \\ \frac{1}{2} & m = n \end{cases} \quad (2.126)$$

$$Z_{mn}^{(c)} = \begin{cases} -\frac{\Delta x}{4i} H_0^{(2)}(k_1 R_{mn}) & m \neq n \\ -\frac{\Delta x}{4i} \left\{ 1 - i \left[\frac{2}{\pi} \ln \left(\frac{\gamma k_1 \Delta x}{4e} \right) \right] \right\} & m = n \end{cases} \quad (2.127)$$

$$Z_{mn}^{(d)} = \begin{cases} \frac{\Delta x}{4i} k_1 \frac{f'(x_n)(x_m - x_n) - [f(x_m) - f(x_n)]}{R_{mn}} H_1^{(2)}(k_d R_{mn}) & m \neq n \\ \frac{1}{2} & m = n \end{cases} \quad (2.128)$$

where $R_{mn} = \sqrt{(x_m - x_n)^2 + [f(x_m) - f(x_n)]^2}$.

2.4.2 TE-wave scattering from homogeneous dielectric cylinders

If the cylinder is illuminated by a TE^z plane wave, the field components present are $H_z(\bar{\rho})$, $E_x(\bar{\rho})$ and $E_y(\bar{\rho})$. The MFIEs are more appropriate in the formulation of TE-wave scattering from an homogeneous cylinder because only one component of \bar{H} is present. Applying the same procedure which was used to formulate the TM-wave scattering in section Section 2.4.1, the MFIEs can be written in the terms of surface electric current J_t and surface magnetic current K_z

$$H_z^{inc}(t) = -J_t(t) + \int i \frac{k_0}{\eta_0} K_z(t') G_0(\bar{\rho}, \bar{\rho}') dt' + \int J_t(t') [\hat{n}' \cdot \nabla G_0(\bar{\rho}, \bar{\rho}')] dt' \quad (2.129)$$

$$0 = J_t(t) + \int i \frac{k_1}{\eta_1} K_z(t') G_1(\bar{\rho}, \bar{\rho}') dt' + \int J_t(t') [\hat{n}' \cdot \nabla G_1(\bar{\rho}, \bar{\rho}')] dt' \quad (2.130)$$

Pulse basis functions are used to represent the unknown electric and magnetic current J_t and K_z . Then the MoM is applied, yielding a $2N \times 2N$ linear system

$$\begin{bmatrix} \bar{\bar{Z}}^{(a)} & \bar{\bar{Z}}^{(b)} \\ \bar{\bar{Z}}^{(c)} & \bar{\bar{Z}}^{(d)} \end{bmatrix} \begin{bmatrix} \bar{k} \\ \bar{j} \end{bmatrix} = \begin{bmatrix} \bar{h}^{inc} \\ \bar{0} \end{bmatrix} \quad (2.131)$$

where the entries of the impedance matrices are given by

$$Z_{mn}^{(a)} = \begin{cases} \frac{k_0}{4\eta_0} \omega_n H_0^{(2)}(k_0 R_m) & m \neq n \\ \frac{k_0 \omega_m}{4\eta_0} \left\{ 1 - i \left[\frac{2}{\pi} \ln \left(\frac{\gamma k_0 \omega_m}{4e} \right) \right] \right\} & m = n \end{cases} \quad (2.132)$$

$$Z_{mn}^{(b)} = \begin{cases} \frac{k_0}{4i} \omega_n \hat{n}_n \cdot \hat{r}_{mn} H_1^{(2)}(k_0 R_m) & m \neq n \\ -\frac{1}{2} & m = n \end{cases} \quad (2.133)$$

$$Z_{mn}^{(c)} = \begin{cases} \frac{k_1}{4\eta_1} \omega_n H_0^{(2)}(k_1 R_m) & m \neq n \\ \frac{k_1 \omega_m}{4\eta_1} \left\{ 1 - i \left[\frac{2}{\pi} \ln \left(\frac{\gamma k_1 \omega_m}{4e} \right) \right] \right\} & m = n \end{cases} \quad (2.134)$$

$$Z_{mn}^{(d)} = \begin{cases} \frac{k_1}{4i} \omega_n \hat{n}_n \cdot \hat{r}_{mn} H_1^{(2)}(k_1 R_m) & m \neq n \\ \frac{1}{2} & m = n \end{cases} \quad (2.135)$$

The surface integral equations for 2D problems are also conveniently, and equivalently expressed in terms of surface field and its normal derivative. The formulation is similar to the TM^z case and given in Appendix A.

2.5 3D wave scattering problem formulation

Section 2.4 described the application of the Method of Moments to solve the problem of scattering from infinite cylinders. In this section, we begin the investigation of numerical techniques for solving the scattering from the two-dimensional random rough surfaces which will be discussed in detail in Chapter 6. Consider an incident electromagnetic wave, $\bar{E}_i(x, y, z)$ and $\bar{H}_i(x, y, z)$ impinging upon a 2D surface with a random height profile $z = f(x, y)$ as shown in Figure 2.11. The region above the surface (region 1) is free space and characterized by relative permittivity ϵ_0 and permeability μ_0 while the region below the surface (region 2) is characterized by permittivity $\epsilon_1 = \epsilon_r \epsilon_0$ and permeability $\mu_1 = \mu_r \mu_0$ where ϵ_r and μ_r are the relative permittivity and permeability of the lower medium. Let $\bar{r} = x\hat{x} + y\hat{y} + z\hat{z}$ and $\bar{r}' = x'\hat{x} + y'\hat{y} + z'\hat{z}$ represent a field point and a source point on the surface, respectively. Using the EFIE and MFIE equations from (2.41-2.42) and (2.47-2.48), the fields in the upper medium and the lower medium satisfy the integral equations for the two media problem

$$\bar{E}^{inc} = \bar{E}_1 - \left\{ \frac{\nabla\nabla \cdot \bar{A}_1 + k_0^2 \bar{A}_1}{i\omega\epsilon_0} - \nabla \times \bar{F}_1 \right\}_{S^+} \quad (2.136)$$

$$0 = -\bar{E}_1 - \left\{ \frac{\nabla\nabla \cdot \bar{A}_2 + k_1^2 \bar{A}_2}{i\omega\epsilon_1} - \nabla \times \bar{F}_2 \right\}_{S^-} \quad (2.137)$$

$$\bar{H}^{inc} = \bar{H}_1 - \left\{ \frac{\nabla\nabla \cdot \bar{F}_1 + k_0^2 \bar{F}_1}{i\omega\mu_0} + \nabla \times \bar{A}_1 \right\}_{S^+} \quad (2.138)$$

$$0 = -\bar{H}_1 - \left\{ \frac{\nabla\nabla \cdot \bar{F}_2 + k_1^2 \bar{F}_2}{i\omega\mu_1} + \nabla \times \bar{A}_2 \right\}_{S^-} \quad (2.139)$$

Note that the subscript S^+ means that the function in the bracket is evaluated an infinitesimal distance outside the surface of the scatterer (the exterior problem). In contrast, the subscript S^- means that the function in the bracket is evaluated an infinitesimal distance inside the surface of the scatterer (the interior problem). The surface integral equations are obtained by taking various combinations of the EFIEs and MFIEs. In this scenarios, the Stratton-Chu formulation is used to formulate the surface integral equations [1]. We take the cross product of the normal vector \hat{n} and the EFIE for the interior problem 2.137, and the MFIE for the exterior problem 2.138. Then we take the dot product of the normal vector \hat{n} and the EFIE for the exterior problem 2.136, and the MFIE for the interior problem 2.139

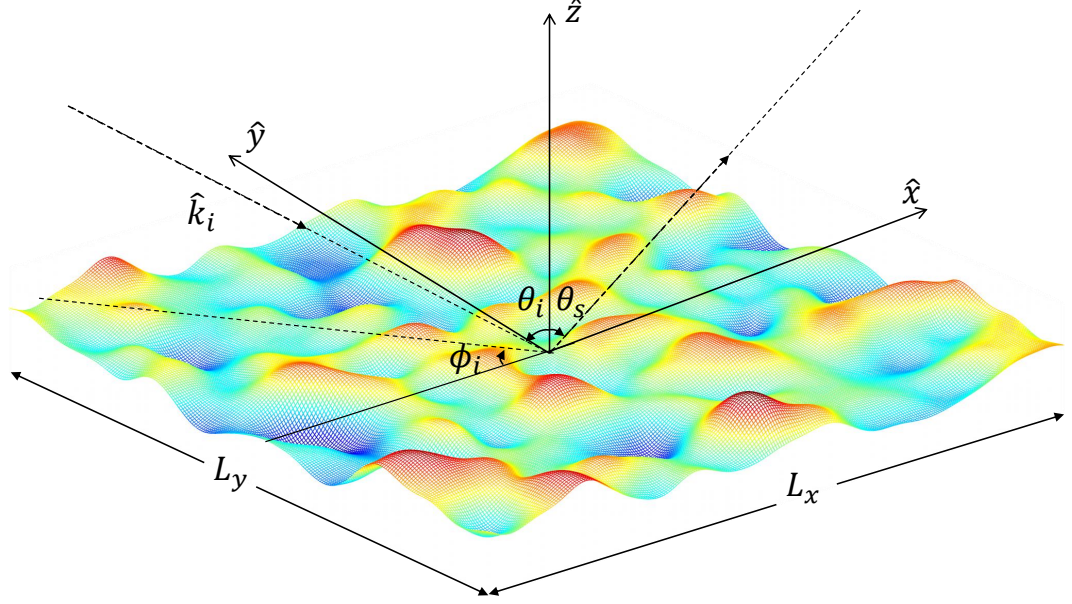


Figure 2.11: Example of two dimensional dielectric rough surface profile illuminated by an incident wave

$$\hat{n} \cdot \bar{E}^{inc} = \hat{n} \cdot \bar{E}_1 - \hat{n} \cdot \left\{ \frac{\nabla \nabla \cdot \bar{A}_1 + k_0^2 \bar{A}_1}{i\omega\epsilon_0} - \nabla \times \bar{F}_1 \right\}_{S^+} \quad (2.140)$$

$$0 = -\hat{n} \times \bar{E}_1 - \hat{n} \times \left\{ \frac{\nabla \nabla \cdot \bar{A}_2 + k_1^2 \bar{A}_2}{i\omega\epsilon_1} - \nabla \times \bar{F}_2 \right\}_{S^-} \quad (2.141)$$

$$\hat{n} \times \bar{H}^{inc} = \hat{n} \times \bar{H}_1 - \hat{n} \times \left\{ \frac{\nabla \nabla \cdot \bar{F}_1 + k_0^2 \bar{F}_1}{i\omega\mu_0} + \nabla \times \bar{A}_1 \right\}_{S^+} \quad (2.142)$$

$$0 = -\hat{n} \cdot \bar{H}_1 - \hat{n} \cdot \left\{ \frac{\nabla \nabla \cdot \bar{F}_2 + k_1^2 \bar{F}_2}{i\omega\mu_1} + \nabla \times \bar{A}_2 \right\}_{S^-} \quad (2.143)$$

where the magnetic potential \bar{A} and electric potential \bar{F} can be expressed in the form of a convolution of the three-dimensional Green's function

$$\bar{A}_\alpha = \int \bar{J}_s(\bar{r}') G_\alpha(\bar{r}, \bar{r}') dS' \quad (2.144)$$

$$\bar{F}_\alpha = \int \bar{K}_s(\bar{r}') G_\alpha(\bar{r}, \bar{r}') dS' \quad (2.145)$$

where the function $G_\alpha(\bar{r}, \bar{r}')$, $\alpha = 0, 1$ are the three-dimensional Green's function. $\bar{K}_s(\bar{r})$ and $\bar{J}_s(\bar{r})$ represent the tangential electric and magnetic fields for the physical problem

$$G_0(\bar{r}, \bar{r}') = \frac{e^{-ik_0|\bar{r}-\bar{r}'|}}{4\pi|\bar{r}-\bar{r}'|} \quad (2.146)$$

$$G_1(\bar{r}, \bar{r}') = \frac{e^{-ik_1|\bar{r}-\bar{r}'|}}{4\pi|\bar{r}-\bar{r}'|} \quad (2.147)$$

$$\bar{K}_s(\bar{r}) = \bar{E}(\bar{r}) \times \hat{n} \quad (2.148)$$

$$\bar{J}_s(\bar{r}) = \hat{n} \times \bar{H}(\bar{r}) \quad (2.149)$$

Recall that $k_0 = \omega\sqrt{\mu_0\epsilon_0}$ and $k_1 = \omega\sqrt{\mu_1\epsilon_1}$ are the wave number of free-space and the scatterer respectively. Using (2.144) and (2.145) in (2.140)-(2.143), the expression can be written

$$\begin{aligned} \hat{n} \cdot \bar{E}^{inc}(\bar{r}) &= \hat{n} \cdot \bar{E}(\bar{r}) + \hat{n} \cdot \int \nabla G_0(\bar{r}_+, \bar{r}') \times \bar{K}_s(\bar{r}') dS' \\ &\quad + i\omega\mu_0\hat{n} \cdot \left[\int G_0(\bar{r}_+, \bar{r}') \bar{J}_s(\bar{r}') dS' + \frac{1}{k_0^2} \int \nabla G_0(\bar{r}_+, \bar{r}') \nabla' \cdot \bar{J}_s(\bar{r}') dS' \right] \end{aligned} \quad (2.150)$$

$$\begin{aligned} 0 &= -\hat{n} \times \bar{E}(\bar{r}) + \hat{n} \times \int \nabla G_1(\bar{r}_-, \bar{r}') \times \bar{K}_s(\bar{r}') dS' \\ &\quad + i\omega\mu_1\hat{n} \times \left[\int \bar{J}_s(\bar{r}') G_1(\bar{r}_-, \bar{r}') dS' + \frac{1}{k_1^2} \int \nabla G_1(\bar{r}_-, \bar{r}') \nabla' \cdot \bar{J}_s(\bar{r}') dS' \right] \end{aligned} \quad (2.151)$$

$$\begin{aligned} -\hat{n} \times \bar{H}^{inc}(\bar{r}) &= -\hat{n} \times \bar{H}(\bar{r}) + \hat{n} \times \int \nabla G_0(\bar{r}_+, \bar{r}') \times \bar{J}_s(\bar{r}') dS' \\ &\quad - i\omega\epsilon_0\hat{n} \times \left[\int G_0(\bar{r}_+, \bar{r}') \bar{K}_s(\bar{r}') dS' + \frac{1}{k_0^2} \int \nabla G_0(\bar{r}_+, \bar{r}') \nabla' \cdot \bar{K}_s(\bar{r}') dS' \right] \end{aligned} \quad (2.152)$$

$$\begin{aligned} 0 &= -\hat{n} \cdot \bar{H}(\bar{r}) - \hat{n} \cdot \int \nabla G_1(\bar{r}_-, \bar{r}') \times \bar{J}_s(\bar{r}') dS' \\ &\quad + i\omega\epsilon_1\hat{n} \cdot \left[\int G_1(\bar{r}_-, \bar{r}') \bar{K}_s(\bar{r}') dS' + \frac{1}{k_1^2} \int \nabla G_1(\bar{r}_-, \bar{r}') \nabla' \cdot \bar{K}_s(\bar{r}') dS' \right] \end{aligned} \quad (2.153)$$

where \bar{r}_+ means that the point is located an infinitesimal distance outside the surface of the scatterer while \bar{r}_- means that the point is located an infinitesimal distance inside the surface of the scatterer. In addition, the surface divergence of the electric and magnetic currents $\nabla' \cdot \bar{J}_s(\bar{r})$, $\nabla' \cdot \bar{K}_s(\bar{r})$ can be written in the form of normal components of surface fields

$$\nabla' \cdot \bar{J}_s(\bar{r}) = -i\omega\epsilon_0 \hat{n}' \cdot \bar{E}(\bar{r}) \quad (2.154)$$

$$\nabla' \cdot \bar{K}_s(\bar{r}) = -i\omega\mu_0 \hat{n}' \cdot \bar{H}(\bar{r}) \quad (2.155)$$

Using (2.154) and (2.155) in the surface integral equations (2.150)-(2.153), we obtain

$$\begin{aligned} \hat{n} \cdot \bar{E}^{inc}(\bar{r}) = & \hat{n} \cdot \bar{E}(\bar{r}) + \hat{n} \cdot \int \nabla' G_0(\bar{r}_+, \bar{r}') \times [\hat{n}' \times \bar{E}(\bar{r}')] dS' \\ & + \hat{n} \cdot \left[\int i\omega\mu_0 G_0(\bar{r}_+, \bar{r}') [\hat{n}' \times \bar{H}(\bar{r}')] - \int \nabla' G_0(\bar{r}_+, \bar{r}') [\hat{n}' \cdot \bar{E}(\bar{r}')] dS' \right] \end{aligned} \quad (2.156)$$

$$\begin{aligned} 0 = & -\hat{n} \times \bar{E}(\bar{r}) + \hat{n} \times \int \nabla' G_1(\bar{r}_-, \bar{r}') \times [\hat{n}' \times \bar{E}(\bar{r}')] dS' \\ & + \hat{n} \times \left[\int i\omega\mu_1 G_1(\bar{r}_-, \bar{r}') [\hat{n}' \times \bar{H}(\bar{r}')] dS' - \int \nabla' G_1(\bar{r}_-, \bar{r}') \left[\frac{\epsilon_0}{\epsilon_1} \hat{n}' \cdot \bar{E}(\bar{r}') \right] dS' \right] \end{aligned} \quad (2.157)$$

$$\begin{aligned} \hat{n} \times \bar{H}^{inc}(\bar{r}) = & \hat{n} \times \bar{H}(\bar{r}) + \hat{n} \times \int \nabla' G_0(\bar{r}_+, \bar{r}') \times [\hat{n}' \times \bar{H}(\bar{r}')] dS' \\ & - \hat{n} \times \left[\int i\omega\epsilon_0 G_0(\bar{r}_+, \bar{r}') [\hat{n}' \times \bar{E}(\bar{r}')] dS' + \int \nabla' G_0(\bar{r}_+, \bar{r}') [\hat{n}' \cdot \bar{H}(\bar{r}')] dS' \right] \end{aligned} \quad (2.158)$$

$$\begin{aligned} 0 = & -\hat{n} \cdot \bar{H}(\bar{r}) + \hat{n} \cdot \int \nabla' G_1(\bar{r}_-, \bar{r}') \times [\hat{n}' \times \bar{H}(\bar{r}')] dS' \\ & + \hat{n} \cdot \left[\int i\omega\epsilon_1 G_1(\bar{r}_-, \bar{r}') [-\hat{n}' \times \bar{E}(\bar{r}')] dS' - \int \nabla' G_1(\bar{r}_-, \bar{r}') \left[\frac{\mu_0}{\mu_1} \hat{n}' \cdot \bar{H}(\bar{r}') \right] dS' \right] \end{aligned} \quad (2.159)$$

The surface integral \int_S can be divided into an integral over a circle S_a of infinitesimal radius a about \bar{r} and the rest which is known as the Cauchy principal value integral

$$\int \nabla G(\bar{r}, \bar{r}') dS' = \int_{S_a} \nabla G(\bar{r}, \bar{r}') dS' + \int_{S-S_a} \nabla G(\bar{r}, \bar{r}') dS' \quad (2.160)$$

$$= \int_{S_a} \nabla G(\bar{r}, \bar{r}') dS' + \oint \nabla G(\bar{r}, \bar{r}') dS' \quad (2.161)$$

where f denotes the Cauchy principal value integral. It can be shown that [1]

$$\int_{S_a} \nabla G(\bar{r}, \bar{r}') dS' = \begin{cases} -\frac{\hat{n}}{2} & \text{for } \bar{r} = \bar{r}_+ \\ \frac{\hat{n}}{2} & \text{for } \bar{r} = \bar{r}_- \end{cases} \quad (2.162)$$

Consequently, using the vector identity $\bar{a} \times (\bar{b} \times \bar{c}) = \bar{b}(\bar{a} \cdot \bar{c}) - \bar{c}(\bar{a} \cdot \bar{b})$, the integral over a circle of infinitesimal radius of the integrals in (2.156)-(2.159) can be found

$$\begin{aligned} \hat{n} \times \int_{S_a} \nabla G_0(\bar{r}_+, \bar{r}') \times \bar{J}_s(\bar{r}') dS' &= -\hat{n} \times \left(\frac{\hat{n}}{2} \times \bar{J}_s(\bar{r}) \right) \\ &= -\frac{1}{2} \hat{n} (\hat{n} \cdot \bar{J}_s(\bar{r})) + \frac{\bar{J}_s(\bar{r})}{2} = \frac{\hat{n} \times \bar{H}(\bar{r})}{2} \end{aligned} \quad (2.163)$$

$$\begin{aligned} \hat{n} \times \int_{S_a} \nabla G_1(\bar{r}_-, \bar{r}') \times \bar{K}_s(\bar{r}') dS' &= \hat{n} \times \left(\frac{\hat{n}}{2} \times \bar{K}_s(\bar{r}) \right) \\ &= \frac{1}{2} \hat{n} (\hat{n} \cdot \bar{K}_s(\bar{r})) - \frac{\bar{K}_s(\bar{r})}{2} = \frac{\hat{n} \times \bar{E}(\bar{r})}{2} \end{aligned} \quad (2.164)$$

$$\hat{n} \times \int_{S_a} \nabla G_1(\bar{r}_-, \bar{r}') \nabla'_s \cdot \bar{J}_s(\bar{r}') dS' = \hat{n} \times \left(\frac{\hat{n}}{2} \nabla'_s \cdot \bar{J}_s(\bar{r}') \right) = 0 \quad (2.165)$$

$$\hat{n} \times \int_{S_a} \nabla G_0(\bar{r}_+, \bar{r}') \nabla'_s \cdot \bar{K}_s(\bar{r}') dS' = \hat{n} \times \left(-\frac{\hat{n}}{2} \nabla'_s \cdot \bar{K}_s(\bar{r}') \right) = 0 \quad (2.166)$$

$$\hat{n} \cdot \int_{S_a} \nabla G_0(\bar{r}_+, \bar{r}') \times \bar{K}_s(\bar{r}') dS' = -\hat{n} \cdot \left(\frac{\hat{n}}{2} \times \bar{K}_s(\bar{r}) \right) = 0 \quad (2.167)$$

$$\hat{n} \cdot \int_{S_a} \nabla G_0(\bar{r}_-, \bar{r}') \times \bar{J}_s(\bar{r}') dS' = \hat{n} \cdot \left(\frac{\hat{n}}{2} \times \bar{J}_s(\bar{r}) \right) = 0 \quad (2.168)$$

$$\hat{n} \cdot \int_{S_a} \nabla G_0(\bar{r}_+, \bar{r}') [\hat{n}' \cdot \bar{E}(\bar{r}')] dS' = \hat{n} \cdot \left(-\frac{\hat{n}}{2} \hat{n} \cdot \bar{E}(\bar{r}) \right) = -\frac{\hat{n} \cdot \bar{E}(\bar{r})}{2} \quad (2.169)$$

$$\hat{n} \cdot \int_{S_a} \nabla G_1(\bar{r}_-, \bar{r}') \left[\frac{\mu_0}{\mu_1} \hat{n}' \cdot \bar{H}(\bar{r}') \right] dS' = \hat{n} \cdot \left(\frac{\hat{n}}{2} \frac{\mu_0}{\mu_1} \hat{n} \cdot \bar{H}(\bar{r}) \right) = \frac{\mu_0}{\mu_1} \frac{\hat{n} \cdot \bar{H}(\bar{r})}{2} \quad (2.170)$$

These results are combined with Equations (2.156)-(2.159) to produce the integral equations for the 3-D dielectric surface

$$\begin{aligned}
 0 = & -\frac{\hat{n} \times \bar{E}(\bar{r})}{2} + \hat{n} \times \int i\omega\mu_1\hat{n}' \times \bar{H}(\bar{r}')G_1dS' \\
 & - \hat{n} \times \left[\int \left\{ \hat{n}' \times \bar{E}(\bar{r}') \times \nabla'G_1 + (\hat{n}' \cdot \bar{E}(\bar{r}')) \frac{\epsilon_0}{\epsilon_1} \nabla'G_1 \right\} dS' \right] \quad (2.171)
 \end{aligned}$$

$$\begin{aligned}
 \hat{n} \times \bar{H}^{inc}(\bar{r}) = & \frac{\hat{n} \times \bar{H}(\bar{r})}{2} - \hat{n} \times \int i\omega\epsilon_0\hat{n}' \times \bar{E}(\bar{r}')G_0dS' \\
 & - \hat{n} \times \left[\int \left\{ \hat{n}' \times \bar{H}(\bar{r}') \times \nabla'G_0 + (\hat{n}' \cdot \bar{H}(\bar{r}')) \nabla'G_0 \right\} dS' \right] \quad (2.172)
 \end{aligned}$$

$$\begin{aligned}
 \hat{n} \cdot \bar{E}^{inc}(\bar{r}) = & \frac{\hat{n} \cdot \bar{E}(\bar{r})}{2} + \hat{n} \cdot \int i\omega\mu_0\hat{n}' \times \bar{H}(\bar{r}')G_0dS' \\
 & - \hat{n} \cdot \left[\int \left\{ \hat{n}' \times \bar{E}(\bar{r}') \times \nabla'G_0 + (\hat{n}' \cdot \bar{E}(\bar{r}')) \nabla'G_0 \right\} dS' \right] \quad (2.173)
 \end{aligned}$$

$$\begin{aligned}
 0 = & -\frac{\hat{n} \cdot \bar{H}(\bar{r})}{2} - \hat{n} \cdot \int i\omega\epsilon_1\hat{n}' \times \bar{E}(\bar{r}')G_1dS' \\
 & - \hat{n} \cdot \left[\int \left\{ \hat{n}' \times \bar{H}(\bar{r}') \times \nabla'G_1 + (\hat{n}' \cdot \bar{H}(\bar{r}')) \nabla'G_1 \right\} dS' \right] \quad (2.174)
 \end{aligned}$$

Note that the normal vector of the surface \hat{n} is given as $\hat{n} = \bar{n}/\|\bar{n}\| = (-\frac{\partial f}{\partial x}\hat{x} - \frac{\partial f}{\partial y}\hat{y} + \hat{z})/\sqrt{1+(\frac{\partial f}{\partial x})^2+(\frac{\partial f}{\partial y})^2}$ and the gradient of the Green's function can be written as

$$\nabla G_\alpha(\bar{r}, \bar{r}') = (\bar{r} - \bar{r}')g_\alpha(R), \quad \alpha = 0, 1 \quad (2.175)$$

$$g_0(R) = \frac{(1 + ik_0R)e^{-ik_0R}}{4\pi R^3} \quad (2.176)$$

$$g_1(R) = \frac{(1 + ik_1R)e^{-ik_1R}}{4\pi R^3} \quad (2.177)$$

The vector integral equations can be written in the form of the coupled scalar integral equations where the unknowns are x, y components of $\hat{n} \times \bar{H}(\bar{r})$, $\hat{n} \times \bar{E}(\bar{r})$ and normal component of $\hat{n} \cdot \bar{H}(\bar{r})$, $\hat{n} \cdot \bar{E}(\bar{r})$. F_x and F_y represent the x and y components of $\hat{n} \times \bar{H}(\bar{r})$ and F_n represents the normal component of $\hat{n} \cdot \bar{H}(\bar{r})$

$$\begin{aligned}
 F_x(\bar{r}) &= \sqrt{1 + \left(\frac{\partial f(x,y)}{\partial x}\right)^2 + \left(\frac{\partial f(x,y)}{\partial y}\right)^2} \hat{n} \times \bar{H}(\bar{r}) \cdot \hat{x} \\
 &= \left(-\frac{\partial f}{\partial y} \hat{z} - \hat{y}\right) \cdot \bar{H}
 \end{aligned} \tag{2.178}$$

$$\begin{aligned}
 F_y(\bar{r}) &= \sqrt{1 + \left(\frac{\partial f(x,y)}{\partial x}\right)^2 + \left(\frac{\partial f(x,y)}{\partial y}\right)^2} \hat{n} \times \bar{H}(\bar{r}) \cdot \hat{y} \\
 &= \left(\frac{\partial f}{\partial x} \hat{z} + \hat{x}\right) \cdot \bar{H}
 \end{aligned} \tag{2.179}$$

$$\begin{aligned}
 F_n(\bar{r}) &= \sqrt{1 + \left(\frac{\partial f(x,y)}{\partial x}\right)^2 + \left(\frac{\partial f(x,y)}{\partial y}\right)^2} \hat{n} \cdot \bar{H}(\bar{r}) \\
 &= \left(-\frac{\partial f}{\partial x} \hat{x} - \frac{\partial f}{\partial y} \hat{y} + \hat{z}\right) \cdot \bar{H}
 \end{aligned} \tag{2.180}$$

In addition I_x and I_y represent the x and y components of $\hat{n} \times \bar{E}(\bar{r})$ and I_n represents the normal component of $\hat{n} \cdot \bar{E}(\bar{r})$

$$\begin{aligned}
 I_x(\bar{r}) &= \sqrt{1 + \left(\frac{\partial f(x,y)}{\partial x}\right)^2 + \left(\frac{\partial f(x,y)}{\partial y}\right)^2} \hat{n} \times \bar{E}(\bar{r}) \cdot \hat{x} \\
 &= \left(-\frac{\partial f}{\partial y} \hat{z} - \hat{y}\right) \cdot \bar{E}
 \end{aligned} \tag{2.181}$$

$$\begin{aligned}
 I_y(\bar{r}) &= \sqrt{1 + \left(\frac{\partial f(x,y)}{\partial x}\right)^2 + \left(\frac{\partial f(x,y)}{\partial y}\right)^2} \hat{n} \times \bar{E}(\bar{r}) \cdot \hat{y} \\
 &= \left(\frac{\partial f}{\partial x} \hat{z} + \hat{x}\right) \cdot \bar{E}
 \end{aligned} \tag{2.182}$$

$$\begin{aligned}
 I_n(\bar{r}) &= \sqrt{1 + \left(\frac{\partial f(x,y)}{\partial x}\right)^2 + \left(\frac{\partial f(x,y)}{\partial y}\right)^2} \hat{n} \cdot \bar{E}(\bar{r}) \\
 &= \left(-\frac{\partial f}{\partial x} \hat{x} - \frac{\partial f}{\partial y} \hat{y} + \hat{z}\right) \cdot \bar{E}
 \end{aligned} \tag{2.183}$$

Note that the z component of $\hat{n} \times \bar{E}(\bar{r})$ and $\hat{n} \times \bar{H}(\bar{r})$ can be expressed as a function of the x and y components of $\hat{n} \times \bar{E}(\bar{r})$ and $\hat{n} \times \bar{H}(\bar{r})$ respectively

$$\begin{aligned}
 F_z(\bar{r}) &= -\frac{\partial f}{\partial x} H_y + \frac{\partial f}{\partial y} H_x \\
 &= -\frac{\partial f}{\partial x} H_y - \frac{\partial f}{\partial x} \frac{\partial f}{\partial y} H_z + \frac{\partial f}{\partial x} \frac{\partial f}{\partial y} H_z + \frac{\partial f}{\partial y} H_x \\
 &= \frac{\partial f}{\partial x} \left(-H_y - \frac{\partial f}{\partial y} H_z\right) + \frac{\partial f}{\partial y} \left(\frac{\partial f}{\partial x} H_z + H_x\right) \\
 &= \frac{\partial f}{\partial x} F_x(\bar{r}) + \frac{\partial f}{\partial y} F_y(\bar{r})
 \end{aligned} \tag{2.184}$$

The method of moment is then applied to discretise the integral equation (2.171)-(2.174) into scalar form in terms of $F_x, F_y, F_n, I_x, I_y, I_n$ as follow

$$\begin{bmatrix} \bar{\bar{Z}}^{(11)} & \bar{\bar{Z}}^{(12)} & \bar{\bar{Z}}^{(13)} & \bar{\bar{Z}}^{(14)} & \bar{\bar{Z}}^{(15)} & \bar{\bar{Z}}^{(16)} \\ \bar{\bar{Z}}^{(21)} & \bar{\bar{Z}}^{(22)} & \bar{\bar{Z}}^{(23)} & \bar{\bar{Z}}^{(24)} & \bar{\bar{Z}}^{(25)} & \bar{\bar{Z}}^{(26)} \\ \bar{\bar{Z}}^{(31)} & \bar{\bar{Z}}^{(32)} & \bar{\bar{Z}}^{(33)} & \bar{\bar{Z}}^{(34)} & \bar{\bar{Z}}^{(35)} & \bar{\bar{Z}}^{(36)} \\ \bar{\bar{Z}}^{(41)} & \bar{\bar{Z}}^{(42)} & \bar{\bar{Z}}^{(43)} & \bar{\bar{Z}}^{(44)} & \bar{\bar{Z}}^{(45)} & \bar{\bar{Z}}^{(46)} \\ \bar{\bar{Z}}^{(51)} & \bar{\bar{Z}}^{(52)} & \bar{\bar{Z}}^{(53)} & \bar{\bar{Z}}^{(54)} & \bar{\bar{Z}}^{(55)} & \bar{\bar{Z}}^{(56)} \\ \bar{\bar{Z}}^{(61)} & \bar{\bar{Z}}^{(62)} & \bar{\bar{Z}}^{(63)} & \bar{\bar{Z}}^{(64)} & \bar{\bar{Z}}^{(65)} & \bar{\bar{Z}}^{(66)} \end{bmatrix} \begin{bmatrix} \bar{I}_x \\ \bar{I}_y \\ \bar{I}_n \\ \bar{F}_x \\ \bar{F}_y \\ \bar{F}_n \end{bmatrix} = \begin{bmatrix} \bar{0} \\ \bar{0} \\ \bar{I}_n^{inc} \\ \bar{F}_x^{inc} \\ \bar{F}_y^{inc} \\ \bar{0} \end{bmatrix} \quad (2.185)$$

The explicit entries for the quantities of the impedance matrix are given in Appendix B.

2.5.1 Scattered field in the far zone

In this section, we derive the scattered field in the far zone that will be used in Chapter 6 to compute the bistatic scattering coefficient. The scattered far field is evaluated by assuming the observation point to be far away from the source. We assume that $\hat{k}_s = \sin\theta_s \cos\phi_s \hat{x} + \sin\theta_s \sin\phi_s \hat{y} + \cos\theta_s \hat{z}$ is the scattering direction. In the far zone, the scattered electric field can be written as the sum of the horizontal and vertical components

$$\bar{E}^s = \bar{E}_{\theta_s}^s \hat{\theta}_s + \bar{E}_{\phi_s}^s \hat{\phi}_s \quad (2.186)$$

These scattered electric field can be approximated in the far zone as

$$\bar{E}_{\theta_s}^s = -ik_0 \eta_0 A_{\theta_s} + \frac{\partial F_{\phi_s}}{\partial r} \quad (2.187)$$

$$\bar{E}_{\phi_s}^s = -ik_0 \eta_0 A_{\phi_s} - \frac{\partial F_{\theta_s}}{\partial r} \quad (2.188)$$

The sources of the scattered field are described in the Cartesian coordinates and it is necessary to transform them to the spherical system

$$A_{\theta_s} = \hat{e}_s \cdot \bar{A} = \iiint \hat{e}_s \cdot \bar{J}(\bar{r}') \frac{e^{-ik_0|\bar{r}-\bar{r}'|}}{4\pi|\bar{r}-\bar{r}'|} d\bar{r}' \quad (2.189)$$

$$A_{\phi_s} = \hat{h}_s \cdot \bar{A} = \iiint \hat{h}_s \cdot \bar{J}(\bar{r}') \frac{e^{-ik_0|\bar{r}-\bar{r}'|}}{4\pi|\bar{r}-\bar{r}'|} d\bar{r}' \quad (2.190)$$

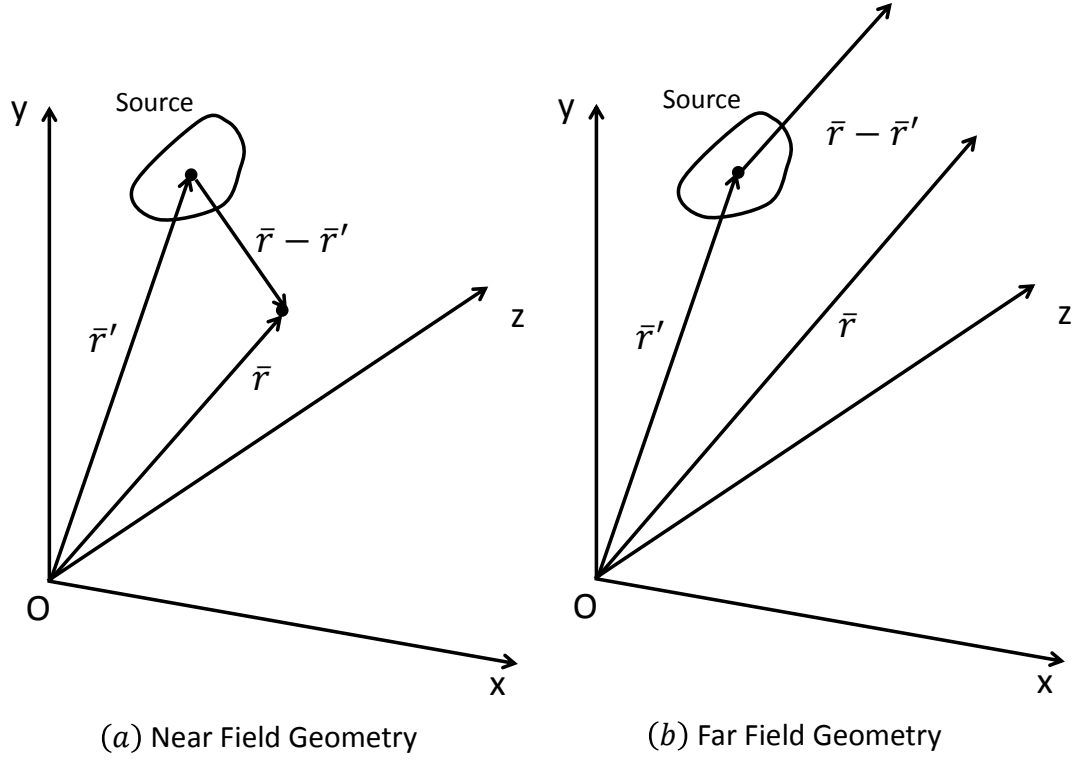


Figure 2.12: Near and far field geometry

where \hat{e}_s and \hat{h}_s denotes the vertical and horizontal polarization directions. \hat{e}_s and \hat{h}_s are defined so that $\{\hat{k}_s, \hat{e}_s, \hat{h}_s\}$ forms an orthonormal system

$$\hat{e}_s = \cos\theta_s \cos\phi_s \hat{x} + \cos\theta_s \sin\phi_s \hat{y} - \sin\theta_s \hat{z} \quad (2.191)$$

$$\hat{h}_s = -\sin\phi_s \hat{x} + \cos\phi_s \hat{y} \quad (2.192)$$

Then the scattered far fields can be calculated by putting \bar{r} in the far zone as shown in Figure 2.12, we can reasonably approximate $|\bar{r} - \bar{r}'|$ as

$$|\bar{r} - \bar{r}'| \simeq \begin{cases} |\bar{r}| - \hat{k}_s \cdot \bar{r}' & \text{for phase variations} \\ |\bar{r}| & \text{for amplitude variations} \end{cases} \quad (2.193)$$

Using the above approximation in (2.189) and (2.190), we obtain

$$A_{\theta_s} = \frac{e^{-ik_0|\bar{r}|}}{4\pi|\bar{r}|} \iiint \hat{e}_s \cdot \bar{J}(\bar{r}') e^{ik_0\hat{k}_s \cdot \bar{r}'} d\bar{r}' \quad (2.194)$$

$$A_{\phi_s} = \frac{e^{-ik_0|\bar{r}|}}{4\pi|\bar{r}|} \iiint \hat{h}_s \cdot \bar{J}(\bar{r}') e^{ik_0\hat{k}_s \cdot \bar{r}'} d\bar{r}' \quad (2.195)$$

Then the far field forms of the scattered field are

$$\bar{E}_{\theta_s}^s = \frac{-ik_0}{4\pi} \frac{e^{-ik_0|\bar{r}|}}{|\bar{r}|} \iiint [\eta_0 \hat{e}_s \cdot \bar{J}(\bar{r}') + \hat{h}_s \cdot \bar{K}(\bar{r}')] e^{ik_0\hat{k}_s \cdot \hat{r}'} d\bar{r}' \quad (2.196)$$

$$\bar{E}_{\phi_s}^s = \frac{-ik_0}{4\pi} \frac{e^{-ik_0|\bar{r}|}}{|\bar{r}|} \iiint [\eta_0 \hat{h}_s \cdot \bar{J}(\bar{r}') - \hat{e}_s \cdot \bar{K}(\bar{r}')] e^{ik_0\hat{k}_s \cdot \hat{r}'} d\bar{r}' \quad (2.197)$$

These scattered fields in the far zone will be used to compute the 3D bistatic scattering coefficient in Chapter 6.

2.6 Conclusions

As detailed in this chapter, electromagnetic scattering problems have been formulated with surface integral equations. Alternative formulations such as 2D, 3D wave scattering problems, integral equation in terms of surface electric and magnetic currents, integral equation in terms of surface electric and magnetic fields have been derived. These integral equation formulations are extensively applied throughout this dissertation.

3 Improved Tabulated Interaction Method for Electromagnetic Wave Scattering From Lossy Irregular Terrain Profiles

3.1 Introduction

Efficient and accurate computation of electromagnetic wave scattering from surfaces remains a core requirement in wireless system planning. A wide range of propagation models has been proposed to solve such scattering problems including empirical models, ray tracing models, full-wave methods etc. Among these methods, full-wave methods offer high accuracy while in particular those based on the method of moments (MoM) only require the discretization of the scatterer boundary and naturally satisfy the radiation condition at infinity through the use of suitable Green's functions. However they result in a dense set of linear equations which require computational complexity of $O(N^3)$ to invert where N is the number of basis functions used in the discretisation process. This computational cost is unviable for large scale problems such as terrain propagation where the number of unknowns could be of the order of millions. Iterative methods reduce the computational complexity to $\mathcal{O}(N^2)$ and can be used to effectively solve these electrically large scale problems [32, 33, 34] (although direct solvers based on compression of the low-rank matrix sub-blocks can also be used, as for example in [84]). Commonly used Krylov-subspace based iterative techniques such as the conjugate gradient (CG) or Generalized Minimal Residual (GMRES) methods [32, 33] are quite robust but can be very slow to converge thereby requiring the use of effective preconditioners. In response to this limitation, the stationary iterative forward-backward method (FBM) [34] have been shown to have a very high convergence rate, yielding an accurate solution for some problems with much fewer iterations. The FBM method is equivalent to the symmetric successive over-relaxation (SSOR) scheme with a unit relaxation factor and zero initial guess vector [33]. However, FBM requires full matrix-vector multiplication resulting in a $\mathcal{O}(N^2)$ computational complexity rendering FBM inefficient as the size of problem is increased. Different techniques have been developed to overcome this limitation of FBM including acceleration methods such as the Forward Backward Method with Spectral Acceleration (FBM-SA) [35, 36, 37] and the Fast Far Field Approximation (FAFFA) [39]. In contrast compression techniques such as the Characteristic Basis Function Method (CBFM) [43, 44] are iteration-free and

potentially quite efficient [43, 44]. The CBFM is a type of Macro Basis Functions (MBFs) approach which rely on a “divide-and-conquer” approach [85]. The Macro Basis Functions (MBFs) approach is a form of domain-decomposition method and has been systematically developed by Suter and Mosig [86] to solve radiation and scattering problems based on integral-equation techniques.

The CBFM constructs the reduced system by using primary (PBFs) and secondary basis functions (SBFs) and solves the reduced system directly thereby not suffering from any convergence problems [44, 43]. To apply the CBFM to scattering from terrain profiles one must decompose the profile into linear groups. The CBFM then defines individual basis functions for each group and generates the reduced matrix using a Galerkin method which requires a considerable computational effort. In this chapter, a similar approach is followed but a common set of basis functions is used to construct the surface currents for *all* groups of the terrain profile. The basis functions are defined as the currents excited on *all* groups in response to a set of impinging plane waves propagating in either free-space or in medium 1 (earth). The proposed method (ITIM) shares some similarities with the Fast Far Field decomposition which in turns related to the Fast Multipole Method (FMM). In both methods, the far field interactions are calculated in a group-to-group manner using the superposition of a finite number of plane waves. The FMM uses this approximation to reduce the complexity of a matrix-vector product (MVP) required by the iterative algorithms such as GMRES, CG, etc from $\mathcal{O}(N^2)$ to $\mathcal{O}(N\log N)$. The ITIM instead applies this approximation and uses a set of predefined basis functions to construct a reduced system with much fewer unknowns. In addition the ITIM enables reduce the near field computations and matrix entries can be computed very rapidly using pre-computed tabulated values. This results in the proposed method having a very low computational complexity and memory storage requirement. The proposed method is referred as the Improved Tabulated Interaction Method (ITIM) which extends the original Tabulated Interaction Method (TIM) [40] in several ways. Firstly the proposed method is formulated for the lossy dielectric case which is more general than the formulation of original TIM for the perfectly conducting terrain case. Secondly the original TIM is described assuming forward scattering, essentially computing a single “forward step” of the FBM.

This chapter instead derives a matrix equation for the amplitudes of the common basis functions which incorporates all backward and forward scattering effects. The original TIM can be thought of as a special case of ITIM, obtained by solving the lower triangular matrix of the reduced system. Finally a two-level ITIM (TL-ITIM) is applied to improve the accuracy of the method. In areas of deep shadow along mountainous profiles the underpinning approximation of the ITIM, namely that terrain blocks interact via a single plane wave becomes inaccurate for neighbouring sub-groups. The TL-ITIM instead approximates the interaction in terms of several plane waves, resulting in a more accurate approximation with only a minimal increase in computation time. The chapter is organ-

ised as follows. In Section 3.2, the integral equation formulation for the dielectric case is reintroduced, based on chapter 2. The ITIM formulation is derived in section 3.3 with two important underpinning approximations being derived in section 3.4. Section 3.4 also introduces the two-level ITIM, designed to increase accuracy for near-neighbour interactions. Some implementational issues as well as computational efficiency are discussed in section 3.5 while results are presented in section 3.6. Section 3.7 introduces an efficient and accurate method to speed up the generation of basis functions and far fields patterns of the proposed Improved Tabulated Interaction method and section 3.8 concludes the chapter.

3.2 Wave scattering from 1D dielectric surfaces

Consider an incident wave $\psi_{inc}(x, y)$ impinging upon a dielectric surface with height profile $y = f(x)$ as shown in Figure 3.1. The upper medium is assumed to be free-space with permittivity ϵ_0 and wavenumber k_0 while the lower medium is assumed to be a dielectric with complex permittivity ϵ_1 and wavenumber k_1 . As derived in Section 2.4.1, for an incident TM^z polarised wave, the field components present are E_z , H_x and H_y and the two coupled electric field integral equations (EFIE) are written as

$$K_t(t) + \int ik_0\eta_0 J_z(t') G_0(\bar{\rho}, \bar{\rho}') dt' - \int K_t(t') [\hat{n}' \cdot \nabla G_0(\bar{\rho}, \bar{\rho}')] dt' = E_z^{inc}(t) \quad (3.1)$$

$$K_t(t) - \int ik_1\eta_1 J_z(t') G_1(\bar{\rho}, \bar{\rho}') dt' + \int K_t(t') [\hat{n}' \cdot \nabla G_1(\bar{\rho}, \bar{\rho}')] dt' = 0 \quad (3.2)$$

where the points $\bar{\rho} = x\hat{x} + y\hat{y}$ and $\bar{\rho}' = x'\hat{x} + y'\hat{y}$ are on the surface. $E_z^{inc}(t)$ is the incident electric field while $J_z(t)$ and $K_t(t)$ are the equivalent surface electric and magnetic current densities. $G_0(\bar{\rho}, \bar{\rho}')$ and $G_1(\bar{\rho}, \bar{\rho}')$ are the Green's function of the upper and lower half-space.

$$G_0(\bar{\rho}, \bar{\rho}') = -\frac{i}{4} H_0^{(2)}(k_0 |\bar{\rho} - \bar{\rho}'|) \quad (3.3)$$

$$G_1(\bar{\rho}, \bar{\rho}') = -\frac{i}{4} H_0^{(2)}(k_1 |\bar{\rho} - \bar{\rho}'|). \quad (3.4)$$

As derived in Section 2.4.2, for an incident TE polarization wave, the field components present are H_z , E_x and E_y and two coupled magnetic field integral equations (MFIE) are written as

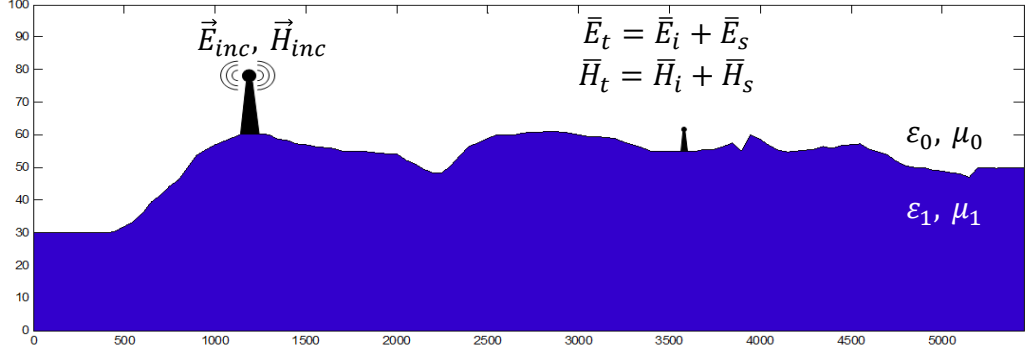


Figure 3.1: Wave impinging upon a dielectric surface

$$-J_t(t) + \int i \frac{k_0}{\eta_0} K_z(t') G_0(\bar{\rho}, \bar{\rho}') dt' + \int J_t(t') [\hat{n}' \cdot \nabla G_0(\bar{\rho}, \bar{\rho}')] dt' = H_z^{inc}(t) \quad (3.5)$$

$$J_t(t) + \int i \frac{k_1}{\eta_1} K_z(t') G_1(\bar{\rho}, \bar{\rho}') dt' + \int J_t(t') [\hat{n}' \cdot \nabla G_1(\bar{\rho}, \bar{\rho}')] dt' = 0 \quad (3.6)$$

The Method of Moments (MoM) is typically applied to solve the relevant integral equation system by expanding the electric current $J(\bar{\rho})$ and magnetic current $K(\bar{\rho})$ into a finite series using N pulse basis functions and evaluating the appropriate equation system at the centres of the N basis function domains, resulting in a dense system of $2N$ linear equations

$$\begin{pmatrix} \overline{\overline{Z}}^{(a)} & \overline{\overline{Z}}^{(b)} \\ \overline{\overline{Z}}^{(c)} & \overline{\overline{Z}}^{(d)} \end{pmatrix} \begin{pmatrix} \bar{j} \\ \bar{k} \end{pmatrix} = \begin{pmatrix} \overline{\psi}^{inc} \\ 0 \end{pmatrix}, \quad (3.7)$$

where $\overline{\overline{Z}}^{(a)}, \overline{\overline{Z}}^{(b)}, \overline{\overline{Z}}^{(c)}, \overline{\overline{Z}}^{(d)}$ are $N \times N$ matrices, $\overline{\psi}^{inc}$ is the $N \times 1$ vector whose elements are the incident fields at the matching points on the surface and \bar{j}, \bar{k} are the $N \times 1$ vectors containing the unknown electric and magnetic surface currents at the center of the basis functions. Once found the surface currents can be used to compute scattered fields, and

thus total fields, above the surface. Explicit entries for the quantities in equation (3.7) can be found in Section 2.4.1 and Section 2.4.2.

3.3 The Improved Tabulated Interaction Method

Equation (3.7) assumes the pulse basis functions to be distributed evenly over the terrain surface. The unknown vector on the left hand side of equation (3.7) comprises the N unknown electric current amplitudes, \bar{j} , followed by the N unknown magnetic current amplitudes, \bar{k} . In order to apply the ITIM the unknowns are first re-ordered. The terrain profile is considered to consist of M connected identical linear segments of a fixed length as shown in Figure 3.2. These identical linear segments are referred to as groups. Each group has $Q \equiv \frac{N}{M}$ pulse basis function domains defined on it. These have width Δ_x . The unknown electric and magnetic current amplitudes associated with group j are collected together and denoted by \bar{i}_j (where it is assumed that the electric currents are listed first, followed by the magnetic currents). The groups define a decomposition of the impedance matrix into sub-matrices and we can use this to re-write equation (3.7) as

$$\sum_{j=1}^M \bar{Z}_{ij} \bar{i}_j = \bar{v}_i \text{ for } i = 1 \cdots M, \quad (3.8)$$

where

$$\bar{Z}_{ij} = \begin{bmatrix} \bar{Z}_{ij}^{(a)} & \bar{Z}_{ij}^{(b)} \\ \bar{Z}_{ij}^{(c)} & \bar{Z}_{ij}^{(d)} \end{bmatrix} \quad (3.9)$$

contains the interactions between the basis functions in group i and group j while \bar{v}_i is a $2N \times 1$ vector containing the N incident field values for group i followed by N zeros.

3.3.1 Basis function definition

Central to the ITIM is the use of basis functions $\phi_0^{(k)}$ and $\phi_1^{(k)}$ each of which is defined over each group. These basis functions have three distinct advantages.

- The same set of basis functions are used for each group as the groups as presumed geometrically identical and, to a certain level of accuracy, are all subject to impinging fields of the same form, namely plane waves. This assumption will be justified in Section 3.4.
- While a complete set of basis functions are defined for each group only a small number are actually excited on each group, so the expansion is efficient. The resultant linear system has relatively few unknowns and can be rapidly inverted.
- The linear system matrix entries can be constructed very efficiently using pre-computed tabulated quantities as well as some geometrical information about relative group locations and some interpolation.

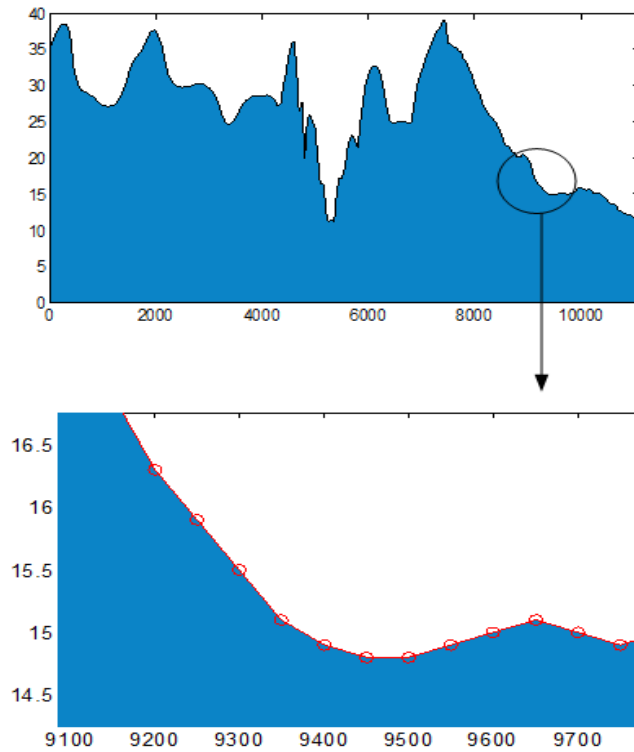


Figure 3.2: A terrain profile (Hjorring - Denmark) is considered to consist of connected identical linear segments.

As the groups are identical linear segments differing only in their slope, it is possible to define the basis functions in the context of a typical reference group. The basis functions are defined as the currents excited on this group in response to a set of impinging plane waves propagating in either free-space or in medium 1 (earth). Referring to Figure 3.3, we introduce the $K + 1$ direction vectors \hat{e}_k where

$$\hat{e}_k = \cos \frac{\pi k}{K} \hat{x} + \sin \frac{\pi k}{K} \hat{y}, \quad k = 0, \dots, K. \quad (3.10)$$

Note that due to symmetry it is only necessary to consider angles in the range $[0, \pi]$. The angular discretisation used is denoted by $\Delta\theta$ and is given by

$$\Delta\theta = \frac{\pi}{K}. \quad (3.11)$$

These direction vectors \hat{e}_k , $k = 0, \dots, K$ are used to define the set of discretised impinging

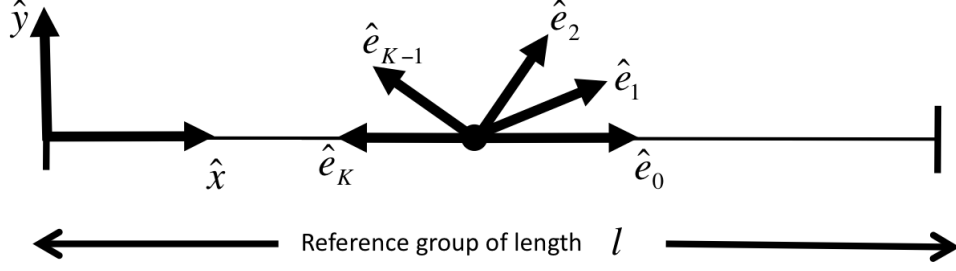


Figure 3.3: $K + 1$ direction vectors \hat{e}_k are defined on a reference group and are used to define the set of common basis functions $\phi_0^{(k)}$ and $\phi_1^{(k)}$

plane waves $\bar{p}_0^{(k)}$ and $\bar{p}_1^{(k)}$ for $k = 0 \dots K$

$$\bar{p}_0^{(k)} = \begin{bmatrix} e^{ik_0 \hat{e}_k \cdot \hat{x} (1 - \frac{Q+1}{2}) \Delta x} \\ e^{ik \hat{e}_k \cdot \hat{x} (2 - \frac{Q+1}{2}) \Delta x} \\ \cdot \\ \cdot \\ e^{ik_0 \hat{e}_k \cdot \hat{x} (Q - \frac{Q+1}{2}) \Delta x} \end{bmatrix}, \quad (3.12)$$

$$\bar{p}_1^{(k)} = \begin{bmatrix} e^{ik_1 \hat{e}_k \cdot \hat{x} (1 - \frac{Q+1}{2}) \Delta x} \\ e^{ik_1 \hat{e}_k \cdot \hat{x} (2 - \frac{Q+1}{2}) \Delta x} \\ \cdot \\ \cdot \\ e^{ik_1 \hat{e}_k \cdot \hat{x} (Q - \frac{Q+1}{2}) \Delta x} \end{bmatrix}. \quad (3.13)$$

Recall that Q is the number of discretisation points on the reference group and Δx is the discretisation step. We now define the ITIM basis functions in terms of these discretised plane waves. In particular we define $\phi_0^{(k)}$ and $\phi_1^{(k)}$ for $k = 0 \dots K$ to be the currents excited on a typical group under plane-wave incidence, that is

$$\bar{\bar{Z}}_{ii} \bar{\phi}_0^{(k)} = \bar{q}_0^{(k)} \quad (3.14)$$

$$\bar{\bar{Z}}_{ii} \bar{\phi}_1^{(k)} = \bar{q}_1^{(k)} \quad (3.15)$$

for any i as the groups are geometrically identical and thus the $\bar{\bar{Z}}_{ii}$ are the same for each i . The right hand side vectors are given by

$$\bar{q}_0^{(k)} = \begin{bmatrix} \bar{p}_0^{(k)} \\ \bar{0} \end{bmatrix}, \quad (3.16)$$

$$\bar{q}_1^{(k)} = \begin{bmatrix} \bar{0} \\ \bar{p}_1^{(k)} \end{bmatrix}, \quad (3.17)$$

where $\bar{0}$ is a $N \times 1$ vector containing N zeros. Each basis function is thus a $2N \times 1$ vector and comprises of a $N \times 1$ electric current and $N \times 1$ magnetic current

$$\bar{\phi}_0^{(m)} = \begin{bmatrix} \bar{j}_0^{(m)} \\ \bar{k}_0^{(m)} \end{bmatrix}, \quad (3.18)$$

$$\bar{\phi}_1^{(m)} = \begin{bmatrix} \bar{j}_1^{(m)} \\ \bar{k}_1^{(m)} \end{bmatrix}. \quad (3.19)$$

3.3.2 Derivation of ITIM linear system

In this subsection a new linear system is derived in terms of the amplitudes of the ITIM basis functions $\phi_0^{(k)}$ and $\phi_1^{(k)}$ and we highlight the efficiencies that they offer. Some derivations are held over until Section 3.4 in order not to impede the flow of the discussion in this section. We expand the unknown currents on each group in terms of these basis functions. For group $i = 1 \dots M$

$$\bar{i}_i \simeq \sum_{k=0}^K \left(\alpha_i^{(k)} \bar{\phi}_0^{(k)} + \beta_i^{(k)} \bar{\phi}_1^{(k)} \right), \quad (3.20)$$

where $\alpha_i^{(k)}$ and $\beta_i^{(k)}$ are coefficients to be determined. Placing this expansion into equation (3.8) and expanding the right hand side vector in terms of plane waves (see Section 3.4.1 for details) yields

$$\sum_{k=0}^K v_i^{(k)} \bar{q}_0^{(k)} = \sum_{j=1}^M \bar{\bar{Z}}_{ij} \sum_{k=0}^K \left(\alpha_j^{(k)} \bar{\phi}_0^{(k)} + \beta_j^{(k)} \bar{\phi}_1^{(k)} \right) \quad \text{for } i = 1 \dots M. \quad (3.21)$$

Separating out the interactions within each group from the interactions between groups yields

$$\begin{aligned} \sum_{k=0}^K v_i^{(k)} \bar{q}_0^{(k)} &= \bar{\bar{Z}}_{ii} \sum_{k=0}^K \left(\alpha_i^{(k)} \bar{\phi}_0^{(k)} + \beta_i^{(k)} \bar{\phi}_1^{(k)} \right) \\ &+ \sum_{\substack{j=1 \\ j \neq i}}^M \bar{\bar{Z}}_{ij} \sum_{k=0}^K \left(\alpha_j^{(k)} \bar{\phi}_0^{(k)} + \beta_j^{(k)} \bar{\phi}_1^{(k)} \right) \quad \text{for } i = 1 \dots M. \end{aligned} \quad (3.22)$$

The success of the ITIM is due to the ability to rapidly compute the unknown coefficients $\alpha_i^{(k)}$ and $\beta_i^{(k)}$ for each group. To see how this is done we recall the definition of $\bar{\bar{Z}}_{ij}$ from equation (3.9) and introduce the following approximations. Each approximation writes one of the four $\bar{\bar{Z}}_{ij}$ interaction matrices in terms of a spectrum of plane waves radiating from the transmitting group j and a spectrum of plane waves impinging on the receiving

group i

$$\overline{\overline{Z}}_{ij}^{(a)} \simeq Z_{ll'}^{(a)} \sum_{k=0}^K a_{ij}^{(k)} \overline{p}_0^{(k)} \sum_{t=0}^K b_{ij}^{(t)} [\overline{p}_0^{(t)}]^T, \quad (3.23)$$

$$\overline{\overline{Z}}_{ij}^{(b)} \simeq Z_{ll'}^{(b)} \sum_{k=0}^K a_{ij}^{(k)} \overline{p}_0^{(k)} \sum_{t=0}^K b_{ij}^{(t)} [\overline{p}_0^{(t)}]^T, \quad (3.24)$$

$$\overline{\overline{Z}}_{ij}^{(c)} \simeq Z_{ll'}^{(c)} \sum_{k=0}^K a_{ij}^{(k)} \overline{p}_1^{(k)} \sum_{t=0}^K b_{ij}^{(t)} [\overline{p}_1^{(t)}]^T, \quad (3.25)$$

$$\overline{\overline{Z}}_{ij}^{(d)} \simeq Z_{ll'}^{(d)} \sum_{k=0}^K a_{ij}^{(k)} \overline{p}_1^{(k)} \sum_{t=0}^K b_{ij}^{(t)} [\overline{p}_1^{(t)}]^T. \quad (3.26)$$

The derivation of these approximations is held over until Section 3.4.2 so as not to impede the flow of this section. At this stage it is only necessary to note that $Z_{ll'}^{(a,b,c,d)}$ represent interactions between the centres of group i and j and that the vast majority of the interpolation coefficients $a_{ij}^{(k)}$ and $b_{ij}^{(l)}$ are zero. Equations (3.23) to (3.26) can be written more compactly as

$$\overline{\overline{Z}}_{ij} \simeq \sum_{k=0}^K a_{ij}^{(k)} \overline{\overline{Q}}^{(k)} \overline{\overline{R}}_{ij} \quad (3.27)$$

where

$$\overline{\overline{Q}}^{(k)} = \begin{bmatrix} \overline{p}_0^{(k)} & \overline{0} \\ \overline{0} & \overline{p}_1^{(k)} \end{bmatrix} \equiv [\overline{q}_0^{(k)} \overline{q}_1^{(k)}] \quad (3.28)$$

$$\overline{\overline{R}}_{ij} = \sum_{t=0}^K \begin{bmatrix} Z_{ll'}^{(a)} b_{ij}^{(t)} [\overline{p}_0^{(t)}]^T & Z_{ll'}^{(b)} b_{ij}^{(t)} [\overline{p}_0^{(t)}]^T \\ Z_{ll'}^{(c)} b_{ij}^{(t)} [\overline{p}_1^{(t)}]^T & Z_{ll'}^{(d)} b_{ij}^{(t)} [\overline{p}_1^{(t)}]^T \end{bmatrix}. \quad (3.29)$$

Inserting this into equation (3.22) yields for $i = 1 \dots M$

$$\begin{aligned} \sum_{k=0}^K v_i^{(k)} \overline{q}_0^{(k)} &= \overline{\overline{Z}}_{ii} \sum_{k=0}^K \left(\alpha_i^{(k)} \overline{\phi}_0^{(k)} + \beta_i^{(k)} \overline{\phi}_1^{(k)} \right) \\ &+ \sum_{j=1, j \neq i}^M \sum_{k=0}^K a_{ij}^{(k)} \overline{\overline{Q}}^{(k)} \overline{\overline{R}}_{ij} \sum_{m=0}^K \left(\alpha_j^{(m)} \overline{\phi}_0^{(m)} + \beta_j^{(m)} \overline{\phi}_1^{(m)} \right). \end{aligned} \quad (3.30)$$

Recalling the definition of the basis functions (equations (3.14) and (3.15)) allows us to write

$$\begin{aligned} \sum_{k=0}^K v_i^{(k)} \overline{q}_0^{(k)} &= \sum_{k=0}^K \left(\alpha_i^{(k)} \overline{q}_0^{(k)} + \beta_i^{(k)} \overline{q}_1^{(k)} \right) \\ &+ \sum_{j=1, j \neq i}^M \sum_{k=0}^K a_{ij}^{(k)} \overline{\overline{Q}}^{(k)} \overline{\overline{R}}_{ij} \sum_{m=0}^K \left(\alpha_j^{(m)} \overline{\phi}_0^{(m)} + \beta_j^{(m)} \overline{\phi}_1^{(m)} \right). \end{aligned} \quad (3.31)$$

3.3 The Improved Tabulated Interaction Method

This can be written in a more compact fashion as, for $i = 1 \dots M$,

$$\sum_{k=0}^K v_i^{(k)} \bar{q}_0^{(k)} = \sum_{k=0}^K \left(\alpha_i^{(k)} \bar{q}_0^{(k)} + \beta_i^{(k)} \bar{q}_1^{(k)} \right) + \sum_{j=1, j \neq i}^M \sum_{k=0}^K a_{ij}^{(k)} \bar{Q}^{(k)} \bar{s}_{ij} \quad (3.32)$$

where \bar{s}_{ij} is a 2×1 vector given by

$$\bar{s}_{ij} = \begin{bmatrix} s_{ij0} \\ s_{ij1} \end{bmatrix}, \quad (3.33)$$

and (recalling the definition of the basis functions (3.18) and (3.19))

$$s_{ij0} = \sum_{m=0}^K \alpha_j^{(m)} \left(\sum_{t=0}^K b_{ij}^{(t)} \left(Z_{ll'}^{(a)} [\bar{p}_0^{(t)}]^T \bar{j}_0^{(m)} + Z_{ll'}^{(b)} [\bar{p}_0^{(t)}]^T \bar{k}_0^{(m)} \right) \right) + \sum_{m=0}^K \beta_j^{(m)} \left(\sum_{t=0}^K b_{ij}^{(t)} \left(Z_{ll'}^{(a)} [\bar{p}_0^{(t)}]^T \bar{j}_1^{(m)} + Z_{ll'}^{(b)} [\bar{p}_0^{(t)}]^T \bar{k}_1^{(m)} \right) \right), \quad (3.34)$$

$$s_{ij1} = \sum_{m=0}^K \alpha_j^{(m)} \left(\sum_{t=0}^K b_{ij}^{(t)} \left(Z_{ll'}^{(c)} [\bar{p}_1^{(t)}]^T \bar{j}_0^{(m)} + Z_{ll'}^{(d)} [\bar{p}_1^{(t)}]^T \bar{k}_0^{(m)} \right) \right) + \sum_{m=0}^K \beta_j^{(m)} \left(\sum_{t=0}^K b_{ij}^{(t)} \left(Z_{ll'}^{(c)} [\bar{p}_1^{(t)}]^T \bar{j}_1^{(m)} + Z_{ll'}^{(d)} [\bar{p}_1^{(t)}]^T \bar{k}_1^{(m)} \right) \right). \quad (3.35)$$

The quantities of the form $\bar{p}^T \bar{j}$ and $\bar{p}^T \bar{k}$ in the right hand side of equations (3.34) and (3.35) are far-field scattering patterns which govern how the basis functions radiate in the discretised directions. *Central to the efficiency of the ITIM is the fact that they are common to all groups and so can be pre-computed and tabulated.* We define these pre-computed tabulated far-fields, for a and b equal to 0 and 1, as

$$[\bar{p}_a^{(t)}]^T \bar{j}_b^{(m)} \equiv f_{ab}^{tm}, \quad (3.36)$$

$$[\bar{p}_a^{(t)}]^T \bar{k}_b^{(m)} \equiv g_{ab}^{tm}. \quad (3.37)$$

Equation (3.32) can be expressed as, for $i = 1 \dots M$,

$$\sum_{k=0}^K v_i^{(k)} \bar{q}_0^{(k)} = \sum_{k=0}^K \left(\alpha_i^{(k)} \bar{q}_0^{(k)} + \beta_i^{(k)} \bar{q}_1^{(k)} \right) + \sum_{j=1, j \neq i}^M \sum_{k=0}^K a_{ij}^{(k)} \left(s_{ij0} \bar{q}_0^{(k)} + s_{ij1} \bar{q}_1^{(k)} \right). \quad (3.38)$$

The quantities $\bar{q}_0^{(k)}$ and $\bar{q}_1^{(k)}$ are linearly independent and so equation (3.38) is solved by extracting an equation for each individual $\bar{q}_0^{(k)}$ and $\bar{q}_1^{(k)}$. The following $2M(K+1) \times 2M(K+1)$ linear system for the unknown coefficients is obtained

$$\alpha_i^{(k)} + \sum_{j \neq i} a_{ij}^{(k)} s_{ij0} = v_i^{(k)} \quad \text{for } k = 1 \dots K, i = 1 \dots M, \quad (3.39)$$

$$\beta_i^{(k)} + \sum_{j \neq i} a_{ij}^{(k)} s_{ij1} = 0 \quad \text{for } k = 1 \dots K, i = 1 \dots M. \quad (3.40)$$

It should be noted that for grazing incidence propagation over gently undulating terrain only a small number of basis functions are actually excited on each group and the majority of the coefficients $\alpha_i^{(k)}$ and $\beta_i^{(k)}$ above are equal to zero. Importantly the non-zero coefficients can easily be identified in advance by consideration of the geometry of the terrain and the source location. This is done in a rapid pre-processing step which identifies which basis functions are actually required given the source location. A compressed matrix of order considerably less than $2M(K+1)$ can then be created and the corresponding matrix equation solved. Indeed in the results section the order of this system is usually two orders of magnitude lower than N , the total number of discretisations on the terrain surface. Another benefit of the ITIM is that while the process is described in terms of the basis functions ϕ_0 and ϕ_1 these are not explicitly used in creating the linear system and do not need to be stored in memory. Instead the far-field patterns (equations (3.36 and (3.37)) are tabulated and used extensively. The Improved Tabulated Interaction Method can be separated into two main algorithms: pre-processing algorithm and main algorithm as described in Table 3.1. Note that the pre-processing algorithm is performed only once for *all* terrain profiles.

Table 3.1: Flowchart of Improved Tabulated Interaction Method.

PRE-PROCESSING ALGORITHM

1. Generate the basis functions and far field patterns.
2. Store the far field patterns.

MAIN ALGORITHM

1. Load profile information and far field patterns.
2. Identify the contributed plane waves and associated basis functions on each groups of the profile.
3. Generate and solve the reduced system.
4. Construct the surface currents from the solution of the reduced system.
5. Use the surface currents to compute the scattered and total field above the surface.

3.4 Derivation of underpinning approximations

Key to the derivation of the ITIM reduced linear system represented by equations (3.39) and (3.40) are two approximations, one modelling the incident field in terms of plane waves (left hand side of equation (3.21)) and the second modelling the interaction between two groups in terms of plane waves (equations (3.23) to (3.26)). These are justified in this section.

3.4.1 Incident field

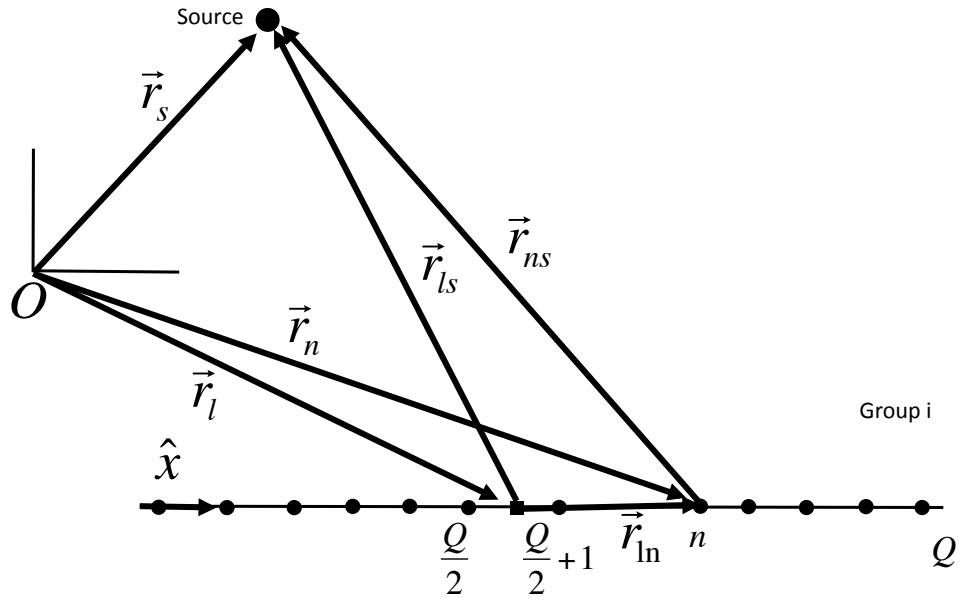


Figure 3.4: Far Field Approximation of Incidence Field. Circular dots represent centre of Q pulse basis domains while square dot represent centre of group. \hat{x} is unit vector tangent to surface of group.

In Figure 3.4 we consider the TM^z case with a line source located at \vec{r}_s producing the incident field which impinges on group i which has been discretised into Q equal domains whose centres are denoted by circular dots. In the following we assume Q is even-valued, but this is not a requirement. The centre of the group is the point \vec{r}_l denoted by a square dot. Note that \vec{r}_l falls half-way between two discretisation centres (namely $\frac{Q}{2}$ and

3.4 Derivation of underpinning approximations

$\frac{Q}{2} + 1$) due to the assumption that Q is even. The incident field produced at point \vec{r}_n (discretisation n) is given by

$$\bar{\psi}_{inc}(\vec{r}_n) = \frac{k_0 \eta_0}{4} H_0^{(2)}(k_0 r_{sn}), \quad (3.41)$$

where $r_{sn} = |\vec{r}_{sn}|$. Referring to Figure 3.4 we see that $r_{sn} \simeq r_{sl} - \hat{r}_{ls} \cdot \vec{r}_{ln}$ for $r_{sn} \gg r_{ln}$. Considering the far-field form of the Hankel function and using the above approximation of the distance r_{sn} allows us to write, for $k_0 r_{sn} \gg 1$ and $r_{sn} \gg r_{ln}$

$$H_0^{(2)}(k_0 r_{sn}) \simeq \sqrt{\frac{2i}{\pi k_0 r_{sn}}} e^{-ik_0 r_{sn}} \quad (3.42)$$

$$\simeq \sqrt{\frac{2i}{\pi k_0 r_{sl}}} e^{-ik_0 r_{sl}} e^{ik_0 \hat{r}_{ls} \cdot \vec{r}_{ln}} \quad (3.43)$$

$$= \sqrt{\frac{2i}{\pi k_0 r_{sl}}} e^{-ik_0 r_{sl}} e^{ik_0 \hat{r}_{ls} \cdot \hat{x} (n - \frac{Q+1}{2}) \Delta_x}. \quad (3.44)$$

If it were the case that $\hat{r}_{ls} = \hat{e}_k$ for some k then it would be possible to write

$$H_0^{(2)}(k_0 r_{sn}) \simeq \sqrt{\frac{2i}{\pi k_0 r_{sl}}} e^{-ik_0 r_{sl}} e^{ik_0 \hat{e}_k \cdot \hat{x} (n - \frac{Q+1}{2}) \Delta_x}, \quad (3.45)$$

and so the vector of incident fields impinging on group i could be approximated using

$$\begin{bmatrix} H_0^{(2)}(k_0 r_{s1}) \\ H_0^{(2)}(k_0 r_{s2}) \\ \vdots \\ H_0^{(2)}(k_0 r_{sQ}) \end{bmatrix} \simeq \sqrt{\frac{2i}{\pi k_0 r_{sl}}} e^{-ik_0 r_{sl}} \begin{bmatrix} e^{ik_0 \hat{e}_k \cdot \hat{x} (1 - \frac{Q+1}{2}) \Delta_x} \\ e^{ik_0 \hat{e}_k \cdot \hat{x} (2 - \frac{Q+1}{2}) \Delta_x} \\ \vdots \\ e^{ik_0 \hat{e}_k \cdot \hat{x} (Q - \frac{Q+1}{2}) \Delta_x} \end{bmatrix} \quad (3.46)$$

$$= \sqrt{\frac{2i}{\pi k_0 r_{sl}}} e^{-ik_0 r_{sl}} \bar{p}_0^{(k)}. \quad (3.47)$$

However in practice \hat{r}_{ls} will not match up exactly with any \hat{e}_k and we must use interpolation (See Figure 3.5). In this case we can write

$$\begin{bmatrix} H_0^{(2)}(k_0 r_{s1}) \\ H_0^{(2)}(k_0 r_{s2}) \\ \vdots \\ H_0^{(2)}(k_0 r_{sQ}) \end{bmatrix} \simeq \sum_{k=1}^K v_i^{(k)} \bar{p}_0^{(k)}. \quad (3.48)$$

We use linear interpolation retaining only two terms in the above expansion corresponding to the directions \hat{e}_m and \hat{e}_{m+1} which bracket \hat{r}_{ls} . For the case depicted in Figure 3.5 this

yields

$$v_i^{(m)} = \frac{\psi}{\Delta\theta} \quad (3.49)$$

$$v_i^{(m+1)} = \frac{\phi}{\Delta\theta} \quad (3.50)$$

$$v_i^{(k)} = 0 \text{ otherwise} \quad (3.51)$$

where $\psi + \phi = \Delta\theta$.

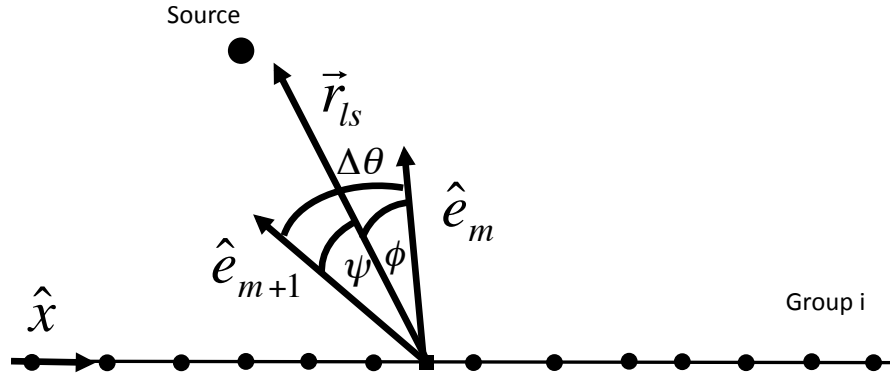


Figure 3.5: Incident field on group can be expressed in terms of two plane waves with amplitudes based on linear interpolation.

Note that an approximation other than the far-field approximation, equation (3.42), could be used to more accurately write the incident field as a denser spectrum of plane waves. However, this reduces the sparsity of the resultant ITIM linear system, and consequently the computational efficiency of the method, with only a modest increase in accuracy. Hence the far-field approximation and linear interpolation is assumed in this work and was used for the simulations described in Section 3.6.

3.4.2 Interaction between groups

Consider Figure 3.6 which depicts the interaction between groups i and j . We shall derive the approximation for $\overline{\overline{Z}}_{ij}^{(a)}$ as introduced in equation (3.23). The details for the other matrices $\overline{\overline{Z}}_{ij}^{(b)}$, $\overline{\overline{Z}}_{ij}^{(c)}$ and $\overline{\overline{Z}}_{ij}^{(d)}$ are similar. Let $Z_{mn}^{(a)}$ represent the interaction between point m in group j and point n in group i . It is thus a particular entry in the matrix $\overline{\overline{Z}}_{ij}^{(a)}$ and is given by

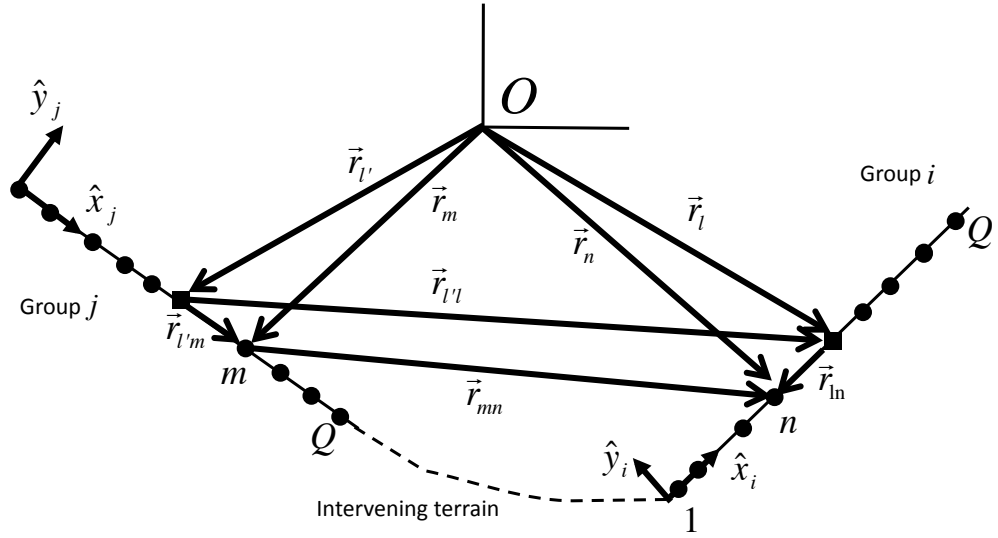


Figure 3.6: Far Field Approximation of interaction between two groups i and j .

$$Z_{mn}^{(a)} = \frac{k_0 \eta_0}{4} H_0^{(2)}(k_0 r_{mn}) \Delta_x \quad (3.52)$$

$$\simeq \frac{k_0 \eta_0}{4} \sqrt{\frac{2i}{\pi k_0 r_{mn}}} e^{-ik_0 r_{mn}} \Delta_x \quad (3.53)$$

3.4 Derivation of underpinning approximations

Referring to Figure 3.6 we see that

$$r_{mn} \simeq r_{l'n} - \hat{r}_{l'n} \cdot \vec{r}_{l'm} \quad (3.54)$$

$$\simeq r_{l'l} - \hat{r}_{l'l} \cdot \vec{r}_{l'm} \quad (3.55)$$

$$\simeq r_{l'l} - \hat{r}_{l'l} \cdot \vec{r}_{l'm} - \hat{r}_{l'l} \cdot \vec{r}_{l'n} \quad (3.56)$$

$$\begin{aligned} &= r_{l'l} - \hat{r}_{l'l} \cdot \hat{x}_j \left(m - \frac{Q+1}{2} \right) \Delta_x \\ &\quad - \hat{r}_{l'l} \cdot \hat{x}_i \left(n - \frac{Q+1}{2} \right) \Delta_x \end{aligned} \quad (3.57)$$

Inserting this into (3.53) yields

$$\begin{aligned} Z_{mn}^{(a)} &\simeq \frac{k_0 \eta_0}{4} \sqrt{\frac{2i}{\pi k_0 r_{ll'}}} e^{-ik_0 r_{ll'}} e^{ik_0 \hat{r}_{l'l} \cdot \hat{x}_j \left(m - \frac{Q+1}{2} \right) \Delta_x} \\ &\quad \times e^{ik_0 \hat{r}_{l'l} \cdot \hat{x}_i \left(n - \frac{Q+1}{2} \right) \Delta_x} \Delta_x \end{aligned} \quad (3.58)$$

$$\simeq Z_{ll'}^{(a)} e^{ik_0 \hat{r}_{l'l} \cdot \hat{x}_j \left(m - \frac{Q+1}{2} \right) \Delta_x} e^{ik_0 \hat{r}_{l'l} \cdot \hat{x}_i \left(n - \frac{Q+1}{2} \right) \Delta_x} \quad (3.59)$$

If it were the case that $\hat{r}_{l'l} = \hat{e}_l$ and $\hat{r}_{l'l} = \hat{e}_k$ we can write

$$Z_{mn}^{(a)} \simeq Z_{ll'}^{(a)} e^{ik_0 \hat{e}_l \cdot \hat{x}_j \left(m - \frac{Q+1}{2} \right) \Delta_x} e^{ik_0 \hat{e}_k \cdot \hat{x}_i \left(n - \frac{Q+1}{2} \right) \Delta_x} \quad (3.60)$$

More generally we interpolate between the discretised angles yielding

$$Z_{mn}^{(a)} \simeq Z_{ll'}^{(a)} \sum_{k=1}^K a_{ij}^{(k)} e^{ik_0 \hat{e}_k \cdot \hat{x}_i \left(n - \frac{Q+1}{2} \right) \Delta_x} \sum_{l=1}^K b_{ij}^{(l)} e^{ik_0 \hat{e}_l \cdot \hat{x}_j \left(m - \frac{Q+1}{2} \right) \Delta_x} \quad (3.61)$$

Therefore the submatrix $\overline{\overline{Z}}_{ij}^{(a)}$ of interactions between all points in groups i and j can be approximated by

$$\overline{\overline{Z}}_{ij}^{(a)} \simeq Z_{ll'}^{(a)} \sum_{k=1}^K a_{ij}^{(k)} \overline{\overline{p}}_0^{(k)} \sum_{l=1}^K b_{ij}^{(l)} \left(\overline{\overline{p}}_0^{(l)} \right)^T \quad (3.62)$$

Linear interpolation is used retaining only two terms in each of the above expansions. For example the terms $k = m$ and $k = m + 1$ corresponding to the directions \hat{e}_m and \hat{e}_{m+1} that bracket $\hat{r}_{l'l}$ as well as the terms $l = n$ and $l = n + 1$ corresponding to the directions \hat{e}_n and \hat{e}_{n+1} which bracket $\hat{r}_{l'l}$ would be retained. The other approximations in equations (3.24) to (3.26) can be derived in a similar fashion to the analysis above. The accuracy of these approximations depend on the geometry, and relative displacement, of the two groups. The physical assumption is that the field scattered from one group to the other can be approximated by a single plane wave (which is further approximated using linear interpolation between two of the discretised plane waves used to define the basis functions). This assumption is better as groups become more separated. However key to the success of the ITIM is that it is used for *all* interacting groups, even near-neighbours.

The justification for this is that the terrain profile varies slowly and near-neighbouring groups are almost collinear and therefore the distance approximations represented by equations (3.54) to (3.56) are almost exact. Consequently the phase of the scattered field is well-approximated by the plane wave assumption. However for certain cases it is necessary to refine this approximation and this is achieved by splitting the scattering group into sub-groups. This process is referred to as the two-level TIM and is described in Section 3.4.3.

3.4.3 Two-level Improved Tabulated Interaction Method (TL-ITIM)

As described in Section 3.4.2 the proposed method approximates the interaction between two linear groups as a plane wave (or more specifically as an interpolation between two plane waves). This is a reasonable approximation for groups which are very far away, and also works well in the case of near-neighbour groups provided that the ground is locally quite flat and the approximations (3.54) to (3.56) are accurate. This is the case for many terrain profiles, but can become less reasonable for profiles where the terrain undulates rapidly. However in these cases it is possible to improve the ITIM approximation by describing the interaction in terms of a greater number of plane waves. Figure 3.7 describes the interaction between group j and group i . Rather than employing a single plane-wave emanating from centre point \vec{r}_j to \vec{r}_i we instead break group j into H sub-groups, each with centre \vec{r}_{j_h} . Employing analysis similar to that of Section 3.4.2 it is possible to show that

$$\overline{\overline{Z}}_{ij}^{(a)} = \left[\overline{\overline{Z}}_{ij_1}^{(a)} \quad \overline{\overline{Z}}_{ij_2}^{(a)} \quad \dots \quad \overline{\overline{Z}}_{ij_H}^{(a)} \right] \quad (3.63)$$

where

$$\overline{\overline{Z}}_{ij_h}^{(a)} \simeq Z_{l_h}^{(a)} \sum_{k=1}^K a_{ij_h}^{(k)} \overline{p}_0^{(k)} \sum_{l=1}^K b_{ij_h}^{(l)} \left[\overline{p}_{h0}^{(l)} \right]^T \quad (3.64)$$

where $\overline{p}_{h0}^{(l)}$ is a discrete plane wave defined with respect to, \vec{r}_{j_h} the centre point of group j_h . It is defined for the $\frac{Q}{H}$ points in sub-group j_h and is given by

$$\overline{p}_{h0}^{(l)} = \begin{bmatrix} e^{ik_0 \hat{e}_k \cdot \hat{x} (1 - \frac{Q+1}{2H}) \Delta x} \\ e^{ik_0 \hat{e}_k \cdot \hat{x} (2 - \frac{Q+1}{2H}) \Delta x} \\ \vdots \\ e^{ik_0 \hat{e}_k \cdot \hat{x} (Q - \frac{Q+1}{2H}) \Delta x} \end{bmatrix} \quad (3.65)$$

Similar approximations hold for $\overline{\overline{Z}}_{ij}^{(b)}$, $\overline{\overline{Z}}_{ij}^{(c)}$, $\overline{\overline{Z}}_{ij}^{(d)}$. Employing the improved approximation given by equations (3.63) and (3.64) means that the surface currents on group l are potentially expressed in terms of more basis functions, with an improved calculation of the associated basis function coefficients. It does result in more computations however, and

for that reason is only used to describe near-neighbour interactions for profiles which have rapidly varying terrain. It should be noted that use of the TL-ITIM requires us to modify equation (3.38) for near-neighbour groups also. For near-neighbour groups one must replace

$$\sum_{k=0}^K a_{ij}^{(k)} \left(s_{ij0} \bar{q}_0^{(k)} + s_{ij1} \bar{q}_1^{(k)} \right) \quad (3.66)$$

with an expanded version based on interactions between the subgroups and group i , namely

$$\sum_{h=1}^H \sum_{k=0}^K a_{ijh}^{(k)} \left(s_{ijh0} \bar{q}_0^{(k)} + s_{ijh1} \bar{q}_1^{(k)} \right) \quad (3.67)$$

with

$$\begin{aligned} s_{ijh0} = & \sum_{m=0}^K \alpha_j^{(m)} \left(\sum_{l=0}^K b_{ijh}^{(l)} \left(Z_{ll'h}^{(a)} f_{h00}^{lm} + Z_{ll'h}^{(b)} g_{h00}^{lm} \right) \right) \\ & + \sum_{m=0}^K \beta_j^{(m)} \left(\sum_{l=0}^K b_{ijh}^{(l)} \left(Z_{ll'h}^{(a)} f_{h01}^{lm} + Z_{ll'h}^{(b)} g_{h01}^{lm} \right) \right) \end{aligned} \quad (3.68)$$

$$\begin{aligned} s_{ijh1} = & \sum_{m=0}^K \alpha_j^{(m)} \left(\sum_{l=0}^K b_{ijh}^{(l)} \left(Z_{ll'h}^{(c)} f_{h10}^{lm} + Z_{ll'h}^{(d)} g_{h10}^{lm} \right) \right) \\ & + \sum_{m=0}^K \beta_j^{(m)} \left(\sum_{l=0}^K b_{ijh}^{(l)} \left(Z_{ll'h}^{(c)} f_{h11}^{lm} + Z_{ll'h}^{(d)} g_{h11}^{lm} \right) \right) \end{aligned} \quad (3.69)$$

where for example $\bar{j}_{h0}^{(k)}$ is a sub-vector of $\bar{j}_0^{(k)}$ containing those elements corresponding to discretisation points in the h^{th} sub-group. Note that the sub-group far-field scattering quantities

$$f_{hab}^{lm} \equiv \left[\bar{p}_{ha}^{(l)} \right]^T \bar{j}_{hb}^{(m)} \quad (3.70)$$

$$g_{hab}^{lm} \equiv \left[\bar{p}_{ha}^{(l)} \right]^T \bar{k}_{hb}^{(m)}. \quad (3.71)$$

for a and b equal to 0 and 1, can be pre-computed and tabulated to speed up calculations.

3.5 Calculation of pathloss and computational complexity

Solution of the reduced ITIM linear system yields information about the fields on the surface of the terrain profile. To compute the fields above the surface an integration must be performed. Two approaches can be used for this task.

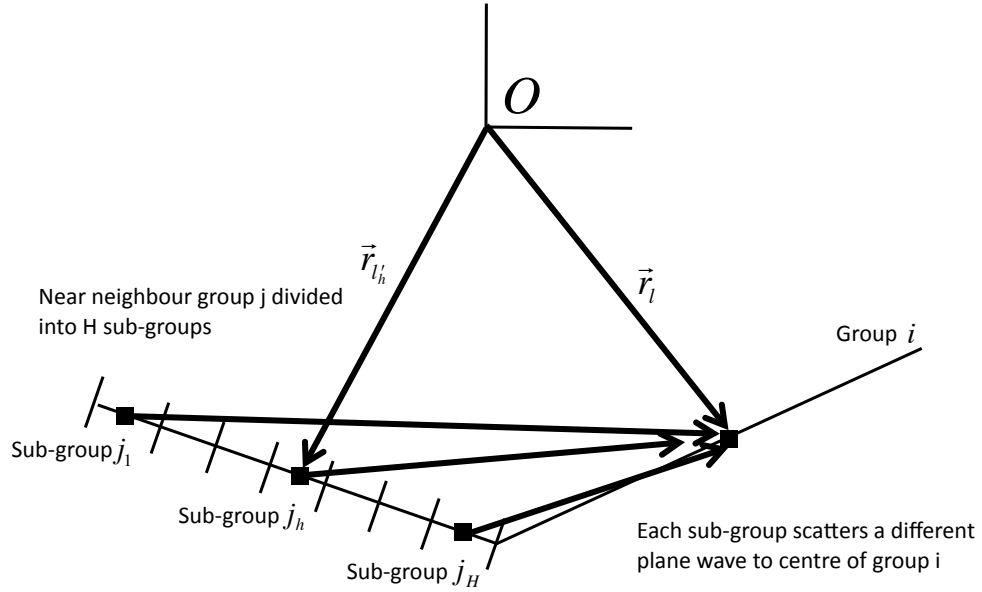


Figure 3.7: Near neighbour group j is sub-divided into H sub-groups with $\frac{Q}{H}$ discretisations each. Each scatters its own plane wave to group i .

- Approach A: Use the solution of the reduced system to explicitly construct the induced surface currents and use these currents to compute the scattered fields at the receiver points above the surface.
- Approach B: Use the solution of the reduced system in conjunction with the tabulated far field patterns to compute the scattered fields at the receivers.

Approach A requires the explicit storage of the basis functions which requires of the order of $\mathcal{O}((K+1)Q)$ where $K+1$ is the number of discretised angles (number of basis functions) and Q is the number of discretisations on each group. This memory requirement is large and increases as the operating frequency increases. It should be noted that the basis functions are not explicitly used in the generation of the reduced system so it would be inefficient to require that they are subsequently used in the computation of the scattered fields. In contrast, approach B does not require the computation and storage of the basis functions. Moreover, assuming that field strengths are required over every linear segment (a typical spacing, in practice around every $25m$), approach A has an associated computational cost of $\mathcal{O}(N \times M)$ where N is the number of unknowns of the original system and M is the number of linear groups. This is due to the need to perform the scattered field integrals independently for each field point. This computational cost can be reduced significantly using approach B. In this section, approach B is analyzed because

it is more efficient than approach A in terms of computational cost and memory storage.

Suppose that the receiver is located at point \vec{r} above the surface. The fields scattered from the surface to the receiver \vec{r} is the sum of scattered fields generated by the individual linear groups, that is

$$E_s(\vec{r}) = \sum_{i=1}^M \left[\sum_{k=0}^K \alpha_i^{(k)} \overline{V}_{ir}^{(a)} \vec{j}_0^{(k)} + \sum_{k=0}^K \beta_i^{(k)} \overline{V}_{ir}^{(b)} \vec{k}_0^{(k)} \right] \quad (3.72)$$

where $\overline{V}_{ir}^{(a,b)}$ are $1 \times N$ vectors containing interaction information between the N discretisations within group i and the receiver point \vec{r} . A similar analysis to that presented in Section 3.4.2 allows us to write

$$\overline{V}_{ir}^{(a)} \simeq V_{lr}^{(a)} \sum_{k=0}^K \gamma_l \left[p_0^{(l)} \right]^T \quad (3.73)$$

$$\overline{V}_{ir}^{(b)} \simeq V_{lr}^{(b)} \sum_{k=0}^K \gamma_l \left[p_0^{(l)} \right]^T \quad (3.74)$$

where the fields are computed in terms of plane waves propagating from \vec{r}_l the centre of group i to the point of interest \vec{r} . Inserting this above yields

$$E_s(\vec{r}) = \sum_{i=1}^M \left[\sum_{k=0}^K \alpha_i^{(k)} V_{lr}^{(a)} \sum_{l=0}^K \gamma_l \left[p_0^{(l)} \right]^T \vec{j}_0^{(k)} + \sum_{k=0}^K \beta_i^{(k)} V_{lr}^{(b)} \sum_{l=0}^K \gamma_l \left[p_0^{(l)} \right]^T \vec{k}_0^{(k)} \right] \quad (3.75)$$

$$= \sum_{i=1}^M \left[\sum_{k=0}^K \alpha_i^{(k)} V_{lr}^{(a)} \sum_{l=0}^K \gamma_l f_{00}^{kl} + \sum_{k=0}^K \beta_i^{(k)} V_{lr}^{(b)} \sum_{l=0}^K \gamma_l g_{00}^{kl} \right] \quad (3.76)$$

where f_{00}^{kl} and g_{00}^{kl} are the pre-computed tabulated far-field patterns associated with the basis functions and introduced earlier in equations (3.36) and (3.37). One should note that the fact that these are tabulated and accessed via a look up table, coupled with the observation that most of the coefficients $\alpha_i^{(k)}$, $\beta_i^{(k)}$ and γ_l are zero makes this an extremely rapid computation. Again a two-level approach can be used for increased accuracy in the near field.

3.5.1 Complexity Analysis

In this section, the computational complexity and memory requirement of the proposed method is investigated. The terrain profile is initially discretised into N discretisation points representing the centre of N pulse basis function domains. These are collected into M identical groups, each group containing $Q = N/M$ points. The basis functions are generated by considering plane waves incident on a typical reference group at $K + 1$

Table 3.2: Computational Complexity and Memory Requirement of the proposed method

| | | CPU Time | Memory |
|----------------|----------------------------|-----------------------------|---------------------------|
| Generate | Compute basis functions | $\mathcal{O}(K \times Q^2)$ | $\mathcal{O}(K \times Q)$ |
| Reduced System | Compute far field patterns | $\mathcal{O}(K \times Q^2)$ | $\mathcal{O}(K^2)$ |
| | Generate reduced system | $\mathcal{O}(R^2)$ | $\mathcal{O}(R^2)$ |
| Total Field | | $\mathcal{O}(R)$ | $\mathcal{O}(M)$ |
| Total | | $\mathcal{O}(R^2)$ | $\mathcal{O}(R^2)$ |

discretised angles $0, \pi/K, 2\pi/K, \dots, \pi$. In practice not all basis functions are actually excited on each group however. The precise number of basis functions that are excited on any group depends on its position relative to the source and the other groups. Assume that the excited basis functions on group i includes \mathcal{H}_i basis functions of type ϕ_0 (excited by the waves from upper medium, or free space) and \mathcal{L}_i basis functions of type ϕ_1 (excited by the waves from lower medium). The total number of excited basis functions for the whole terrain profile represents the number of unknowns of the reduced system and is given by

$$R = \sum_{i=1}^M (\mathcal{H}_i + \mathcal{L}_i) \quad (3.77)$$

It is assumed that the computation of the basis functions and associated far-field patterns is performed off-line and does not contribute to the computational cost of any given simulation as they can be re-used and the computational cost amortised over many simulations. A simulation for a given profile then involves the identification of the basis functions needed, the generation and solution of the reduced linear system and the computation of the total fields above the surface. The memory requirements comprise the memory used to store the far field patterns (a total of $(K + 1)^2$ for the main patterns and $H(K + 1)^2$ for the sub-group patterns) as well as the reduced system (which is equivalent to $\mathcal{O}(R^2)$). Note that the forward backward method (will be later described in detail in chapter 4 and 5) can be used to solve the reduced system iteratively [87] in which case the memory requirement of the proposed method is reduced to order of $\mathcal{O}(K^2)$.

3.6 Numerical results

In this section, the accuracy, efficiency and robustness of the proposed method is evaluated. The path-loss results generated by the proposed method are compared against those generated by a numerically precise solution as well as measurement data. Moreover, a comparison of the ITIM with the Forward Backward Method is performed in terms of accuracy and processing time. The computer used in the simulation was a Dell Precision Workstation 670 which has a Xeon 3.6 GHz CPU and 3GB of memory. The simulation environment was Matlab 7.8.0.

3.6.1 Rural terrain profile

In order to illustrate the accuracy of the ITIM, the pathloss generated by the ITIM is compared against that generated by a numerically precise solution, an empirical model and measured data. The chosen reference empirical model is Hata-Okumura with Knife Edge Diffraction Extension due to its popularity in recent planning tools. The Epstein Peterson knife edge diffraction theory is applied to improve the accuracy of the Hata-Okumura in the shadowed areas [4, 9]. The precise solution is obtained by running Forward Backward Method until the normalized error norm is less than 10^{-3} . The measured data was kindly made available by the University of Aalborg [25]. The transmitting antenna was a dipole radiating TM^z polarized fields with a gain of $8dBi$, transmitting power of $10W$ and located at a height of $10.4m$ over the left most point. The receiver antenna was a monopole located at a height of $2.4m$ and moved along the terrain surface. The terrain was modeled as a lossy dielectric with $\epsilon_r = 4.5$ and loss tangent $\tan \delta = 0.07$ [76]. The chosen terrain profiles for the simulation are the Hadsund and Jerslev profiles [25] illustrated in Figure 3.8(a) and Figure 3.9(a) having length of $8km$ and $5.5km$ respectively. The pathloss is computed at a frequency of $144MHz$ for the Hadsund terrain profile and $435MHz$ for the Jerslev terrain profile and is shown in Figure 3.8(b) and Figure 3.9(b). The chosen group size for the ITIM method is $50m$ and the number of discretized angles are $K = 50$. Figure 3.8(b) and Figure 3.9(b) show that the pathloss computed by the proposed method match the precise solution and both of them are in very good agreement with the measured data. In addition Figure 3.9(b) demonstrates that the pathloss generated by the ITIM has a better agreement with the measurement data than those generated by the Hata-Okumura model with the Epstein Peterson multiple knife edge diffraction (HT-KED) [4, 9]. Results for other scenarios are provided in Appendix C.

A comparison in computational complexity was performed by evaluating the CPU time of the proposed method and 1 iteration of FBM. Note that in order to get a precise solution (where the relative error norm is less than 10^{-3}), one must run the FBM for more than 10 iterations. The CPU time of the proposed method for 3 different profiles, Jerslev, Hadsund and Hjorring is compared against those of 1 iteration of FBM and shown in Table 3.3. For the case of the Jerslev terrain profile, the number of unknowns of the original system was 114688 which represent the electric and magnetic currents at $114688/2 = 57344$ discretization points on the terrain profile. To apply the ITIM these discretization points were collected into 113 groups of length of $50m$ and the basis functions needed on each group were identified and the reduced system formed. The reduced system has 914 unknowns which represent the coefficients of the excited basis functions. This is equivalent to approximately 10 basis functions for each group. The run time of the ITIM method for the Jerslev terrain profile is 1.36 seconds, significantly less than the run time of 1 iteration of FBM which is 41594 seconds. Note that in order to get a precise solution, FBM needs to run more than 10 iterations. The detailed run time for other terrain profiles are shown in Table 3.3. The

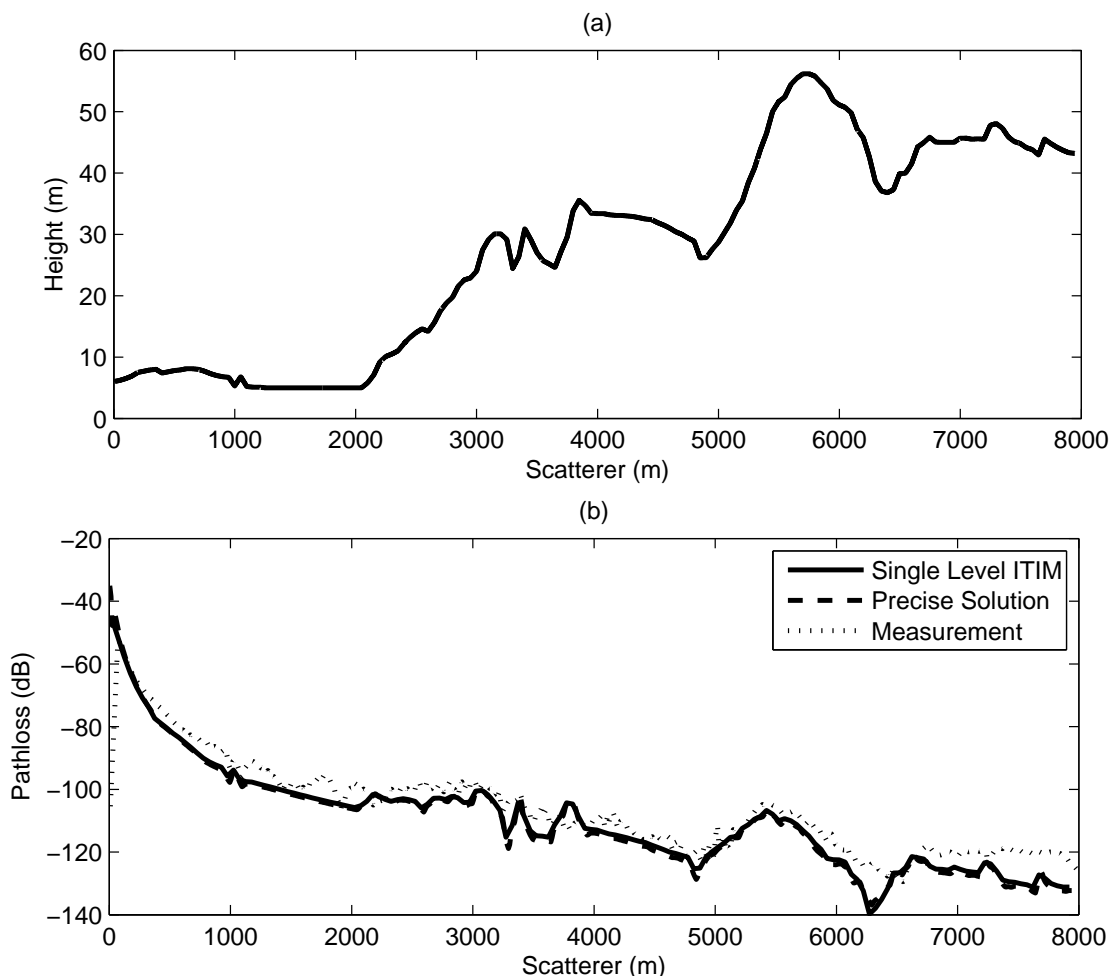


Figure 3.8: Pathloss generated by proposed method, precise solution and measured data over Hadsund terrain profile. Length of profile: $8km$. (a) Hadsund terrain profile, (b) Pathloss at $144MHz$ with TM^z Polarization.

proposed method is approximately 30000 times faster than the run time of 1 iteration of FBM (and hence approximately 300000 times faster than what is required for an accurate solution using FBM).

An interesting quality of the ITIM becomes apparent as we consider simulations at higher frequencies. A detailed run time of the proposed method for increasing frequency is given in Table 3.4. As the operating frequency increases, we note that the run-time for the ITIM does not increase. The reason for this is that although as the frequency increases a finer grid is required to get the precise solution this only impacts on the time needed to compute the basis functions and tabulated far-field patterns. These are done off-line and stored and hence do not impact the simulation time for any given profile. In addition the run time to generate the basis functions can be significantly reduced by using the new Fast Fourier Transform (FFT) based method, details of which will be discussed in Section 3.7. In contrast the run time of the FBM increases linearly with frequency. For example in

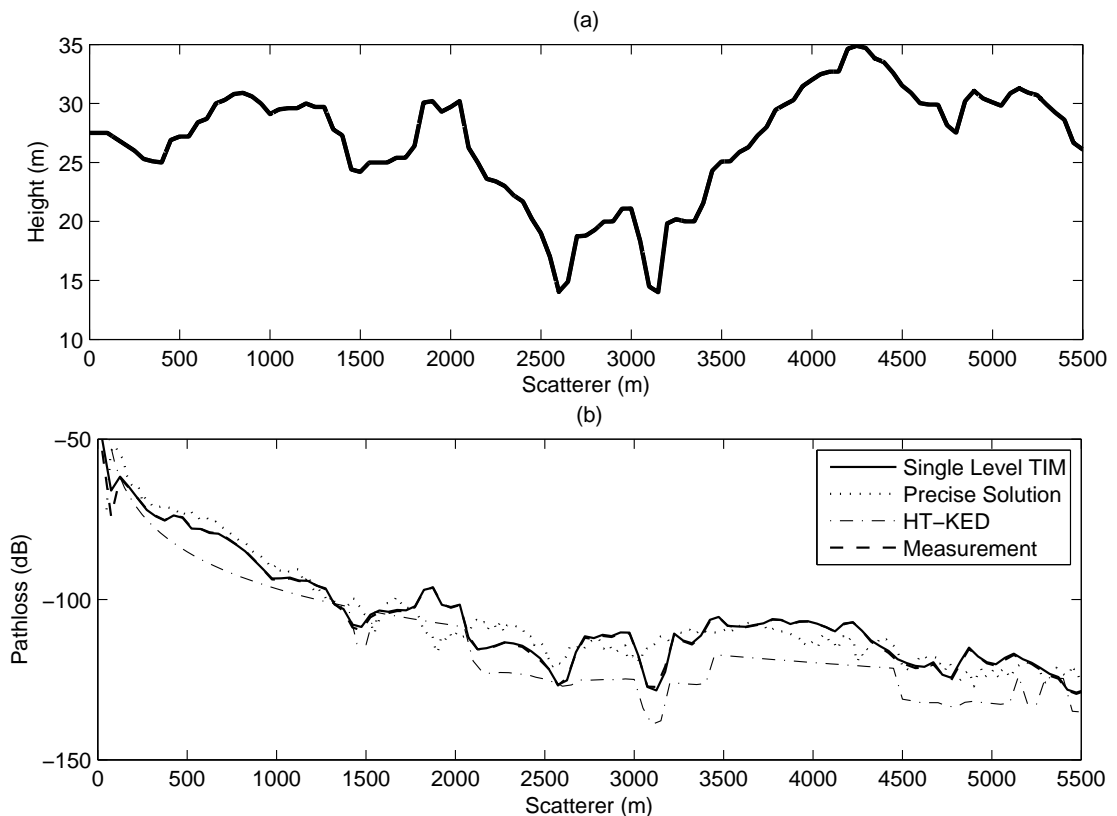


Figure 3.9: Pathloss generated by proposed method, precise solution and measured data over Jerslev terrain profile. Length of profile: 5.5km . (a) Jerslev terrain profile, (b) Pathloss at 435MHz with TM^z Polarization.

the case of Hadsund profile, as the frequency increases from 144MHz to 435MHz , the run time of FBM increases approximately by a factor of 4, from 20970 seconds to 83832 seconds. The run time required to generate the basis functions and far field patterns also increases from 26.96 seconds to 126.48 seconds. However, the run time of the generation and solution of the reduced system is not affected by the increase in frequency.

3.6.2 Mountainous terrain profile

In order to demonstrate the use of the two-level ITIM a profile from a mountainous region in Wicklow, south of Dublin, Ireland is chosen. Figure 3.10(a) illustrates the profile. This terrain profile has an appreciable height variation of 600m over a distance of 6km . The transmitting antenna was chosen to be a dipole radiating at frequency of 300MHz with a gain of 8dBi , transmitting power of 10W and located at a height of 20m . The receiver antenna is a monopole located at the height of 2.4m which was moved along the terrain surface. The group size of the proposed method is reduced to 25m to improve the accuracy of the proposed method. The pathloss results generated by the proposed method

3.6 Numerical results

Table 3.3: Comparison of run time (in seconds) of the proposed method and FBM. Operating Frequency: 435MHz.

| Profile | Number of unknowns | Number of blocks | Number of unknowns of reduced system | Run Time (in seconds) | | |
|----------|--------------------|------------------|--------------------------------------|-----------------------|--------------|---------|
| | | | | ITIM | FBM (1 iter) | Ratio |
| Jerslev | 114688 | 113 | 914 | 1.36 | 41594 | 1:30584 |
| Hadsund | 162816 | 160 | 1310 | 2.40 | 83832 | 1:34930 |
| Hjorring | 227328 | 222 | 1814 | 4.09 | 163420 | 1:39956 |

Table 3.4: Run time (in seconds) for different stages of the proposed method at different frequency. Terrain profile: Hadsund.

| Frequency | Number of unknowns | Number of blocks | Run Time of ITIM | | | Run Time of FBM (1 iteration) |
|-----------|--------------------|------------------|------------------|---------------|-------|-------------------------------|
| | | | Basis Funcs. | Reduced Syst. | Total | |
| 144 MHz | 81408 | 160 | 14.98 | 2.40 | 2.40 | 20970 |
| 435 MHz | 162816 | 160 | 72.88 | 2.37 | 2.37 | 83832 |
| 970 MHz | 651264 | 160 | 1266 | 2.42 | 2.42 | 1341312 (est) |

for both of TM^z and TE^z polarization are shown in Figure 3.10(b) and Figure 3.11(b). The pathloss results are generated by TL-ITIM with the number of sub-groups in a group set as $H = 8$. The TL-ITIM is applied for the cases where the angle of scattered wave to the group is greater than a pre-set threshold angle. The threshold angle was set $\theta_t = 10^\circ$. An alternate, simpler, way to improve the accuracy is just to reduce the group sizes, so this was also done. However this greatly increases the order of the reduced system (and associated run time).

Table 3.5: Run time (in seconds) and accuracy of proposed method with SL-ITIM and TL-ITIM at different group size. Terrain profile: Wicklow. Number of discretization points: 62464.

| Scenario | Number of unknowns of reduced system | Run Time (in seconds) | |
|---------------------------|--------------------------------------|-----------------------|------------------|
| | | Reduced System | Compute Pathloss |
| Two Level ITIM - 25m | 3030 | 27.9 | 3.35 |
| Single Level ITIM - 25m | 3030 | 10.9 | 1.35 |
| Single Level ITIM - 12.5m | 7762 | 41.8 | 2.54 |

Figure 3.12 shows the accuracy of three implementations of the proposed method: TL-ITIM with $H = 8$ and group size of $25m$; standard ITIM with group size of $25m$ and standard ITIM with group size of $12.5m$ by comparing the pathloss generated by these implementations against the precise solution. The detailed run time of the implementations are shown in Table 3.5. As the block size of standard ITIM is reduced from $25m$ to $12.5m$, the number of unknowns of the reduced system is doubled from 3030 unknowns to 7762 unknowns. This leads to a quadrupling of the memory storage and run time which increases from 10.9 seconds to 41.8 seconds as shown in Table 3.5. However the accuracy of the pathloss does not improve significantly when compared to that of the TL-ITIM im-

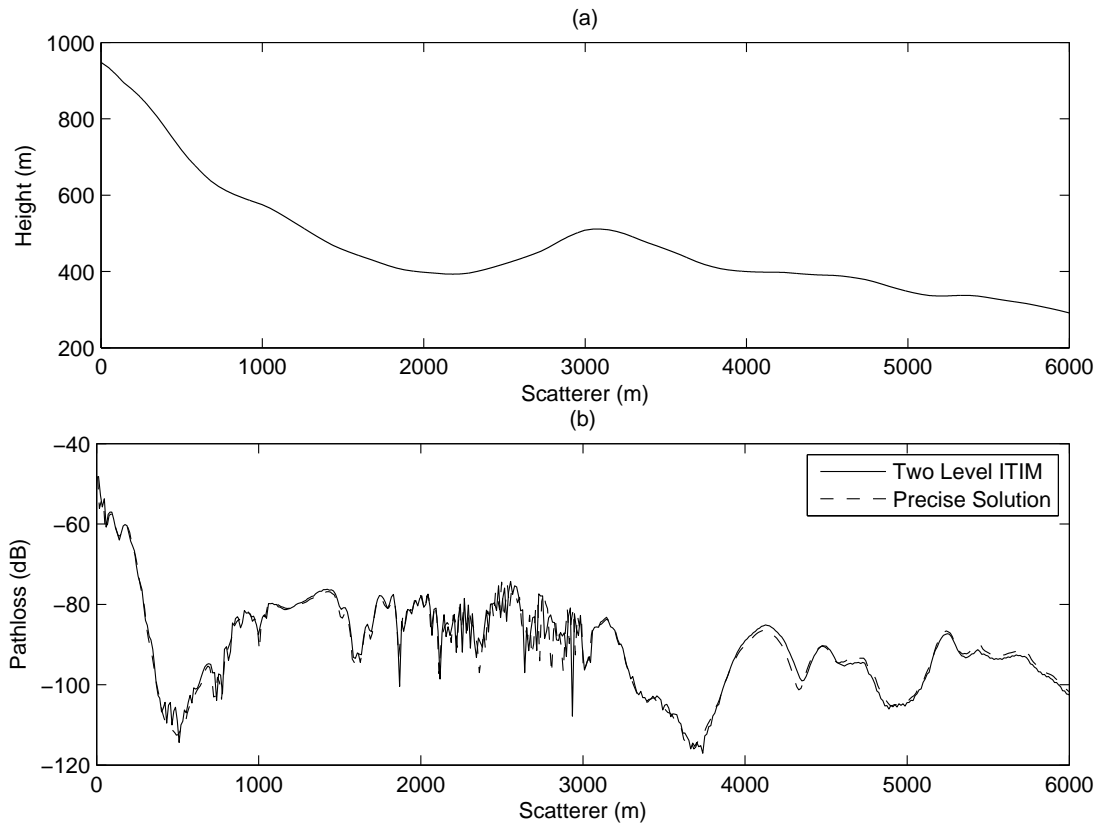


Figure 3.10: Pathloss generated by proposed method and precise solution over mountainous terrain profile. Length of profile: 6km. (a) Wicklow terrain profile, (b) Pathloss at 300MHz with TM^z Polarization

plementation. It is clear that the TL-ITIM provides a better agreement with the precise solution than the standard ITIM especially at the deep shadow region. In addition the TL-ITIM does not significantly increase the number of unknowns of the reduced system. As a result, we conclude that the TL-ITIM is the better solution than the reduction of the block size to improve the accuracy of the proposed method.

3.7 Efficient numerical method for computing ITIM basis functions

The generation of basis functions (equation (3.14)-(3.15)) and far fields patterns (equation (3.36)-(3.37)) of the Improved Tabulated Method described in previous sections requires the the computation of EM wave scattering from 1D flat surfaces at different incident angles. This can be efficiently computed by using the Fast Fourier Transform (FFT). In this section, a novel iterative method is derived basing on a similar implementation to the GMRES Fast Fourier Transform (GMRES-FFT), where acceleration of the matrix-vector multiplications is achieved using fast Fourier transforms (FFT). However, the iterative

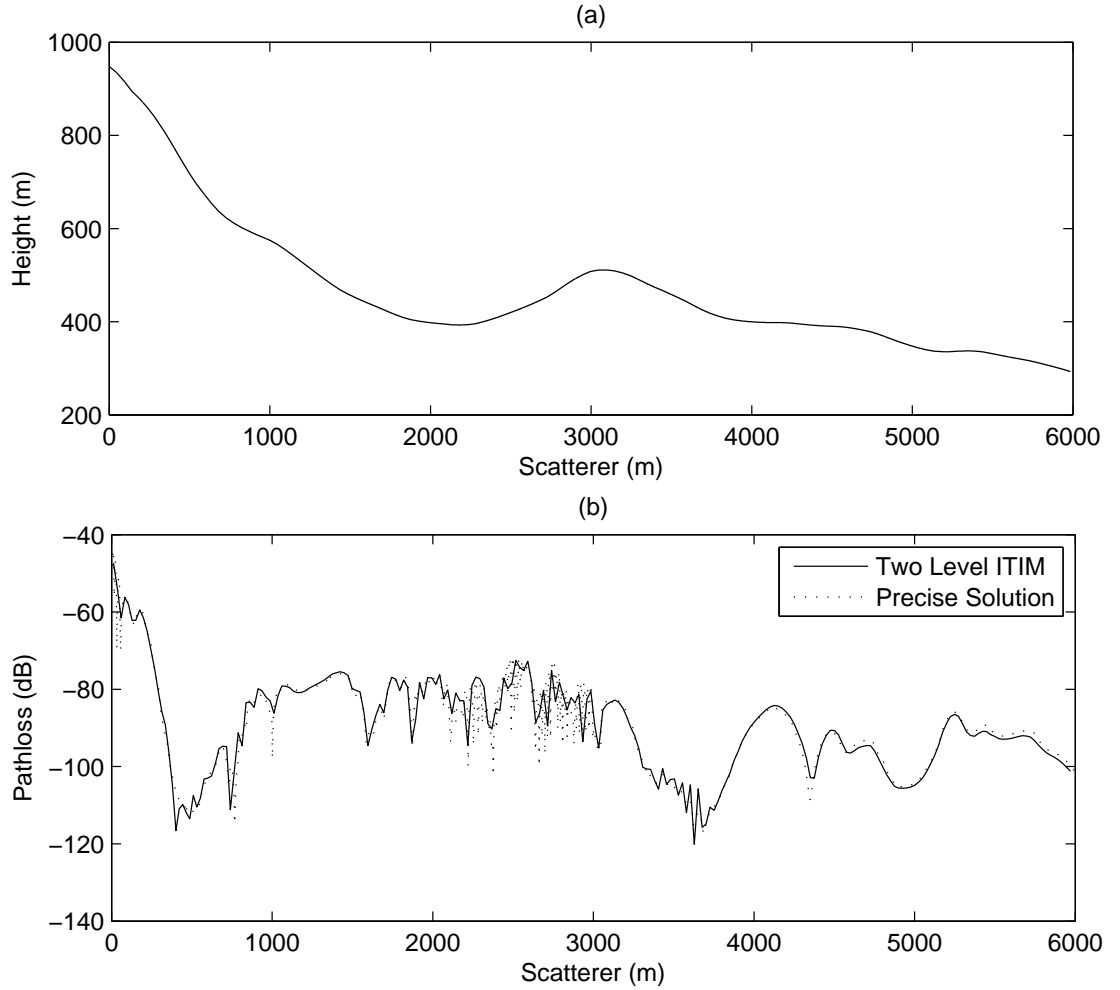


Figure 3.11: Pathloss generated by proposed method and precise solution over mountainous terrain profile. Length of profile: 6km. (a) Wicklow terrain profile, (b) Pathloss at 300MHz with TE^z Polarization

method proposed is not based on Krylov subspace expansions and is shown to converge faster than GMRES-FFT while maintaining the computational complexity and memory usage of those methods.

For a 1D flat surface, all elements of the impedance matrices $\overline{\overline{Z}}^{(b)}$ and $\overline{\overline{Z}}^{(d)}$ approach zero except the self terms. As the result the $2Q \times 2Q$ system in equation (3.7) can be reduced to a $Q \times Q$ system

$$\left(\overline{\overline{Z}}^{(a)} + \overline{\overline{Z}}^{(c)} \right) \vec{j} = \vec{V} \quad (3.78)$$

$$k_m = 2 \sum_{n=1}^Q Z_{mn}^{(c)} j_n, \quad m = 1, \dots, Q \quad (3.79)$$

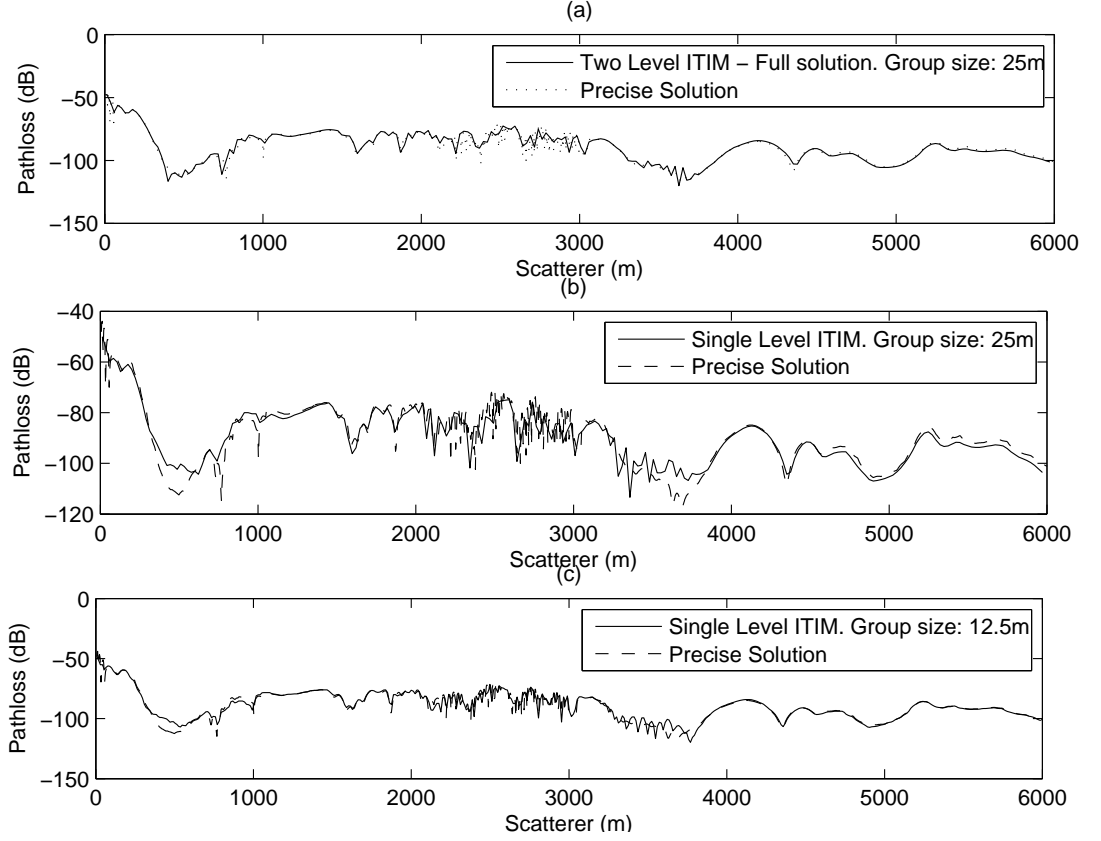


Figure 3.12: Pathloss generated by proposed method and precise solution over Wicklow terrain profile. Length of profile: $6km$. Operating frequency: $300MHz$. (a) Pathloss generated by TL-TIM with block size of $25m$, (b) Pathloss generated by standard TIM with block size of $25m$, (c) Pathloss generated by standard TIM with block size of $12.5m$

Recall that Q is the number of discretisation points on the reference group. The impedance matrix $\bar{\bar{A}} = \bar{\bar{Z}}^{(a)} + \bar{\bar{Z}}^{(c)}$ is a symmetric Toeplitz matrix [74] and equation (3.78) can be written as

$$\begin{bmatrix} A_0 & A_{-1} & A_{-2} & \cdots & A_{1-Q} \\ A_1 & A_0 & A_{-1} & \cdots & A_{2-Q} \\ A_2 & A_1 & A_0 & \cdots & A_{3-Q} \\ \vdots & \vdots & \vdots & \ddots & \vdots \\ A_{Q-1} & A_{Q-2} & A_{Q-3} & \cdots & A_0 \end{bmatrix} \begin{bmatrix} j_0 \\ j_1 \\ j_2 \\ \vdots \\ j_{Q-1} \end{bmatrix} = \begin{bmatrix} v_0 \\ v_1 \\ v_2 \\ \vdots \\ v_{Q-1} \end{bmatrix} \quad (3.80)$$

where $A_{-k} = A_k$.

In order to apply the FFT to the impedance matrix, one must first embed $\bar{\bar{A}}$ within a circulant matrix. To achieve this, equation (3.80) is extended from a system of Q equations into a system of $2Q$ equations by appending Q further unknowns to \bar{j} . As a result, equation (3.80) is embedded into a system of equations which has the form of circulant convolution:

$$\bar{v}' = \bar{z}' \circledast \bar{j}' \quad (3.81)$$

where

$$\bar{j}' = [j_0 \ j_1 \ \dots \ j_{Q-1} \ j_Q \ j_{Q+1} \ \dots \ j_{2Q-1}]^T \quad (3.82)$$

$$\bar{z}' = [A_0 \ A_{-1} \ \dots \ A_{1-Q} \ 0 \ A_{Q-1} \ \dots \ A_1]^T \quad (3.83)$$

$$\bar{v}' = [e_0 \ e_1 \ \dots \ e_{Q-1} \ e_Q \ e_{Q+1} \ \dots \ e_{2Q-1}]^T \quad (3.84)$$

The original Q unknowns have now been embedded inside a system of $2Q$ linear equations. In general the values j_0, j_1, \dots, j_{Q-1} obtained by solving equation (3.81) will not equal those obtained by solving equation (3.80). They will only match if one chooses to extend the right hand side vector with values $e_Q, e_{Q+1}, \dots, e_{2Q-1}$ that force $j_Q, j_{Q+1}, \dots, j_{2Q-1}$ to equal zero. This is achieved using the iterative technique outlined later in this section. The iterative process involves sequentially updating j'_k and e'_k and at each step forcing j_k to be zero for $k = Q, \dots, 2Q - 1$. The advantage of expanding the linear system in this fashion is to facilitate the use of the FFT to speed up the matrix-vector multiplication as in the CG-FFT[72, 74]. As equation (3.81) is a circulant discrete convolution of length $2Q$, the discrete convolution theorem states that it is equivalent to

$$\tilde{v}' = \tilde{z}' \times \tilde{j}' \quad (3.85)$$

where the symbol \times denotes component by component multiplication of two vectors and $\tilde{v}', \tilde{z}', \tilde{j}'$ are the Discrete Fourier Transforms (DFT) for the sequence of length $2Q$ of $\bar{v}', \bar{z}', \bar{j}'$. This can be efficiently computed using the FFT

$$\tilde{v}' = \text{FFT}_{2Q}(\bar{v}') \quad (3.86)$$

$$\tilde{z}' = \text{FFT}_{2Q}(\bar{z}') \quad (3.87)$$

$$\tilde{j}' = \text{FFT}_{2Q}(\bar{j}') \quad (3.88)$$

Hence \tilde{j}' can be obtained using component-wise division

$$\tilde{j}' = \frac{\tilde{v}'}{\tilde{z}'} \quad (3.89)$$

To start the new iterative method as given in Table 3.6, the additional components on the RHS are initialised with zeros, i.e. $v_k^{(0)} = 0$ for $k = Q, \dots, 2Q - 1$. Next, $\bar{j}'^{(0)}$ is efficiently calculated using the FFT as shown in equation (3.89). The zero in brackets indicates that this is the zeroth iteration of the solution. Inside the "for" loop, the vector components

$j_k^{(0)}$, $k = Q, \dots, 2Q - 1$ are set to zero and then the revised $\bar{j}^{(0)}$ is used to update $\bar{v}^{(1)}$, by using equation (3.85). Subsequently, $v_k^{(1)}$ are reset to the incident field values v_k for $k = 0, \dots, Q - 1$ and this revised $\bar{v}^{(1)}$ is then used to calculate $\bar{j}^{(1)}$, by using equation (3.89). The process continues to form the iterative chain $\bar{v}^{(i)} \rightarrow \bar{j}^{(i)} \rightarrow \bar{v}^{(i+1)} \rightarrow \bar{j}^{(i+1)} \rightarrow \dots$ as depicted in Table 3.6.

Table 3.6: New Iterative Method for Electromagnetic Scattering From Flat Surfaces.

```

Input: Array  $\bar{z}, \bar{e}$ , number of steps  $M$ 
Initialize  $\bar{v}^{(0)} = \{v_0, v_1, \dots, v_{Q-1}, 0, 0, \dots, 0\}$ 
 $\bar{z}'_{\text{FFT}} = \text{FFT}(\bar{z})$ 
 $\bar{e}'_{\text{FFT}} = \text{FFT}(\bar{e}^{(0)})$ 
 $\bar{j}'_{\text{FFT}} = \bar{v}'_{\text{FFT}} / \bar{z}'_{\text{FFT}}$ 
for  $m = 0, \dots, M$ 
     $\bar{j}^{(m)} = \text{IFFT}(\bar{j}'_{\text{FFT}})$ 
     $\bar{j}^{(m)} = \{x_0^{(m)}, x_1^{(m)}, \dots, x_{Q-1}^{(m)}, 0, 0, \dots, 0\}$ 
     $\bar{j}'_{\text{FFT}} = \text{FFT}(\bar{j}^{(m)})$ 
     $\bar{v}^{(m)} = \text{IFFT}(\bar{j}'_{\text{FFT}} \times \bar{z}'_{\text{FFT}})$ 
     $\bar{v}^{(m)} = \{v_0, v_1, \dots, v_{Q-1}, v_Q^{(m)}, v_{Q+1}^{(m)}, \dots, v_{2Q-1}^{(m)}\}$ 
     $\bar{v}'_{\text{FFT}} = \text{FFT}(\bar{v}^{(m)})$ 
     $\bar{j}'_{\text{FFT}} = \bar{v}'_{\text{FFT}} / \bar{z}'_{\text{FFT}}$ 
end  $m$ .
 $\bar{j}^{(M+1)} = \text{IFFT}(\bar{j}'_{\text{FFT}})$ 
 $\bar{j}^{(M+1)} = \{j_0^{(M+1)}, j_1^{(M+1)}, \dots, j_{Q-1}^{(M+1)}\}$ 
    
```

3.7.1 Complexity Analysis of the New FFT Based Method

As outlined in Table 3.6, the proposed method requires 4 FFT, 1 array multiplication and 1 array division operations for each iteration. In addition, it requires 3 FFT operations and 1 array division operation for the initialisation and finalisation. In terms of memory usage, the new approach requires $6 \times 2Q = 12Q$ cells to store the entries of $\bar{v}'_{\text{FFT}}, \bar{z}'_{\text{FFT}}, \bar{j}'_{\text{FFT}}$ in the frequency and spatial domains. In short, the computational complexity of the proposed approach is equivalent to that of the CG-FFT approach[72], requiring $\mathcal{O}(Q \log Q)$ operations per iteration, while the memory costs are $\mathcal{O}(Q)$. The complexity of the GMRES-FFT is similar to the CG-FFT in terms of the number of FFTs needed, but requires other operations which slows it further.

3.7.2 Convergence Analysis

In this section a requirement on the structure of \bar{A} that ensures that the solution of the proposed approach converges to the solution of equation (3.78) is derived. Firstly, we

write equation (3.81) in its matrix form

$$\begin{bmatrix} \bar{\bar{A}}_a & \bar{\bar{A}}_b \\ \bar{\bar{A}}_c & \bar{\bar{A}}_d \end{bmatrix} \begin{bmatrix} \bar{j}_1 \\ \bar{j}_{\text{PAD}} \end{bmatrix} = \begin{bmatrix} \bar{v} \\ \bar{v}_{\text{PAD}} \end{bmatrix} \quad (3.90)$$

where $\bar{\bar{A}}_a$ is the impedance matrix $\bar{\bar{A}}_a \equiv \bar{\bar{A}}$, $\bar{\bar{A}}_b$ is a symmetric Toeplitz matrix whose first row is $\begin{bmatrix} 0 & A_{N-1} & \dots & A_1 \end{bmatrix}$ and \bar{v} is the right hand side vector of equation (3.78) respectively. \bar{j}_{PAD} and \bar{v}_{PAD} are the additional components added to the solution vector and right hand side vector to enable the use of the FFT such that $\bar{j}' = \begin{bmatrix} \bar{j}_1 & \bar{j}_{\text{PAD}} \end{bmatrix}^T$ and $\bar{v}' = \begin{bmatrix} \bar{v} & \bar{v}_{\text{PAD}} \end{bmatrix}^T$. Because the matrix on the LHS of equation (3.90) is a circulant matrix, we obtain $\bar{\bar{A}}_c \equiv \bar{\bar{A}}_b$ and $\bar{\bar{A}}_a \equiv \bar{\bar{A}}_d$. This is a system of $2Q$ equations where \bar{v}_{PAD} must be chosen to ensure that $\bar{j}_{\text{PAD}} = 0$ which will force \bar{j}_1 to equal the desired solution \bar{j} from equation (3.78). The correct choice of \bar{v}_{PAD} will thus yield

$$\begin{bmatrix} \bar{\bar{A}}_a & \bar{\bar{A}}_b \\ \bar{\bar{A}}_c & \bar{\bar{A}}_d \end{bmatrix} \begin{bmatrix} \bar{j} \\ \bar{0} \end{bmatrix} = \begin{bmatrix} \bar{v} \\ \bar{v}_{\text{PAD}} \end{bmatrix} \quad (3.91)$$

The iterative method uses the FFT to solve the more general Equation (3.90), the solution of which can be written as:

$$\begin{aligned} \begin{bmatrix} \bar{j}_1 \\ \bar{j}_{\text{PAD}} \end{bmatrix} &= \begin{bmatrix} \bar{\bar{A}}_a & \bar{\bar{A}}_b \\ \bar{\bar{A}}_c & \bar{\bar{A}}_d \end{bmatrix}^{-1} \begin{bmatrix} \bar{v} \\ \bar{v}_{\text{PAD}} \end{bmatrix} \\ &= \begin{bmatrix} \bar{\bar{T}}^{-1} & -\bar{\bar{T}}^{-1}\bar{\bar{A}}_b\bar{\bar{A}}_d^{-1} \\ -\bar{\bar{A}}_d^{-1}\bar{\bar{A}}_c\bar{\bar{T}}^{-1} & \times \end{bmatrix} \begin{bmatrix} \bar{v} \\ \bar{v}_{\text{PAD}} \end{bmatrix} \end{aligned} \quad (3.92)$$

where $\bar{\bar{T}} = \left(\bar{\bar{A}}_a - \bar{\bar{A}}_b\bar{\bar{A}}_d^{-1}\bar{\bar{A}}_c \right)$. One entry in the inverse matrix is unused in the subsequent calculation and is marked as a cross sign. The proposed iterative approach will converge if

$$\lim_{n \rightarrow \infty} \left(\bar{j}_1^{(n)} \right) = \bar{\bar{A}}_a^{-1} \bar{v} \quad (3.93)$$

From Table 3.6, $\bar{v}_{\text{PAD}}^{(0)} = \{0, 0, \dots, 0\}$ and from equation (3.92), it follows that

$$\begin{aligned}
 \bar{j}_1^{(0)} &= \bar{T}^{-1} \bar{v} \\
 &= \left(\bar{A}_a - \bar{A}_b \bar{A}_d^{-1} \bar{A}_c \right)^{-1} \bar{v} \\
 &= \left(\bar{I} - \bar{A}_a^{-1} \bar{A}_b \bar{A}_d^{-1} \bar{A}_c \right)^{-1} \bar{A}_a^{-1} \bar{v} \\
 &= \left(\bar{I} - \bar{N} \right)^{-1} \bar{A}_a^{-1} \bar{v} \\
 &= \bar{M}^{-1} \bar{A}_a^{-1} \bar{v}
 \end{aligned} \tag{3.94}$$

where

$$\bar{N} = \bar{A}_a^{-1} \bar{A}_b \bar{A}_d^{-1} \bar{A}_c \tag{3.95}$$

$$\bar{M} = \bar{I} - \bar{N} = \bar{I} - \bar{A}_a^{-1} \bar{A}_b \bar{A}_d^{-1} \bar{A}_c \tag{3.96}$$

The proposed method uses equation (3.89) to efficiently solve for \bar{j}' (and thus $\bar{j}_1^{(0)}$). At this point the $Q, Q+1, \dots, 2Q-1$ components of \bar{j}' are set to zero and equation (3.85) is used to update \bar{v}' (and thus $\bar{v}_{\text{PAD}}^{(1)}$). From equation (3.90) we see that

$$\begin{aligned}
 \bar{v}_{\text{PAD}}^{(1)} &= \bar{A}_c \bar{j}_1^{(0)} \\
 &= \bar{A}_c \bar{M}^{-1} \bar{A}_a^{-1} \bar{v}
 \end{aligned} \tag{3.97}$$

\bar{v}' is then used to calculate $\bar{j}_1^{(1)}$ and the iterations continue in this manner. Using equation (3.92)

$$\begin{aligned}
 \bar{j}_1^{(1)} &= \bar{M}^{-1} \bar{A}_a^{-1} \bar{v} - \bar{M}^{-1} \bar{A}_a^{-1} \bar{A}_b \bar{A}_d^{-1} \bar{v}_{\text{PAD}}^{(1)} \\
 &= \bar{M}^{-1} \bar{A}_a^{-1} \bar{v} - \bar{M}^{-1} \bar{N} \bar{M}^{-1} \bar{A}_a^{-1} \bar{v} \\
 &= \bar{M}^{-1} \left[\bar{I} - \bar{N} \bar{M}^{-1} \right] \bar{A}_a^{-1} \bar{v}
 \end{aligned} \tag{3.98}$$

After n iterations we obtain

$$\begin{aligned}
 \bar{j}_1^{(n)} &= \bar{M}^{-1} \bar{A}_a^{-1} \bar{v} - \bar{M}^{-1} \bar{A}_a^{-1} \bar{A}_b \bar{A}_d^{-1} \bar{v}_{\text{PAD}}^{(n)} \\
 &= \bar{M}^{-1} \bar{A}_a^{-1} \bar{v} - \bar{M}^{-1} \bar{N} \bar{j}_1^{(n-1)} \\
 &= \bar{M}^{-1} \left[\sum_{k=0}^n \left(-\bar{N} \bar{M}^{-1} \right)^k \right] \bar{A}_a^{-1} \bar{v}
 \end{aligned} \tag{3.99}$$

As n approaches infinity, then

$$\lim_{n \rightarrow \infty} \left(\bar{j}_1^{(n)} \right) = \bar{M}^{-1} \left[\sum_{k=0}^{\infty} \left(-\bar{N} \bar{M}^{-1} \right)^k \right] \bar{A}_a^{-1} \bar{v} \tag{3.100}$$

The Neumann series $\sum_{n=0}^{\infty} \bar{K}^n$ converges to $(\bar{I} - \bar{K})^{-1}$ provided that $\rho(\bar{K}) < 1$ and so, assuming this with $\bar{K} = -\bar{N} \bar{M}^{-1}$

$$\begin{aligned}
 \lim_{n \rightarrow \infty} \left(\bar{j}_1^{(n)} \right) &= \bar{M}^{-1} \left(\bar{I} + \bar{N} \bar{M}^{-1} \right)^{-1} \bar{A}_a^{-1} \bar{v} \\
 &= \bar{M}^{-1} \left(\bar{I} + \left(\bar{I} - \bar{M} \right) \bar{M}^{-1} \right)^{-1} \bar{A}_a^{-1} \bar{v} \\
 &= \bar{A}_a^{-1} \bar{v}
 \end{aligned} \tag{3.101}$$

This analysis shows that the proposed iterative method converges provided that the spectral radius of $\bar{N} \bar{M}^{-1}$ is smaller than unity.

$$\rho \left(\bar{N} \bar{M}^{-1} \right) < 1 \tag{3.102}$$

3.7.3 Investigation of convergence versus problem size

It has been shown that the new approach converges if the spectral radius of $\bar{N} \bar{M}^{-1}$ is smaller than unity, $\rho \left(\bar{N} \bar{M}^{-1} \right) < 1$. In this section, we investigate the relationship between the spectral radius and the size of the scatterer, as well as discretisation size.

The spectral radius of $\bar{N} \bar{M}^{-1}$ was computed for different discretisation sizes: $\lambda/4$, $\lambda/8$, $\lambda/10$ and $\lambda/20$. For each discretisation size, the scatterer size is varied from 10λ to 190λ with step size 10λ . In all cases pulse basis functions were used along with point-matching. The spectral radius of the iteration matrix $\bar{N} \bar{M}^{-1}$ is shown in Figure 3.13. The spectral radius of the iteration matrix increases when the discretisation size decreases, it varies around 0.18 for discretisation size $\lambda/4$ and around 0.43 for discretisation size $\lambda/20$. Moreover, the spectral radius tends to converge as the scatterer size increase. It is not proportional to

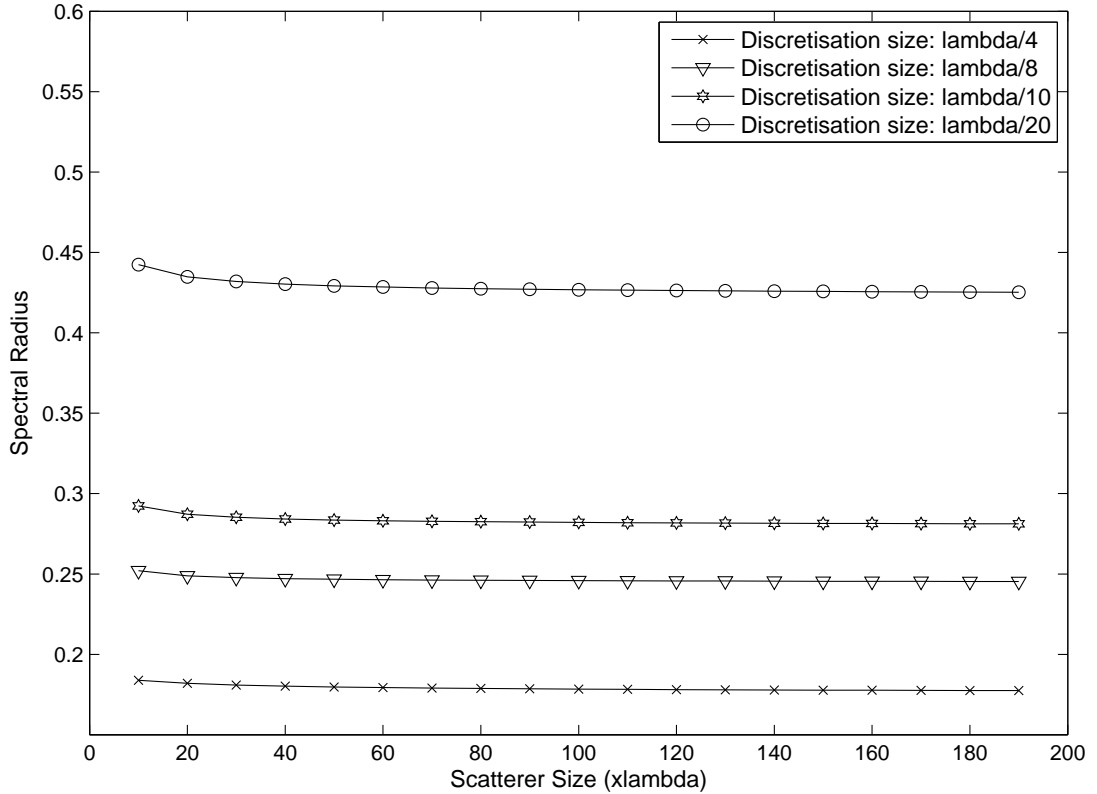


Figure 3.13: Spectral Radius of matrix \overline{NM}^{-1}

the size of the system and smaller than unity. This result is important because it suggests that the convergence of the proposed approach is broadly independent of scatterer size and that the method converges for typically used discretisation lengths.

3.7.4 Convergence comparison with Krylov methods

In this section the convergence rate of the new method is compared against that of Krylov-subspace based solvers. A comparison of the proposed approach with the GMRES-FFT and Preconditioned GMRES-FFT is performed in terms of convergence rate and processing time required to achieve a desired relative error norm.

Figure 3.14 shows the relative error norm defined by

$$\log_{10} \left(\frac{\|\overline{Z_j} - \overline{v}\|}{\|\overline{v}\|} \right)$$

against total number of iterations performed for the method proposed, as well as for the GMRES-FFT and preconditioned GMRES-FFT. The problem solved involved a plane wave source radiating at $970MHz$ over a flat plate of size $50m$. The plate was modeled

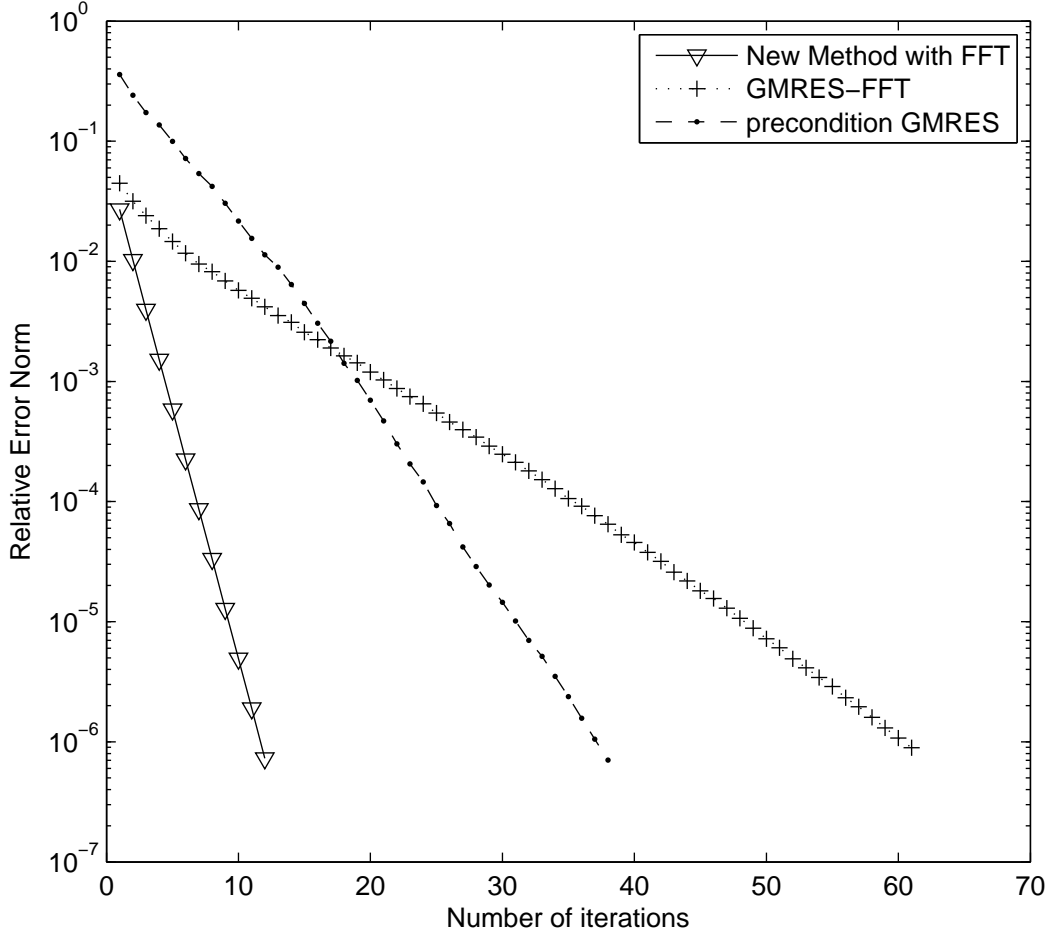


Figure 3.14: Comparison of convergence rate between proposed method, GMRES-FFT and block-diagonal preconditioned GMRES-FFT

as a lossy dielectric with $\varepsilon_r = 4.5$ and loss tangent $\tan \delta = 0.07$ [76]. The discretisation size was less than $\lambda/10$, the number of unknowns was 4096 and each method ran until it achieved a relative residual error of less than 10^{-6} . The preconditioner used in this simulation is the block-diagonal preconditioner [88] with the block size of $N_{Block} = 128$. As the block size of the preconditioned GMRES-FFT is increased, the convergence rate is improved as expected. However, more computations and memory storage are required for the preconditioned case. Different block sizes were investigated and the block size $N_{Block} = 128$ was identified as the optimized choice for the preconditioned GMRES-FFT. As shown in Figure 3.14, the new iterative approach needs 12 iterations to achieve the expected relative residual error while the GMRES-FFT requires 61 iterations and preconditioned GMRES-FFT requires 38 iterations. It is clear that the convergence rate of the proposed new approach is better than that of GMRES-FFT and block-diagonal preconditioned GMRES-FFT.

To investigate the methods further, a detailed investigation of run time and number of iterations required to achieve a desired relative error norm was performed. The desired relative error norm was set to 10^{-6} which is a relatively high accuracy threshold. The results are given in Table 3.7. The number outside of the parentheses denotes the run time in seconds while the number inside the parentheses denotes the number of iterations required to achieve the desired relative error norm. As demonstrated in Table 3.7, the proposed method is approximately 8 times faster than the preconditioned GMRES-FFT and 14 times faster than the preconditioned GMRES-FFT.

Table 3.7: Total run time (in seconds) and average number of iterations required to generate the basis functions (50 basis functions) for ITIM at different frequencies.

| Frequency | 970MHz | 1970MHz |
|--------------------------|-----------|-----------|
| Number of Unknowns | 4096 | 8192 |
| New Approach | 4.74 (12) | 9.34 (12) |
| GMRES-FFT | 62.7 (61) | 163 (70) |
| Preconditioned GMRES-FFT | 29.1 (38) | 56.0 (37) |

3.8 Conclusions

In this chapter, an extension of the TIM to compute the electromagnetic wave scattering from lossy dielectric terrain profiles was presented. The accuracy, complexity and performance of the proposed method has been evaluated and compared to those of precise solution generated by Forward Backward Method and Hata Okumura - Knife Edge Diffraction (HT-KED) which is a widely used empirical model. The robustness of the proposed method has also been verified by various terrain profile at different operating frequencies. The proposed method has shown that it has an extremely low computational cost and memory storage which is comparable to empirical models. It is also noted that in order to achieve the very low computational complexity and memory requirement, the large argument approximations are applied for both near field and far field interactions which makes the proposed method be suitable for terrain propagation problems.

4 Fullwave Computation of Path Loss in Urban Areas

4.1 Introduction

In chapter 3, we have seen that due to their potentially high accuracy, fullwave methods, especially those based on integral equation formulations, have been studied extensively for computing wave propagation in rural areas since the influential paper on the application of integral equation methods by Hviid et al [25]. Many techniques have been subsequently proposed to accelerate the integral equation method. However in the case of propagation in urban areas, ray tracing is more typically used and investigated [13, 15, 16, 17, 18, 19] while fullwave methods have seen little application due to the large scale of the problem. It is the aim of this chapter to document an initial study in using integral equations to model EM wave propagation in urban areas. We assume that the base station is sufficiently high that roof-top diffraction is the dominant mechanism and the problem thus is a 2D one consisting of scattering objects lying in the vertical plane containing source and receiver point. It is also worth to note that the integral equation based method is not restricted by the complex structure of the buildings while in the ray tracing models, walls with complex structures are usually approximated by uniform walls [18].

Application of the method of moments (MoM) to the integral equations results in a dense set of linear equations which pose difficulty in terms of storage, and whose solution by direct inversion has computational complexity $O(N^3)$ where N is the number of basis functions used to represent the surface fields on the 2D profile. This computational cost is extremely expensive for large scale problems where the number of unknowns could be of the order of hundreds of thousands to millions. Iterative methods where the computational complexity is reduced to order $O(N^2)$ can instead be used to effectively solve these electrically large scale problems. The stationary iterative forward-backward method (FBM) [34] has been shown to have a high convergence rate in some cases, yielding an accurate solution with few iterations. However, the FBM does not converge in the urban areas where the buildings have very sharp edges. In order to overcome this limitation of FBM, the Generalized FBM where the discretisation points are collected into groups is proposed in this chapter.

The chapter is structured as follows. Section 4.2 provides a brief description of the algo-

rithm for extracting the vertical plane profiles from a 3D city map which will be used as the input for the proposed method. Then in Section 4.3, the integral equation formulation and the proposed solution method are described. Numerical analysis of the computational efficiency and accuracy of the proposed method is investigated in Section 4.4. The comparison against measurement pathloss data collected in Munich city is also given in this section. Section 4.5 concludes this chapter.

4.2 Description of the algorithm for extracting vertical plane profiles from 3D city map

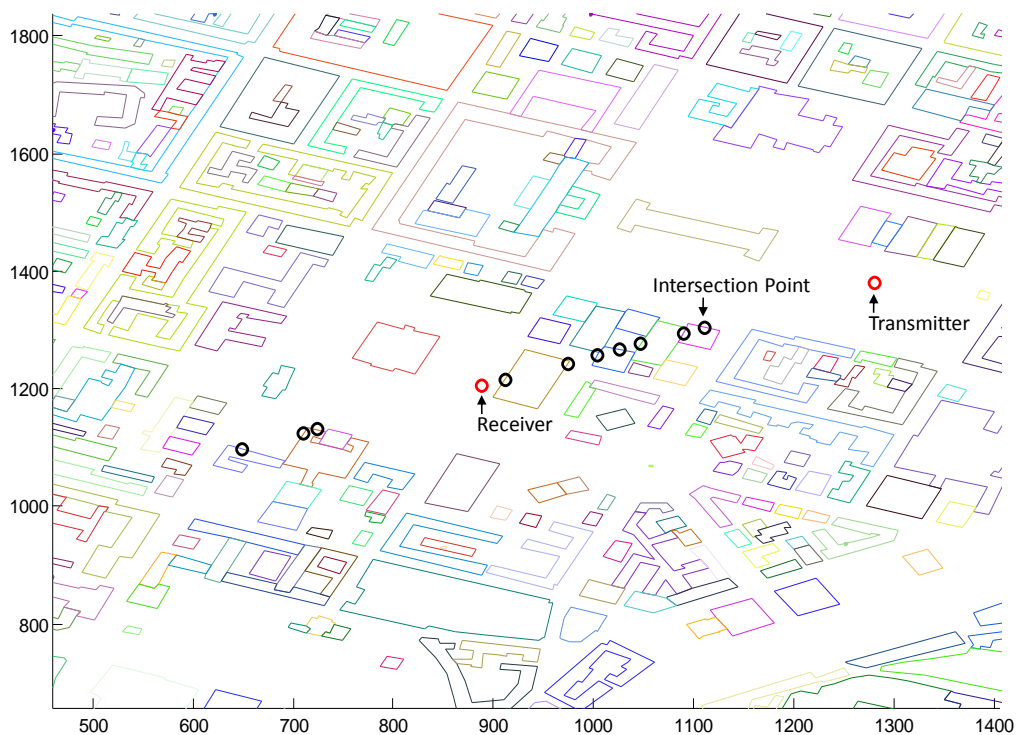


Figure 4.1: A example of base station, mobile station and the associated intersection points.

As stated in the introduction, we assume that the base station is sufficiently high that roof-top diffraction is the dominant propagation mechanism and the problem can be approximated as a 2D vertical problem. Then the extraction of the vertical plane profile from the 3D city map is required. Initially all intersections between buildings and the line connecting the base station (Tx) and mobile station (Rx) are identified as demonstrated in Figure 4.1. Note that the walls having the same colour belong to the same building. Only

one building behind the mobile station is retained while the other buildings behind the Rx and Tx are removed. It has been shown in [16] that retaining one building behind the Rx does not affect the accuracy of the vertical models. In order to reduce the complexity of the identification of the intersection points, only the buildings near the line connecting the base station and mobile station are considered. The size of the investigated region depends on the size of the largest building in the city. Then the intersection points are re-arranged in order of decreasing distance from the base station to the mobile station using the bubble sort algorithm. Finally the vertical plane profile is extracted from the information of the base station, mobile station and sorted intersection points as illustrated in Figure 4.2. Note that two special cases where buildings share the same wall or where one building is located inside another building need to be carefully handled.

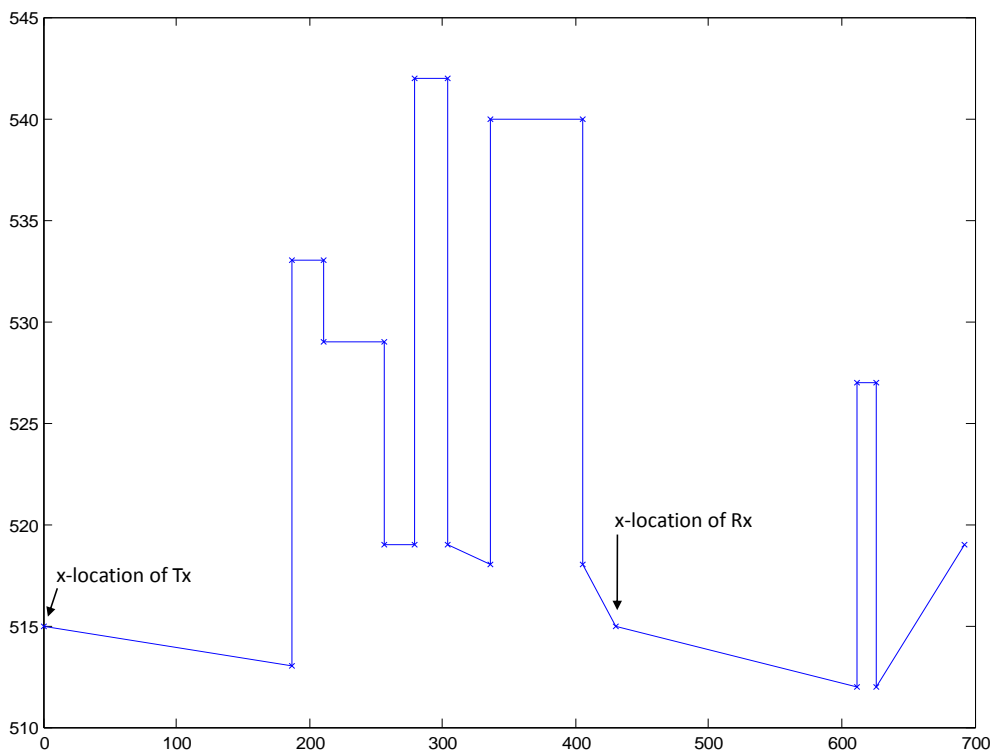


Figure 4.2: A example of vertical plane profile extraction from the intersection points shown in Figure 4.1.

4.3 The Generalized Forward Backward Method (GFBM)

In this section, the equations derived in Section 2.4 are reprised. Consider an incident wave $\psi_{inc}(x, y)$ impinging upon a dielectric surface which represents a 2D vertical plane profile with height profile $y = f(x)$. The upper medium is assumed to be free-space with

permittivity ϵ_0 and wavenumber k_0 while the lower medium is assumed to be a dielectric with permittivity ϵ_1 and wavenumber k_1 . As discussed in Section 2.4, for an incident TM^z polarization wave, the field components present are E_z , H_x and H_y and two coupled electric field integral equations (EFIE) are written as

$$K_t(t) + \int ik_0\eta_0 J_z(t') G_0(\bar{\rho}, \bar{\rho}') dt' - \int K_t(t') [\hat{n}' \cdot \nabla G_0(\bar{\rho}, \bar{\rho}')] dt' = E_z^{inc}(t) \quad (4.1)$$

$$K_t(t) - \int ik_1\eta_1 J_z(t') G_1(\bar{\rho}, \bar{\rho}') dt' + \int K_t(t') [\hat{n}' \cdot \nabla G_1(\bar{\rho}, \bar{\rho}')] dt' = 0 \quad (4.2)$$

For an incident TE^z polarization wave, the field components present are H_z , E_x and E_y and two coupled magnetic field integral equations (MFIE) are written as [2]

$$-J_t(t) + \int i\frac{k_0}{\eta_0} K_z(t') G_0(\bar{\rho}, \bar{\rho}') dt' + \int J_t(t') [\hat{n}' \cdot \nabla G_0(\bar{\rho}, \bar{\rho}')] dt' = H_z^{inc}(t) \quad (4.3)$$

$$J_t(t) + \int i\frac{k_1}{\eta_1} K_z(t') G_1(\bar{\rho}, \bar{\rho}') dt' + \int J_t(t') [\hat{n}' \cdot \nabla G_1(\bar{\rho}, \bar{\rho}')] dt' = 0 \quad (4.4)$$

where the points $\bar{\rho} = x\hat{x} + y\hat{y}$ and $\bar{\rho}' = x'\hat{x} + y'\hat{y}$ are on the surface while $G_0(\bar{\rho}, \bar{\rho}')$ and $G_1(\bar{\rho}, \bar{\rho}')$ are the Green's function of the upper and lower half-space

$$G_0(\bar{\rho}, \bar{\rho}') = -\frac{i}{4} H_0^{(2)}(k_0 |\bar{\rho} - \bar{\rho}'|) \quad (4.5)$$

$$G_1(\bar{\rho}, \bar{\rho}') = -\frac{i}{4} H_0^{(2)}(k_1 |\bar{\rho} - \bar{\rho}'|) \quad (4.6)$$

The Method of Moments (MoM) is applied to solve the integral equations (4.1,4.2) or (4.3,4.4) by expanding $J(t)$ and $K(t)$ into a finite series using N pulse basis functions and evaluating these equations at the centre of the basis function domains, resulting in a system of $2N$ linear equations whose entries are given in Section 2.4.

$$\begin{pmatrix} \overline{\overline{Z}}^{(a)} & \overline{\overline{Z}}^{(b)} \\ \overline{\overline{Z}}^{(c)} & \overline{\overline{Z}}^{(d)} \end{pmatrix} \begin{pmatrix} \bar{j} \\ \bar{k} \end{pmatrix} = \begin{pmatrix} \overline{\psi}_{inc} \\ \mathbf{0} \end{pmatrix} \quad (4.7)$$

where $\overline{\overline{Z}}^{(a)}$, $\overline{\overline{Z}}^{(b)}$, $\overline{\overline{Z}}^{(c)}$, $\overline{\overline{Z}}^{(d)}$ are the $N \times N$ impedance matrices, $\overline{\psi}_{inc}$ is the $N \times 1$ vector whose elements are the incident fields at the matching points on the surface and \bar{j} , \bar{k} are the $N \times 1$ vectors containing the unknown electric and magnetic surface currents at the center of the basis functions. Once found the surface currents can be used to compute scattered fields, and thus total fields, above the surface.

Direct inversion of equation (4.7) is not an option as the large value of N makes storage of the matrix (and inverse) impossible. Even if storage was not an issue the associated

computational complexity is $O(N^3)$ which would be extremely slow for practical problems. Instead we consider iterative solutions which have a computational complexity of $\mathcal{O}(N^2)$ which can be lowered further by application of acceleration techniques. Note that the popular Forward Backward Method (FBM) [33] will be shown to diverge in this scenario and hence the Generalized Forward Backward Method (GFBM) is developed. The operation of GFBM is similar to that of the conventional FBM. The FBM iterates a solution from pulse basis domain to basis domain while the GFBM instead groups these together (using varying group sizes) and iterates a solution from group to group. Note that this reduces to conventional FBM in areas where the group size is chosen to be one. Implementing a forward-backward method involves sequentially updating the unknowns, first in a forward sweep and then a backward sweep. The FBM diverges in the case of EM wave propagation over buildings because of the sharp corners of the buildings. In order to make the FBM converge in this scenario, the currents near the corners need to be computed simultaneously instead of being computed iteratively. The forward and backward sweep of the GFBM is described by

$$\begin{aligned} \overline{\overline{Z}}_{ii} \overline{\overline{x}}_i^{(k+\frac{1}{2})} &= \overline{b}_i - \overline{l}_i^{(k+\frac{1}{2})} - \overline{u}_i^{(k)} \\ &\text{for } i = 1 \dots M \end{aligned} \quad (4.8)$$

$$\begin{aligned} \overline{\overline{Z}}_{ii} \overline{\overline{x}}_i^{(k+1)} &= \overline{b}_i - \overline{l}_i^{(k+\frac{1}{2})} - \overline{u}_i^{(k+1)} \\ &\text{for } i = M \dots 1 \end{aligned} \quad (4.9)$$

where M is the number of groups, $\overline{l}_i^{(k)}$ and $\overline{u}_i^{(k)}$ are vectors containing fields scattered in the forward and backward directions respectively to group G_i at the k^{th} iteration, \overline{b}_i is the incident field on group G_i and \overline{x}_i are the unknown surface electric and magnetic currents on group G_i .

$$\overline{l}_i^{(k)} = \sum_{j < i} \overline{\overline{Z}}_{ij} \overline{\overline{x}}_j^{(k)} \quad (4.10)$$

$$\overline{u}_i^{(k)} = \sum_{j > i} \overline{\overline{Z}}_{ij} \overline{\overline{x}}_j^{(k)} \quad (4.11)$$

where $\overline{\overline{Z}}_{ij} = \begin{pmatrix} \overline{\overline{Z}}_{ij}^{(a)} & \overline{\overline{Z}}_{ij}^{(b)} \\ \overline{\overline{Z}}_{ij}^{(c)} & \overline{\overline{Z}}_{ij}^{(d)} \end{pmatrix}$. In the GFBM this group approach is applied to compute the currents on the vertical edges of the buildings while the conventional FBM is applied to compute the currents at the other points along the profile. This is a hybrid between the conventional FBM and the Block FBM and called Generalized FBM (GFBM). The concept of this method is based on the Generalized FBM [35] which was developed for random rough surface scattering problems. However the conventional GFBM supposes to choose the whole structure as a group while the GFBM proposed in this chapter chooses

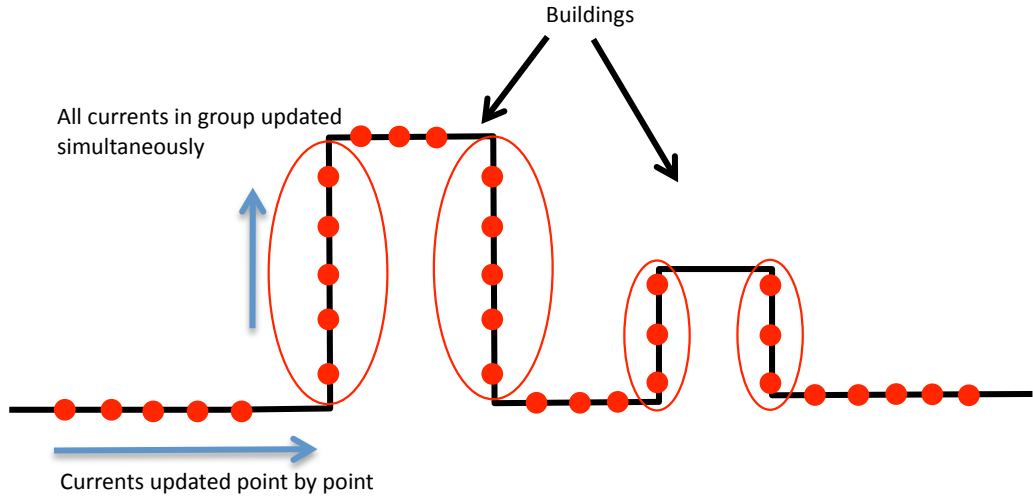


Figure 4.3: GFBM Algorithm.

only the vertical edges of the building as groups. This reduces the memory requirement considerably and makes it possible to apply the method for practical radio frequencies.

In cases where propagation is predominantly in the forward direction, a forward scattering approximation can be obtained by ignoring the back-scattered fields. This requires only a single iteration and requires that we solve

$$\overline{\overline{Z}}_{ii} \overline{x}_i = \overline{b}_i - \overline{l}_i \quad \text{for } i = M \dots 1 \quad (4.12)$$

4.4 Numerical analysis

In this section the accuracy and robustness against profiles' elevation of the proposed method is evaluated. The path-loss results generated by the Generalized FBM with forward scattering assumption are compared against those generated using a numerically exact solution and measurement data. The proposed method is also compared against the slope diffraction method [89, 16] in terms of accuracy.

4.4.1 Accuracy of the forward scattering assumption

In order to illustrate the accuracy of the forward scattering assumption, the pathloss results generated by the GFBM with forward scattering assumption are compared to those generated by a numerically precise solution. The precise solution is obtained by running GFBM until the normalized error norm

$$\log_{10} \frac{\|\bar{\bar{Z}}\bar{x} - \bar{b}\|}{\|\bar{b}\|} \quad (4.13)$$

is less than 10^{-3} . The transmitting antenna radiates TM^z polarized fields and is located at the left edge of the profile at a height of $13m$. The antenna of mobile station is located at a height of $1.5m$ and moves along the profile. The terrain and building was assumed to be made of the same material and modelled as a lossy dielectric with $\epsilon_r = 4.5$ and loss tangent $\tan \delta = 0.211$ (brick). The chosen profile for the simulation is extracted from the map of Munich city illustrated in Figure 4.4(a) and has a length of $1.1km$. The pathloss is computed at the frequency of $945MHz$ and shown in Figure 4.4(b). It is shown in Figure 4.4(b) that the pathloss computed by the GFBM with forward scattering assumption (GFBM-FS) has a very good agreement with that generated by the precise solution. The RMSE between two methods is $3.07dB$ which is acceptable compared to the differences between the numerical method and measurement data as shown in the next section. We conclude that the forward scattering assumption is a reasonable approximation for the EM scattering in the urban areas. Note that forward scattering in this context only refers to the computation of the surface currents. Integrating these along the entire surface profile in order to compute the fields above the surface implicitly introduces some element of back-scattering to these fields.

4.4.2 Comparison with slope diffraction method and measurement data

In order to gauge the accuracy of the IE formulations, the pathloss results generated by the proposed method are compared against those generated by the slope diffraction method (SDM) [89, 16] and measurement data collected along three metro routes in Munich City by Mannesmann Mobilfunk GmbH. The slope diffraction method which is used as the reference method was firstly proposed by J.B. Andersen [89] and then has been widely applied as part of vertical plane ray tracing method[16]. The SDM improves the accuracy of Uniform Diffraction Theory (UTD) in modeling radio wave propagation in rural and urban areas. In the case of wave propagation in urban areas, the row of buildings can be modeled as knife edges, with wedges to improve the accuracy. The UTD provides inaccurate results in the case of multiple edges diffraction due to the discontinuity of the fields on the transition zones. The Slope Diffraction Method enforces the continuity of amplitude

and slope on each transition zones and therefore improve the accuracy of the UTD. In the implementation of the slope diffraction method, all buildings were approximated by knife edges although we note that more accurate results can be obtained by modelling each building as a wedge [16]. The measurement was performed in an area of $2400\text{m} \times 3400\text{m}$ containing 2088 buildings and 17445 walls. The transmitting antenna was located in the middle of a square at a height of 13m and radiates TM^z polarized fields at 945MHz . The height of the mobile station is 1.5m . The pathloss is measured along three routes: Metro 200, Metro 201 and Metro 202 as shown in Figure 4.5. The fields at each measurement point were averaged over a distance of 10m around the stated point and then converted to path loss. The length of the routes Metro 200, Metro 201 and Metro 202 are approximately 9km , 3.5km and 10km respectively. Application of the GFBM involved extracting the appropriate vertical building profile for each measurement point and applying the numerical methods described above. The number of unknowns for each profile varies from $10,000$ to $100,000$. Due to the large computational overheads involved we did not compute path loss for each measurement point, but rather did so for every third point. Then the simulation results are smoothed using a moving average with a window length of 7 (equivalent to 21 measurement points). The moving average removes the local peaks therefore enhancing the accuracy of the predictions.

As noted in [16], if the mobile stations are located far away from the base station then the propagation in the vertical plane represents the dominant contribution and the 2D vertical plane problem is appropriate to capture the physics. This is borne out by the pathloss generated by the GFBM with forward scattering assumption showing a very good agreement with the measurement data. In contrast, if the mobile stations are located near the base station (less than 400m), lateral propagation in the horizontal plane becomes more important. The proposed method does not incorporate such lateral propagation and hence does not show a good agreement with the measurement data for mobile station points close to the base station. 3D ray tracing (or a suitably formulated integral equation) is more appropriate for this scenario and will be pursued in future work. (Figure 4.6), (Figure 4.7) and (Figure 4.8) show the predicted pathloss versus measurement for the METRO 200, 201 and 202 and demonstrate that the pathloss generated by the GFBM with a forward scattering assumption has a better agreement with the measurement data than those generated by the slope diffraction method. Table 4.1 compares the mean and standard deviation of the errors for the three routes. Results quoted in [16] based on slope diffraction method applied to buildings modelled as wedges rather than knife edges are also included. Note that the statistics quoted only consider mobile station locations a distance of more than 400m from the base station as the proposed formulation is not suitable for nearby mobile station locations.

Table 4.1: Mean (η) and standard deviation (σ) of error between Slope Diffraction Method (SDP), GFBM-FS and measurements

| | METRO 200 | | METRO 201 | | METRO 202 | |
|--------------------------|-----------|----------|-----------|----------|-----------|----------|
| | η | σ | η | σ | η | σ |
| GFBM-FS | -1.2 | 7.3 | 4.26 | 7.95 | 0.57 | 9.7 |
| SDP (Knife edges) | 14.8 | 8.1 | 15.6 | 8.24 | 14.3 | 10.1 |
| SDP (Wedges) (from [16]) | -1.1 | 8.0 | - | - | -3.8 | 10.8 |

4.5 Conclusion

A novel method for computing EM wave scattering in urban areas was presented in this chapter. The GFBM was proposed to overcome the divergence of the conventional FBM in the case of propagation in urban areas and the forward scattering variant (GFBM-FS) was shown to be reasonable. The accuracy of the proposed method was also investigated by comparing against experimental data provided by Mannesmann Mobilfunk GmbH. The proposed method has a better accuracy than the slope diffraction method, a widely used vertical propagation model. The proposed method is valid for mobile stations located far from the base station and there is a potential to combine the proposed method with available methods to correct the pathloss for the mobile stations near the base station. Moreover acceleration techniques such as Fast Far Field Approximation (FAFFA) [39], Spectral Acceleration (SA) [70, 71] should be applied to accelerate the proposed method. It is also worth to note the proposed method is also valid for 2D horizontal propagation. This will form the basis of our future investigations.

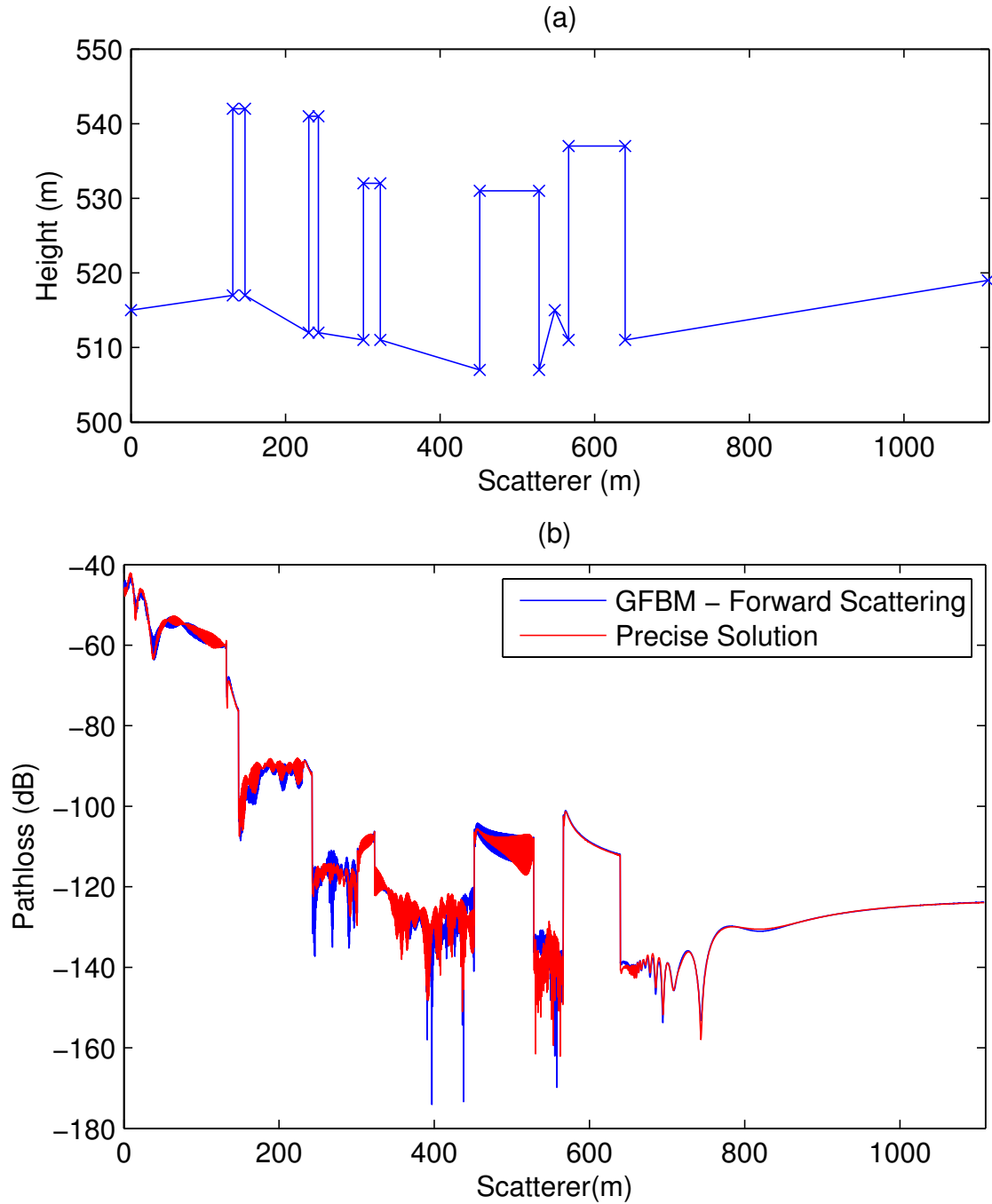


Figure 4.4: Pathloss generated by proposed method, precise solution over a sample profile (a) Sample profile extracted from Munich city (b) Pathloss at 945MHz with TM^z Polarization.

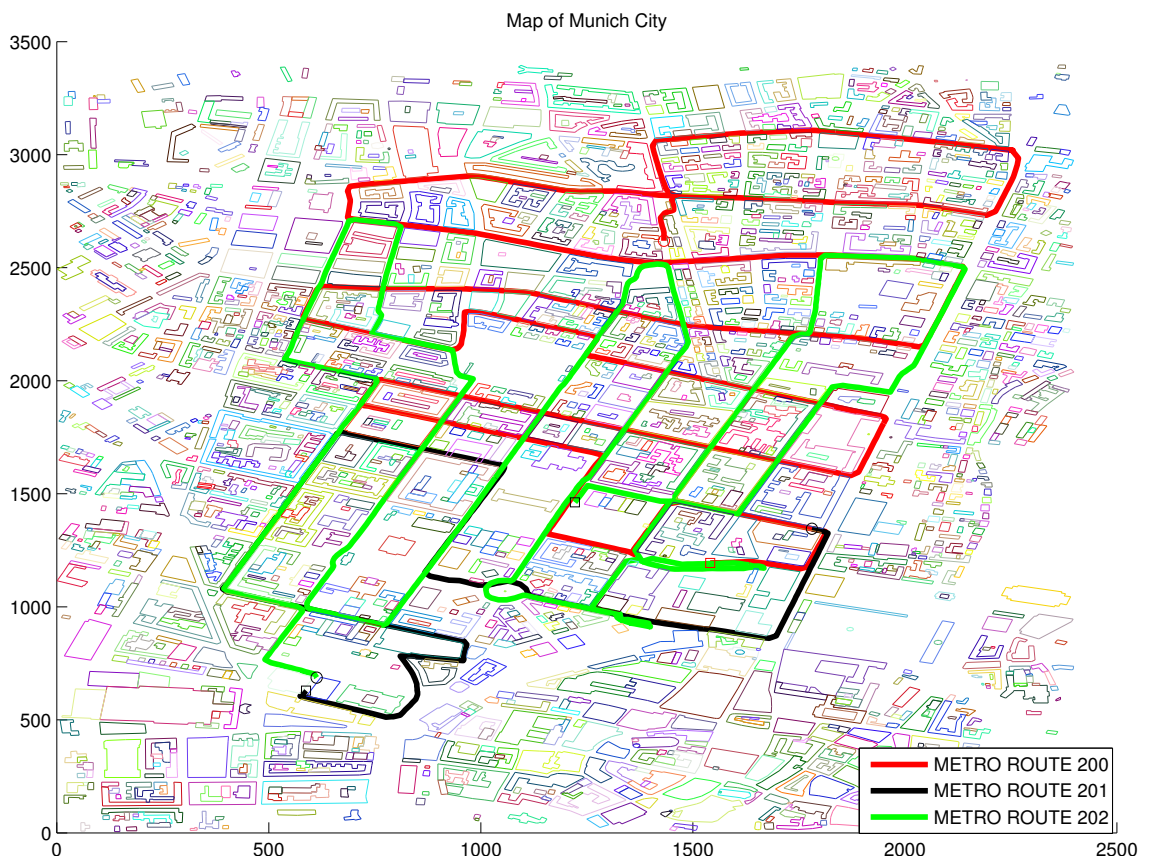


Figure 4.5: Map of Munich City with 3 Metro routes

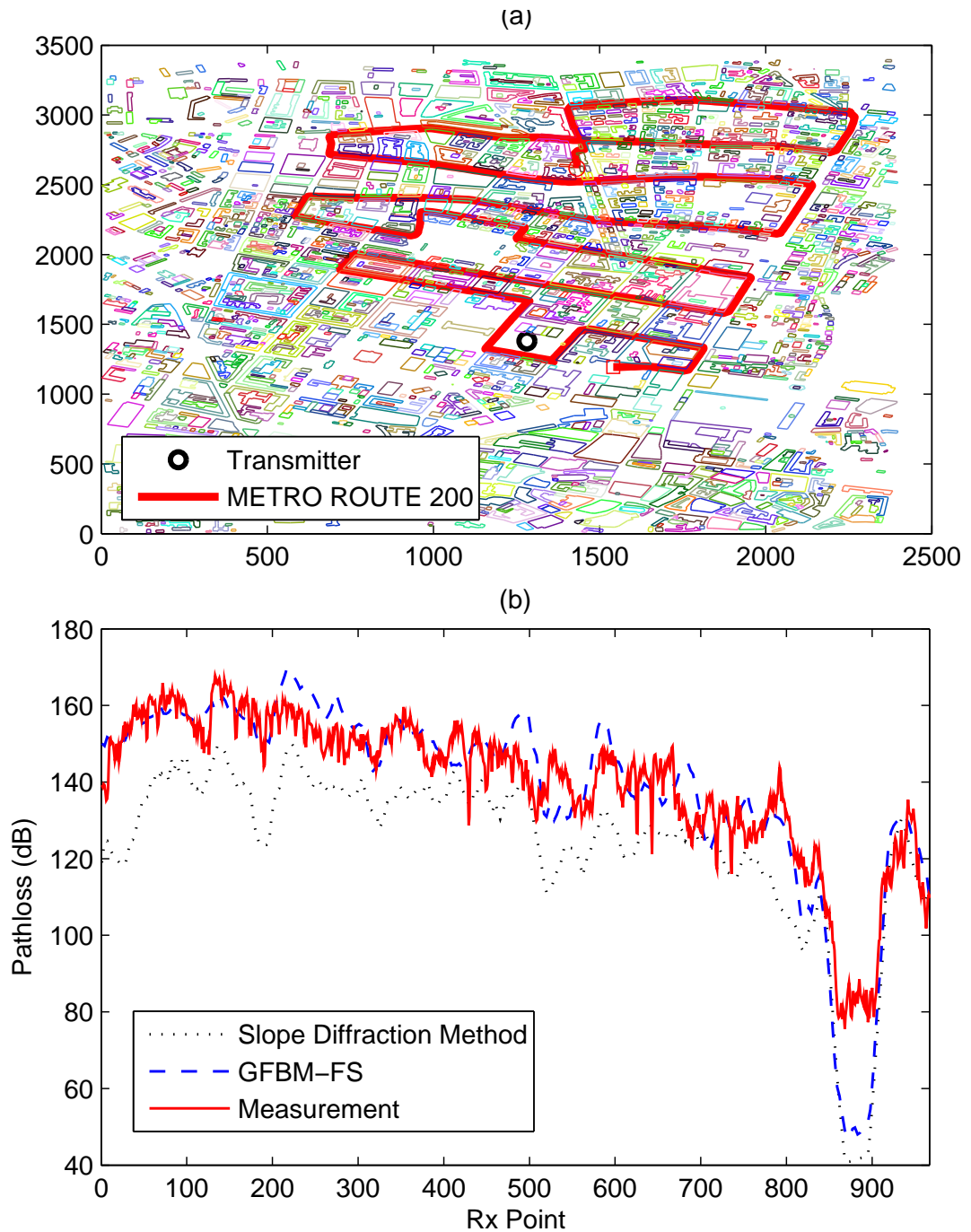


Figure 4.6: (a) Partial map of Munich city and Metro 200 (b) Comparison between measurements, GFBM with forward scattering assumption and Slope Diffraction Method. Route: Metro 200

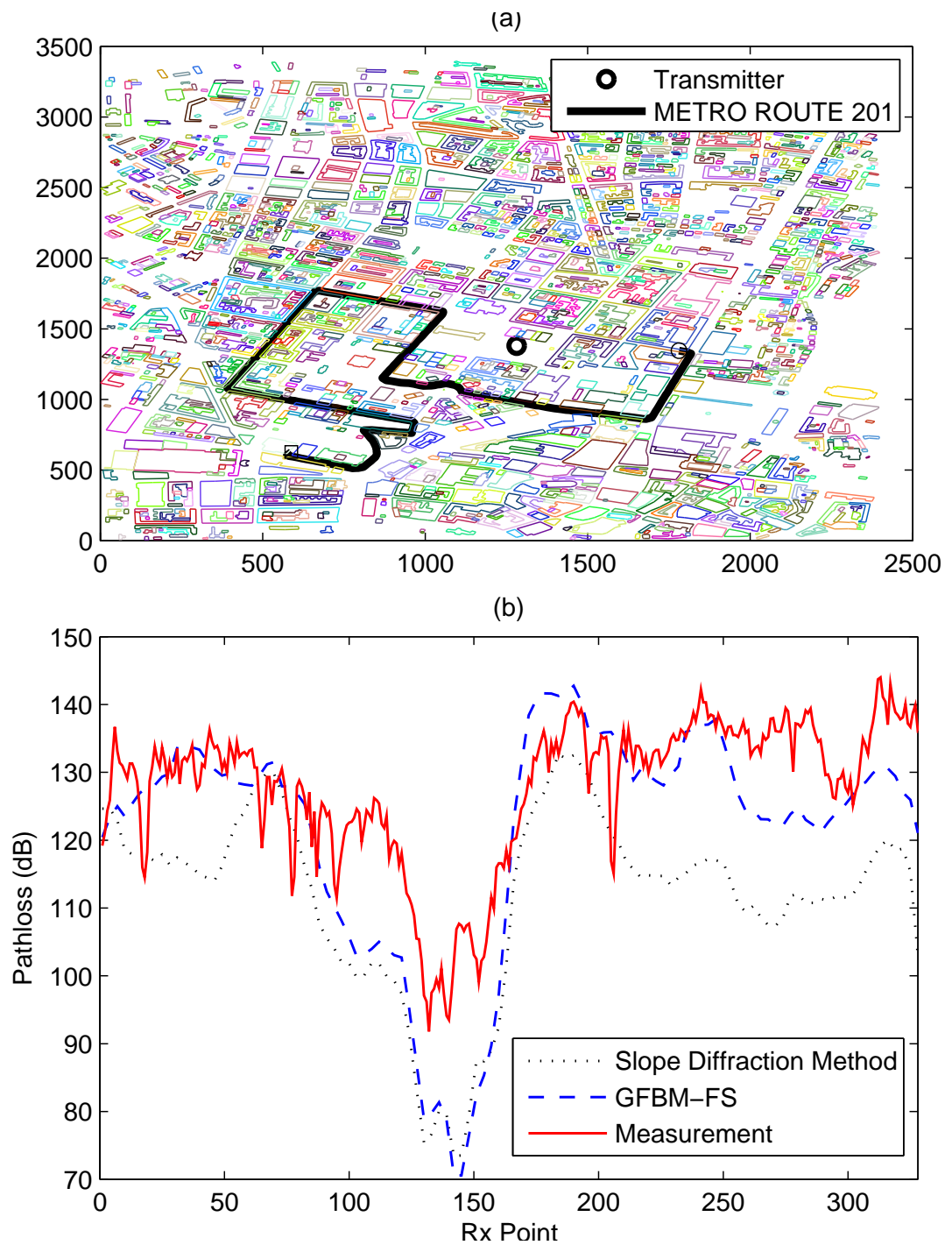


Figure 4.7: (a) Partial map of Munich city and Metro 201 (b) Comparison between measurements, GFBM with forward scattering assumption and Slope Diffraction Method. Route: Metro 201

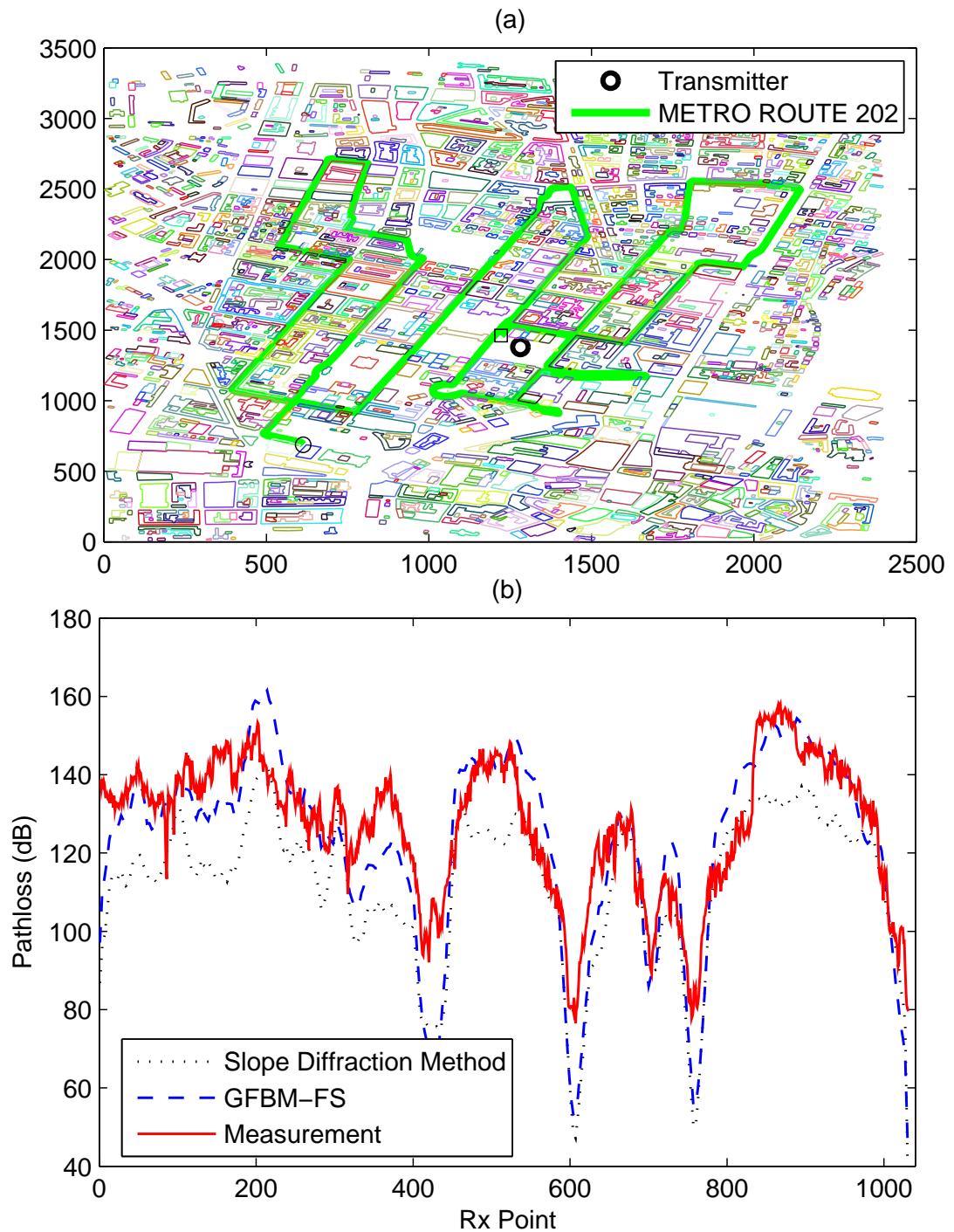


Figure 4.8: (a) Partial map of Munich City and Metro 202 (b) Comparison between measurements, GFBM with forward scattering assumption and Slope Diffraction Method. Route: Metro 202

5 Improved Forward Backward Method with Spectral Acceleration for Scattering From Randomly Rough Lossy Surfaces

5.1 Introduction

As discussed in chapter 1, the computation of EM wave scattering from randomly rough surfaces is a classic problem with many important applications such as soil moisture estimation [45, 3, 46], sea surface salinity evaluation [47, 48], glacier monitoring, infrastructure defect detection, etc. In this dissertation, we focus on the application of random rough surface scattering to the soil moisture estimation. Bistatic scattering coefficients (BSC) of the rough surfaces are directly related to their dielectric properties and roughness of the surfaces and can be used to sense them as illustrated in Figure 5.1, 5.2 and 5.3. For a flat surface as shown in Figure 5.1, most of the energy is reflected in the specular direction (30°). When the surfaces become rougher, the energy is broadened in other directions as shown in Figure 5.2 and 5.3.

Due to the low-complexity nature of the problem, scattering from 1D rough surfaces has been studied extensively and many techniques have been proposed in order to achieve a better efficiency, accuracy and robustness. The proposed methods can be classified into two main groups, approximate analytical methods such as Kirchoff's approximation (KA) or small perturbation method (SPM) [49] and fullwave methods. More recently fullwave methods, especially those based on the method of moments discretisation of boundary integral equations, have attracted more attention due to the limited regime of validity of the analytical theories. These offer high accuracy, only require the discretisation of the rough boundary between the two regions and naturally satisfy the radiation condition at infinity through the use of suitable Green's functions. However they result in a dense set of linear equations which, for large problems, can only be solved by using iterative methods. Commonly used Krylov-subspace based iterative techniques such as the conjugate gradient (CG) or Generalized Minimal Residual (GMRES) methods are quite robust but can be very slowly convergent and require the use of effective preconditioners. In addition the need to perform matrix-vector multiplications results in a $\mathcal{O}(N^2)$ computational complexity for each iteration where N is the number of basis functions used in the method of

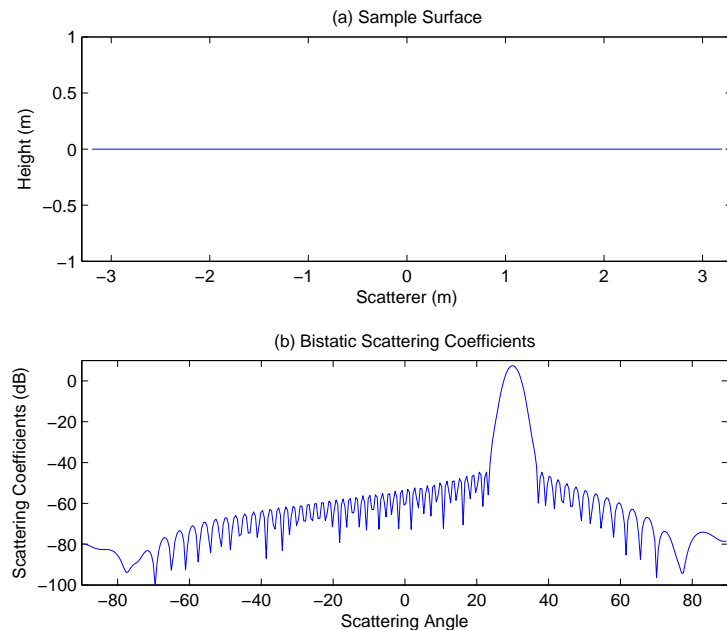


Figure 5.1: Bistatic scattering coefficient of a flat surface. root mean squared height $h_{rms} = 0.0\lambda$ and correlation length: $l_c = 0.5\lambda$. Incident angle: 30° . (a) Flat surface (b) Bistatic scattering coefficients of the surface

moments. In response to these limitations several efficient techniques have been proposed in recent years. These include the Fast Multipole Method (FMM) [54], the banded matrix iterative approach with canonical grid (BMIA/CAG) [56, 57] for perfectly conducting (PEC) rough surfaces, the physics-based two grid method (PBTG) [60, 59] for dielectric surfaces etc. The latter two methods proceed by distinguishing weakly interacting (far) regions from strongly interacting (near) regions for each observation point. The scattered field computation from far regions represents the majority of the computational burden and can be accelerated. An interesting recent technique in this area was introduced by Liu *et al* [62], and demonstrated good performance. However, Liu *et al's* method decreases in efficiency as the slope of the surface increases. Moreover, the selection of a near field region equal to one tenth of the overall length is a limitation of this method when one considers problems of a larger electrical size. Another popular technique is the Forward-Backward Method (FBM) [34] which has been shown in certain cases to outperform Krylov-subspace based solvers, achieving machine-precision solutions in fewer iterations. However, in scattering by lossy surfaces with high permittivity (wet soil surfaces, ocean surfaces), a dense grid with a large number of sampling points per free space wavelength is used [59]. In this case, the convergence rate of the FBM starts to reduce and the technique can diverge for scattering from extremely rough surfaces (although hybridised versions can be used to mitigate this somewhat) [90]. The convergence rate of the forward backward method can be shown to be dependent on the spectral radius of the associated iteration matrix. Anal-

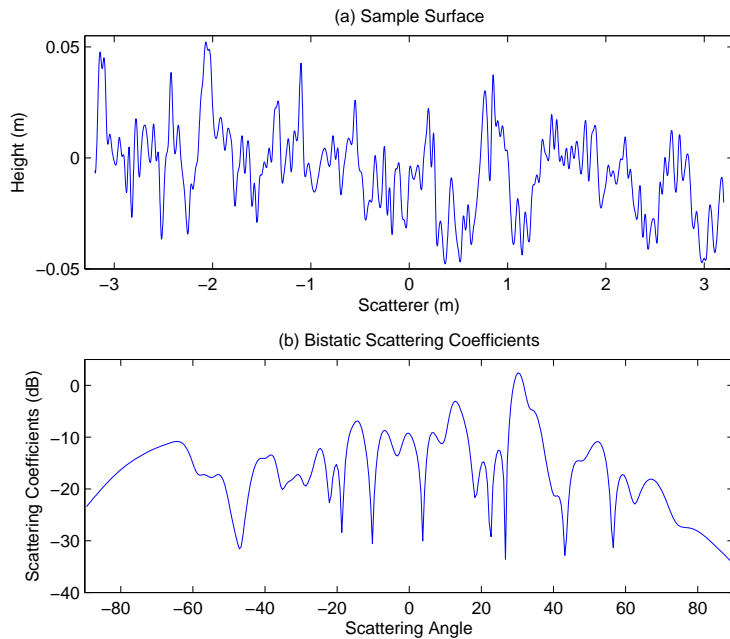


Figure 5.2: Bistatic scattering coefficient of a rough surface. root mean squared height $h_{rms} = 0.1\lambda$ and correlation length: $l_c = 0.5\lambda$. Incident angle: 30° . (a) Rough surface (b) Bistatic scattering coefficients of the surface

ysis carried out in [73] suggested that after several iterations the error vector is dominated by a component in the direction of the eigenvector associated with the largest eigenvalue. Continued application of the forward backward method will ultimately lead to convergence but this can be quite slow if the spectral radius is close to 1. It is also demonstrated that this situation can be numerically identified and the simple expedient of taking an optimized step in the direction of this dominant eigenvector can significantly reduce the error. This technique is referred as the Improved Forward Backward Method (IFBM) and in this chapter it is extended in several ways. Firstly an improved analysis provides a more thorough explanation of the workings of the IFBM, in this case in the context of scattering from lossy dielectrics. Secondly this chapter demonstrates how to reduce the cost of the optimisation step from 2.5 matrix-vector products to 1 matrix-vector product (and 0.5 products in some cases). Finally Spectral Acceleration (SA) is then applied to reduce the complexity of the optimization step from $\mathcal{O}(N^2)$ to $\mathcal{O}(N)$ [36, 37] to yield a highly efficient method called Improved Forward Backward Method with Spectral Acceleration (IFBM-SA).

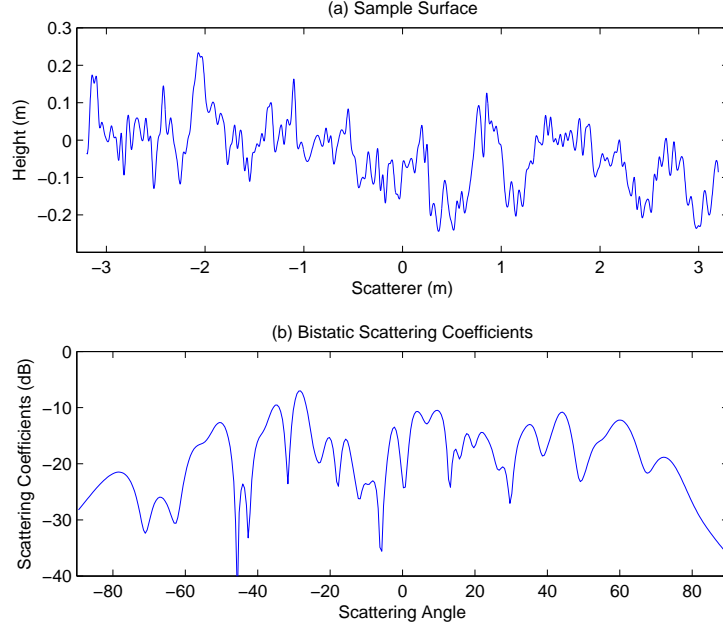


Figure 5.3: Bistatic scattering coefficient of a flat surface. root mean squared height $h_{rms} = 0.5\lambda$ and correlation length: $l_c = 1.0\lambda$. Incident angle: 30° . (a) Rough surface (b) Bistatic scattering coefficients of the surface

5.2 Formulation

Consider an incident plane wave $\psi_{inc}(x, z)$ impinging upon a dielectric random surface with height profile $y = f(x)$ as shown in Figure 5.4. The upper medium is assumed to be free-space with permittivity ϵ_0 and permeability μ_0 while the lower medium is assumed to be a dielectric with permittivity ϵ_1 and permeability μ_1 . It has been demonstrated in Section 2.4 that the field ψ on the surface satisfies the dual integral equations for the two media problem

$$\frac{1}{2}\psi(\bar{\rho}) - \mathcal{P} \int \psi(\bar{\rho}') [\hat{n}' \cdot \nabla G_0(\bar{\rho}, \bar{\rho}')] dl' + \int_S G_0(\bar{\rho}, \bar{\rho}') [\hat{n}' \cdot \nabla \psi(\bar{\rho}')] = \psi^{inc}(\bar{\rho}) \quad (5.1)$$

$$\frac{1}{2}\psi(\bar{\rho}) + \mathcal{P} \int \psi(\bar{\rho}') [\hat{n}' \cdot \nabla G_1(\bar{\rho}, \bar{\rho}')] dl' - \int_S G_1(\bar{\rho}, \bar{\rho}') \rho [\hat{n}' \cdot \nabla \psi(\bar{\rho}')] = 0 \quad (5.2)$$

where $\rho = 1$ for the TM^z wave and $\rho = \frac{\epsilon_1}{\epsilon_0}$ for the TE^z wave. $\bar{\rho} = x\hat{x} + y\hat{y}$ and $\bar{\rho}' = x'\hat{x} + y'\hat{y}$ represent points on the surface, \mathcal{P} denotes the Cauchy principle value integral and $G_0(\bar{\rho}, \bar{\rho}')$,

$G_1(\bar{\rho}, \bar{\rho}')$ are the Green's functions of the upper and lower half-space respectively

$$G_0(\bar{\rho}, \bar{\rho}') = \frac{1}{4i} H_0^2(k_0 |\bar{\rho} - \bar{\rho}'|) \quad (5.3)$$

$$G_1(\bar{\rho}, \bar{\rho}') = \frac{1}{4i} H_0^{(2)}(k_1 |\bar{\rho} - \bar{\rho}'|) \quad (5.4)$$

where $H_0^{(2)}$ denotes the Hankel function of the first kind and k_0 and k_1 are the wave numbers of the upper and lower medium. We apply the MoM to solve the integral equation (5.1) and (5.2) by expanding $\psi(\bar{r})$ into a finite series using N pulse basis functions of width Δx and applying collocation at the domain centres. This yields the linear system whose entries are given in Section 2.4.1 and Section 2.4.2.

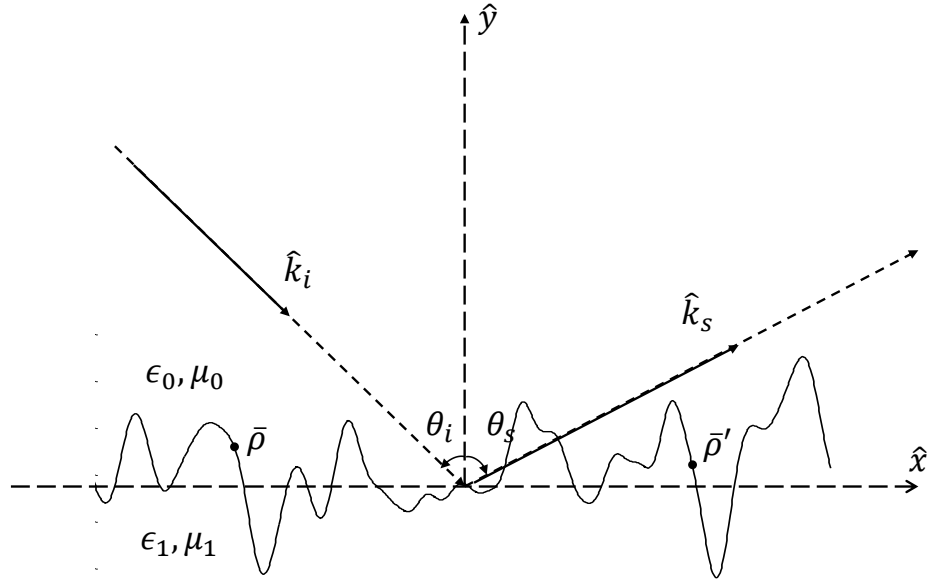


Figure 5.4: One dimensional dielectric rough surface profile $z = f(x)$ illuminated by an incident wave

$$\begin{pmatrix} \bar{Z}_a & \bar{Z}_b \\ \bar{Z}_c & \bar{Z}_d \end{pmatrix} \begin{pmatrix} \bar{U} \\ \bar{\psi} \end{pmatrix} = \begin{pmatrix} \bar{\psi}^{inc} \\ \bar{0} \end{pmatrix} \quad (5.5)$$

where $\psi(x)$ is a vector sampling the unknown field on the boundary while \bar{U} contains information about the unknown normal derivative on the boundary, specifically it samples $U(x) = \sqrt{1 + [f'(x)]^2} \partial\psi/\partial n$.

In order to reduce unwanted edge effects from the end points of the surface, the incident wave, centered in the direction $\hat{k}_i = \sin\theta_i\hat{x} - \cos\theta_i\hat{y}$ where θ_i denotes the incident angle, is tapered so that the illuminated surface can be confined to the rough surface length L_x as shown in Figure 5.4. The incident fields are given as

$$\psi^{inc}(\bar{\rho}) = e^{-ik_0(\sin\theta_i x - \cos\theta_i z)(1+\omega(\bar{\rho}))} e^{-\frac{(x+y\tan\theta_i)^2}{g^2}} \quad (5.6)$$

The parameter g controls the tapering of the incident wave and the term $\omega(\bar{\rho})$ is introduced to correct the phase term of the incident wave [91]

$$\omega(\bar{\rho}) = \frac{2\frac{(x+y\tan\theta_i)^2}{g^2} - 1}{(k_0 g \cos\theta_i)^2} \quad (5.7)$$

5.2.1 Forward Backward Method

In order to apply the forward backward method, the unknowns of equation (5.5) need to be interleaved to form the equation

$$\begin{bmatrix} Z_{a,11} & Z_{b,11} & Z_{a,12} & Z_{b,12} & \cdots & Z_{a,1N} & Z_{b,1N} \\ Z_{d,11} & Z_{c,11} & Z_{d,12} & Z_{c,12} & \cdots & Z_{d,1N} & Z_{c,1N} \\ Z_{a,21} & Z_{b,21} & Z_{a,22} & Z_{b,22} & \cdots & Z_{a,2N} & Z_{b,2N} \\ Z_{d,21} & Z_{c,21} & Z_{d,22} & Z_{c,22} & \cdots & Z_{d,2N} & Z_{c,2N} \\ \vdots & \vdots & \vdots & \vdots & \ddots & \vdots & \vdots \\ Z_{a,N1} & Z_{b,N1} & Z_{a,N2} & Z_{b,N2} & \cdots & Z_{a,NN} & Z_{b,NN} \\ Z_{d,N1} & Z_{c,N1} & Z_{d,N2} & Z_{c,N2} & \cdots & Z_{d,NN} & Z_{c,NN} \end{bmatrix} \begin{bmatrix} U_1 \\ \psi_1 \\ U_2 \\ \psi_2 \\ \vdots \\ U_N \\ \psi_N \end{bmatrix} = \begin{bmatrix} \psi_1^{inc} \\ 0 \\ \psi_2^{inc} \\ 0 \\ \vdots \\ \psi_N^{inc} \\ 0 \end{bmatrix} \quad (5.8)$$

This equation can be written in the more compact form as

$$\begin{bmatrix} \bar{\bar{Z}}_{11} & \bar{\bar{Z}}_{12} & \cdots & \bar{\bar{Z}}_{1N} \\ \bar{\bar{Z}}_{21} & \bar{\bar{Z}}_{22} & \cdots & \bar{\bar{Z}}_{2N} \\ \vdots & \vdots & \ddots & \vdots \\ \bar{\bar{Z}}_{N1} & \bar{\bar{Z}}_{N2} & \cdots & \bar{\bar{Z}}_{NN} \end{bmatrix} \begin{bmatrix} \bar{x}_1 \\ \bar{x}_2 \\ \vdots \\ \bar{x}_N \end{bmatrix} = \begin{bmatrix} \bar{b}_1 \\ \bar{b}_2 \\ \vdots \\ \bar{b}_N \end{bmatrix} \quad (5.9)$$

where the elements of $\overline{\overline{Z}}_{mn}$, \overline{x}_m and \overline{b}_m can be written as

$$\overline{\overline{Z}}_{mn} = \begin{bmatrix} Z_{a,mn} & Z_{b,mn} \\ Z_{c,mn} & Z_{d,mn} \end{bmatrix} \quad (5.10)$$

$$\overline{x}_m = \begin{bmatrix} U_m \\ \psi_m \end{bmatrix} \quad (5.11)$$

$$\overline{b}_m = \begin{bmatrix} \psi_m^{inc} \\ 0 \end{bmatrix} \quad (5.12)$$

The forward backward method consists of a forward sweep through the unknowns $m = 1, \dots, N$ followed by a backward sweep in the order $m = N, \dots, 1$. Mathematically the k^{th} iteration can be written in terms of two sweeps

$$\overline{\overline{Z}}^s \overline{x}^{(k-\frac{1}{2})} = \overline{b} - \overline{\overline{Z}}^f \overline{x}^{(k-\frac{1}{2})} - \overline{\overline{Z}}^b \overline{x}^{(k-1)} \quad (5.13)$$

$$\overline{\overline{Z}}^s \overline{x}^{(k)} = \overline{b} - \overline{\overline{Z}}^f \overline{x}^{(k-\frac{1}{2})} - \overline{\overline{Z}}^b \overline{x}^{(k)} \quad (5.14)$$

where $\overline{\overline{Z}}^f, \overline{\overline{Z}}^b, \overline{\overline{Z}}^s$ are the lower, upper and diagonal matrices of $\overline{\overline{Z}}$. In this context, the superscript f stands for forward scattering, b stands for backward scattering and s stands for self interaction. The computational cost of each FBM iteration is one matrix vector product. This comprises a half matrix-vector product to compute $\overline{\overline{Z}}^f \overline{x}^{(k-\frac{1}{2})}$ in the forward sweep and a half matrix-vector product to compute $\overline{\overline{Z}}^b \overline{x}^{(k)}$ in the backward sweep. The values of $\overline{\overline{Z}}^b \overline{x}^{(k-1)}$ in the forward sweep and $\overline{\overline{Z}}^f \overline{x}^{(k-\frac{1}{2})}$ in the backward sweep can be re-used from previous calculations.

5.2.2 Improved Forward Backward Method

The k^{th} estimate of \overline{x} in the forward backward method can be considered to equal to the exact value \overline{x} plus an error $\overline{\epsilon}^{(k)}$ as given by,

$$\overline{x}^{(k)} = \overline{x} + \overline{\epsilon}^{(k)} \quad (5.15)$$

It can be shown [73] that $\overline{\epsilon}^{(k)}$ evolves as

$$\overline{\epsilon}^{(k)} = \overline{\overline{M}} \overline{\epsilon}^{(k-1)} \quad (5.16)$$

where the iteration matrix $\overline{\overline{M}}$ for the forward backward method is defined as

$$\overline{\overline{M}} = \left(\overline{\overline{Z}}^s + \overline{\overline{Z}}^b \right)^{-1} \overline{\overline{Z}}^f \left(\overline{\overline{Z}}^s + \overline{\overline{Z}}^f \right)^{-1} \overline{\overline{Z}}^b \quad (5.17)$$

The error $\bar{\epsilon}^{(k)}$ can be written in terms of eigenvalues λ_n and eigenvectors \bar{e}_n of matrix \bar{M} respectively. Suppose the initial error can be represented as

$$\bar{\epsilon}^{(0)} = \sum_{n=1}^N \beta_n^{(0)} \bar{e}_n \quad (5.18)$$

where the coefficients $\beta_n^{(0)}$ are not explicitly known. Subsequent errors are thus given by

$$\bar{\epsilon}^{(k)} = \sum_{n=1}^N \lambda_n^k \beta_n^{(0)} \bar{e}_n = \sum_{n=1}^N \beta_n^{(k)} \bar{e}_n \quad (5.19)$$

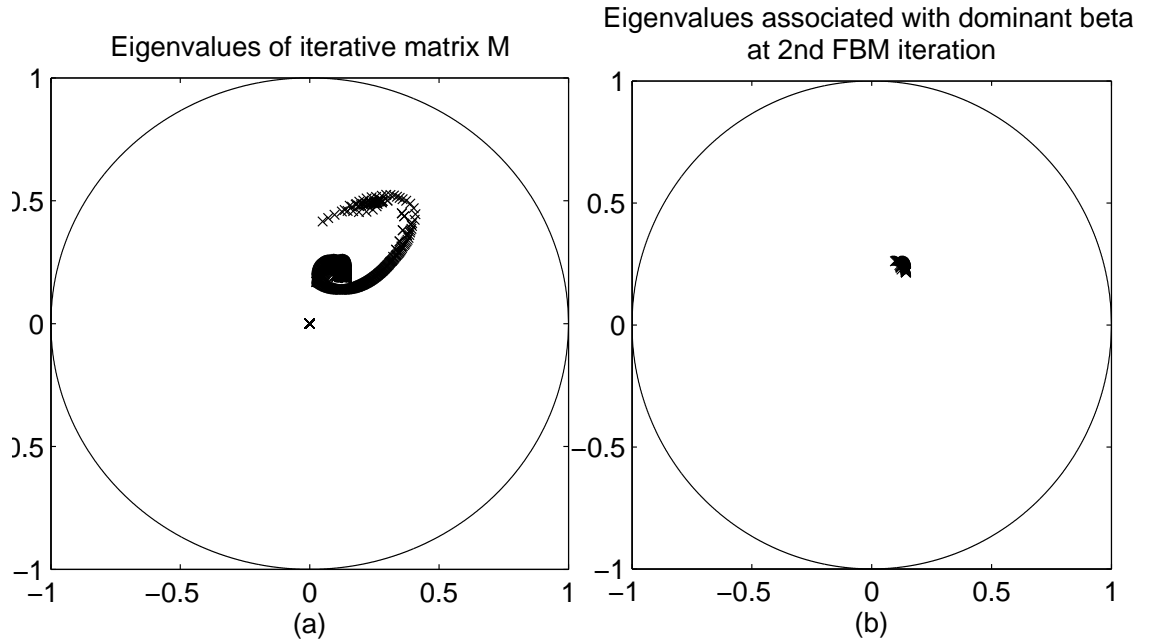


Figure 5.5: (a) Eigenvalues of iterative matrix M for random rough surface (b) Eigenvalues associated with dominant value of $\beta_n^{(2)}$, that is the dominant error coefficients after two iterations.

In order to motivate and explain the improved forward backward method a brief numerical experiment is described. A random surface was created using a Gaussian correlation function, with rms height $\sigma = 0.5\lambda$ and correlation length $l_c = 2.5\lambda$. The relative electric constant was $\epsilon_r = 20 + 4i$. The surface length was $L = 64\lambda$ and was sampled at 32 points per wavelength. Figure 5.5a shows the eigenvalues of the iteration matrix M while Figure 5.5b shows the eigenvalues associated with the largest $\beta_n^{(k)}$, namely the dominant error coefficients after k iterations of the FBM. In this particular example we used $k = 2$. The dominant β_n were chosen to be those that satisfied

$$|\beta_n| > \frac{1}{10} |\beta_{max}| \quad (5.20)$$

where β_{max} is the coefficient with the largest amplitude. Figure 5.5 demonstrates that the eigenvalues associated with the dominant error coefficients are approximately equal to some value $\lambda_{dom} \simeq 0.1 + 0.2i$. Denoting the set of indices of dominant error coefficients as Ω we can write

$$\bar{\epsilon}^{(k)} = \sum_{n=1}^N \lambda_n^k \beta_n^{(0)} \bar{e}_n \quad (5.21)$$

$$\simeq \lambda_{dom}^k \bar{v} \quad (5.22)$$

where

$$\bar{v} = \sum_{n \in \Omega} \beta_n^{(0)} \bar{e}_n \quad (5.23)$$

Equation 5.22 suggests that after a number of iterations $\bar{\epsilon}^{(k)}$ lies essentially in the direction \bar{v} and repeated application of the FBM will only succeed in scaling this vector by λ_{dom} each time. In such a situation, it is more useful to take an optimally sized step in the approximate direction of \bar{v} rather than waiting for the error to slowly decay due to repeated premultiplication of \bar{M} . In order to identify such situations the improved forward backward method (IFBM) examines the last three estimates of \bar{x} and computes the update correction used at the last two steps,

$$\bar{\zeta}^{(k-1)} = \bar{x}^{(k-1)} - \bar{x}^{(k-2)} \quad (5.24)$$

$$\bar{\zeta}^{(k)} = \bar{x}^{(k)} - \bar{x}^{(k-1)} \quad (5.25)$$

The direction of the last two update correction vectors can be compared by computing the parameter

$$\eta = \left| \hat{\zeta}^{(k)} \cdot \hat{\zeta}^{(k-1)} \right| \quad (5.26)$$

where $\hat{\zeta}$ is a unit vector in the direction of $\bar{\zeta}$. If η is above a defined threshold one concludes that $\hat{\zeta}^{(k)} \simeq \hat{\zeta}^{(k-1)} \simeq \hat{v}$ and the next estimate for \bar{x} therefore incorporates an optimized correction in the direction $\hat{\zeta}^{(k)}$. This next estimate is given by

$$\bar{x}^{(k)'} = \bar{x}^{(k)} + \alpha \hat{\zeta}^{(k)} \quad (5.27)$$

where α is chosen to minimize the norm of the residual error. To minimize α we write the residual

$$\bar{r}^{(k)'} = \bar{Z} \bar{x}^{(k)'} - \bar{b} \quad (5.28)$$

$$= \bar{r}^{(k)} + \alpha \bar{\chi}^{(k)} \quad (5.29)$$

where $\bar{\chi}^{(k)} = \bar{Z} \hat{\zeta}^{(k)}$ and $\bar{r}^{(k)} = \bar{Z} \bar{x}^{(k)} - \bar{b}$. Minimizing the norm of $\bar{r}^{(k)'}$ with respect to the

real and imaginary parts of α gives

$$\alpha^{re} = -\frac{\langle \bar{r}^{(k)}, \bar{\chi}^{(k)} \rangle + \langle \bar{\chi}^{(k)}, \bar{r}^{(k)} \rangle}{2\langle \bar{\chi}^{(k)}, \bar{\chi}^{(k)} \rangle} \quad (5.30)$$

$$\alpha^{im} = -i\frac{\langle \bar{\chi}^{(k)}, \bar{r}^{(k)} \rangle - \langle \bar{r}^{(k)}, \bar{\chi}^{(k)} \rangle}{2\langle \bar{\chi}^{(k)}, \bar{\chi}^{(k)} \rangle} \quad (5.31)$$

where $\langle \cdot, \cdot \rangle : \mathbb{V} \times \mathbb{V} \rightarrow \mathbb{C}$ represents the Hermitian inner product. It should be stressed that the correction step is not applied at every iteration, rather only when η as defined in equation (5.26) is greater than the pre-defined threshold. It should also be noted that equation (5.27) operates like the method of steepest descent and the occasional inclusion of this step means that the overall proposed method is no longer a purely stationary iterative technique.

5.2.3 Reduction of computational complexity of improvement step

The computational cost of the improvement step comprises the two matrix-vector products required to compute α and the half matrix-vector product required to update the values of the backward sweep. In this section, we demonstrate that the complexity of the improvement step can be reduced from 2.5 matrix-vector products to 1 matrix vector product and even to 0.5 matrix-vector products in situations where two improvement steps are required one immediately after the next. In order to compute α , it is necessary to compute the residual error $\bar{r}^{(k)}$ and $\bar{\chi}^{(k)}$. We have

$$\begin{aligned} \bar{r}^{(k)} &= \overline{\overline{Zx}}^{(k)} - \bar{b} \\ &= (\overline{\overline{Z^f}} + \overline{\overline{Z^s}} + \overline{\overline{Z^b}})\bar{x}^{(k)} - \bar{b} \\ &= (\overline{\overline{Z^s}} + \overline{\overline{Z^f}})\bar{x}^{(k)} + \overline{\overline{Z^b}}\bar{x}^{(k)} - b \end{aligned} \quad (5.32)$$

However it should be noted that $\overline{\overline{Z^b}}\bar{x}^{(k)}$ would have already been computed in the backward sweep of the FBM immediately preceding the improvement step. Therefore, it only remains to compute $(\overline{\overline{Z^s}} + \overline{\overline{Z^f}})\bar{x}^{(k)}$ which costs 0.5 matrix-vector product. Besides that, $\bar{\chi}^{(k)}$ is defined by

$$\bar{\chi}^{(k)} = \bar{Z}\hat{\zeta}^{(k)} \quad (5.33)$$

$$\begin{aligned} &= \frac{\bar{Z}(\bar{x}^{(k)} - \bar{x}^{(k-1)})}{\|\bar{\zeta}^{(k)}\|} \\ &= \frac{\bar{Z}\bar{x}^{(k)} - (\bar{Z}^s + \bar{Z}^f + \bar{Z}^b)\bar{x}^{(k-1)}}{\|\bar{\zeta}^{(k)}\|} \\ &= \frac{\bar{Z}\bar{x}^{(k)} - (\bar{Z}^s + \bar{Z}^f)\bar{x}^{(k-1)} - \bar{Z}^b\bar{x}^{(k-1)}}{\|\bar{\zeta}^{(k)}\|} \end{aligned} \quad (5.34)$$

$\bar{Z}\bar{x}^{(k)}$ is easily computed by adding \bar{b} to the previously computed $\bar{r}^{(k)}$. $\bar{Z}^b\bar{x}^{(k-1)}$ would have been computed in the previous backward sweep of FBM immediately preceding the improvement step and should be retained in memory. Only the value of $(\bar{Z}^s + \bar{Z}^f)\bar{x}^{(k-1)}$ remains to be calculated at a cost of 0.5 matrix-vector products. Hence a total of 1 matrix-vector product is required to perform the improvement step. If the improvement step is followed by another FBM iteration then the backward scattered field must be updated as

$$\begin{aligned} \bar{Z}^b\bar{x}^{(k)'} &= \bar{Z}^b(\bar{x}^{(k)} + \alpha\hat{\zeta}^{(k)}) \\ &= \bar{Z}^b\bar{x}^{(k)} + \alpha\bar{Z}^b\hat{\zeta}^{(k)} \end{aligned} \quad (5.35)$$

Both $\bar{Z}^b\bar{x}^{(k)}$ and $\bar{Z}^b\hat{\zeta}^{(k)}$ are computed in the previous step and so the results of these calculations can be reused in the computation of $\bar{Z}^b\bar{x}^{(k)'}$ which subsequently requires no further matrix-vector multiplications. In short, the computational cost of the improvement step is one matrix-vector product. Moreover, if improvement steps are performed in two adjacent FBM iterations, the computational cost of the second improvement step is only 0.5 matrix-vector products. This is the cost to compute $(\bar{Z}^s + \bar{Z}^f)\bar{x}^{(k)}$.

5.2.4 Spectral Acceleration of matrix-vector products

IFBM requires repeated computation of the matrix-vector products $\bar{Z}^f\bar{x}$ and $\bar{Z}^b\bar{x}$, which represent the forward and backward radiation produced by surface current elements. These computations can be accelerated using Spectral Acceleration [36, 37]. $\bar{Z}^f\bar{x}$ and $\bar{Z}^b\bar{x}$ represent fields produced by the source elements in the medium above and below the surface. Let these fields be denoted by $E^{f,(i)}$ and $E^{b,(i)}$ for $i = 1, 2$ where $i = 1$ refers to the medium above the surface and $i = 2$ refers to the medium below the surface. To apply SA $E^{f,(i)}$, $i = 1, 2$ is decomposed into a strong interactions part (comprising the N_s current elements immediately adjacent to the point of interest) and a weak interactions part (comprising all other points). Let $\vec{\rho}_m$ denote the centre of the m^{th} basis function domain. Then

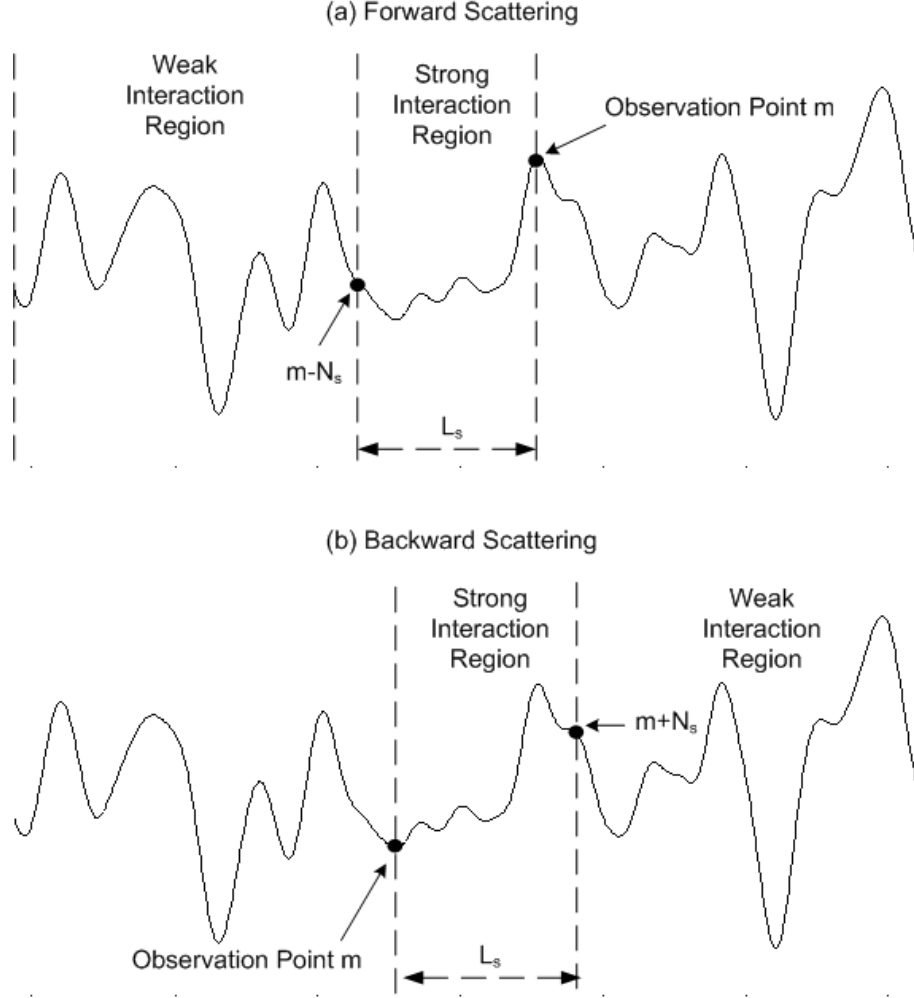


Figure 5.6: Strong and weak regions in the forward and backward scattering direction
 (a) Forward Scattering (b) Backward Scattering

$$E^{f,(1)}(\vec{\rho}_m) = \sum_{n=m-N_s}^{m-1} (Z_{a,mn}U_n + Z_{b,mn}\psi_n) + \sum_{n=1}^{m-N_s-1} (Z_{a,mn}U_n + Z_{b,mn}\psi_n) \quad (5.36)$$

$$E^{f,(2)}(\vec{\rho}_m) = \sum_{n=m-N_s}^{m-1} (Z_{c,mn}U_n + Z_{d,mn}\psi_n) + \sum_{n=1}^{m-N_s-1} (Z_{c,mn}U_n + Z_{d,mn}\psi_n) \quad (5.37)$$

In both equations the strong interactions component (the first sum) is computed by direct evaluation while the weak interaction part is accelerated using SA. Use of Spectral Acceleration reduces the complexity of a matrix-vector product from $\mathcal{O}(N^2)$ to $\mathcal{O}(N)$ [36, 37]. The spectral acceleration begins with the spectral integral representation of the Green's function, for $x - x' > 0$

$$G_\alpha(\bar{\rho}, \bar{\rho}') = -\frac{i}{4\pi} \int_{C_\phi} e^{-ik_\alpha[(x-x')\cos\phi+(y-y')\sin\phi]} d\phi, \quad \alpha = 0, 1 \quad (5.38)$$

where C_ϕ is the contour of integration in the complex space. x, y and x', y' denote the x - and y -coordinates of a field (receiving) point and a source point. Applying the gradient operator ∇ to $G(\bar{\rho}, \bar{\rho}')$, the spectral integral representation of $\nabla G(\bar{\rho}, \bar{\rho}')$ is obtained as

$$\begin{aligned} \hat{n}' \cdot \nabla G_\alpha(\bar{\rho}, \bar{\rho}') &= \left(-\frac{\frac{\partial f}{\partial x'}}{\sqrt{1 + \left(\frac{\partial f}{\partial x'}\right)^2}} \frac{\partial G_\alpha(\bar{\rho}, \bar{\rho}')}{\partial x'} + \frac{1}{\sqrt{1 + \left(\frac{\partial f}{\partial x'}\right)^2}} \frac{\partial G_\alpha(\bar{\rho}, \bar{\rho}')}{\partial y'} \right) \quad (5.39) \\ &= \frac{k_\alpha}{4\pi} \frac{1}{\sqrt{1 + \left(\frac{\partial f}{\partial x'}\right)^2}} \int_{C_\phi} \left(-\cos\phi \left(\frac{\partial f}{\partial x'}\right) + \sin\phi \right) e^{-ik_\alpha[(x-x')\cos\phi+(y-y')\sin\phi]} d\phi \end{aligned} \quad (5.40)$$

where \hat{n}' represents the uniform normal vector at a point on the surface and defined as

$$\hat{n}' = \left(-\frac{\frac{\partial f}{\partial x'}}{\sqrt{1 + \left(\frac{\partial f}{\partial x'}\right)^2}}, \frac{1}{\sqrt{1 + \left(\frac{\partial f}{\partial x'}\right)^2}} \right) \quad (5.41)$$

Substituting equation (5.38) and (5.40) into the weak interaction part of the forward scattering fields can be written as

$$\sum_{n=1}^{m-N_s-1} (Z_{a,mn}U_n + Z_{b,mn}\psi_n) = \frac{-i\Delta x}{4\pi} \int_{C_\delta} F_m^{(1)}(\phi) e^{-iky_m\sin\phi} d\phi \quad (5.42)$$

$$\sum_{n=1}^{m-N_s-1} (Z_{c,mn}U_n + Z_{d,mn}\psi_n) = \frac{-i\Delta x}{4\pi} \int_{C_\delta} F_m^{(2)}(\phi) e^{-iky_m\sin\phi} d\phi \quad (5.43)$$

where $F_m(\phi)$ can be calculated through a recursive procedure:

$$\begin{aligned} F_m^{(1)} &= F_{m-1}^{(1)} e^{-ik_0\Delta x\cos\phi} + \left[ik_0 \left(-\sin\phi + f'_{x_{m-N_s-1}} \cos\phi \right) \psi_{m-N_s-1} + U_{m-N_s-1} \right] \\ &\quad \times e^{-ik_0(N_s+1)\Delta x\cos\phi} e^{ik_0y_{m-N_s-1}\sin\phi} \end{aligned} \quad (5.44)$$

$$\begin{aligned} F_m^{(2)} &= F_{m-1}^{(2)} e^{-ik_1\Delta x\cos\phi} + \left[ik_1 \left(-\sin\phi + f'_{x_{m-N_s-1}} \cos\phi \right) \psi_{m-N_s-1} + U_{m-N_s-1} \right] \\ &\quad \times e^{-ik_1(N_s+1)\Delta x\cos\phi} e^{ik_1y_{m-N_s-1}\sin\phi} \end{aligned} \quad (5.45)$$

with $F_m(\phi) = 0$ for $m < N_s + 1$ in the forward sweep. A similar formulation can be derived to accelerate the calculation of the backward scattering components $E^{b,(i)}$, $i = 1, 2$. The great acceleration in computation is obtained by the recursive property of the radiation functions $F_m(\phi)$ where $F_m(\phi)$ is directly related to $F_{m-1}(\phi)$. Use of Spectral Acceleration reduces the complexity of a matrix-vector product from $\mathcal{O}(N^2)$ to $\mathcal{O}(N)$ [36]. In order to efficiently evaluate the double integrals involving the radiation functions $F_m(\phi)$, the original contour C_δ is deformed to yield a smaller integration interval requiring smaller sampling rates. The details of the deformations are described in [36].

5.2.5 Scattered wave, Normalised Bistatic Scattering Coefficient, Emissivity and Brightness temperature

Once found the surface fields $\psi(\bar{\rho})$ and their normal derivative components $\hat{n} \cdot \nabla \psi(\bar{\rho})$ are found can be used to computed the scattered wave

$$\psi_S(\bar{\rho}) = - \oint [\psi(\bar{\rho}') \hat{n}' \cdot \nabla G_0(\bar{\rho}, \bar{\rho}') - G_0(\bar{\rho}, \bar{\rho}') \hat{n}' \cdot \nabla \psi(\bar{\rho}')] dl' \quad (5.46)$$

Then the scattered far fields can be calculated by assuming $\bar{\rho}$ to be in the far field. For the scattering angle $\hat{k}_s = \sin\theta_s \hat{x} + \cos\theta_s \hat{z}$, we obtain

$$G_0(\bar{\rho}, \bar{\rho}') = \frac{1}{4i} \sqrt{\frac{2}{\pi k_0 |\bar{\rho} - \bar{\rho}'|}} e^{-ik_0(|\bar{\rho} - \bar{\rho}'| - \frac{\pi}{4})} \quad (5.47)$$

$$= \frac{1}{4i} \sqrt{\frac{2}{\pi k_0 |\bar{\rho}|}} e^{i\frac{\pi}{4}} e^{-ik_0|\bar{\rho}|} e^{ik_0 \hat{k}_s \cdot \bar{\rho}'} \quad (5.48)$$

and

$$\hat{n}' \cdot \nabla G_0(\bar{\rho}, \bar{\rho}') = \left(- \frac{\frac{\partial f}{\partial x'}}{\sqrt{1 + \left(\frac{\partial f}{\partial x'}\right)^2}} \frac{\partial G_\alpha(\bar{\rho}, \bar{\rho}')}{\partial x'} + \frac{1}{\sqrt{1 + \left(\frac{\partial f}{\partial x'}\right)^2}} \frac{\partial G_\alpha(\bar{\rho}, \bar{\rho}')}{\partial z'} \right) \quad (5.49)$$

$$= \frac{1}{\sqrt{1 + \left(\frac{\partial f}{\partial x'}\right)^2}} \frac{1}{4i} \sqrt{\frac{2}{\pi k_0 |\bar{\rho}|}} e^{i\frac{\pi}{4}} e^{-ik_0|\bar{\rho}|} e^{ik_0 \hat{k}_s \cdot \bar{\rho}'} ik_0 \left[- \left(\frac{\partial f}{\partial x'}\right) \sin\theta_s + \cos\theta_s \right] \quad (5.50)$$

Substituting (5.48) and (5.50) into (5.46), we have

$$\psi_S(\bar{\rho}) = \frac{1}{4i} \sqrt{\frac{2}{\pi k_0 |\bar{\rho}|}} e^{i\frac{\pi}{4}} e^{-ik_0|\bar{\rho}|} \psi_S^{(N)}(\theta_s) \quad (5.51)$$

where

$$\psi_S^{(N)}(\theta_s) = \int_{-\infty}^{+\infty} \left\{ U(x') - \psi(x') ik_0 \left[-\left(\frac{\partial f}{\partial x'} \right) \sin\theta_s + \cos\theta_s \right] \right\} e^{ik_0 \hat{k}_s \cdot \bar{\rho}'} dx' \quad (5.52)$$

The scattered fields are then used to compute the normalized bistatic scattering coefficient (NBSC)

$$\sigma(\theta_s) = \frac{|\psi_S(\bar{\rho})|^2}{2\eta_0 P^{inc}} \quad (5.53)$$

$$= \frac{\frac{1}{2\eta_0} \frac{1}{8\pi k_0 |\bar{\rho}|} |\psi_S^{(N)}(\theta_s)|^2}{P^{inc}} \quad (5.54)$$

where the power received by the rough surface P^{inc} can be shown to be [1]

$$P^{inc} = \frac{g}{2\eta_0} \sqrt{\frac{\pi}{2}} \cos\theta_i \left[1 - \frac{1 + 2 \tan^2 \theta_i}{2k_0^2 g^2 \cos^2 \theta_i} \right] \quad (5.55)$$

In the case of scattering from dielectric surfaces, the rule of energy conservation stating that the total of absorptivity $a(\theta_i)$ and reflectivity $r(\theta_i)$ is unity must hold [1]. The emissivity $e(\theta_i)$ is equal to the absorptivity then the emissivity of the surface is given by

$$e(\theta_i) = a(\theta_i) = 1 - r(\theta_i) \quad (5.56)$$

$$= 1 - \int_{-\frac{\pi}{2}}^{\frac{\pi}{2}} \sigma(\theta_s) d\theta_s \quad (5.57)$$

Then the brightness temperature T_B at the observation angle (θ_s, ϕ_s) can be obtained from the emissivity and physical temperature T of the surface

$$T_B(\theta_s, \phi_s) = e_\beta(\theta_i, \phi_i) T \quad (5.58)$$

5.2.6 Absorptivity, Reflectivity and Energy Conservation Check

Due to the dependence of the emissivity on the energy conservation, it is necessary to verify the energy conservation test to ensure that the emissivity predictions are reliable. The energy conservation test is performed by adding the value of absorptivity and reflectivity of the rough surface where the absorptivity $a(\theta_i)$ and reflectivity $r(\theta_i)$ can be computed in terms of the surface fields

$$a(\theta_i, \phi_i) = \frac{P_a}{P_{inc}} = \frac{-\int_S \hat{n} \cdot \frac{1}{2} \text{Re} [\bar{E} \times \bar{H}^*] dS}{2\eta_0 k_0 P_{inc}} \quad (5.59)$$

$$r(\theta_i, \phi_i) = \frac{P_r}{P_{inc}} = \frac{-\int_S \hat{n} \cdot \frac{1}{2} \text{Re} [\bar{E}_s \times \bar{H}_s^*] dS}{2\eta_0 k_0 P_{inc}} \quad (5.60)$$

where \bar{E} and \bar{H} are the total electrical and magnetic surface fields, respectively while the \bar{E}_s and \bar{H}_s are the surface scattered fields.

$$\bar{E} = \begin{cases} \psi \hat{z} & \text{for } TM^z \text{ case} \\ \frac{1}{i\omega\epsilon_0} \nabla \times \bar{H} & \text{for } TE^z \text{ case} \end{cases} \quad (5.61)$$

$$\bar{H} = \begin{cases} -\frac{1}{i\omega\mu_0} \nabla \times \bar{E} & \text{for } TM^z \text{ case} \\ \psi \hat{z} & \text{for } TE^z \text{ case} \end{cases} \quad (5.62)$$

Inserting these into (5.59) and (5.60) yields

$$a(\theta_i, \phi_i) = \frac{\text{Im} \int \psi(x) u^*(x) dx}{P_{inc}} \quad (5.63)$$

$$r(\theta_i, \phi_i) = \frac{\text{Im} \int \psi_s(x) u_s^*(x) dx}{P_{inc}} \quad (5.64)$$

where $u(x) = \sqrt{1 + \left(\frac{\partial f}{\partial x}\right)^2} (\hat{n} \cdot \nabla \psi)_{y=f(x)}$ and

$$\psi_s(x) = \psi(x) - \psi_{inc}(x) \quad (5.65)$$

$$u_s(x) = u(x) - u_{inc}(x) \quad (5.66)$$

5.3 Results

In this section the accuracy and convergence of the proposed IFBM-SA method is evaluated. A comparison of the IFBM-SA with the original FBM-SA and the fast numerical method introduced by Liu *et al* [62] is performed in terms of convergence rate and processing time required to achieve a desired residual error norm. Liu *et al* method which is also an integral equation based method can be considered as the combination of the BMIA/CAG and the FBM-SA to reduce their limitation and enhance the advantages. The surface was modelled as a soil surface with the average permittivity of $\epsilon_r = 20 + 4i$. The incidence angle is 60° and a tapering parameter of $g = L/4$ was used to remove edge effects. The threshold of η used in the simulation is $\eta_t = 0.5$. In order to illustrate the robustness of the proposed method, two types of surfaces were investigated, a Gaussian surface with a Gaussian correlation function and a Gaussian surface with an exponential correlation function. In addition, the robustness of the method against the roughness of the surface was also considered. In addition a comparison against measurement data is also performed.

5.3.1 Gaussian Correlation Function

Two distinct types of surface were considered. Slightly rough surfaces had rms height of $h_{rms} = 0.5\lambda$ and correlation length of $l_c = 2.5\lambda$. Very rough surfaces had rms height of $h_{rms} = 3.0\lambda$ and correlation length of $l_c = 3.75\lambda$. The surface length is $L = 256\lambda$ and 32 basis functions per wavelength were used giving a total number of unknowns equal to 16384. A normalized residual error was used to assess how accurate the solution was after iteration and was defined as

$$\log_{10} \frac{\|\overline{\overline{Zx}} - \overline{b}\|}{\|\overline{b}\|} \quad (5.67)$$

Each method was ran until it achieved a normalized residual error of less than 10^{-6} . Figure 5.7 compares the convergence rate of the FBM-SA and the IFBM-SA for one realisation of very rough surface profile as well as one realisation of slightly rough surface.

It is clear that the convergence rate of IFBM-SA is several times better than that of FBM-SA. Liu *et al*'s method [62] is based on the Generalized Minimal Residual Method with Fast Fourier Transform (GMRES-FFT) and Spectral Acceleration (SA) and is referred to in what follows as the reference method. In contrast IFBM-SA and FBM-SA are based on SA only. In order to make a comparison of the efficiency of IFBM-SA, the reference method and FBM-SA, a run time comparison is performed. Figure 6.11 shows the run time of IFBM-SA, the reference method and FBM-SA as a function of the number of unknowns. The rms height of the surface is $h_{rms} = 2.0\lambda$ and the correlation length is $l_c = 6.0\lambda$. It is

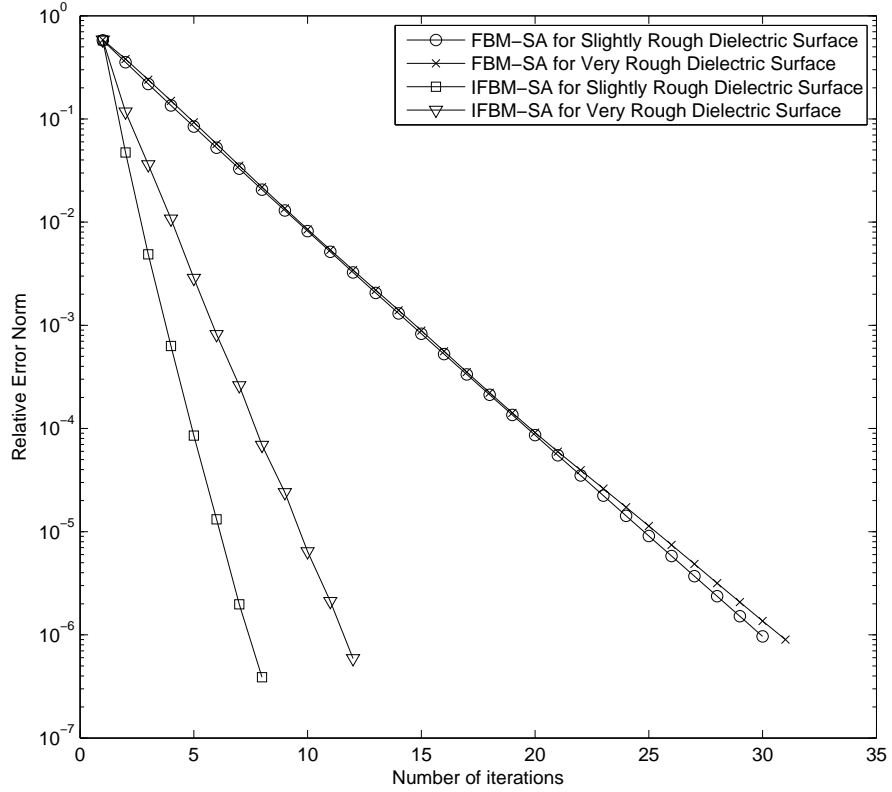


Figure 5.7: Comparison of residual error norm of proposed method (IFBM-SA) and FBM-SA

seen that the run time of IFBM-SA and FBM-SA is approximately doubled as the number of unknowns is doubled. However the run time of the reference method is approximately tripled as the number of unknowns is doubled. Therefore, the efficiency gain between the reference method and FBM-SA narrows as the number of unknowns increases. In contrast the efficiency gain of IFBM-SA over FBM-SA is maintained as the number of unknowns increases. Moreover, in the case of 65536 unknowns, the memory requirement of the reference method becomes too large for the system used to conduct the test. This is due to the fact that the near field size used in the reference method follows the guidelines of the BMIA/CAG method [62, 91] and equals one tenth of the overall length which becomes impractical as the problem size grows. It is clear that IFBM-SA outperforms the reference method and FBM-SA in terms of run time to achieve the same value of residual error norm and storage.

To investigate the methods further a detailed investigation of run time and number of iterations required to achieve a desired residual error norm was performed for rough surfaces with different rms heights and correlation lengths. The desired residual error norm was set to 10^{-4} which is a commonly used threshold for such convergence testing. The rms heights

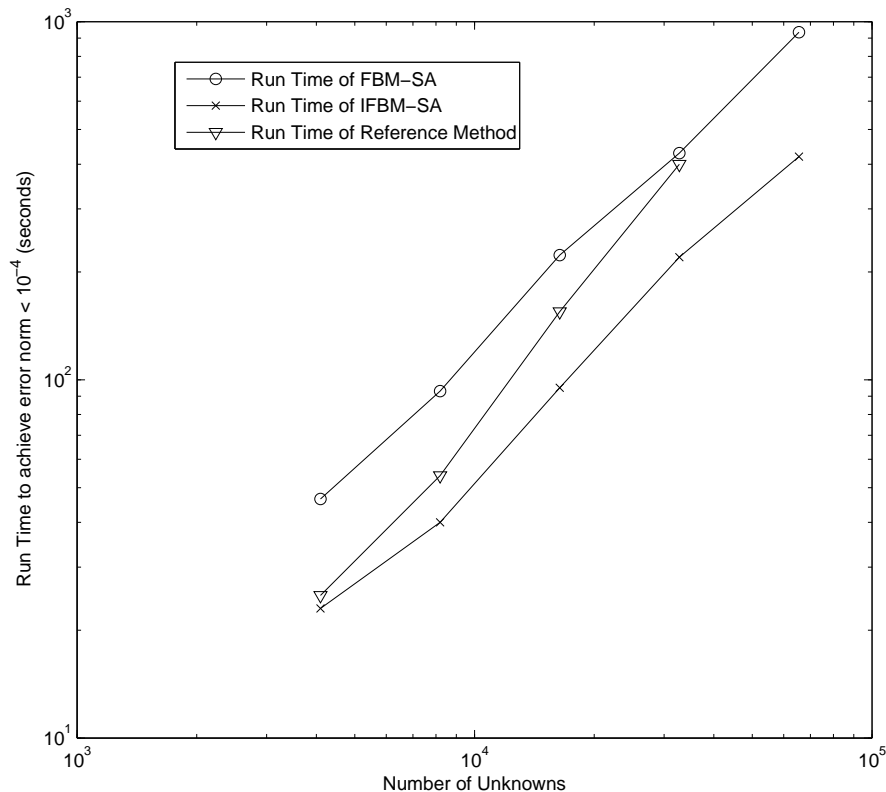


Figure 5.8: Comparison of Run Time between IFBM-SA, reference method and FBM-SA

are chosen as 0.5λ and 2.0λ while the ratios of rms height to correlation length vary from 0.2 to 0.6. The results are shown in Table 5.1 and Table 5.2 for TM^z polarization and TE^z polarization respectively. The number outside of the parentheses denotes the run time in seconds while the number inside the parentheses denotes the number of iterations required to achieve the desired residual error norm. For the case of TM^z polarization, as demonstrated in Table 5.1, IFBM-SA is approximately 3 times faster than FBM-SA and 1.5 times faster than the reference method when the ratio of rms height to correlation length is 0.2. The efficiency gain of IFBM-SA over FBM-SA is narrowed as the rms slope of the surface increases although IFBM-SA is still 1.5 times faster than FBM-SA in the worst case ($h_{rms}/l_c = 0.6$). We should note that the run time of the reference method is strongly affected by the correlation length of the surface. This is due to the dependence of the required number of GMRES iterations on the roughness of the surface. As the surface becomes rougher the number of GMRES iterations required increases, increasing the run-time [62].

For the case of TE^z polarization, as shown in Table 5.2, the run time of IFBM-SA is slightly better than FBM-SA while the reference method is slower than FBM-SA in most

Table 5.1: Average run time and number of iterations required to achieve residual error norm 10^{-4} . TM^z polarization. Autocorrelation function: Gaussian. Number of unknowns: 16384.

| h_{rms}/l_c | $h_{rms} = 0.5\lambda$ | | | $h_{rms} = 2.0\lambda$ | | |
|---------------|------------------------|--------|---------|------------------------|--------|---------|
| | IFBM-SA | Ref | FBM-SA | IFBM-SA | Ref | FBM-SA |
| 0.20 | 40(5) | 60(4) | 120(21) | 70(5) | 125(6) | 207(21) |
| 0.30 | 48(6) | 83(5) | 118(21) | 89(6) | 159(7) | 220(22) |
| 0.45 | 56(7) | 97(5) | 118(21) | 103(7) | 184(7) | 222(22) |
| 0.60 | 74(9) | 114(5) | 119(21) | 106(7) | 245(8) | 216(21) |

Table 5.2: Average run time and number of iterations required to achieve residual error norm 10^{-4} . TE^z polarization. Autocorrelation function: Gaussian. Number of unknowns: 16384.

| h_{rms}/l_c | $h_{rms} = 0.5\lambda$ | | | $h_{rms} = 2.0\lambda$ | | |
|---------------|------------------------|---------|--------|------------------------|---------|---------|
| | IFBM-SA | Ref | FBM-SA | IFBM-SA | Ref | FBM-SA |
| 0.20 | 41(5) | 138(11) | 52(9) | 73(5) | 117(9) | 100(10) |
| 0.30 | 41(5) | 230(17) | 52(9) | 74(5) | 167(12) | 103(10) |
| 0.45 | 42(5) | 370(27) | 53(9) | 73(5) | 264(18) | 93(9) |
| 0.60 | 41(5) | 874(56) | 52(9) | 74(5) | 331(21) | 84(8) |

of the investigated cases.

5.3.2 Exponential Correlation Function

In this scenario the method proposed by L. Tsang [92] was used to generate the exponential correlation surface. A real surface is generated with a discretization rate of 1000 points per wavelength. Then, the CSI (Cubic Spline Interpolation) surface is generated by sampling the real surface. The convergence of the bistatic scattering and emissivities for the real surfaces and CSI surfaces has been shown in [92]. In this work, the CSI surfaces are sampled from the real surface with a discretisation rate of 128 points per wavelength. The configurations of the simulation are similar to the case of Gaussian correlation.

Table 5.3: Average run time and number of iterations required to achieve residual error norm 10^{-4} . TM^z polarization. Autocorrelation function: Exponential. Number of unknowns: 25600.

| h_{rms}/l_c | $h_{rms} = 0.5\lambda$ | | | $h_{rms} = 2.0\lambda$ | | |
|---------------|------------------------|----------|---------|------------------------|---------|---------|
| | IFBM-SA | Ref | FBM-SA | IFBM-SA | Ref | FBM-SA |
| 0.20 | 232(17) | 695(10) | diverge | 629(29) | diverge | diverge |
| 0.30 | 281(20) | 779(10) | diverge | 771(34) | diverge | diverge |
| 0.45 | 275(19) | 1403(16) | diverge | 866(36) | diverge | diverge |
| 0.60 | 387(26) | 1888(20) | diverge | 931(38) | diverge | diverge |

Table 5.3 and 5.4 show the run time of the proposed method and FBM-SA for the case

Table 5.4: Average run time and number of iterations required to achieve residual error norm 10^{-4} . TE^z polarization. Autocorrelation function: Exponential. Number of unknowns: 25600.

| h_{rms}/l_c | $h_{rms} = 0.5\lambda$ | | | $h_{rms} = 2.0\lambda$ | | |
|---------------|------------------------|---------|---------|------------------------|---------|---------|
| | IFBM-SA | Ref | FBM-SA | IFBM-SA | Ref | FBM-SA |
| 0.20 | 189(13) | diverge | 266(23) | 308(14) | diverge | 566(28) |
| 0.30 | 209(14) | diverge | 278(23) | 362(15) | diverge | 596(30) |
| 0.45 | 214(14) | diverge | 280(23) | 424(18) | diverge | 670(33) |
| 0.60 | 228(14) | diverge | 284(23) | 458(18) | diverge | 721(34) |

of a Gaussian profile with exponential spectrum. It is clear that IFBM-SA is better than FBM-SA and the reference method in terms of robustness and run time.

5.3.3 Emissivity and energy conservation

In order to validate the simulation, the energy conservation test needs to be performed. The energy conservation test is performed by adding the value of absorptivity and reflectivity of the rough surface. In Table 5.5-5.8, the energy conservation check is performed for various surfaces roughness, permittivity and polarisation to illustrate that the energy conservation is obeyed. The energy conservation *in all cases* was better than 1.5% and the energy conservation for the TM^z cases are better than the TE^z cases. Table 5.6 and 5.7 show the emissivity and energy conservation for surfaces with soil moisture of 20% and 30.6% at 5GHz (C-band), corresponding to the equivalent relative permittivity of $9.09 + 1.43i$ and $15.57 + 3.71i$, respectively. As the soil moisture increases, the emissivities becomes smaller for both TM^z and TE^z cases because of the increasing contrast between two media. It is also shown in Table 5.7 and 5.8 that the rougher surfaces exhibit higher emissivities. This is due to the fact that the rough surfaces have a greater surface area and therefore absorb (then emit) more electromagnetic energy than the smooth surfaces.

Table 5.5: Emissivity of surfaces with Gaussian and Exponential Correlation Functions. $\sigma = 0.4\lambda$, $l_c = 2.0\lambda$

| Correlation Function | Polarization | Emissivities | Energy Cons |
|----------------------|--------------|--------------|-------------|
| Gaussian | TM^z | 0.4324 | 0.9992 |
| | TE^z | 0.6991 | 0.9993 |
| Exponential | TM^z | 0.5415 | 0.9990 |
| | TE^z | 0.8150 | 0.9927 |

Finally, in order to illustrate the accuracy of the IFBM-SA, the normalized bistatic scattering coefficient (NBSC) [1] obtained by the proposed method is compared to that obtained by Direct Matrix Inversion (DMI). Because of the memory requirement to apply DMI, the total number of unknowns chosen is 4096. The value of bistatic scattering coefficient was averaged over 100 realisations. Figure 5.9 shows that the averaged NBSCs obtained using

Table 5.6: Reflectivity, emissivity and energy conservation of rough surfaces. $h_{rms} = 0.2\lambda$. $l_c = 1.0\lambda$. $\epsilon_r = 9.09 + 1.43i$

| Polar | Incident angle | Emissivity | Energy Conservation |
|--------|----------------|------------|---------------------|
| TM^z | 30° | 0.7544 | 0.9972 |
| TM^z | 40° | 0.7348 | 0.9957 |
| TM^z | 50° | 0.6941 | 0.9952 |
| TE^z | 30° | 0.8665 | 0.9991 |
| TE^z | 40° | 0.8702 | 0.9939 |
| TE^z | 50° | 0.8822 | 0.9879 |

Table 5.7: Reflectivity, emissivity and energy conservation of rough surfaces. $h_{rms} = 0.2\lambda$. $l_c = 1.0\lambda$. $\epsilon_r = 15.57 + 3.71i$

| Polar | Incident angle | Emissivity | Energy Conservation |
|--------|----------------|------------|---------------------|
| TM^z | 30° | 0.6405 | 0.9962 |
| TM^z | 40° | 0.6173 | 0.9956 |
| TM^z | 50° | 0.5774 | 0.9929 |
| TE^z | 30° | 0.7807 | 0.9854 |
| TE^z | 40° | 0.7935 | 0.9879 |
| TE^z | 50° | 0.8088 | 0.9939 |

the proposed method completely overlap the NBSCs obtained by DMI for both cases of TM^z and TE^z polarisation.

5.3.4 Comparison against measurement data

In this section the brightness temperatures generated by the simulation are compared against the brightness temperature measurements of actual soil surfaces. The measurements were provided by Texas A&M university. The details of the experiment is given in [93]. The brightness temperatures were measured at the wavelength of $21.4cm$ (L-band) over a range of incident angles from 20° to 50° . The experiment was designed to record the full range of soil moisture variations for a typical agricultural field situation from fully saturated to completely dry. Three uniform soil surface with rectangular sections, $45m \times 15m$ were used in the experiment. Three sections were smoothed to an rms surface height of $0.88cm$ (slightly rough), $2.6cm$ (medium rough) and $4.3cm$ (rough). A soil moisture of $0.35 \text{ cm}^3/\text{cm}^3$ which corresponds to the equivalent relative permittivity of $19.2 + 2.41i$ [1] is used in the comparison. The physical temperature provided in the measurement is $300K$. Since the correlation length of the surfaces were not provided in the measurement data of Texas A&M university [93], the correlation length of $8.4cm$, given in the measurement of *Oh et al* [94, 63] is assumed in the simulation.

Table 5.9 and Table 5.10 show that the brightness temperatures generated by the pro-

Table 5.8: Reflectivity, emissivity and energy conservation of rough surfaces. $h_{rms} = 0.4\lambda$. $l_c = 1.0\lambda$. $\epsilon_r = 15.57 + 3.71i$

| Polar | Incident angle | Emissivity | Energy Conservation |
|--------|----------------|------------|---------------------|
| TM^z | 30° | 0.8233 | 0.9965 |
| TM^z | 40° | 0.8144 | 0.9970 |
| TM^z | 50° | 0.7783 | 0.9958 |
| TE^z | 30° | 0.9185 | 0.9887 |
| TE^z | 40° | 0.9098 | 0.9894 |
| TE^z | 50° | 0.9102 | 0.9890 |

Table 5.9: Comparison of brightness temperature between the proposed method and measurement data. Roughness of the surfaces: $\sigma = 0.88cm$. Permittivity: $\epsilon_r = 19.2 + 2.41i$.

| Polar. | Incident angle | Brightness temperature (K) | | | |
|--------|----------------|--------------------------------|-------------|------------|--------------|
| | | Simulation | Measurement | Difference | % Difference |
| TM^z | 20° | 155.85 | 167.56 | 11.71 | 6.98% |
| TM^z | 35° | 144.51 | 153.29 | 8.78 | 5.73% |
| TM^z | 50° | 124.07 | 135.73 | 11.65 | 8.58% |
| TE^z | 20° | 191.28 | 181.46 | 9.82 | 5.41% |
| TE^z | 35° | 209.37 | 196.83 | 12.54 | 6.37% |
| TE^z | 50° | 233.07 | 223.81 | 9.26 | 2.07% |

posed method are in sufficiently good agreement with the measurements for different polarizations, incident angles and roughnesses of the surface. The difference between the simulation and measurement is around $10K - 15K$, providing a sufficiently accuracy since the difference of the brightness temperatures between the various moistures of the surfaces can be more than $30K$, corresponding to an approximate difference of 0.1 in the emissivity as shown in Table 5.6 and Table 5.8. Note that the agreement with the measurement data can be improved by using the 2D surface scattering model, corresponding to the full 3D vector wave problem that will be investigated in Chapter 6.

5.4 Conclusions

In this chapter, a novel improved forward backward approach with spectral acceleration (IFBM-SA) has been developed in order to efficiently compute electromagnetic wave scattering from random rough surfaces. The accuracy and performance of the proposed method was evaluated and compared to those of the FBM-SA and the reference method. The numerical analysis suggested a better performance in terms of convergence rate and run time of IFBM-SA when compared to FBM-SA and the reference method. It also displayed greater robustness than the reference method and was capable of scaling to larger

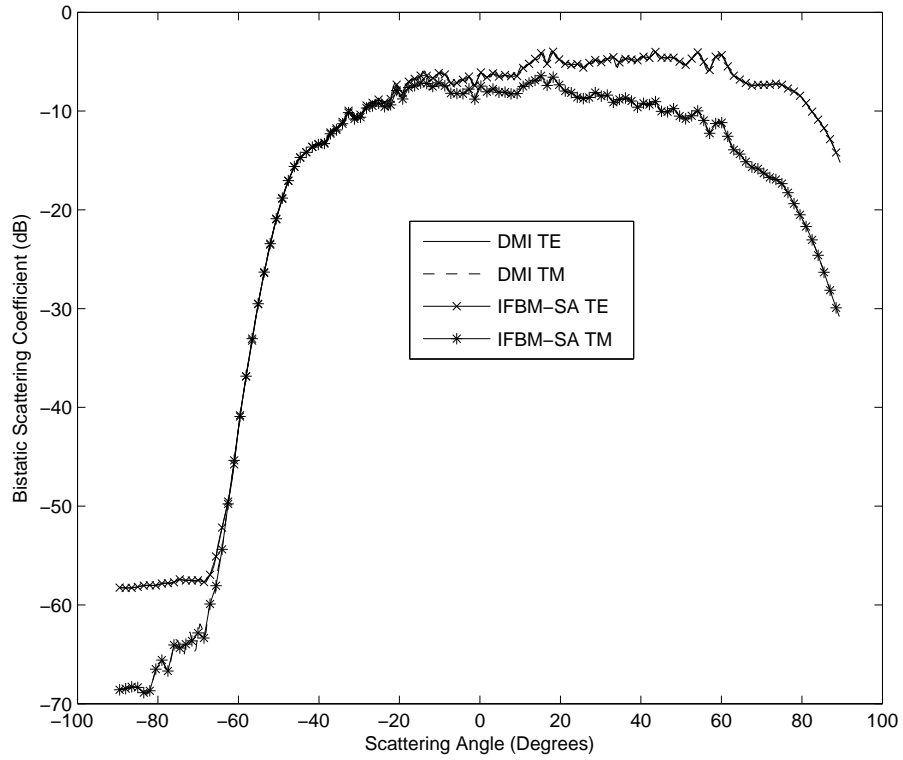


Figure 5.9: Comparison of averaged TE and TM NBSCs of proposed method and Direct Matrix Inversion (DMI) over 100 realisations. Relative dielectric constant: $\epsilon_r = 20 + 4i$. Autocorrelation function is Gaussian with Gaussian spectrum. $h_{rms} = 2.0\lambda$ and $l_c = 6.0\lambda$.

problems. The method presented is used to solve a problem involving scattering from a 1D surface. Application to compute the wave scattering from the 2D surfaces is presented in the next chapter.

Table 5.10: Comparison of brightness temperature between the proposed method and measurement data. Roughness of the surfaces: $\sigma = 2.60\text{cm}$. Permittivity: $\epsilon_r = 19.2 + 2.41i$.

| Polar. | Incident angle | Brightness temperature (K) | | | |
|--------|----------------|--------------------------------|-------------|------------|--------------|
| | | Simulation | Measurement | Difference | % Difference |
| TM^z | 20° | 185.34 | 203.40 | 18.06 | 8.87% |
| TM^z | 35° | 181.98 | 197.10 | 15.11 | 7.76% |
| TM^z | 50° | 156.96 | 172.68 | 15.71 | 9.10% |
| TE^z | 20° | 227.67 | 210.72 | 16.94 | 8.04% |
| TE^z | 35° | 229.08 | 215.85 | 13.2 | 6.11% |
| TE^z | 50° | 239.28 | 230.85 | 8.43 | 3.65% |

6 Block Forward Backward Method with Spectral Acceleration for Scattering from Two Dimensional Dielectric Random Rough Surfaces

6.1 Introduction

In chapter 5, a novel method has been proposed to compute the scattering from the one dimensional surfaces. However with the increasing computational capacities of modern computers and the two dimensional nature of real rough surfaces, the numerical computation of scattering from 2D surfaces, corresponding to the full 3D vector wave problem becomes more attractive. The full 3D vector wave scattering problem poses great computational challenge even for a medium-sized problem. Several methods have been proposed to reduce the computational complexity such as Fast Multipole Method (FMM), Sparse Matrix Canonical Grid (SMCG) method [63, 64, 66] which is an extension of the banded matrix iterative approach with canonical grid (BMIA/CAG) [56, 57, 58] for the full 3D problem, the physics-based two grid method (PBTG) [67], the multilevel UV partitioning method [69, 95] and various hybrid methods [96, 97]. These methods are based on Krylov-subspace iterative methods such as the conjugate gradient (CG) or Generalized Minimal Residual (GMRES) methods whose computational complexity is dominated by matrix-vector multiplications. The SMCG method proceeds by distinguishing weakly interacting (far) regions from strongly interacting (near) regions for each observation point. The scattered field computation from far regions represents the majority of the computational burden and can be accelerated by using the Fast Fourier Transform (FFT) while the near field interactions can be accelerated by the multilevel UV method. Another interesting technique is the 3D Forward Backward Method with Spectral Acceleration (FBM-SA) which is an extension of the 2D FBM-SA in computing the 3D wave scattering from 2D rough surfaces[70, 71]. The 3D FBM-SA was first developed for PEC surfaces [70] and then extended for impedance surfaces [71]. The 3D FBM-SA inherits the fast convergence and the extremely low computational complexity from the 2D FBM-SA. However it was found to diverge frequently if applied to compute 3D wave scattering from realistic 2D dielectric surfaces. In order to overcome this limitation of FBM-SA, the Block Forward

Backward Method where the discretisation points of the surfaces are collected into groups before iteratively solving for the surface fields is proposed. It is shown that the proposed method improves the scope of application of the Forward Backward Method, rendering it applicable to realistic profiles. In addition the Spectral Acceleration was also modified and adapted to the BFBM method to reduce the computational complexity of the proposed method.

The chapter is structured as follows. In Section 6.2, the integral equation formulation for the dielectric case and the proposed method is described. Numerical analysis of the computational efficiency and accuracy of the proposed method is investigated in Section 6.3. A comparison against the measurement data of the brightness temperature data is also given in this section. Section 6.4 concludes this chapter.

6.2 Block Forward Backward Method with Spectral Acceleration

6.2.1 Wave scattering by dielectric surfaces

Consider an incident electromagnetic wave, $\bar{E}_i(x, y, z)$ and $\bar{H}_i(x, y, z)$ impinging upon a 2D surface with a random height profile $z = f(x, y)$. The region above the surface (region 1) is free space and characterized by relative permittivity ϵ_0 and permeability μ_0 while the region below the surface (region 2) is characterized by permittivity $\epsilon_1 = \epsilon_r \epsilon_0$ and permeability $\mu_1 = \mu_r \mu_0$ where ϵ_r and μ_r are the relative permittivity and permeability of the lower medium. As discussed in Section 2.5, the fields in the upper medium and the lower medium satisfy the integral equations for the two media problem

$$0 = -\frac{\hat{n} \times \bar{E}(\bar{r})}{2} + \hat{n} \times \int i\omega\mu_1 \hat{n}' \times \bar{H}(\bar{r}') G_1 dS' - \hat{n} \times \left[\int \left\{ \hat{n}' \times \bar{E}(\bar{r}') \times \nabla' G_1 + (\hat{n}' \cdot \bar{E}(\bar{r}')) \frac{\epsilon_0}{\epsilon_1} \nabla' G_1 \right\} dS' \right] \quad (6.1)$$

$$\hat{n} \times \bar{H}^{inc}(\bar{r}) = \frac{\hat{n} \times \bar{H}(\bar{r})}{2} - \hat{n} \times \int i\omega\epsilon_0 \hat{n}' \times \bar{E}(\bar{r}') G_0 dS' - \hat{n} \times \left[\int \left\{ \hat{n}' \times \bar{H}(\bar{r}') \times \nabla' G_0 + (\hat{n}' \cdot \bar{H}(\bar{r}')) \nabla' G_0 \right\} dS' \right] \quad (6.2)$$

$$\hat{n} \cdot \bar{E}^{inc}(\bar{r}) = \frac{\hat{n} \cdot \bar{E}(\bar{r})}{2} + \hat{n} \cdot \int i\omega\mu_0 \hat{n}' \times \bar{H}(\bar{r}') G_0 dS' - \hat{n} \cdot \left[\int \left\{ \hat{n}' \times \bar{E}(\bar{r}') \times \nabla' G_0 + (\hat{n}' \cdot \bar{E}(\bar{r}')) \nabla' G_0 \right\} dS' \right] \quad (6.3)$$

$$0 = -\frac{\hat{n} \cdot \bar{H}(\bar{r})}{2} - \hat{n} \cdot \int i\omega\epsilon_1 \hat{n}' \times \bar{E}(\bar{r}') G_1 dS' - \hat{n} \cdot \left[\int \left\{ \hat{n}' \times \bar{H}(\bar{r}') \times \nabla' G_1 + (\hat{n}' \cdot \bar{H}(\bar{r}')) \nabla' G_1 \right\} dS' \right] \quad (6.4)$$

where $\bar{r} = x\hat{x} + y\hat{y} + z\hat{z}$ and $\bar{r}' = x'\hat{x} + y'\hat{y} + z'\hat{z}$ represent points on the surface. f denotes the Cauchy principal value integral performed over the boundary surface, \hat{n} and \hat{n}' are the normal vector at the field (receiving) and source point.

$$\hat{n} = \bar{n}/\|\bar{n}\| = \left(-\frac{\partial f}{\partial x}\hat{x} - \frac{\partial f}{\partial y}\hat{y} + \hat{z}\right) / \sqrt{1 + \left(\frac{\partial f}{\partial x}\right)^2 + \left(\frac{\partial f}{\partial y}\right)^2} \quad (6.5)$$

$$\hat{n}' = \bar{n}'/\|\bar{n}'\| = \left(-\frac{\partial f}{\partial x'}\hat{x}' - \frac{\partial f}{\partial y'}\hat{y}' + \hat{z}'\right) / \sqrt{1 + \left(\frac{\partial f}{\partial x'}\right)^2 + \left(\frac{\partial f}{\partial y'}\right)^2} \quad (6.6)$$

$G_0(\bar{r}, \bar{r}')$, $G_1(\bar{r}, \bar{r}')$ are the Green's functions of the upper and lower half-space respectively. They and their gradients can be written as.

$$G_0(\bar{r}, \bar{r}') = \frac{e^{-ik_0 R}}{4\pi R} \quad (6.7)$$

$$G_1(\bar{r}, \bar{r}') = \frac{e^{-ik_1 R}}{4\pi R} \quad (6.8)$$

$$\nabla' G_0(\bar{r}, \bar{r}') = (\bar{r} - \bar{r}') g_0(R) \quad (6.9)$$

$$\nabla' G_1(\bar{r}, \bar{r}') = (\bar{r} - \bar{r}') g_1(R) \quad (6.10)$$

where

$$g_0(R) = \frac{(1 + ik_0 R) e^{-ik_0 R}}{4\pi R^3} \quad (6.11)$$

$$g_1(R) = \frac{(1 + ik_1 R) e^{-ik_1 R}}{4\pi R^3} \quad (6.12)$$

$$R = |\bar{r} - \bar{r}'| = \sqrt{(x - x')^2 + (y - y')^2 + (z - z')^2} \quad (6.13)$$

The Method of Moments (MoM) is applied to solve the integral equation system by expanding the x, y components of $\hat{n} \times \bar{H}(\bar{r})$, $\hat{n} \times \bar{E}(\bar{r})$ and the normal components $\hat{n} \cdot \bar{H}(\bar{r})$, $\hat{n} \cdot \bar{E}(\bar{r})$ into a finite series using $N = N_x \times N_y$ pulse basis functions where N_x and N_y are the number of discretisation points in the x and y direction of the surface. Then the appropriate equation system is evaluated at the centres of the N basis function domains, resulting in a dense system of $6N$ linear equations whose explicit entries for the quantities are given in Section 2.5 and the Appendix C.

$$\begin{bmatrix} \overline{\overline{Z}}^{(11)} & \overline{\overline{Z}}^{(12)} & \overline{\overline{Z}}^{(13)} & \overline{\overline{Z}}^{(14)} & \overline{\overline{Z}}^{(15)} & \overline{\overline{Z}}^{(16)} \\ \overline{\overline{Z}}^{(21)} & \overline{\overline{Z}}^{(22)} & \overline{\overline{Z}}^{(23)} & \overline{\overline{Z}}^{(24)} & \overline{\overline{Z}}^{(25)} & \overline{\overline{Z}}^{(26)} \\ \overline{\overline{Z}}^{(31)} & \overline{\overline{Z}}^{(32)} & \overline{\overline{Z}}^{(33)} & \overline{\overline{Z}}^{(34)} & \overline{\overline{Z}}^{(35)} & \overline{\overline{Z}}^{(36)} \\ \overline{\overline{Z}}^{(41)} & \overline{\overline{Z}}^{(42)} & \overline{\overline{Z}}^{(43)} & \overline{\overline{Z}}^{(44)} & \overline{\overline{Z}}^{(45)} & \overline{\overline{Z}}^{(46)} \\ \overline{\overline{Z}}^{(51)} & \overline{\overline{Z}}^{(52)} & \overline{\overline{Z}}^{(53)} & \overline{\overline{Z}}^{(54)} & \overline{\overline{Z}}^{(55)} & \overline{\overline{Z}}^{(56)} \\ \overline{\overline{Z}}^{(61)} & \overline{\overline{Z}}^{(62)} & \overline{\overline{Z}}^{(63)} & \overline{\overline{Z}}^{(64)} & \overline{\overline{Z}}^{(65)} & \overline{\overline{Z}}^{(66)} \end{bmatrix} \begin{bmatrix} \overline{I}_x \\ \overline{I}_y \\ \overline{I}_n \\ \overline{F}_x \\ \overline{F}_y \\ \overline{F}_n \end{bmatrix} = \begin{bmatrix} \overline{0} \\ \overline{0} \\ \overline{I}_n^{inc} \\ \overline{F}_x^{inc} \\ \overline{F}_y^{inc} \\ \overline{0} \end{bmatrix} \quad (6.14)$$

where $\overline{\overline{Z}}^{(pq)}$, $p, q = 1, 2, \dots, 6$ are $N \times N$ impedance matrices, \overline{I}_n^{inc} , \overline{F}_x^{inc} and \overline{F}_y^{inc} are $N \times 1$ vectors whose elements are the incident fields at the matching points on the surface. \overline{I}_x , \overline{I}_y , \overline{I}_n , \overline{F}_x , \overline{F}_y and \overline{F}_n are $N \times 1$ vectors containing the unknown x, y components of the tangential fields and the normal component of the fields at the center of the basis functions.

$$F_{x,m} = S_{xy}(\bar{r}_m) \left[\hat{n} \times \overline{H}(\bar{r}_m) \right] \cdot \hat{x} \quad (6.15)$$

$$F_{y,m} = S_{xy}(\bar{r}_m) \left[\hat{n} \times \overline{H}(\bar{r}_m) \right] \cdot \hat{y} \quad (6.16)$$

$$F_{n,m} = S_{xy}(\bar{r}_m) \hat{n} \cdot \overline{H}(\bar{r}_m) \quad (6.17)$$

$$I_{x,m} = S_{xy}(\bar{r}_m) \left[\hat{n} \times \overline{E}(\bar{r}_m) \right] \cdot \hat{x} \quad (6.18)$$

$$I_{y,m} = S_{xy}(\bar{r}_m) \left[\hat{n} \times \overline{E}(\bar{r}_m) \right] \cdot \hat{y} \quad (6.19)$$

$$I_{n,m} = S_{xy}(\bar{r}_m) \hat{n} \cdot \overline{E}(\bar{r}_m) \quad (6.20)$$

where $S_{xy}(\bar{r}) = \sqrt{1 + \left(\frac{\partial f(x,y)}{\partial x} \right)^2 + \left(\frac{\partial f(x,y)}{\partial y} \right)^2}$.

6.2.2 Tapered incident wave

In order to reduce undesired edge effects, the incident wave centered in the direction $\hat{k}_i = \sin\theta_i \cos\phi_i \hat{x} + \sin\theta_i \sin\phi_i \hat{y} - \cos\theta_i \hat{z}$ where θ_i and ϕ_i denotes the incident polar and azimuthal angle respectively, is tapered so that the illuminated surface can be confined to the surface area $L_x \times L_y$ as shown in Figure 6.1. The incident fields are given as [1]

$$\overline{E}_i(\bar{r}) = \int_{-\infty}^{+\infty} \int_{-\infty}^{+\infty} e^{-i\bar{k} \cdot \bar{r}} E(k_x, k_y) \left[E_{TE} \hat{e} - E_{TM} \hat{h} \right] dk_x dk_y \quad (6.21)$$

$$\overline{H}_i(\bar{r}) = -\frac{1}{\eta} \int_{-\infty}^{+\infty} \int_{-\infty}^{+\infty} e^{-i\bar{k} \cdot \bar{r}} E(k_x, k_y) \left[E_{TE} \hat{h} + E_{TM} \hat{e} \right] dk_x dk_y \quad (6.22)$$

where $\bar{k} = k_x \hat{x} + k_y \hat{y} - k_z \hat{z}$, $\bar{r} = x \hat{x} + y \hat{y} + z \hat{z}$ and $\bar{r}' = x' \hat{x} + y' \hat{y} + z' \hat{z}$ represent a field point and a source point on the surface, respectively and two polarisation vectors are defined so that $\{\hat{k}_i, \hat{e}, \hat{h}\}$ forms an orthonormal system

$$\hat{e} = \frac{1}{k_\rho} (k_y \hat{x} - k_x \hat{y}) \quad (6.23)$$

$$\hat{h} = \frac{k_z}{k k_\rho} (k_x \hat{x} + k_y \hat{y}) + \frac{k_\rho}{k} \hat{z} \quad (6.24)$$

$$k_\rho = \sqrt{k_x^2 + k_y^2} \quad (6.25)$$

$$k_z = \sqrt{k^2 - k_\rho^2} \quad (6.26)$$

For the case of TE wave, $E_{TE} = 1$ and $E_{TM} = 0$ while for the TM wave $E_{TE} = 0$ and $E_{TM} = 1$. $E(k_x, k_y)$ is the tapered spectrum of the incident wave and given as

$$E(k_x, k_y) = \frac{1}{4\pi^2} \int_{-\infty}^{+\infty} \int_{-\infty}^{+\infty} e^{(-ik_x x - ik_y y)} e^{i(k_{ix} x + k_{iy} y)(1+\omega)} e^{-t} dx dy \quad (6.27)$$

where $k_{ix} = k \sin \theta_i \cos \phi_i$, $k_{iy} = k \sin \theta_i \sin \phi_i$, θ_i and ϕ_i refer to the polar and azimuthal angle of the incident waves, respectively. $t = t_x + t_y = x^2 + y^2 / g^2$ and

$$t_x = \frac{(\cos \theta_i \cos \phi_i x + \cos \theta_i \sin \phi_i y)}{g^2 \cos^2 \theta_i} \quad (6.28)$$

$$t_y = \frac{(-\sin \phi_i x + \cos \phi_i y)^2}{g^2} \quad (6.29)$$

$$\omega = \frac{1}{k^2} \left(\frac{2t_x - 1}{g^2 \cos^2 \theta_i} + \frac{2t_y}{g^2} \right) \quad (6.30)$$

The parameter g controls the tapering of the incident wave and the term ω and t are introduced to approximate the tapered wave solution [64]. Figure 6.2, Figure 6.3 and Figure 6.4 demonstrate the effect of changing the tapering parameter g on the incident wave.

6.2.3 Block Forward Backward Method

6.2.3.1 A brief review of Forward Backward Method for 2D Random Rough Surface Scattering

The unknowns on the left hand side of equation (6.14) is composed of N unknown x component of tangential magnetic fields, $F_x(\bar{r})$, followed by N unknown y component of

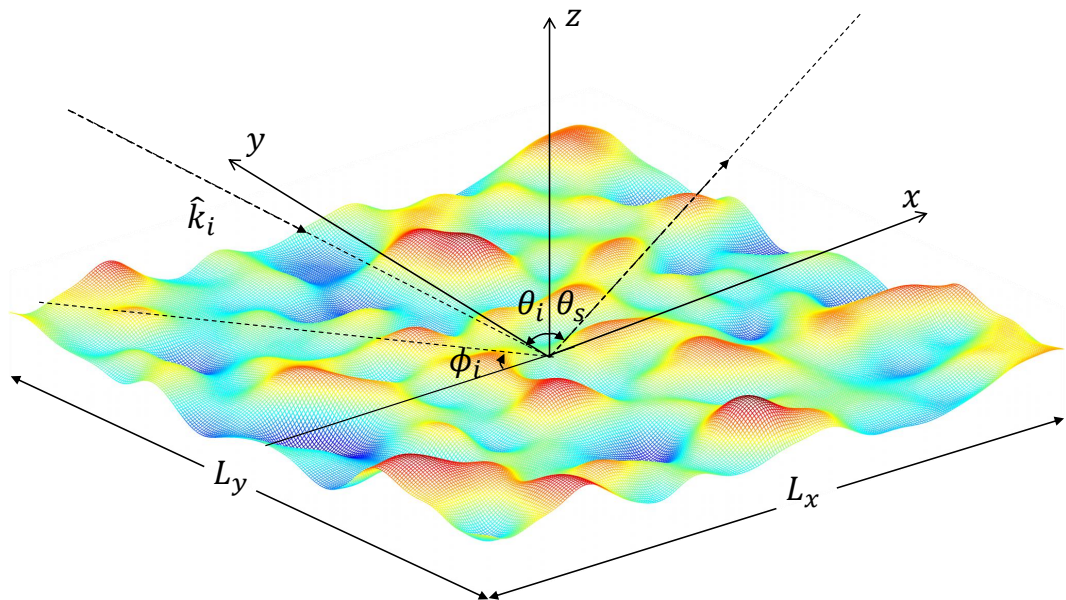


Figure 6.1: Two dimensional dielectric rough surface profile $z = f(x, y)$ illuminated by an incident wave

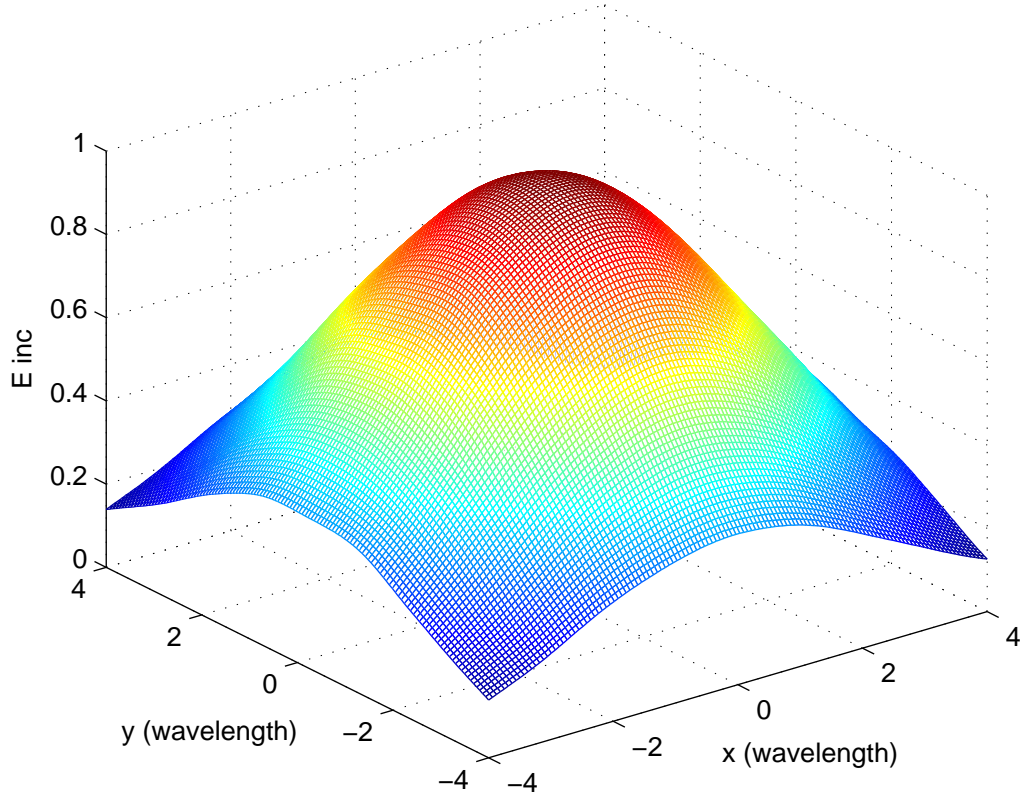


Figure 6.2: A $8\lambda \times 8\lambda$ surface illuminated by a tapered plane wave with $g = L_x/2 = L_y/2$.

tangential magnetic fields, $F_y(\vec{r})$, etc. In order to apply the Forward Backward Method, the unknowns are first interleaved. We recast equation (6.14) as

$$\overline{\overline{Z}}\overline{J} = \overline{V} \quad (6.31)$$

where

$$\overline{\overline{Z}}_{mn} = \begin{bmatrix} Z_{mn}^{(11)} & Z_{mn}^{(12)} & Z_{mn}^{(13)} & Z_{mn}^{(14)} & Z_{mn}^{(15)} & Z_{mn}^{(16)} \\ Z_{mn}^{(21)} & Z_{mn}^{(22)} & Z_{mn}^{(23)} & Z_{mn}^{(24)} & Z_{mn}^{(25)} & Z_{mn}^{(26)} \\ Z_{mn}^{(31)} & Z_{mn}^{(32)} & Z_{mn}^{(33)} & Z_{mn}^{(34)} & Z_{mn}^{(35)} & Z_{mn}^{(36)} \\ Z_{mn}^{(41)} & Z_{mn}^{(42)} & Z_{mn}^{(43)} & Z_{mn}^{(44)} & Z_{mn}^{(45)} & Z_{mn}^{(46)} \\ Z_{mn}^{(51)} & Z_{mn}^{(52)} & Z_{mn}^{(53)} & Z_{mn}^{(54)} & Z_{mn}^{(55)} & Z_{mn}^{(56)} \\ Z_{mn}^{(61)} & Z_{mn}^{(62)} & Z_{mn}^{(63)} & Z_{mn}^{(64)} & Z_{mn}^{(65)} & Z_{mn}^{(66)} \end{bmatrix} \quad (6.32)$$

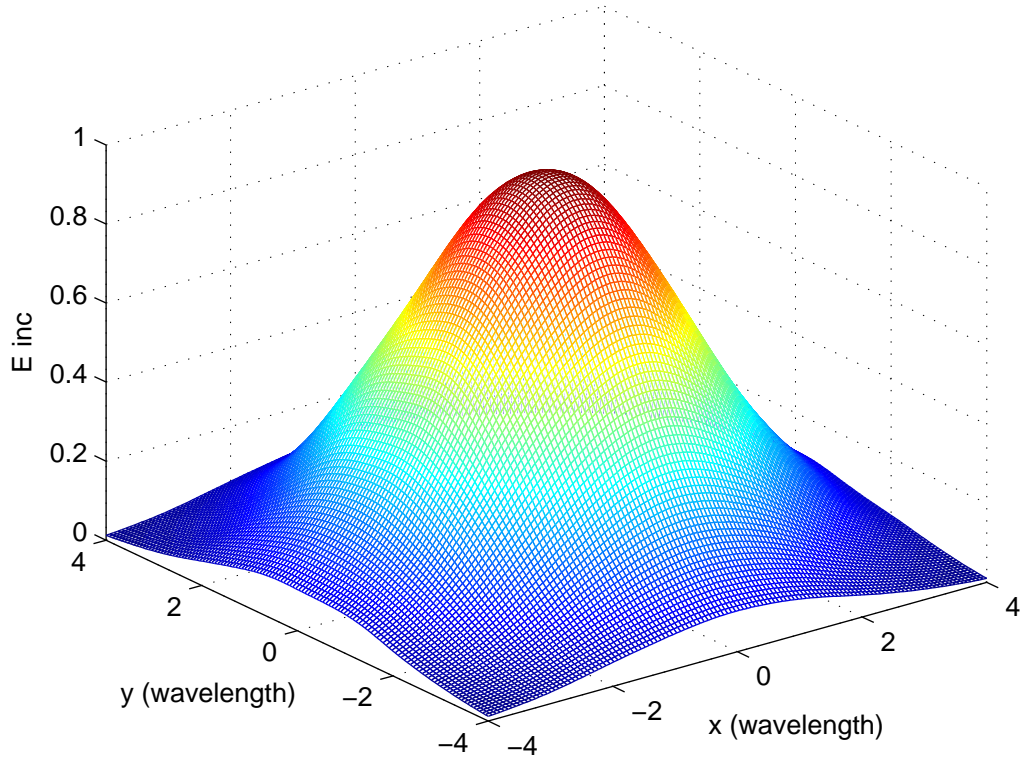


Figure 6.3: A $8\lambda \times 8\lambda$ surface illuminated by a tapered plane wave with $g = L_x/3 = L_y/3$.

$$\bar{\mathbf{J}}_m = \left[I_x(\bar{\mathbf{r}}_m) \quad I_y(\bar{\mathbf{r}}_m) \quad I_n(\bar{\mathbf{r}}_m) \quad F_x(\bar{\mathbf{r}}_m) \quad F_y(\bar{\mathbf{r}}_m) \quad F_n(\bar{\mathbf{r}}_m) \right]^T \quad (6.33)$$

$$\bar{\mathbf{V}}_m = \left[0 \quad 0 \quad I_n^{inc}(\bar{\mathbf{r}}_m) \quad F_x(\bar{\mathbf{r}}_m) \quad F_y(\bar{\mathbf{r}}_m) \quad 0 \right]^T \quad (6.34)$$

Implementing a forward-backward method involves sequentially updating the unknowns, first in a forward sweep and then a backward sweep as shown in Figure 6.5. For the forward sweep as illustrated in Figure 6.5a, the induced currents are updated from bottom to top and then left to right. For the backward sweep as illustrated in Figure 6.5b, the induced currents are updated from top to bottom and then right to left. At each receiving element, the currents generated by the scattered fields from other source points need to be computed. We solve

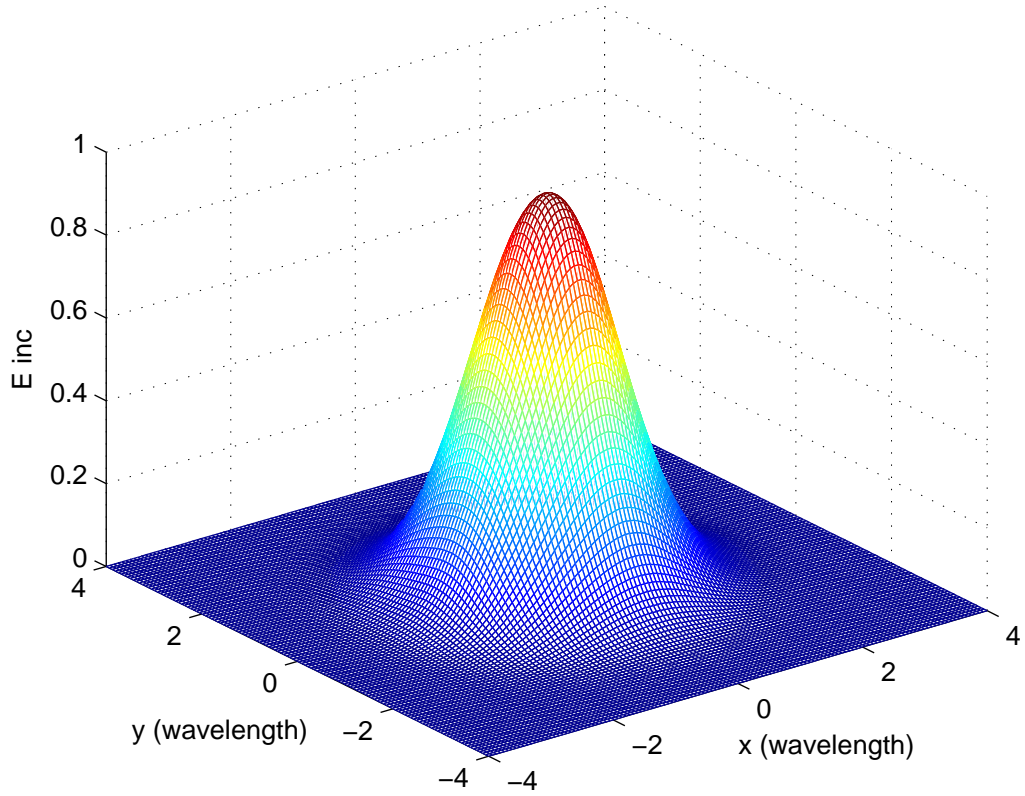


Figure 6.4: A $8\lambda \times 8\lambda$ surface illuminated by a tapered plane wave with $g = L_x/6 = L_y/6$.

$$\bar{\bar{Z}}_{mm} \bar{J}_m^{(k+\frac{1}{2})} = \bar{V}_m - \bar{l}_m^{(k+\frac{1}{2})} - \bar{u}_m^{(k)} \quad (6.35)$$

$$\text{for } m = 1 \dots N$$

$$\bar{\bar{Z}}_{mm} \bar{J}_m^{(k+1)} = \bar{V}_m - \bar{l}_m^{(k+\frac{1}{2})} - \bar{u}_m^{(k+1)} \quad (6.36)$$

$$\text{for } m = N \dots 1$$

where $\bar{l}_m^{(k)}$ and $\bar{u}_m^{(k)}$ are the fields scattered in the forward and backward directions respectively to discretisation centre \vec{r}_m at the k^{th} iteration.

$$\bar{l}_m^{(k)} = \sum_{n < m} \bar{\bar{Z}}_{mn} \bar{J}_n^{(k)} \quad (6.37)$$

$$\bar{u}_m^{(k)} = \sum_{n > m} \bar{\bar{Z}}_{mn} \bar{J}_n^{(k)} \quad (6.38)$$

Mathematically the k^{th} iteration can be written in the matrix form

$$\overline{\overline{Z}}^s \mathbf{J}^{(k-\frac{1}{2})} = \overline{\overline{b}} - \overline{\overline{Z}}^f \mathbf{J}^{(k-\frac{1}{2})} - \overline{\overline{Z}}^b \mathbf{J}^{(k-1)} \quad (6.39)$$

$$\overline{\overline{Z}}^s \mathbf{J}^{(k)} = \overline{\overline{b}} - \overline{\overline{Z}}^f \mathbf{J}^{(k-\frac{1}{2})} - \overline{\overline{Z}}^b \mathbf{J}^{(k)} \quad (6.40)$$

where $\overline{\overline{Z}}^f, \overline{\overline{Z}}^b, \overline{\overline{Z}}^s$ are the block lower, upper and diagonal matrices of $\overline{\overline{Z}}$. In this context, the superscript f stands for forward scattering, b stands for backward scattering and s stands for self interaction.

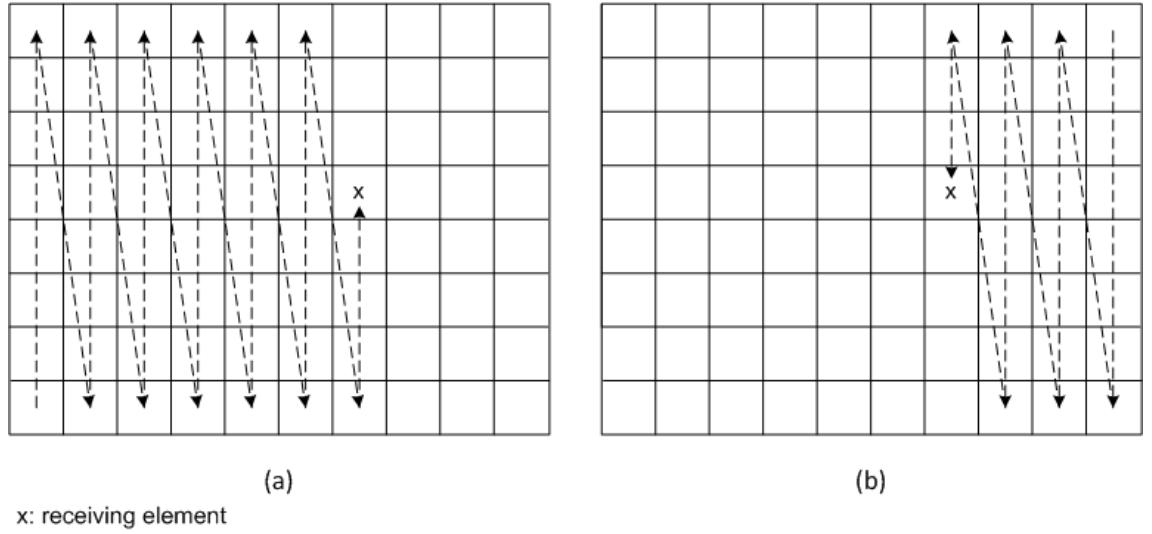


Figure 6.5: Forward sweep (FS) and backward sweep (BS) of the Forward Backward Method (FBM)

6.2.3.2 Block Forward Backward Method for 2D Random Rough Surface Scattering

The Block Forward Backward Method (BFBM) extends the scope of the Forward Backward Method by collecting the points on the strips into groups. The 2D surface is considered to consist of M non-overlapping groups, each group has $\frac{6N}{M}$ pulse basis function domain defined in it as shown in Figure 6.6. The currents on each group are computed simultaneously instead of being computed iteratively and the currents are updated in the direction of wave propagation, from the left to the right of the surface. The forward and backward sweep of group G_i is described in equations

$$\overline{\overline{Z}}_{ii} \overline{\overline{J}}_i^{(k+\frac{1}{2})} = \overline{\overline{V}}_i - \overline{\overline{l}}_i^{(k+\frac{1}{2})} - \overline{\overline{u}}_i^{(k)} \quad (6.41)$$

for $i = 1 \dots M$

$$\overline{\overline{Z}}_{ii} \overline{\overline{J}}_i^{(k+1)} = \overline{\overline{V}}_i - \overline{\overline{l}}_i^{(k+\frac{1}{2})} - \overline{\overline{u}}_i^{(k+1)} \quad (6.42)$$

for $i = M \dots 1$

where M is the number of groups, $\overline{\overline{l}}_i^{(k)}$ and $\overline{\overline{u}}_i^{(k)}$ are the vectors containing radiations scattered in the forward and backward directions respectively to group G_i at the k^{th} iteration, $\overline{\overline{V}}_i$ is the incident field on group G_i and $\overline{\overline{J}}_i$ are the unknown surface electric and magnetic components on group G_i .

$$\overline{\overline{l}}_i^{(k)} = \sum_{j < i} \overline{\overline{Z}}_{ij} \overline{\overline{J}}_j^{(k)} \quad (6.43)$$

$$\overline{\overline{u}}_i^{(k)} = \sum_{j > i} \overline{\overline{Z}}_{ij} \overline{\overline{J}}_j^{(k)} \quad (6.44)$$

The k^{th} iteration can be equivalently written in the matrix form

$$\overline{\overline{Z}}_{s,g} \overline{\overline{J}}^{(k-\frac{1}{2})} = \overline{\overline{V}} - \overline{\overline{Z}}_{f,g} \overline{\overline{J}}^{(k-\frac{1}{2})} - \overline{\overline{Z}}_{b,g} \overline{\overline{J}}^{(k-1)} \quad (6.45)$$

$$\overline{\overline{Z}}_{s,g} \overline{\overline{J}}^{(k)} = \overline{\overline{V}} - \overline{\overline{Z}}_{f,g} \overline{\overline{J}}^{(k-\frac{1}{2})} - \overline{\overline{Z}}_{b,g} \overline{\overline{J}}^{(k)} \quad (6.46)$$

where $\overline{\overline{Z}}_{f,g}, \overline{\overline{Z}}_{b,g}, \overline{\overline{Z}}_{s,g}$ are the block lower, upper and diagonal matrices of $\overline{\overline{Z}}$. Ideally from a computational perspective, the inverses of the diagonal blocks $\overline{\overline{Z}}_{s,g}^{-1}$ should be pre-computed and stored. The implementation of the BFBM algorithm is equivalent to implementation of standard FBM on a pre-conditioned $\overline{\overline{A}}$ matrix where the pre-conditioner is composed of the diagonal blocks $\overline{\overline{Z}}_{s,g}^{-1}$. The BFBM requires the repeated computation of the matrix-vector products $\overline{\overline{Z}}_{f,g} \overline{\overline{J}}^{(k)}$ and $\overline{\overline{Z}}_{b,g} \overline{\overline{J}}^{(k)}$ which are the forward and backward radiations produced by surface current elements. These computations can be accelerated using Spectral Acceleration.

6.2.4 Spectral Acceleration (SA) for 2D lossy surface

The matrix-vector products in the forward and backward sweep of the BFBM require a computational cost of $\mathcal{O}(N^2)$ for each iteration. In order to accelerate the BFBM, the Spectral Acceleration is applied to lower the computational cost to $\mathcal{O}(N)$. In addition, the memory storage is also reduced to order $\mathcal{O}(N)$. For convenience, only the spectral

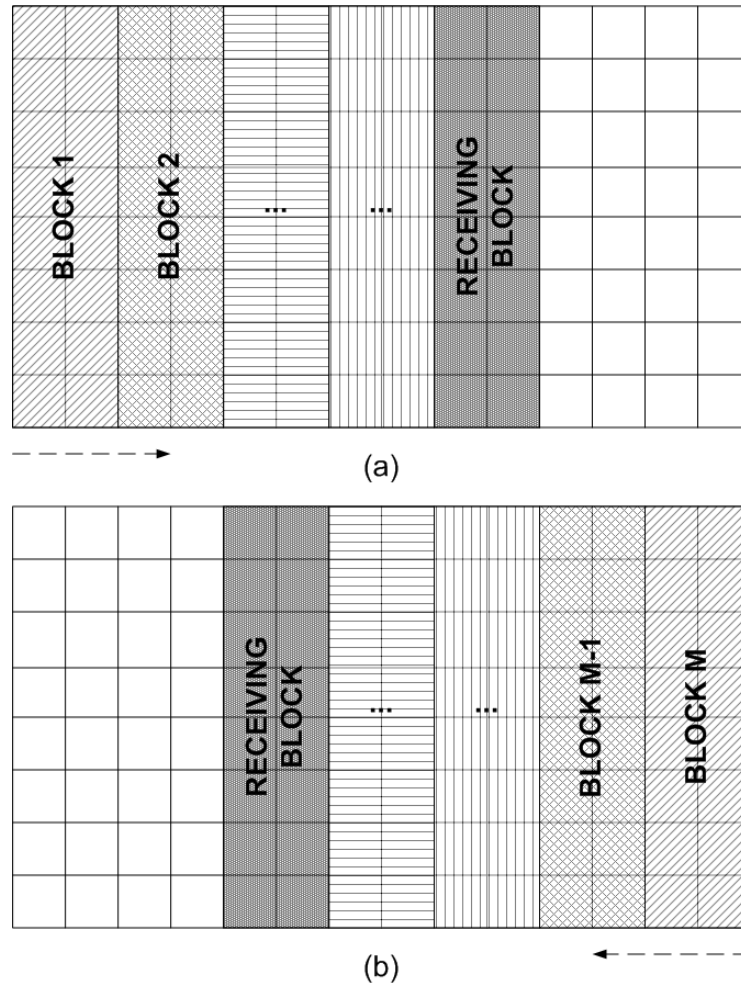


Figure 6.6: Forward sweep (FS) and backward sweep (BS) of the Block Forward Backward Method (BFBM)

acceleration process for the forward propagation sweep is described. The spectral acceleration process for the backward propagation sweep can be obtained using the same procedure. To apply the SA, the scattered contributions from the source points to the field point are decomposed into a strongly interacting part (comprising the $N_{s,x} \times N_y$ elements immediately adjacent to the receiving point. Note that $N_{s,x}$ denotes the size of the strong interactions region in the x -direction) and a weakly interacting part, as illustrated in Figure 6.7. Let these scattered components be denoted by $\bar{E}^{f,(i)}$ and $\bar{E}^{b,(i)}$ for $i = 1, 2, \dots, 6$ where $i = 1, 2, 3$ refer to the medium above the surface and $i = 4, 5, 6$ refer to the medium below the surface. Applying this decomposition the forward scattered components can be written as

$$\bar{E}^{f,(i)}(\bar{r}) = \bar{E}_s^{f,(i)}(\bar{r}) + \bar{E}_w^{f,(i)}(\bar{r}) \quad (6.47)$$

where

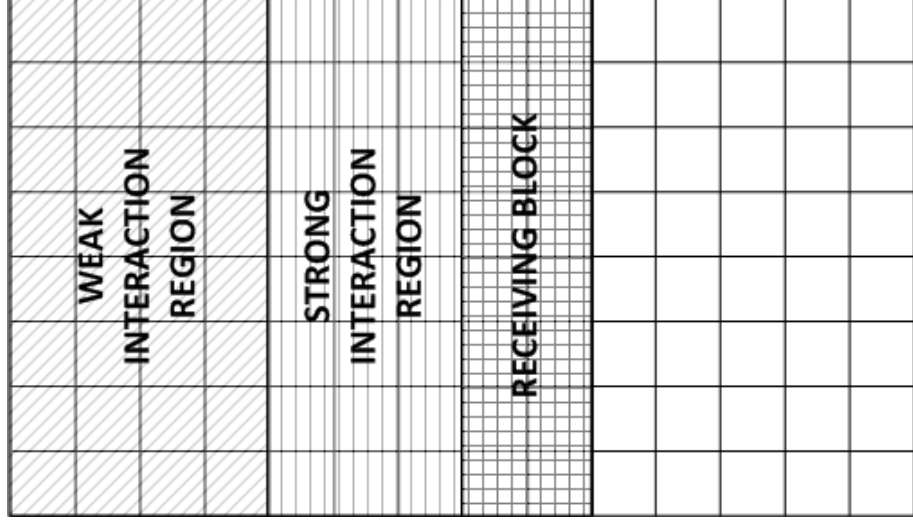


Figure 6.7: Strong and weak regions in the FS direction

$$\begin{aligned} \overline{E}_s^{f,(1,2)}(\bar{r}) = & -\hat{n} \times \int_{S_{xy,s}^f} \left\{ i\omega \hat{n}' \times \overline{E}(\bar{r}') \epsilon_0 G_0 \right. \\ & \left. + \hat{n}' \times \overline{H}(\bar{r}') \times \nabla' G_0 + (\hat{n}' \cdot \overline{H}(\bar{r}')) \nabla' G_0 \right\} dS' \end{aligned} \quad (6.48)$$

$$\begin{aligned} \overline{E}_w^{f,(1,2)}(\bar{r}) = & -\hat{n} \times \int_{S_{xy,w}^f} \left\{ i\omega \hat{n}' \times \overline{E}(\bar{r}') \epsilon_0 G_0 \right. \\ & \left. + \hat{n}' \times \overline{H}(\bar{r}') \times \nabla' G_0 + (\hat{n}' \cdot \overline{H}(\bar{r}')) \nabla' G_0 \right\} dS' \end{aligned} \quad (6.49)$$

$$\begin{aligned} \overline{E}_s^{f,(3)}(\bar{r}) = & \hat{n} \cdot \int_{S_{xy,s}^f} \left\{ i\omega \hat{n}' \times \overline{H}(\bar{r}') \mu_0 G_0 \right. \\ & \left. - \hat{n}' \times \overline{E}(\bar{r}') \times \nabla' G_0 - (\hat{n}' \cdot \overline{E}(\bar{r}')) \nabla' G_0 \right\} dS' \end{aligned} \quad (6.50)$$

$$\begin{aligned} \overline{E}_w^{f,(3)}(\bar{r}) = & \hat{n} \cdot \int_{S_{xy,w}^f} \left\{ i\omega \hat{n}' \times \overline{H}(\bar{r}') \mu_0 G_0 \right. \\ & \left. - \hat{n}' \times \overline{E}(\bar{r}') \times \nabla' G_0 - (\hat{n}' \cdot \overline{E}(\bar{r}')) \nabla' G_0 \right\} dS' \end{aligned} \quad (6.51)$$

The FS surface S_{xy}^f is decomposed into the FS strong $S_{xy,s}^f$ and weak $S_{xy,w}^f$ regions, $S_{xy}^f = S_{xy,s}^f + S_{xy,w}^f$. The strong interactions component $\overline{E}_s^{f,(i)}(\bar{r})$ is computed in the conventional manner and the SA algorithm is applied to compute the weak interactions component $\overline{E}_w^{f,(i)}(\bar{r})$. The spectral acceleration begins with the spectral integral representation of the Green's function, for $x - x' > 0$

$$G_{0,1}(\bar{r}, \bar{r}') = -\frac{i}{8\pi^2} \int_{C_{k_z}} \int_{C_{k_y}} \frac{e^{-i\bar{k}\cdot\bar{R}}}{k_{x0,1}} dk_z dk_y \quad (6.52)$$

where C_{k_y} and C_{k_z} are the contour of integration in the complex k_y and k_z space, respectively and

$$\bar{k} = k_x \hat{x} + k_y \hat{y} + k_z \hat{z} \quad (6.53)$$

$$\bar{R} = \bar{r} - \bar{r}' = (x - x') \hat{x} + (y - y') \hat{y} + (z - z') \hat{z} \quad (6.54)$$

$$k_{x0,1} = \left(k_{0,1}^2 - k_y^2 - k_z^2\right)^{\frac{1}{2}} \quad (6.55)$$

x and x' denotes the x -coordinates of a field (receiving) point and a source point respectively. Applying the gradient operator ∇ to $G(\bar{r}, \bar{r}')$, the spectral integral representation of $\nabla G(\bar{r}, \bar{r}')$ is obtained as

$$\nabla G_{0,1}(\bar{r}, \bar{r}') = -\frac{1}{8\pi^2} \int_{C_{k_z}} \int_{C_{k_y}} \frac{\bar{k} e^{-i\bar{k}\cdot\bar{R}}}{k_{x0,1}} dk_z dk_y. \quad (6.56)$$

Substituting equation (6.56) into (6.49) and (6.51), we obtain

$$\overline{E}_w^{f,(1,2)}(\bar{r}) = -\frac{1}{8\pi^2} \hat{n} \times \int_{C_{k_z}} \int_{C_{k_y}} \frac{F^{(1)}(\bar{r}, k_z, k_y)}{k_{x0}} dk_z dk_y, \quad (6.57)$$

$$\overline{E}_w^{f,(3)}(\bar{r}) = \frac{1}{8\pi^2} \hat{n} \cdot \int_{C_{k_z}} \int_{C_{k_y}} \frac{F^{(3)}(\bar{r}, k_z, k_y)}{k_{x0}} dk_z dk_y \quad (6.58)$$

where the radiation functions $F(\bar{r}, k_z, k_y)$ are defined as

$$F^{(1)}(\bar{r}, k_z, k_y) = \oint_{S_{xy,w}^f} \left[\omega \epsilon_0 \hat{n}' \times \overline{E}(\bar{r}') + \bar{k} \times \hat{n}' \times \overline{H}(\bar{r}') - \bar{k} (\hat{n}' \cdot \overline{H}(\bar{r}')) \right] e^{i\bar{k}\cdot\bar{R}} dS' \quad (6.59)$$

$$F^{(3)}(\bar{r}, k_z, k_y) = \oint_{S_{xy,w}^f} \left[\omega \mu_0 \hat{n}' \times \overline{H}(\bar{r}') - \bar{k} \times \hat{n}' \times \overline{E}(\bar{r}') + \bar{k} (\hat{n}' \cdot \overline{E}(\bar{r}')) \right] e^{i\bar{k}\cdot\bar{R}} dS' \quad (6.60)$$

The great acceleration in computation is obtained by the recursive property of the radiation functions $F(\bar{r}, k_z, k_y)$. The computation of radiation functions $F(\bar{r}, k_z, k_y)$ is divided into two cases:

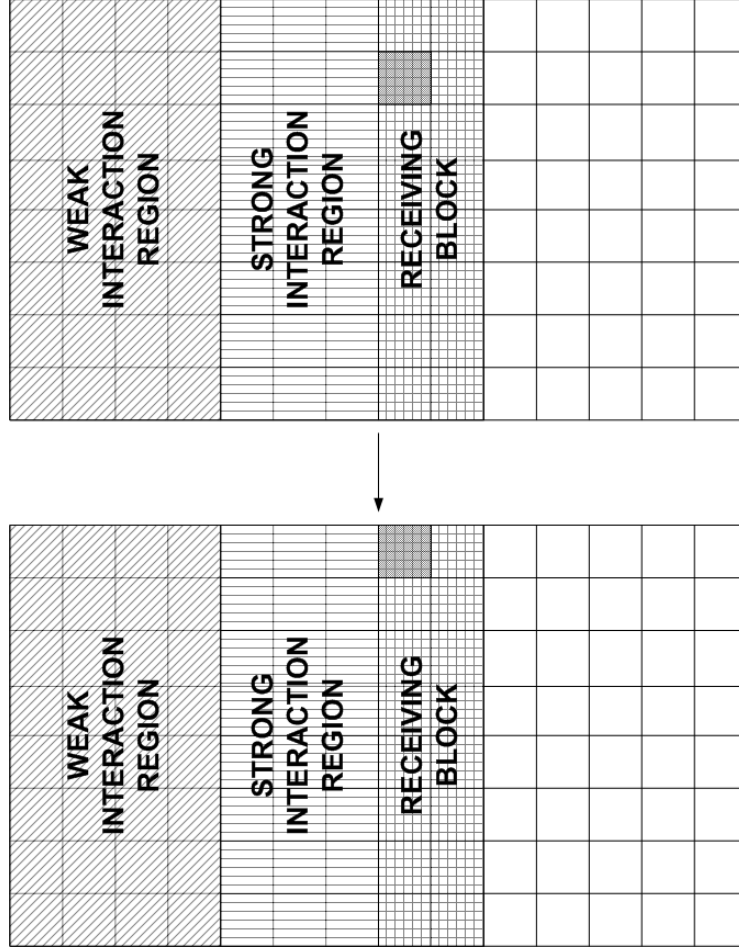


Figure 6.8: Case 1: Field point is NOT the first point of the block.

- Case 1: $m \neq 1$ or $n \bmod N_{B,x} \neq 1$ where $N_{B,x} = N_x/M$ is the number of discretisation points in the x -direction of a block (the field point is not the first point of the block) as illustrated in Figure 6.8. In this case the radiation functions $F(\bar{r}_{n,m}, k_z, k_y)$ can be recursively computed by multiplying the previous radiation functions $F(\bar{r}_{n,m-1}, k_z, k_y)$ by a “phase” function, for $n > N_{s,x}$

$$\begin{aligned}
 F^{(1)}(\bar{r}_{n,m}, k_z, k_y) &= \int_{S_{xy,w}^f} \left[\omega \epsilon_0 \hat{n}' \times \bar{E}(\bar{r}') \right. \\
 &\quad \left. + \bar{k} \times \hat{n}' \times \bar{H}(\bar{r}') - \bar{k} (\bar{n}' \cdot \bar{H}(\bar{r}')) \right] e^{-i\bar{k} \cdot (\bar{r}_{n,m} - \bar{r}')} dS' \quad (6.61)
 \end{aligned}$$

$$\begin{aligned}
 &= \int_{S_{xy,w}^f} \left[\omega \epsilon_0 \hat{n}' \times \bar{E}(\bar{r}') \right. \\
 &\quad \left. + \bar{k} \times \hat{n}' \times \bar{H}(\bar{r}') - \bar{k} (\bar{n}' \cdot \bar{H}(\bar{r}')) \right] e^{-i\bar{k} \cdot (\bar{r}_{n,m-1} - \bar{r}')} \\
 &\quad \times e^{-i\bar{k} \cdot (\bar{r}_{n,m} - \bar{r}_{n,m-1})} dS' \quad (6.62)
 \end{aligned}$$

$$= F^{(1)}(\bar{r}_{n,m-1}, k_z, k_y) e^{-i\bar{k} \cdot (\bar{r}_{n,m} - \bar{r}_{n,m-1})} \quad (6.63)$$

$$F^{(3)}(\bar{r}_{n,m}, k_z, k_y) = \int_{S_{xy,w}^f} \left[\omega \mu_0 \hat{n}' \times \bar{H}(\bar{r}') + \bar{k} \times \hat{n}' \times \bar{H}(\bar{r}') - \bar{k} (\bar{n}' \cdot \bar{H}(\bar{r}')) \right] e^{-i\bar{k} \cdot (\bar{r}_{n,m} - \bar{r}')} dS' \quad (6.64)$$

$$= \int_{S_{xy,w}^f} \left[\omega \mu_0 \hat{n}' \times \bar{H}(\bar{r}') + \bar{k} \times \hat{n}' \times \bar{H}(\bar{r}') - \bar{k} (\bar{n}' \cdot \bar{H}(\bar{r}')) \right] e^{-i\bar{k} \cdot (\bar{r}_{n,m-1} - \bar{r}')} \times e^{-i\bar{k} \cdot (\bar{r}_{n,m} - \bar{r}_{n,m-1})} dS' \quad (6.65)$$

$$= F^{(3)}(\bar{r}_{n,m-1}, k_z, k_y) e^{-i\bar{k} \cdot (\bar{r}_{n,m} - \bar{r}_{n,m-1})} \quad (6.66)$$

- Case 2: $m = 1$ and $n \bmod N_{B,x} = 1$ (the field point is the first point of the block) as illustrated in Figure 6.9. In this case, we move from the last field point of previous block to the first field point of current block, a new group of weak source elements enters the weak interaction group (called weak region 2 as shown in Figure 6.9). The radiation functions $F(\bar{r}_{n,m}, k_z, k_y)$ are updated as follows

$$F^{(1)}(\bar{r}_{n,m}, k_z, k_y) = \int_{S_{xy,w}^f} \left[\omega \epsilon_0 \hat{n}' \times \bar{E}(\bar{r}') + \bar{k} \times \hat{n}' \times \bar{H}(\bar{r}') - \bar{k} (\bar{n}' \cdot \bar{H}(\bar{r}')) \right] e^{-i\bar{k} \cdot (\bar{r}_{n,1} - \bar{r}')} dS' \quad (6.67)$$

$$= \int_{S_{xy,w_1}^f} \left[\omega \epsilon_0 \hat{n}' \times \bar{E}(\bar{r}') + \bar{k} \times \hat{n}' \times \bar{H}(\bar{r}') - \bar{k} (\bar{n}' \cdot \bar{H}(\bar{r}')) \right] e^{-i\bar{k} \cdot (\bar{r}_{n,1} - \bar{r}')} dS' + \int_{S_{xy,w_2}^f} \left[\omega \epsilon_0 \hat{n}' \times \bar{E}(\bar{r}') + \bar{k} \times \hat{n}' \times \bar{H}(\bar{r}') - \bar{k} (\bar{n}' \cdot \bar{H}(\bar{r}')) \right] e^{-i\bar{k} \cdot (\bar{r}_{n,1} - \bar{r}')} dS' \quad (6.68)$$

$$= F^{(1)}(\bar{r}_{n-1, N_y}, k_z, k_y) e^{-i\bar{k} \cdot (\bar{r}_{n,1} - \bar{r}_{n-1, M})} + F_{add}^{(1)} \quad (6.69)$$

$$F^{(3)}(\bar{r}_{n,m}, k_z, k_y) = \int_{S_{xy,w}^f} \left[\omega \mu_0 \hat{n}' \times \bar{H}(\bar{r}') - \bar{k} \times \hat{n}' \times \bar{E}(\bar{r}') + \bar{k} (\bar{n}' \cdot \bar{E}(\bar{r}')) \right] e^{-i\bar{k} \cdot (\bar{r}_{n,1} - \bar{r}')} dS' \quad (6.70)$$

$$= \int_{S_{xy,w_1}^f} \left[\omega \mu_0 \hat{n}' \times \bar{H}(\bar{r}') - \bar{k} \times \hat{n}' \times \bar{E}(\bar{r}') + \bar{k} (\bar{n}' \cdot \bar{E}(\bar{r}')) \right] e^{-i\bar{k} \cdot (\bar{r}_{n,1} - \bar{r}')} dS' + \int_{S_{xy,w_2}^f} \left[\omega \mu_0 \hat{n}' \times \bar{H}(\bar{r}') - \bar{k} \times \hat{n}' \times \bar{E}(\bar{r}') + \bar{k} (\bar{n}' \cdot \bar{E}(\bar{r}')) \right] e^{-i\bar{k} \cdot (\bar{r}_{n,1} - \bar{r}')} dS' \quad (6.71)$$

$$= F^{(3)}(\bar{r}_{n-1, N_y}, k_z, k_y) e^{i\bar{k} \cdot (\bar{r}_{n,1} - \bar{r}_{n-1, M})} + F_{add}^{(3)} \quad (6.72)$$

where

$$F_{add}^{(1)} = \int_{S_{xy,w_2}^f} \left[\omega \epsilon_0 \hat{n}' \times \bar{E}(\bar{r}') + \bar{k} \times \hat{n}' \times \bar{H}(\bar{r}') - \bar{k} (\bar{n}' \cdot \bar{H}(\bar{r}')) \right] e^{-i\bar{k} \cdot (r_{n,1} - r')} dS' \quad (6.73)$$

$$F_{add}^{(3)} = \int_{S_{xy,w_2}^f} \left[\omega \mu_0 \hat{n}' \times \bar{H}(\bar{r}') - \bar{k} \times \hat{n}' \times \bar{E}(\bar{r}') + \bar{k} (\bar{n}' \cdot \bar{E}(\bar{r}')) \right] e^{-i\bar{k} \cdot (r_{n,1} - r')} dS' \quad (6.74)$$

The formulation of the spectral acceleration for the backward scattering and the scattered components from the medium below the surface ($i = 4, 5, 6$) can be formulated using the same procedure as the forward scattering components for the medium above the surface. In order to efficiently evaluate the double integrals involving the radiation functions $F(\bar{r}_{n,m}, k_z, k_y)$, the original contours C_{k_y} and C_{k_z} are deformed to yield a smaller integration intervals and smaller sampling rates. The details of the deformations are described in [70, 71].

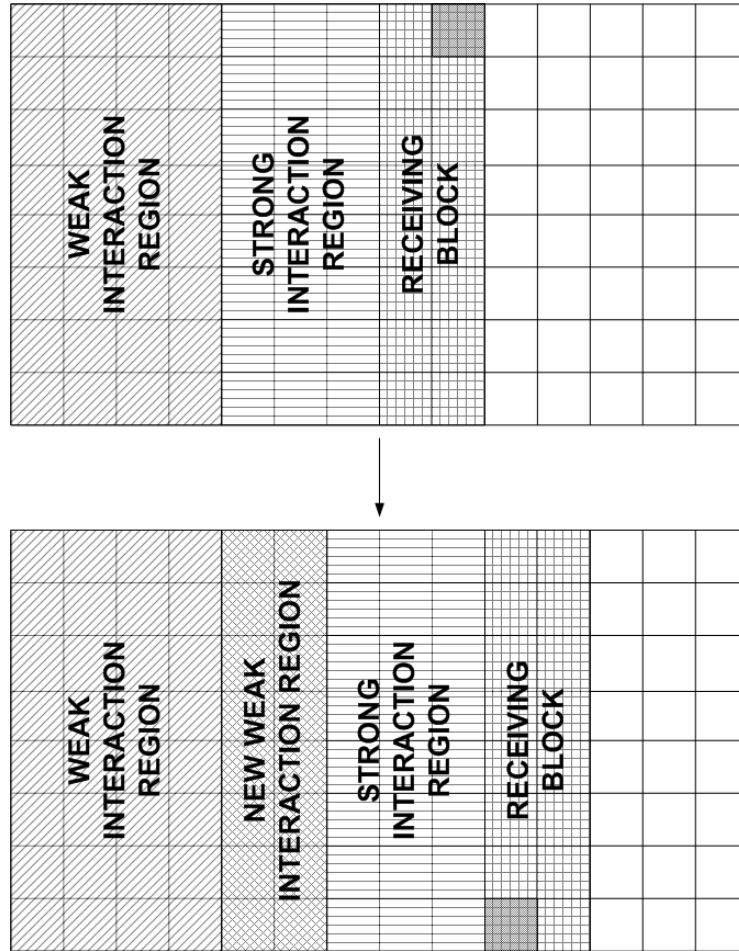


Figure 6.9: Case 2: Field point is the first point of the block.

6.2.5 Normalized Bistatic Scattering Coefficient, Emissivity and Brightness Temperature

Once found the tangential normal components of the fields can be used to compute the scattered horizontal and vertical fields in the far zone as shown in Section 2.5.1

$$E_h(\theta_s, \phi_s; \bar{r}) = -\frac{ik_0}{4\pi} \frac{e^{-ik_0|\bar{r}|}}{|\bar{r}|} \int_S [\hat{h}_s \cdot \eta_0 \bar{F} + \hat{e}_s \cdot \bar{I}] e^{ik_0 \hat{k}_s \cdot \hat{r}'} dS' \quad (6.75)$$

$$E_v(\theta_s, \phi_s; \bar{r}) = -\frac{ik_0}{4\pi} \frac{e^{-ik_0|\bar{r}|}}{|\bar{r}|} \int_S [\hat{e}_s \cdot \eta_0 \bar{F} - \hat{h}_s \cdot \bar{I}] e^{ik_0 \hat{k}_s \cdot \hat{r}'} dS' \quad (6.76)$$

where $\hat{k}_s = \sin\theta_s \cos\phi_s \hat{x} + \sin\theta_s \sin\phi_s \hat{y} + \cos\theta_s \hat{z}$ is the scattering direction, \hat{e}_s and \hat{h}_s denotes the vertical and horizontal polarization directions. Similar to the incident wave, \hat{e}_s and \hat{h}_s are defined so that $\{\hat{k}_s, \hat{e}_s, \hat{h}_s\}$ forms an orthonormal system

$$\hat{e}_s = \cos\theta_s \cos\phi_s \hat{x} + \cos\theta_s \sin\phi_s \hat{y} - \sin\theta_s \hat{z} \quad (6.77)$$

$$\hat{h}_s = -\sin\phi_s \hat{x} + \cos\phi_s \hat{y} \quad (6.78)$$

Then equation (6.75) and (6.76) can be written more explicitly as follows

$$\begin{aligned} E_h(\theta_s, \phi_s; \bar{r}) = & -\frac{ik_0}{4\pi} \frac{e^{-ik_0|\bar{r}|}}{|\bar{r}|} \int_S e^{ik_0\beta'} [\eta_0 \{-F_x(x', y') \sin\phi_s + F_y(x', y') \cos\phi_s\} \\ & + \{I_x(x', y') \cos\theta_s \cos\phi_s + I_y(x', y') \cos\theta_s \sin\phi_s \\ & - I_x(x', y') \frac{\partial f(x', y')}{\partial x'} \sin\theta_s - I_y(x', y') \frac{\partial f(x', y')}{\partial y'} \sin\theta_s\}] dS' \end{aligned} \quad (6.79)$$

$$\begin{aligned} E_v(\theta_s, \phi_s; \bar{r}) = & -\frac{ik_0}{4\pi} \frac{e^{-ik_0|\bar{r}|}}{|\bar{r}|} \int_S e^{ik_0\beta'} [\{I_x(x', y') \sin\phi_s - I_y(x', y') \cos\phi_s\} \\ & + \eta_0 \{F_x(x', y') \cos\theta_s \cos\phi_s + F_y(x', y') \cos\theta_s \sin\phi_s \\ & - F_x(x', y') \frac{\partial f(x', y')}{\partial x'} \sin\theta_s - F_y(x', y') \frac{\partial f(x', y')}{\partial y'} \sin\theta_s\}] dS' \end{aligned} \quad (6.80)$$

where $\beta' = \hat{k}_s \cdot \hat{r}' = x' \sin\theta_s \cos\phi_s + y' \sin\theta_s \sin\phi_s + z' \cos\theta_s$. The scattered horizontal and vertical components are then used to compute the normalized bistatic scattering coefficients

$$\gamma_{\beta\alpha}(\theta_s, \phi_s; \theta_i, \phi_i) = \lim_{r \rightarrow \infty} 4\pi r^2 \frac{|\overline{E}_\beta(\theta_s, \phi_s; \theta_i, \phi_i)|^2}{|\overline{E}^{inc}(\theta_i, \phi_i)|^2} \quad (6.81)$$

$$= \lim_{r \rightarrow \infty} 4\pi r^2 \frac{|\overline{E}_\beta(\theta_s, \phi_s; \theta_i, \phi_i)|^2}{2\eta_0 P_\alpha^{inc}} \quad (6.82)$$

with α and β denotes the polarization of the incident and scattered waves, respectively while P_α^{inc} denotes the power of the incident wave. The emissivity of the surface represents the ability to radiate energy in comparison to a blackbody (a medium which perfectly absorbs and emits energy) at the same temperature and can be computed by applying the rule of energy conservation [63]

$$e_\beta(\theta_i, \phi_i) = 1 - \frac{1}{4\pi} \int_0^{2\pi} \int_0^{\pi/2} [\gamma_{\beta h}(\theta_s, \phi_s; \theta_i, \phi_i) + \gamma_{\beta v}(\theta_s, \phi_s; \theta_i, \phi_i)] \sin\theta_s d\theta_s d\phi_s \quad (6.83)$$

Then the brightness temperature T_B at the observation angle (θ_s, ϕ_s) can be obtained from the emissivity and physical temperature T of the surface

$$T_B(\theta_s, \phi_s) = e_\beta(\theta_i, \phi_i) T \quad (6.84)$$

6.2.6 Absorptivity, Reflectivity and Energy Conservation Check

The brightness temperature is computed based on the assumption that the energy conservation is satisfied. Therefore it is necessary to verify the energy conservation test to ensure that the results of the brightness temperature and emissivity are reliable. The energy conservation test is performed by adding the value of absorptivity and reflectivity (respectively the amount of energy absorbed, expressed as a percentage of the total energy of the incident EM wave) of the rough surface where the absorptivity $a(\theta_i)$ and reflectivity $r(\theta_i)$ can be computed in terms of the surface fields [63]

$$a(\theta_i, \phi_i) = \frac{P_a}{P_{inc}} = \frac{\int_S \hat{n} \cdot \frac{1}{2} \text{Re} [\overline{E} \times \overline{H}^*] dS}{P_{inc}} \quad (6.85)$$

$$r(\theta_i, \phi_i) = \frac{P_r}{P_{inc}} = \frac{\int_S \hat{n} \cdot \frac{1}{2} \text{Re} [\overline{E}_s \times \overline{H}_s^*] dS}{P_{inc}} \quad (6.86)$$

where \overline{E} and \overline{H} are the total electrical and magnetic surface fields, respectively while the \overline{E}_s and \overline{H}_s are the surface scattered fields

$$\overline{E}_s = \overline{E} - \hat{n} \times \overline{E}^{inc} = \overline{I} - \hat{n} \times \overline{E}^{inc} \quad (6.87)$$

$$\overline{H}_s = \overline{H} - \hat{n} \times \overline{H}^{inc} = \overline{F} - \hat{n} \times \overline{H}^{inc} \quad (6.88)$$

and the incident power is computed as

$$P_{inc} = \int_S \hat{n} \cdot \frac{1}{2} \text{Re} [\overline{E}^{inc} \times \overline{H}^{inc*}] dS \quad (6.89)$$

The energy conservation check is satisfied if the total of the absorptivity $a(\theta_i)$ and reflectivity $r(\theta_i)$ is equal to unity.

6.3 Numerical analysis

In this section the accuracy and convergence of the proposed BFBM-SA method is evaluated. The backscattering coefficients, reflectivity, emissivity and energy conservation are also computed to demonstrate that the energy conservation is obeyed. In addition a comparison against measurement data is also performed.

6.3.1 Comparison against 2D model and measurement data

In this section the brightness temperatures generated by the simulation are compared against the brightness temperature measurements of actual soil surfaces. The measurements were provided by Texas A&M university [93]. The brightness temperatures were measured at the wavelength of 21.4cm (L-band) over a range of incident angles from 20° to 50° . A soil moisture of $0.35\text{ cm}^3/\text{cm}^3$ which corresponds to the equivalent relative permittivity of $19.2 + 2.41i$ [1] is used in the comparison. Two surface roughnesses are investigated, namely slightly rough surfaces ($\sigma = 0.88\text{cm}$) and medium rough surfaces ($\sigma = 2.6\text{cm}$). The physical temperature provided in the measurement is 300K . Since the correlation length of the surfaces were not provided in the measurement data of Texas A&M university [93], the correlation length of 8.4cm , given in the measurement of *Oh et al* [94, 63] is assumed in the simulation. Note that in the numerical analysis of *L. Tsang et al* [63], the correlation lengths of the surfaces are not a fixed number. They varies from 7cm to 13cm to match the measurement data. This suggests that the agreement between the results generated by the simulation and measurement data can be improved.

Table 6.1 and Table 6.2 show that the brightness temperatures generated by the proposed method are in very good agreement with the measurements for different polarizations, incident angles and roughnesses of the surface. The difference between the simulation and measurement is around 3K which represents good accuracy since the difference of the

Table 6.1: Comparison of brightness temperature between the proposed method and measurement data. Roughness of the surfaces: $\sigma = 0.88cm$. Permittivity: $\epsilon_r = 19.2 + 2.41i$. Physical temperature: $300K$.

| Polar. | Incident angle | Meas. | Brightness tempt. (K) - 2D | | | Brightness tempt. (K) - 3D | | |
|--------|----------------|--------|----------------------------|------------|---------|----------------------------|------------|---------|
| | | | Sim. | Difference | % diff. | Sim. | Difference | % diff. |
| TE | 20° | 167.56 | 155.85 | 11.71 | 6.98% | 165 | 2.56 | 1.53% |
| TE | 35° | 153.29 | 144.51 | 8.78 | 5.73% | 152.7 | 0.59 | 0.38% |
| TE | 50° | 135.73 | 124.07 | 11.65 | 8.58% | 133.77 | 1.96 | 1.44% |
| TM | 20° | 181.46 | 191.28 | 9.82 | 5.41% | 184.35 | 2.89 | 1.59% |
| TM | 35° | 196.83 | 209.37 | 12.54 | 6.37% | 199.08 | 2.25 | 1.14% |
| TM | 50° | 223.81 | 233.07 | 9.26 | 2.07% | 225.21 | 1.40 | 0.62% |

Table 6.2: Comparison of brightness temperature between the proposed method and measurement data. Roughness of the surfaces: $\sigma = 2.60cm$. Permittivity: $\epsilon_r = 19.2 + 2.41i$. Physical temperature: $300K$.

| Polar. | Incident angle | Meas. | Brightness tempt. (K) - 2D | | | Brightness tempt. (K) -3D | | |
|--------|----------------|--------|----------------------------|------------|---------|---------------------------|------------|---------|
| | | | Sim. | Difference | % diff. | Sim. | Difference | % diff. |
| TE | 20° | 203.40 | 185.34 | 18.06 | 8.87% | 200.93 | 2.47 | 1.21% |
| TE | 35° | 197.10 | 181.98 | 15.11 | 7.76% | 194.46 | 2.64 | 1.34% |
| TE | 50° | 172.68 | 156.96 | 15.71 | 9.10% | 171.84 | 0.84 | 0.49% |
| TM | 20° | 210.72 | 227.67 | 16.94 | 8.04% | 207.36 | 3.36 | 1.59% |
| TM | 35° | 215.85 | 229.08 | 13.2 | 6.11% | 212.52 | 3.33 | 1.54% |
| TM | 50° | 230.85 | 239.28 | 8.43 | 3.65% | 225.93 | 4.92 | 2.28% |

brightness temperatures between the various roughnesses or moisture of the surfaces can be more than $30K$. It is also shown in Table 6.1 and Table 6.2 that the results generated by the 3D model have a better agreement with measurement data than those generated by the 1D model.

6.3.2 Convergence of the BFBM-SA

In order to demonstrate the computational efficiency of the proposed method, a comparison of the BFBM-SA with the conventional FBM-SA and the GMRES-SA is performed in terms of convergence rate and processing time required to achieve a desired relative error norm. A Gaussian surface is considered with Gaussian correlation function. The surfaces used for simulation are wet soil surfaces whose relative permittivity is $\epsilon_r = 15.57 + 3.71i$ at frequency of $1.5GHz$ (L Band). The surface area is $4\lambda \times 4\lambda$ and 16 basis functions per wavelength were used giving a total number of unknowns equal to 24756. The block size of the BFBM-SA defined in the simulation is 4 strips (equivalent to $\lambda/4$). The rough surface was illuminated by a tapered plane wave with the tapering parameter of $g = L/3$ to remove edge effects at an incident angle of 40° . Three distinct types of surface were considered. Slightly rough surfaces had rms height of $h_{rms} = 0.05\lambda$. Medium rough surfaces had rms

height of $h_{rms} = 0.2\lambda$. The correlation length of the slightly rough and medium rough surface is $l_c = 0.8\lambda$. Very rough surfaces had rms height of $h_{rms} = 0.5\lambda$ and correlation length of $l_c = 1.0\lambda$. A relative residual error was defined as

$$\log_{10} \frac{\|\bar{z}\bar{x} - \bar{b}\|}{\|\bar{b}\|} \quad (6.90)$$

Each method was ran until it achieved a relative residual error of less than 10^{-3} . In the implementation of spectral acceleration, the strong interaction distance needed to be defined to ensure a compromise between accuracy and the computational cost. In this study, a near field size of 1.5 wavelengths was chosen to achieve the desired relative residual error and minimize the computational cost. Figure 6.10 compares the convergence rate of the BFBM-SA and the GMRES for one realisation of slightly rough surface profile as well as one realisation of medium rough surface and one realisation of very rough surface. Note that the FBM-SA diverges in these cases. It is clear that the convergence rate of BFBM-SA is several times better than that of GMRES-SA. In addition the convergence of the proposed method is less affected by the roughness of the surfaces than the GMRES-SA. As the surface changes from slightly rough to very rough, the number of iterations required for GMRES-SA to achieve the desired relative error norm is doubled while the required number of iterations of the proposed method only slightly increases, from 4 iterations for the slightly rough surface to 5 iterations for the very rough surface.

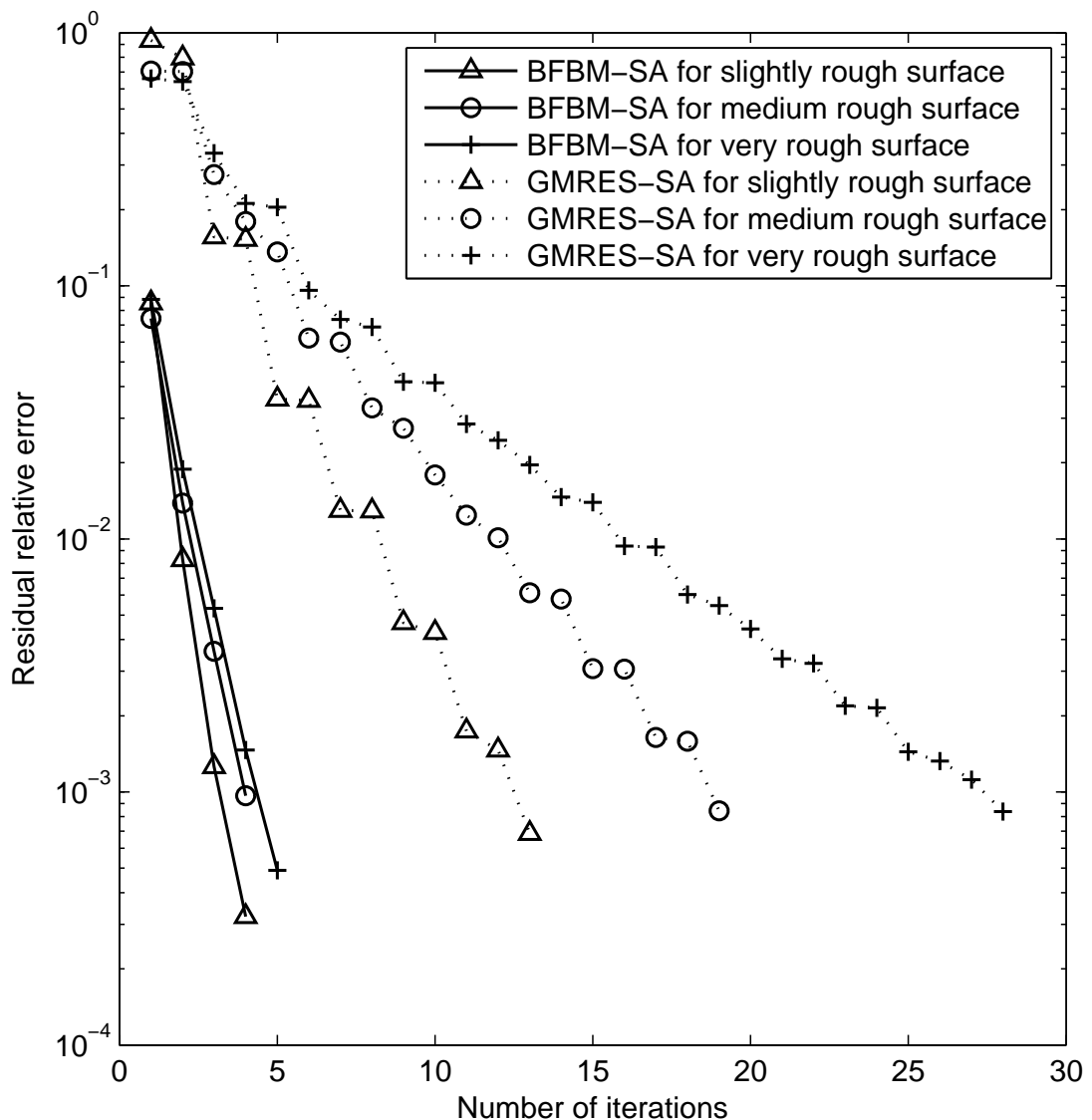


Figure 6.10: Comparison of the convergence rate of the proposed method (BFBM-SA) and GMRES.

In order to make a fair comparison of the efficiency between BFBM-SA and the GMRES-SA, a run time comparison is performed. An investigation of run time and number of iterations required to achieve a desired residual relative error was performed for rough surfaces with different rms heights and correlation lengths and is shown in Table 6.3 for the case of TE wave and in Table 6.4 for the case of TM wave respectively. The correlation lengths chosen are 0.5λ and 1.5λ while the rms heights vary from 0.05λ to 0.2λ . The number inside the parentheses denotes the number of iterations and the number outside the parentheses denotes the run time in seconds required to achieve the desired residual relative error. The run time of the BFBM-SA is approximately 3 times faster than that of the GMRES-SA for the case of slightly rough surfaces ($\sigma = 0.05\lambda$). The GMRES-SA

is strongly affected by the roughness of the surfaces therefore the efficiency gain of the BFBM-SA over the GMRES-SA is expanded significantly as the surface becomes rougher.

The effect of the size of the problem on the convergence of the proposed method was also examined. Figure 6.11 shows the run time of the BFBM-SA and GMRES-SA as a function of the number of unknowns. Due to the decomposition of the Green's function in the x-direction of the 2D spectral acceleration [70], the efficiency of the SA depends on the vertical length L_y of the surface. Therefore two types of surfaces were considered. For case 1, the vertical length of the surface is fixed at $L_y = 4\lambda$ and the horizontal length L_x varied from 4λ to 64λ , resulting in the number of unknowns increasing from 24576 to 393216. For case 2, the vertical length of the surface is fixed at $L_y = 8\lambda$ and the horizontal length L_x vary from 4λ to 32λ . As demonstrated in Figure 6.11, as the number of unknowns is doubled, the run time of both the BFBM-SA and GMRES-SA is approximately doubled. The efficiency gain of the BFBM-SA over the GMRES-SA is slightly expanded as the size of problem increases. In addition for the same number of unknowns, due to the greater size of the strongly interacting region and the required number of plane waves in the 2D spectral acceleration [70, 71], the run time of case 2 (for both of BFBM-SA and GMRES-SA) is greater than that of case 1. It is also shown in Figure 6.11 that the computational complexity of the GMRES-SA and BFBM-SA is approximately in $\mathcal{O}(N)$ scaling.

Table 6.3: Average run time (in seconds) and number of iterations required to achieve residual error norm 10^{-3} . TE Polarization. Size of the surface: $4\lambda \times 4\lambda$. Number of unknowns: 24576.

| l_c | $\sigma = 0.05\lambda$ | | $\sigma = 0.2\lambda$ | |
|--------------|------------------------|-------------|-----------------------|-------------|
| | BFBM-SA | GMRES-SA | BFBM-SA | GMRES-SA |
| 0.5λ | 667.8 (4) | 1822.4 (16) | 870.6 (5) | 6949.5 (48) |
| 0.8λ | 672.4 (4) | 1481.9 (13) | 694.3 (4) | 2376.3 (19) |
| 1.5λ | 688.5(4) | 1432.0 (12) | 519.4 (3) | 1538.2 (13) |

Table 6.4: Average run time (in seconds) and number of iterations required to achieve residual error norm 10^{-3} . TM Polarization. Size of the surface: $4\lambda \times 4\lambda$. Number of unknowns: 24576.

| l_c | $\sigma = 0.05\lambda$ | | $\sigma = 0.2$ | |
|--------------|------------------------|-------------|----------------|-------------|
| | BFBM-SA | GMRES-SA | BFBM-SA | GMRES-SA |
| 0.5λ | 500.4 (3) | 1383.2 (12) | 1051.8 (6) | 5330.6 (42) |
| 0.8λ | 326.5 (2) | 1028.1 (9) | 688.3 (4) | 2084.2 (17) |
| 1.5λ | 333.2 (2) | 927.4 (7) | 332.6 (2) | 1320.0 (11) |

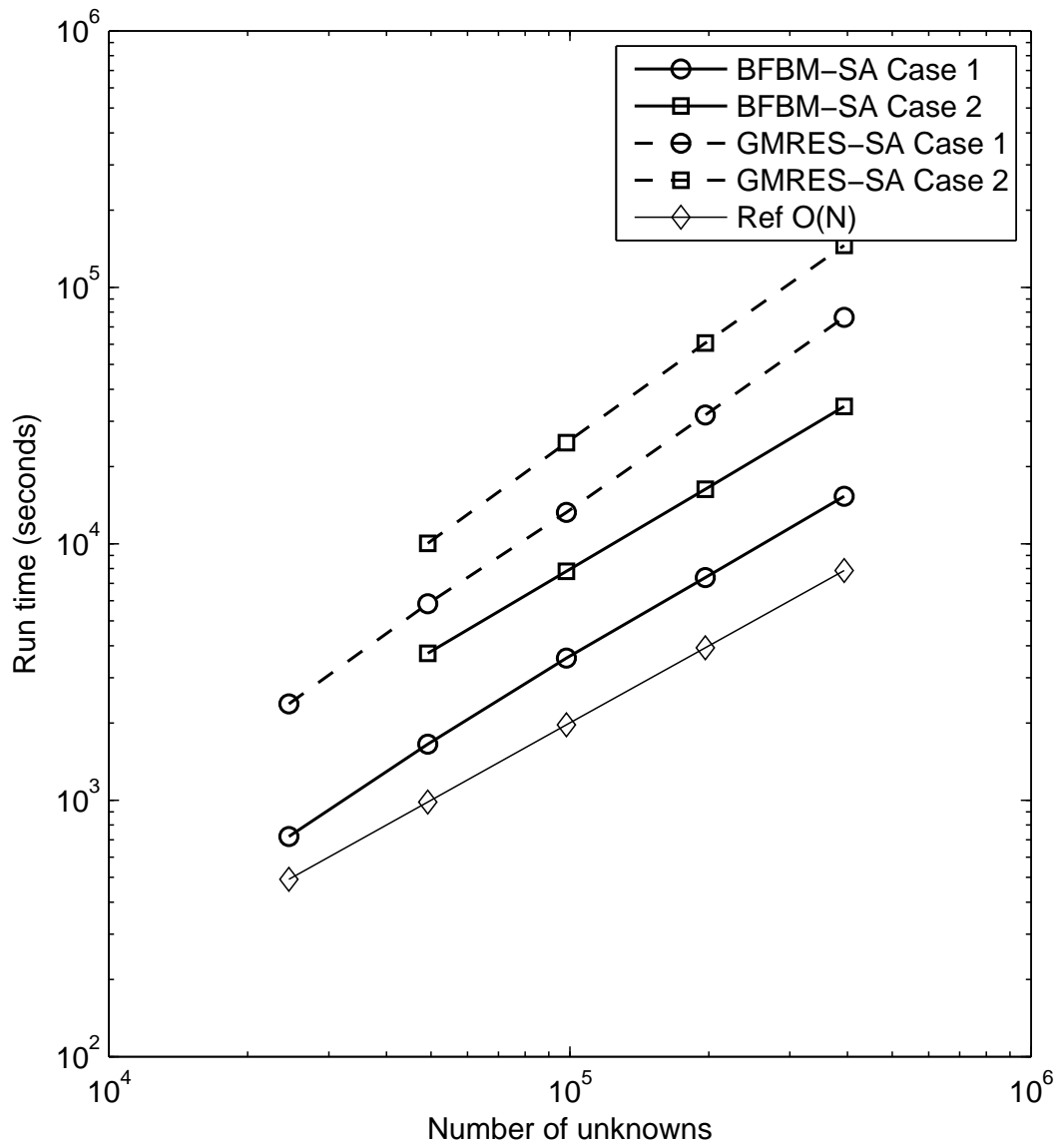


Figure 6.11: Comparison of run time to achieve the desired residual relative error versus number of unknowns between BFBM-SA and GMRES-SA for the 2D dielectric problem.

Finally, in order to illustrate the accuracy of the BFBM-SA, the normalized bistatic scattering coefficient (NBSC) for a single implementation obtained by the proposed method is compared to that obtained by the precise solution. The precise solution is generated by running the BFBM (without spectral acceleration) until it achieved a residual relative error of 10^{-6} . Figure 6.12, Figure 6.13 and Figure 6.14 show that the NBSC obtained using the proposed method completely overlap the NBSC obtained by the precise solution for different simulation scenarios.

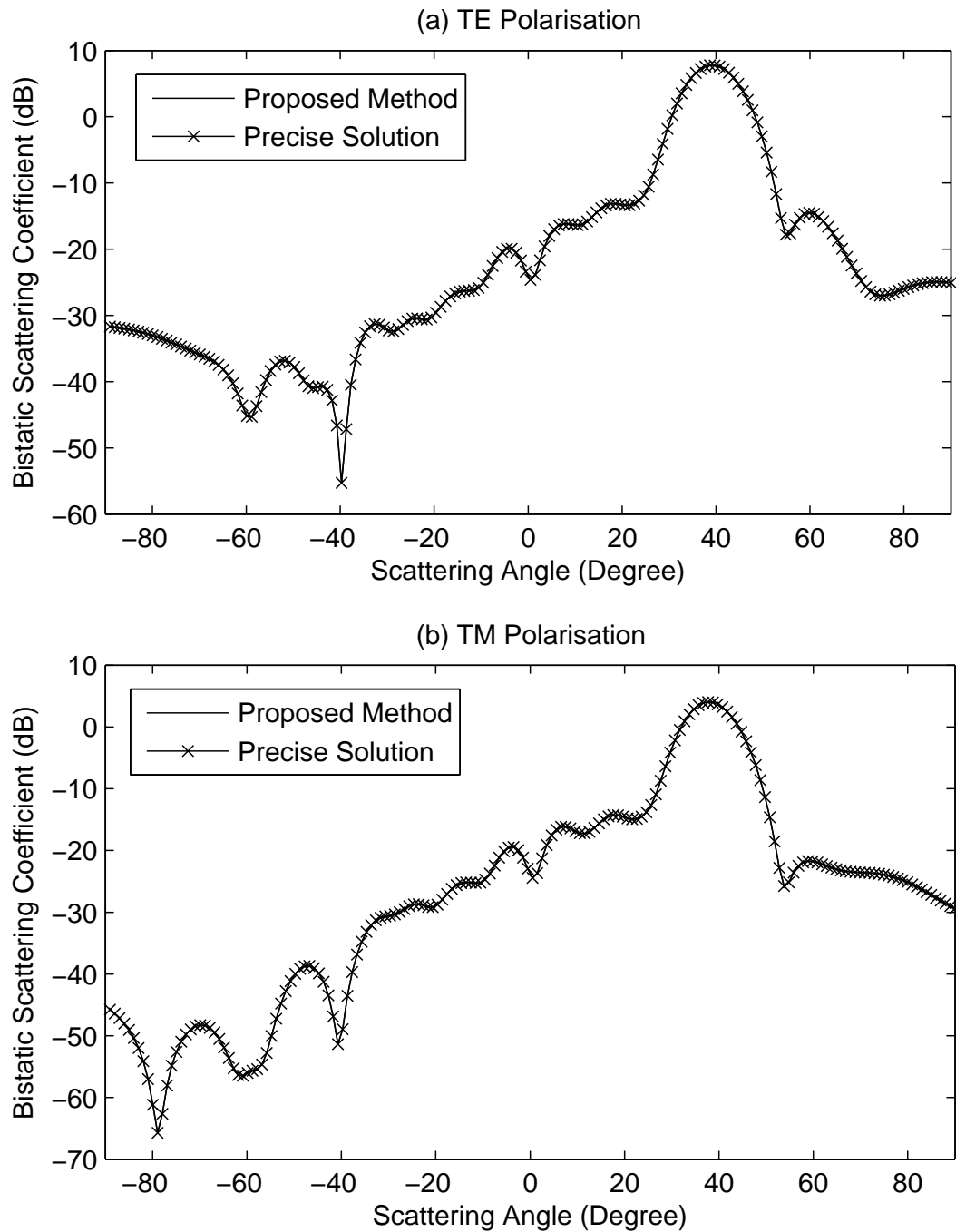


Figure 6.12: Comparison of co-polarisation bistatic scattering coefficients generated by the proposed method and precise solution. Incident angle: 40° . Rms height of the surface: $\sigma = 0.05\lambda$. Correlation length of the surface: $l_c = 0.8\lambda$. Size of the surface: $8\lambda \times 8\lambda$. Relative permittivity: $5.46 + 0.37i$. Number of unknowns: 98304. (a) TE Polarization. (b) TM Polarization.

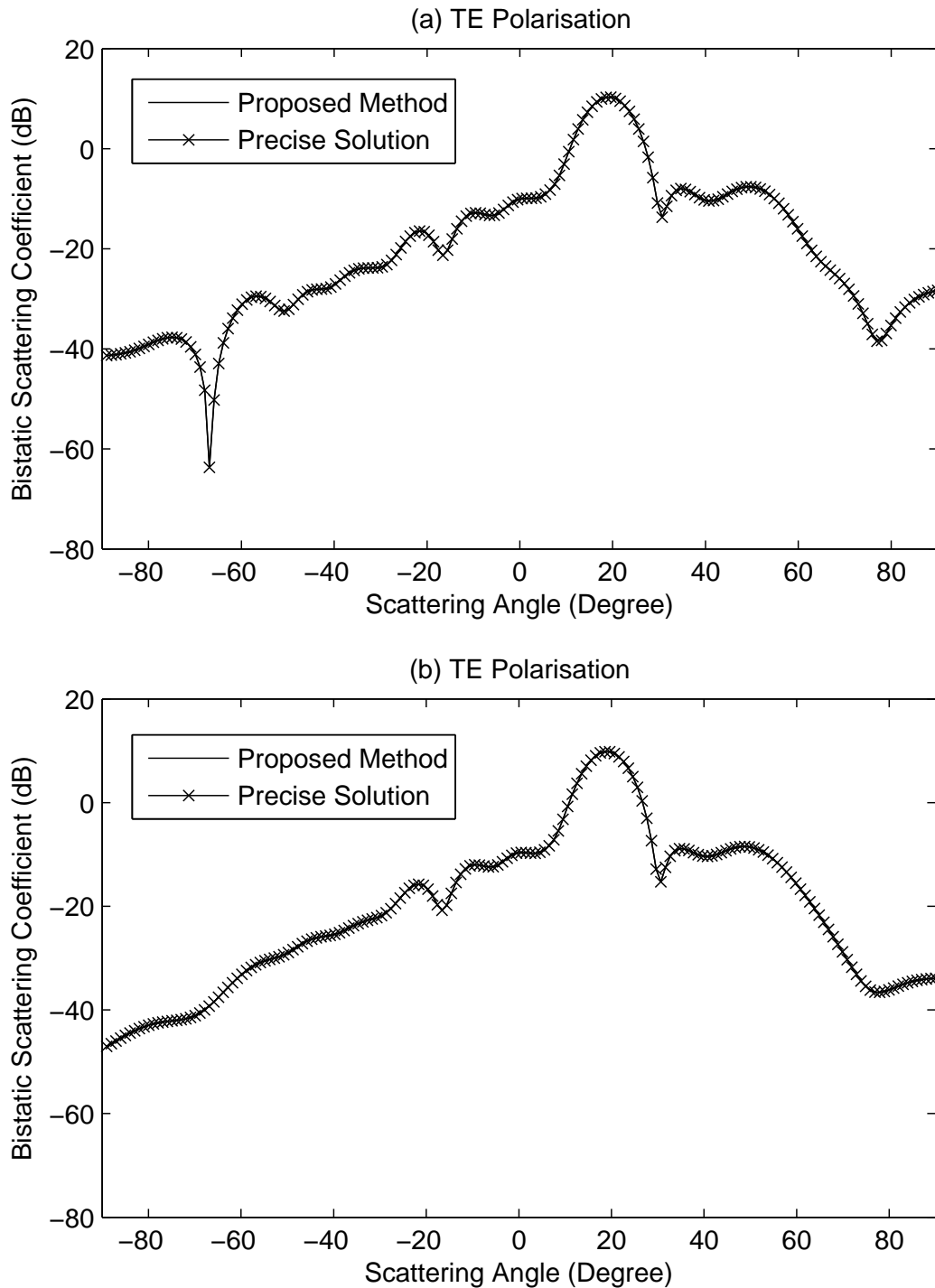


Figure 6.13: Comparison of co-polarisation bistatic scattering coefficients generated by the proposed method and precise solution. Incident angle: 20° . Rms height of the surface: $\sigma = 0.05\lambda$. Correlation length of the surface: $l_c = 0.8\lambda$. Size of the surface: $8\lambda \times 8\lambda$. Relative permittivity: $15.57 + 3.71i$. Number of unknowns: 98304. (a) TE Polarization. (b) TM Polarization..

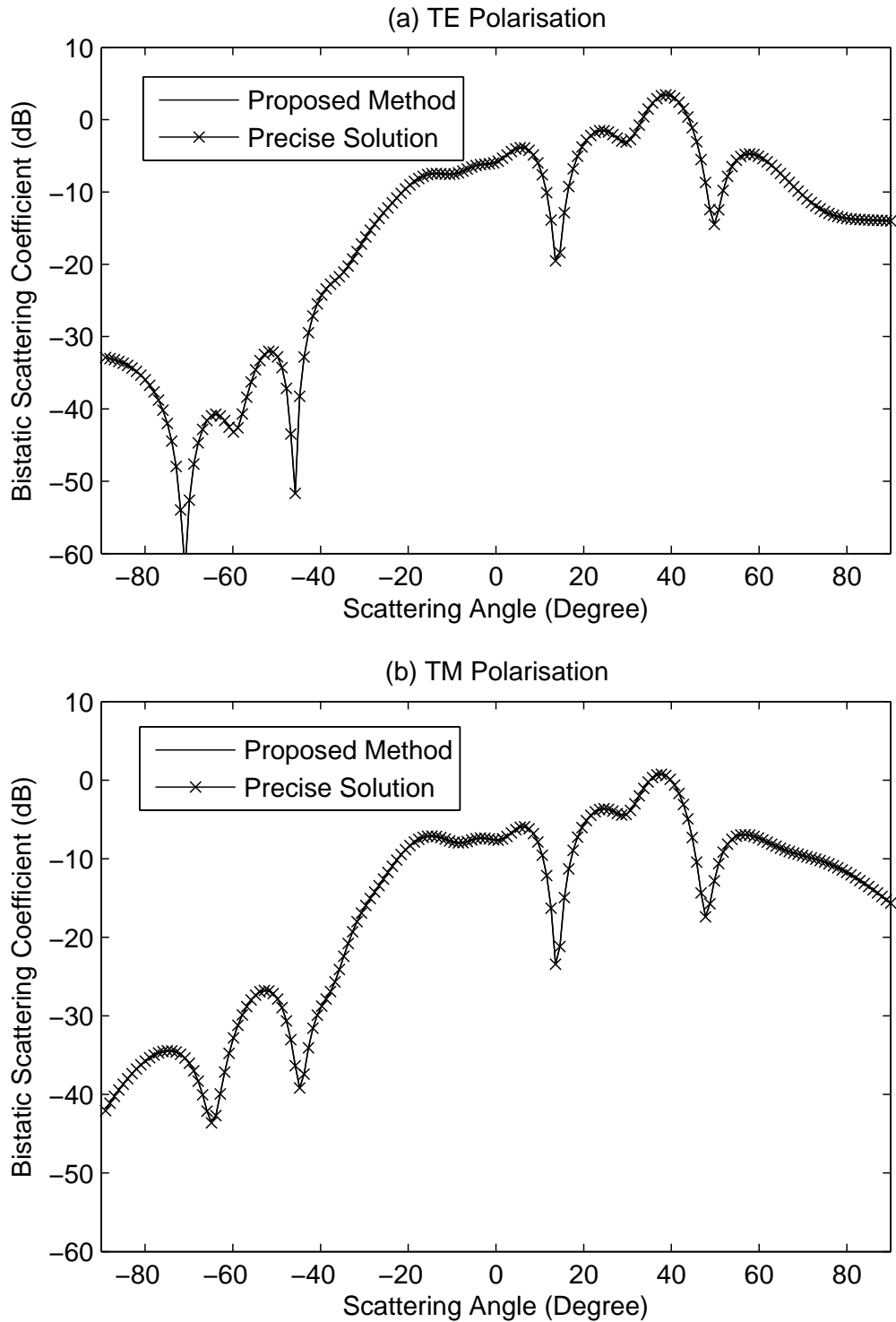


Figure 6.14: Comparison of co-polarisation bistatic scattering coefficients generated by the proposed method and precise solution. Incident angle: 40° . Rms height of the surface: $\sigma = 0.15\lambda$. Correlation length of the surface: $l_c = 0.8\lambda$. Size of the surface: $8\lambda \times 8\lambda$. Relative permittivity: $15.57 + 3.71i$. Number of unknowns: 98304. (a) TE Polarization. (b) TM Polarization..

6.3.3 Emissivity, Reflectivity and Energy Conservation

In order to validate the simulation, the energy conservation test needs to be performed. The energy conservation test is performed by adding the value of absorptivity and reflectivity of the rough surface. The rough surface had the rms height of 0.4cm and the correlation length of 8.4cm which were provided by Oh et al [94]. The incidence angle varies from 30° to 50° and a tapering parameter of $g = L/3$ was used to remove edge effects. In Table 6.5, 6.6 and 6.7, the energy conservation check is performed for various surface roughnesses, permittivities and polarisations to illustrate that the energy conservation is obeyed and effect of the roughness on the emissivities of the surfaces is also investigated. The energy conservation *in most cases* (except the case of TM wave scattering from very rough surface with $h_{rms} = 0.2\lambda$, $l_c = 0.5\lambda$) was better than 2% and the energy conservation for the *TE* cases are better than the *TM* cases. This level of accuracy is sufficient for soil moisture remote sensing applications since they can suffer the error more than 10% which is equivalent to the difference of 0.1 in emissivity.

Table 6.5: Reflectivity, emissivity and energy conservation of rough surfaces. $h_{rms} = 0.4\text{cm}$. $l_c = 8.4\text{cm}$. Frequency: $f = 1.5\text{GHz}$.

| Polar | Incident angle | Emissivity | Reflectivity | Energy Conservation |
|-------|----------------|------------|--------------|---------------------|
| TE | 30° | 0.5936 | 0.4408 | 1.002 |
| TE | 40° | 0.5553 | 0.4770 | 0.994 |
| TE | 50° | 0.5032 | 0.5228 | 0.987 |
| TM | 30° | 0.6945 | 0.3329 | 1.011 |
| TM | 40° | 0.7340 | 0.2890 | 1.013 |
| TM | 50° | 0.7832 | 0.2260 | 1.019 |

Table 6.6 and 6.7 also show the emissivity and energy conservation for soil moistures of 20% and 30.6% at 5GHz (C-band), corresponding to the equivalent relative permittivity of $9.09 + 1.43i$ and $15.57 + 3.71i$, respectively. As the soil moisture increases, the emissivities become smaller for both polarisations because of the increasing contrast between two media. It is also shown in Table 6.7 and 6.7 that the rougher surfaces exhibit higher emissivities. This is due to the fact that the rough surfaces have a greater surface area and hence absorb (then emit) more electromagnetic energy than the smooth surfaces.

6.4 Conclusion

In this chapter, a novel block forward backward approach with spectral acceleration (BFBM-SA) for efficiently computing electromagnetic wave scattering from two dimensional dielectric randomly rough surfaces was presented. The accuracy and performance of the proposed method was evaluated and compared to those of the GMRES-SA. The nu-

Table 6.6: Emissivity and Energy Conservation of rough surfaces. Permittivity: $\epsilon_r = 15.57 + 3.71i$. Incident angle: $\theta_i = 40^\circ$.

| rms height | Correlation length | TE Polarization | | TM Polarization | |
|----------------|--------------------|-----------------|------------|-----------------|------------|
| | | Emissivity | Ener. Cons | Emissivity | Ener. Cons |
| 0.05 λ | 0.5 λ | 0.5360 | 0.9968 | 0.7201 | 1.0151 |
| 0.05 λ | 0.8 λ | 0.5254 | 0.9991 | 0.7193 | 1.0153 |
| 0.05 λ | 1.5 λ | 0.5205 | 0.9993 | 0.7196 | 1.0148 |
| 0.2 λ | 0.5 λ | 0.7488 | 0.9871 | 0.7952 | 1.0314 |
| 0.2 λ | 0.8 λ | 0.6208 | 1.0016 | 0.7392 | 1.0146 |
| 0.2 λ | 1.5 λ | 0.5602 | 1.0034 | 0.7222 | 1.0145 |

Table 6.7: Emissivity and Energy Conservation of rough surfaces. Permittivity: $\epsilon_r = 9.09 + 1.43i$. Incident angle: $\theta_i = 40^\circ$.

| rms height | Correlation length | TE Polarization | | TM Polarization | |
|----------------|--------------------|-----------------|------------|-----------------|------------|
| | | Emissivity | Ener. Cons | Emissivity | Ener. Cons |
| 0.05 λ | 0.5 λ | 0.6594 | 0.9989 | 0.8199 | 1.0191 |
| 0.05 λ | 0.8 λ | 0.6419 | 1.0002 | 0.8178 | 1.0184 |
| 0.05 λ | 1.5 λ | 0.6417 | 1.0000 | 0.8182 | 1.0179 |
| 0.2 λ | 0.5 λ | 0.8010 | 0.9959 | 0.8396 | 1.0406 |
| 0.2 λ | 0.8 λ | 0.7278 | 1.0051 | 0.7943 | 1.0313 |
| 0.2 λ | 1.5 λ | 0.6829 | 1.0016 | 0.7939 | 1.0189 |

numerical analysis suggested a better performance in terms of convergence rate and run time of BFBM-SA when compared to GMRES-SA. The proposed method also shows a great robustness against the roughness of the surface, size of problems and wave polarization. In addition the numerical results has shown a very good agreement with the measurement data for the passive remote sensing applications.

7 Conclusions

The main focus of this dissertation is on the development of robust, efficient and accurate numerical methods for computing electromagnetic (EM) wave propagation and scattering in urban, rural areas and from random rough surfaces. The general EM wave scattering problem and the use of surface electric and magnetic field integral equations (EFIE and MFIE, respectively) in conjunction with the Method of Moments technique to solve the problem numerically were described in Chapter 2. Specifically the formulations for both the two-dimensional scattering problem (one-dimensional boundary surface) and three-dimensional scattering problem (two-dimensional boundary surface) were derived in this chapter. These integral equation (IE) formulations provide the basis for the novel numerical techniques proposed in Chapter 3-6. Chapter 3 and 4 focus on the development of numerical methods to compute wave propagation in rural and urban areas while Chapter 5 and 6 focus on the application of numerical techniques to solve the problem of wave scattering from 1D and 2D random rough surfaces.

In Chapter 3, an extension of the Tabulated Interaction Method (TIM) to solve the problem of wave propagation in rural areas was presented. The proposed method referred to as Improved Tabulated Interaction Method (ITIM) extends the original Tabulated Interaction Method (TIM) [40] in several ways. Firstly the proposed method was formulated for the lossy dielectric case which is more general than the formulation of original TIM for the perfectly conducting terrain case. Secondly the original TIM was formulated assuming forward scattering, essentially computing a single "forward step" of the FBM. The proposed method instead generates a matrix equation incorporating all backward and forward scattering effects. Finally a two-level ITIM (TL-ITIM) was derived to improve the accuracy of the method. The accuracy, complexity, performance and robustness of the proposed method have been evaluated and compared to those of precise solution generated by Forward Backward Method (FBM). Like the Characteristic Basis Function Method (CBFM) the proposed method is an iteration-free method and numerical analysis demonstrates that it has a very high accuracy. However, it is based on more aggressive approximations which are appropriate for the particular problem of propagation over gently undulating terrain and therefore is much more efficient than the CBFM for this particular application. The ITIM has a low computational cost and memory storage which is comparable to empirical models. It was also shown that the results generated by the ITIM were in a close agreement with measured data.

Due to the sharp corners of the buildings, it is more computationally challenging to apply the integral equation method to compute EM wave propagation in urban areas than in rural areas. In Chapter 4, an initial study in using integral equations to compute EM wave propagation in urban areas was presented. The Generalized FBM was proposed to overcome the divergence of the conventional FBM and the forward scattering variant (GFBM-FS) was shown to be reasonable. The accuracy of the proposed method was also investigated by comparing against experimental data comprising pathloss measurements along three routes in Munich city provided by Mannesmann Mobilfunk GmbH. The proposed method was shown to achieve a better accuracy than the slope diffraction method, a widely used vertical propagation model.

In Chapter 5, a novel numerical technique was proposed in order to efficiently compute electromagnetic wave scattering from 1D random rough surfaces. The proposed method referred to as Improved Forward Backward Method with Spectral Acceleration (IFBM-SA) extends the original IFBM in several ways. Firstly an improved analysis provides a more thorough explanation of the workings of the IFBM, in this case in the context of scattering from lossy dielectrics. Secondly this chapter demonstrated how to reduce the cost of the optimisation step from 2.5 matrix-vector products to 1 matrix-vector product (and 0.5 products in some cases). Thirdly Spectral Acceleration (SA) was applied to reduce the complexity of the IFBM-SA from $\mathcal{O}(N^2)$ to $\mathcal{O}(N)$. The accuracy and performance of the proposed method was evaluated and compared to those of the FBM-SA and a recently proposed method by Liu *et al*[62]. The numerical analysis suggested a better performance in terms of convergence rate and run time of IFBM-SA when compared to FBM-SA and the method proposed by Liu *et al*. It also displayed greater robustness than the reference method and was capable of scaling to larger problems.

The numerical solutions for the EM wave scattering from 1D random rough surfaces have an advantage of low computational complexity but they also provide a less accurate results when compared to measured data than models involving realistic two dimensional surfaces. In Chapter 6, a novel block forward backward approach with spectral acceleration (BFBM-SA) for efficiently computing electromagnetic wave scattering from two dimensional dielectric random rough surfaces was presented. The accuracy and performance of the proposed method were evaluated and compared to those of the GMRES-SA. The numerical analysis suggested a better performance in terms of convergence rate and run time of BFBM-SA when compared to GMRES-SA. The proposed method also showed robustness against the roughness of the surface, size of problems and wave polarization. In addition the numerical results displayed very good agreement with the measurement data.

Future study

There are several areas of future study leading from the work in this dissertation. The Improved Tabulated Interaction method has been successfully applied to accelerate the computation of 2D wave propagation in rural areas. There is a potential to extend the ITIM to speed up the calculation of 3D wave propagation.

The GFBM developed in this dissertation has been applied successfully to compute the wave propagation in urban areas. However the proposed method is only valid for the receivers far from the transmitter. There is a potential to combine the proposed method with other available methods such as ray tracing to correct the pathloss for the receivers near the transmitter. In additions the acceleration techniques such as Fast Far Field Approximation (FAFFA) should be applied to accelerate the proposed methods.

Another future study may involve the wave scattering from 2D random rough surfaces. The BFBM described in Chapter 6 has only been applied to compute the wave scattering from 2D Gaussian correlation rough surfaces. It can be extended to solve the problem of wave scattering from exponentially correlated rough surfaces. This requires the use of the Rao-Wilton-Glisson (RWG) basis functions in the discretisation of the integral equations. In addition, acceleration techniques such as Fast Multipole Method (FMM), etc can be modified and adapted to the BFBM to speed up the calculation. The extension to the case of exponential rough surfaces may further improve the agreement between the simulation results and measurement data.

Appendix A - Magnetic Field Integral Equation in terms of surface field and its normal derivative

An alternative formulation of the integral equation in terms of surface field and its normal derivative is derived and used for the random rough surface scattering literature. It is possible to recast the EFIEs in terms of surface field and its normal derivative by using the following relations

$$\bar{H}_1 = H_z \hat{z} \quad (\text{A-1})$$

$$\bar{E}_1 = \frac{1}{i\omega\epsilon_0} \nabla \times \bar{H}_1 \quad (\text{A-2})$$

$$\hat{n} \times \bar{E}_1 = -\frac{\hat{z}}{i\omega\epsilon_0} (\hat{n} \cdot \nabla H_z) \quad (\text{A-3})$$

Using these equations in (2.73) and (2.74) gives, for $\bar{\rho} = x\hat{x} + y\hat{y}$ and $\bar{\rho}' = x'\hat{x} + y'\hat{y}$ on the surface S

$$H_z^{inc}(\bar{\rho}) = H_z(\bar{\rho}) + \int \frac{\partial H_z(\bar{\rho}')}{\partial n'} G_0(\bar{\rho}, \bar{\rho}') dt' - \int H_z(\bar{\rho}') [\hat{n}' \cdot \nabla G_0(\bar{\rho}, \bar{\rho}')] dt' \quad (\text{A-4})$$

$$0 = H_z(\bar{\rho}) - \int \frac{\epsilon_1}{\epsilon_0} \frac{\partial H_z(\bar{\rho}')}{\partial n'} G_1(\bar{\rho}, \bar{\rho}') dt' + \int H_z(\bar{\rho}') [\hat{n}' \cdot \nabla G_1(\bar{\rho}, \bar{\rho}')] dt' \quad (\text{A-5})$$

We define

$$u(x) = \sqrt{1 + \left(\frac{df(x)}{dx}\right)^2} \left(\frac{\partial H_z(\bar{\rho}')}{\partial n'}\right)_{y=f(x)} \quad (\text{A-6})$$

$$\psi(x) = (H_z(\bar{\rho}))_{y=f(x)} \quad (\text{A-7})$$

Then the MoM is applied to solve the integral equation (A-4) and (A-5) by expanding $u(x)$ and $\psi(x)$ into a finite series using pulse basis functions and evaluating equation (A-4) and (A-5) at N different points, resulting in a system of $2N$ linear equations

$$\begin{bmatrix} \overline{\overline{Z}}^{(a)} & \overline{\overline{Z}}^{(b)} \\ \overline{\overline{Z}}^{(c)} & \overline{\overline{Z}}^{(d)} \end{bmatrix} \begin{bmatrix} \overline{u} \\ \overline{\psi} \end{bmatrix} = \begin{bmatrix} \overline{\psi}^{inc} \\ \overline{0} \end{bmatrix} \quad (\text{A-8})$$

The entries of the impedance matrices are given by

$$Z_{mn}^{(a)} = \begin{cases} \frac{\Delta x}{4i} H_0^{(2)}(k_0 R_{mn}) & m \neq n \\ \frac{\Delta x}{4i} \left\{ 1 - i \left[\frac{2}{\pi} \ln \left(\frac{\gamma k_0 \Delta x}{4e} \right) \right] \right\} & m = n \end{cases} \quad (\text{A-9})$$

$$Z_{mn}^{(b)} = \begin{cases} -\frac{\Delta x}{4i} k_0 \frac{f'(x_n)(x_m - x_n) - [f(x_m) - f(x_n)]}{R_{mn}} H_1^{(2)}(k_0 R_m) & m \neq n \\ \frac{1}{2} & m = n \end{cases} \quad (\text{A-10})$$

$$Z_{mn}^{(c)} = \begin{cases} -\frac{\epsilon_1}{\epsilon_0} \frac{\Delta x}{4i} H_0^{(2)}(k_1 R_{mn}) & m \neq n \\ -\frac{\epsilon_1}{\epsilon_0} \frac{\Delta x}{4i} \left\{ 1 - i \left[\frac{2}{\pi} \ln \left(\frac{\gamma k_1 \Delta x}{4e} \right) \right] \right\} & m = n \end{cases} \quad (\text{A-11})$$

$$Z_{mn}^{(d)} = \begin{cases} \frac{\Delta x}{4i} k_1 \frac{f'(x_n)(x_m - x_n) - [f(x_m) - f(x_n)]}{R_{mn}} H_1^{(2)}(k_1 R_{mn}) & m \neq n \\ \frac{1}{2} & m = n \end{cases} \quad (\text{A-12})$$

Appendix B - MoM Formulation for wave scattering from 2D dielectric surface

In this appendix, the six coupled integral equations for the wave scattering from 2D dielectric surfaces are discretised into the MoM matrix equation. In addition the explicit entries for the quantities of the impedance matrix are given. The surface integral equation (2.171)-(2.174) are recasted into the form

$$\begin{aligned}
0 &= -\frac{I_x(\bar{r})}{2} + \iint \left\{ I_x(\bar{r}')g_1(R) \left[\frac{\partial f(x,y)}{\partial y} (y-y') + \frac{\partial f(x',y')}{\partial x'} (x-x') - (z-z') \right] \right. \\
&\quad + I_y(\bar{r}')g_1(R) \left[\frac{\partial f(x,y)}{\partial y} (x-x') + \frac{\partial f(x',y')}{\partial y'} (x-x') \right] \\
&\quad + I_n(\bar{r}')\frac{\epsilon_0}{\epsilon_1}g_1(R) \left[\frac{\partial f(x,y)}{\partial y} (z-z') + (y-y') \right] \left. \right\} dx'dy' \\
&\quad + \int \left\{ ik_0\eta_0 G_1 F_x(\bar{r}') \frac{\partial f(x,y)}{\partial y} \frac{\partial f(x',y')}{\partial x'} \right. \\
&\quad \left. + ik_0\eta_0 G_1 F_y(\bar{r}') \left[\frac{\partial f(x,y)}{\partial y} \frac{\partial f(x',y')}{\partial y'} + 1 \right] \right\} dx'dy' \tag{B-13}
\end{aligned}$$

$$\begin{aligned}
0 &= -\frac{I_y(\bar{r})}{2} + \iint \left\{ I_x(\bar{r}')g_1(R) \left[\frac{\partial f(x',y')}{\partial x'} (y-y') - \frac{\partial f(x,y)}{\partial x} (y-y') \right] \right. \\
&\quad + I_y(\bar{r}')g_1(R) \left[\frac{\partial f(x',y')}{\partial y'} (y-y') + \frac{\partial f(x,y)}{\partial x} (x-x') - (z-z') \right] \\
&\quad + I_n(\bar{r}')\frac{\epsilon_0}{\epsilon_1}G_2(R) \left[-\frac{\partial f(x,y)}{\partial x} (z-z') - (x-x') \right] \left. \right\} dx'dy' \\
&\quad + \int \left\{ ik_0\eta_0 G_1 F_x(\bar{r}') \left[-\frac{\partial f(x,y)}{\partial x} \frac{\partial f(x',y')}{\partial x'} - 1 \right] \right. \\
&\quad \left. + ik_0\eta_0 G_1 F_y(\bar{r}') \left[-\frac{\partial f(x,y)}{\partial x} \frac{\partial f(x',y')}{\partial y'} \right] \right\} dx'dy' \tag{B-14}
\end{aligned}$$

$$\begin{aligned}
 I_n^{inc}(\bar{r}) &= \frac{I_n(\bar{r})}{2} + \int \left\{ I_x(\bar{r}') g_0(R) \left[-\frac{\partial f(x', y')}{\partial x'} \frac{\partial f(x, y)}{\partial x} (y - y') \right. \right. \\
 &\quad \left. \left. + \frac{\partial f(x, y)}{\partial y} \left[\frac{\partial f(x', y')}{\partial x'} (x - x') - (z - z') \right] - (y - y') \right] \right. \\
 &\quad \left. + I_y(\bar{r}') g_0(R) \left[\frac{\partial f(x, y)}{\partial x} \left[(z - z') - \frac{\partial f(x', y')}{\partial y'} (y - y') \right] \right. \right. \\
 &\quad \left. \left. + \frac{\partial f(x, y)}{\partial y} \frac{\partial f(x', y')}{\partial y'} (x - x') + (x - x') \right] \right. \\
 &\quad \left. + I_n(\bar{r}') g_0(R) \left[\frac{\partial f(x, y)}{\partial x} (x - x') + \frac{\partial f(x, y)}{\partial y} (y - y') - (z - z') \right] \right\} dx' dy' \\
 &\quad + \int \left\{ ik_0 \eta_0 G_0 F_x(\bar{r}') \left[\frac{\partial f(x, y)}{\partial x} - \frac{\partial f(x', y')}{\partial x'} \right] \right. \\
 &\quad \left. + ik_0 \eta_0 G_0 F_y(\bar{r}') \left[\frac{\partial f(x, y)}{\partial y} - \frac{\partial f(x', y')}{\partial y'} \right] \right\} dx' dy' \tag{B-15}
 \end{aligned}$$

$$\begin{aligned}
 F_x^{inc}(\bar{r}) &= \frac{F_x(\bar{r})}{2} + \int \left\{ -i \frac{k_0}{\eta_0} G_0 I_x(\bar{r}') \frac{\partial f(x, y)}{\partial y} \frac{\partial f(x', y')}{\partial x'} \right. \\
 &\quad \left. - i \frac{k_0}{\eta_0} G_0 F_y(\bar{r}') \left[\frac{\partial f(x, y)}{\partial y} \frac{\partial f(x', y')}{\partial y'} + 1 \right] \right\} dx' dy' \\
 &\quad + \int \left\{ F_x(\bar{r}') g_0(R) \left[\frac{\partial f(x, y)}{\partial y} (y - y') + \frac{\partial f(x', y')}{\partial x'} (x - x') - (z - z') \right] \right. \\
 &\quad \left. + F_y(\bar{r}') g_0(R) \left[-\frac{\partial f(x, y)}{\partial y} (x - x') + \frac{\partial f(x', y')}{\partial y'} (x - x') \right] \right. \\
 &\quad \left. + F_n(\bar{r}') g_0(R) \left[\frac{\partial f(x, y)}{\partial y} (z - z') + (y - y') \right] \right\} dx' dy' \tag{B-16}
 \end{aligned}$$

$$\begin{aligned}
 F_y^{inc}(\bar{r}) &= \frac{F_y(\bar{r})}{2} + \int \left\{ -i \frac{k_0}{\eta_0} G_0 I_x(\bar{r}') \left[-\frac{\partial f(x, y)}{\partial x} \frac{\partial f(x', y')}{\partial x'} - 1 \right] \right. \\
 &\quad \left. - i \frac{k_0}{\eta_0} G_0 I_y(\bar{r}') \left[-\frac{\partial f(x, y)}{\partial x} \frac{\partial f(x', y')}{\partial y'} \right] \right\} dx' dy' \\
 &\quad + \int \left\{ F_x(\bar{r}') g_0(R) \left[\frac{\partial f(x', y')}{\partial x'} (y - y') - \frac{\partial f(x, y)}{\partial x} (y - y') \right] \right. \\
 &\quad \left. + F_y(\bar{r}') g_0(R) \left[\frac{\partial f(x', y')}{\partial y'} (y - y') + \frac{\partial f(x, y)}{\partial x} (x - x') - (z - z') \right] \right. \\
 &\quad \left. + F_n(\bar{r}') g_0(R) \left[-\frac{\partial f(x, y)}{\partial x} (z - z') - (x - x') \right] \right\} dx' dy' \tag{B-17}
 \end{aligned}$$

$$\begin{aligned}
 0 = & -\frac{F_n(\bar{r})}{2} + \int \left\{ -i \frac{k_0 \epsilon_1}{\eta_0 \epsilon_0} G_1 I_x(\bar{r}') \left[\frac{\partial f(x, y)}{\partial x} - \frac{\partial f(x', y')}{\partial x'} \right] \right. \\
 & \left. - i \frac{k_0 \epsilon_1}{\eta_0 \epsilon_0} G_1 F_y(\bar{r}') \left[\frac{\partial f(x, y)}{\partial y} - \frac{\partial f(x', y')}{\partial y'} \right] \right\} dx' dy' \\
 & + \int \left\{ F_x(\bar{r}') g_1(R) \left[-\frac{\partial f(x', y')}{\partial x'} \frac{\partial f(x, y)}{\partial x} (y - y') \right. \right. \\
 & \left. \left. + \frac{\partial f(x, y)}{\partial y} \left[\frac{\partial f(x', y')}{\partial x'} (x - x') - (z - z') \right] - (y - y') \right] \right. \\
 & \left. + F_y(\bar{r}') g_1(R) \left[\frac{\partial f(x, y)}{\partial x} \left[(z - z') - \frac{\partial f(x', y')}{\partial y'} (y - y') \right] \right. \right. \\
 & \left. \left. + \frac{\partial f(x, y)}{\partial y} \frac{\partial f(x', y')}{\partial y'} (x - x') + (x - x') \right] \right. \\
 & \left. + F_n(\bar{r}') g_1(R) \left[\frac{\partial f(x, y)}{\partial x} (x - x') + \frac{\partial f(x, y)}{\partial y} (y - y') - (z - z') \right] \right\} \\
 & dx' dy' \tag{B-18}
 \end{aligned}$$

In order to apply the method of moment formulation, the 2D surface is discretised into $N = N_x \times N_y$ rectangular grid where N_x and N_y are the number of discretisation points in the x and y direction of the surface. Each element has the dimension of $\Delta x \times \Delta y$. Using pulse basis functions and delta testing functions (point matching), the above equations are discretised into a dense system of $6N$ linear equations.

Appendix C - Results for chapter 3

In this appendix, the comparison between the pathloss generated by the ITIM and measurements are provided for 5 different profiles: Hjørringvej, Jerslev, Hadsund, Ravnstru and Mjels. We assume that the source is a line source radiating the TM^z polarised waves and located over the left most points of the profiles at the height of $10.4m$. The receiver antenna was a monopole located at a height of $2.4m$ and moved along the terrain surface. The pathloss is computed at 3 different frequencies: $144MHz$, $435MHz$ and $970MHz$.

Table C-1: Mean (η) and standard deviation (σ) of error in dB between the ITIM and measurements.

| Profile | Frequency | | | | | |
|-------------|-----------|----------|---------|----------|---------|----------|
| | 144 MHz | | 435 MHz | | 970 MHz | |
| | η | σ | η | σ | η | σ |
| Jerslev | 2.22 | 4.20 | 0.60 | 5.53 | -2.86 | 5.64 |
| Hadsund | 0.85 | 6.27 | 2.04 | 6.21 | -20.1 | 8.08 |
| Hjørringvej | -0.37 | 3.66 | -1.53 | 6.05 | -5.86 | 6.71 |
| Ravnstru | -4.46 | 4.14 | -0.53 | 5.20 | -6.52 | 7.91 |
| Mjels | 1.89 | 3.82 | 2.83 | 4.01 | 3.27 | 4.91 |

Table C-2: Mean (η) and standard deviation (σ) of error in dB between the HT-KED and measurements.

| Profile | Frequency | | | | | |
|-------------|-----------|----------|---------|----------|---------|----------|
| | 144 MHz | | 435 MHz | | 970 MHz | |
| | η | σ | η | σ | η | σ |
| Jerslev | 6.48 | 3.54 | 8.38 | 4.70 | 10.12 | 5.61 |
| Hadsund | 6.35 | 4.36 | 12.39 | 7.96 | 8.42 | 5.26 |
| Hjørringvej | 3.62 | 3.09 | 7.18 | 4.81 | 8.79 | 6.01 |
| Ravnstru | 5.25 | 3.31 | 13.39 | 7.29 | 14.43 | 9.17 |
| Mjels | 9.11 | 5.17 | 12.41 | 6.24 | 13.42 | 6.67 |

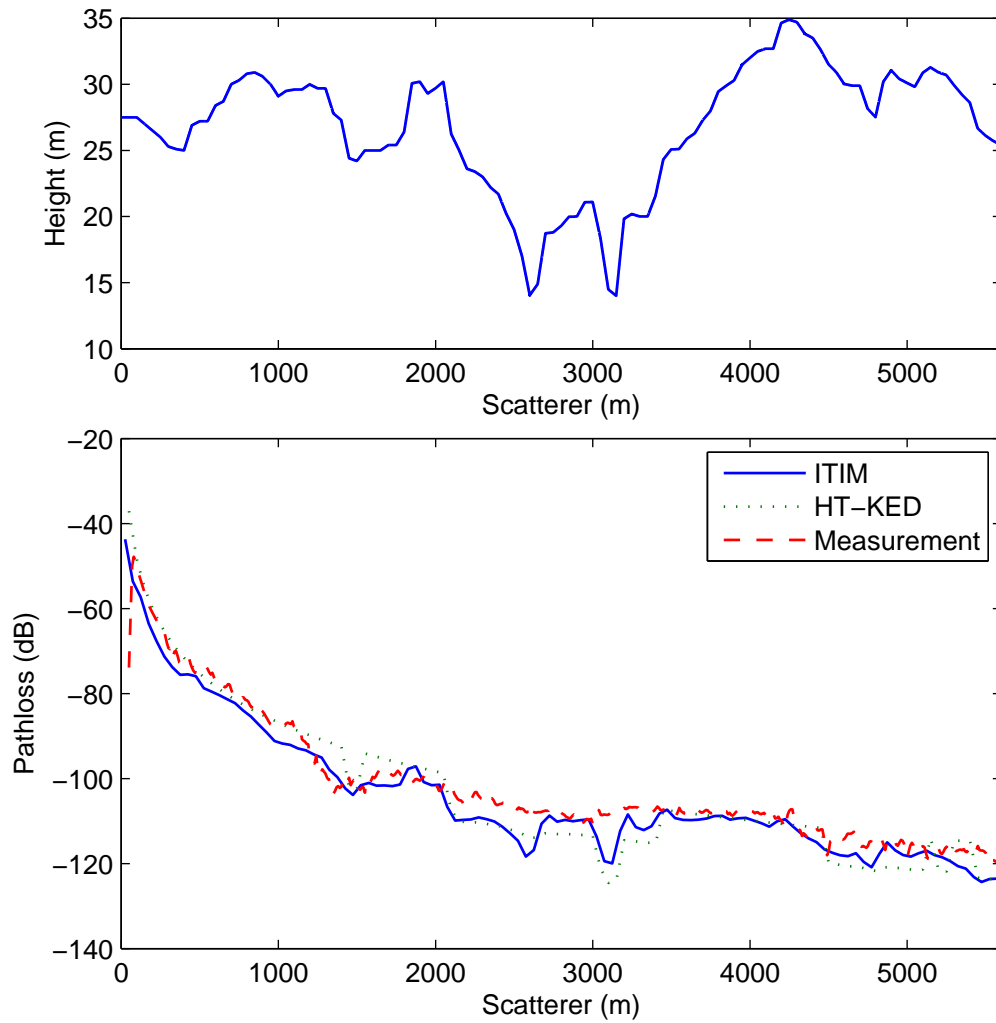


Figure C-1: Pathloss generated by ITIM, Hata Okumura model with multiple knife edge diffraction and measured data over Jerslev terrain profile. (a) Jerslev terrain profile, (b) Pathloss at 144MHz with TM^z Polarization.

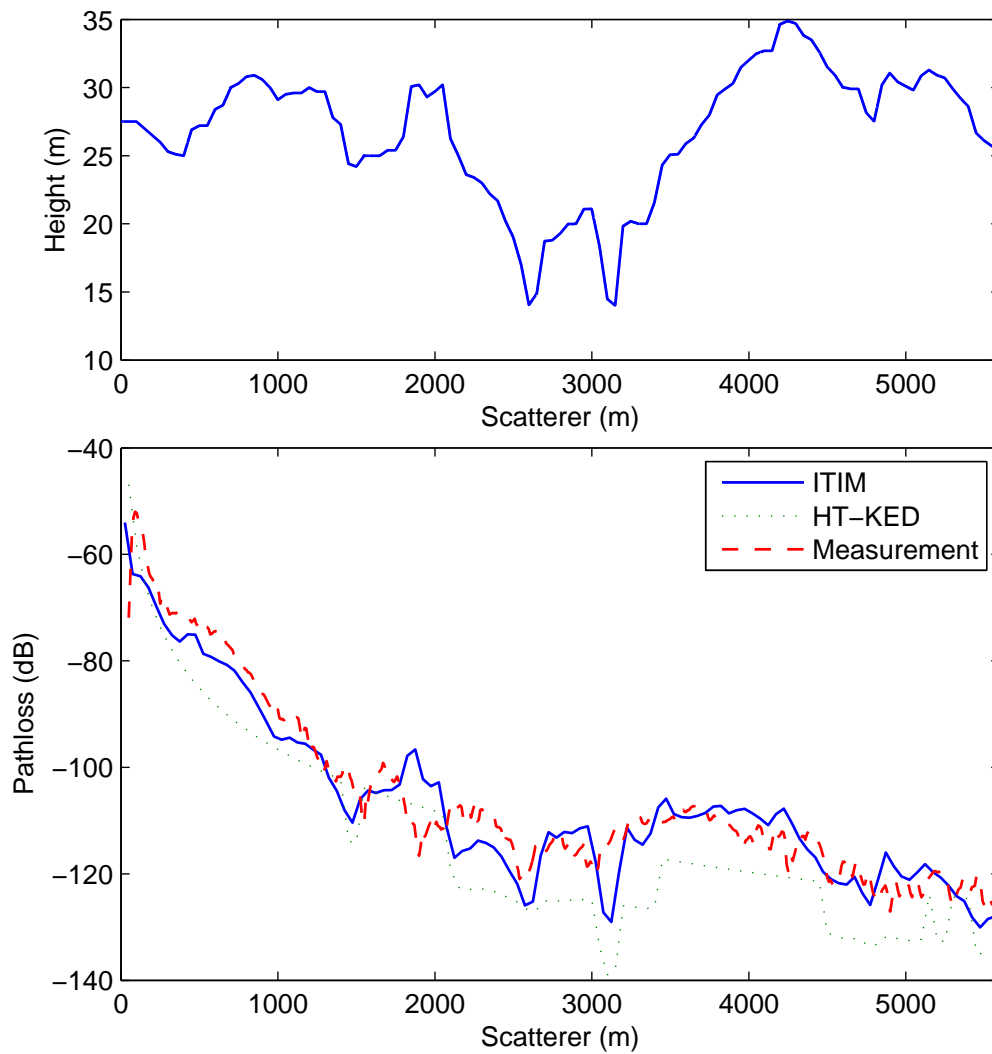


Figure C-2: Pathloss generated by ITIM, Hata Okumura model with multiple knife edge diffraction and measured data over Jerslev terrain profile. (a) Jerslev terrain profile, (b) Pathloss at 435MHz with TM^z Polarization.

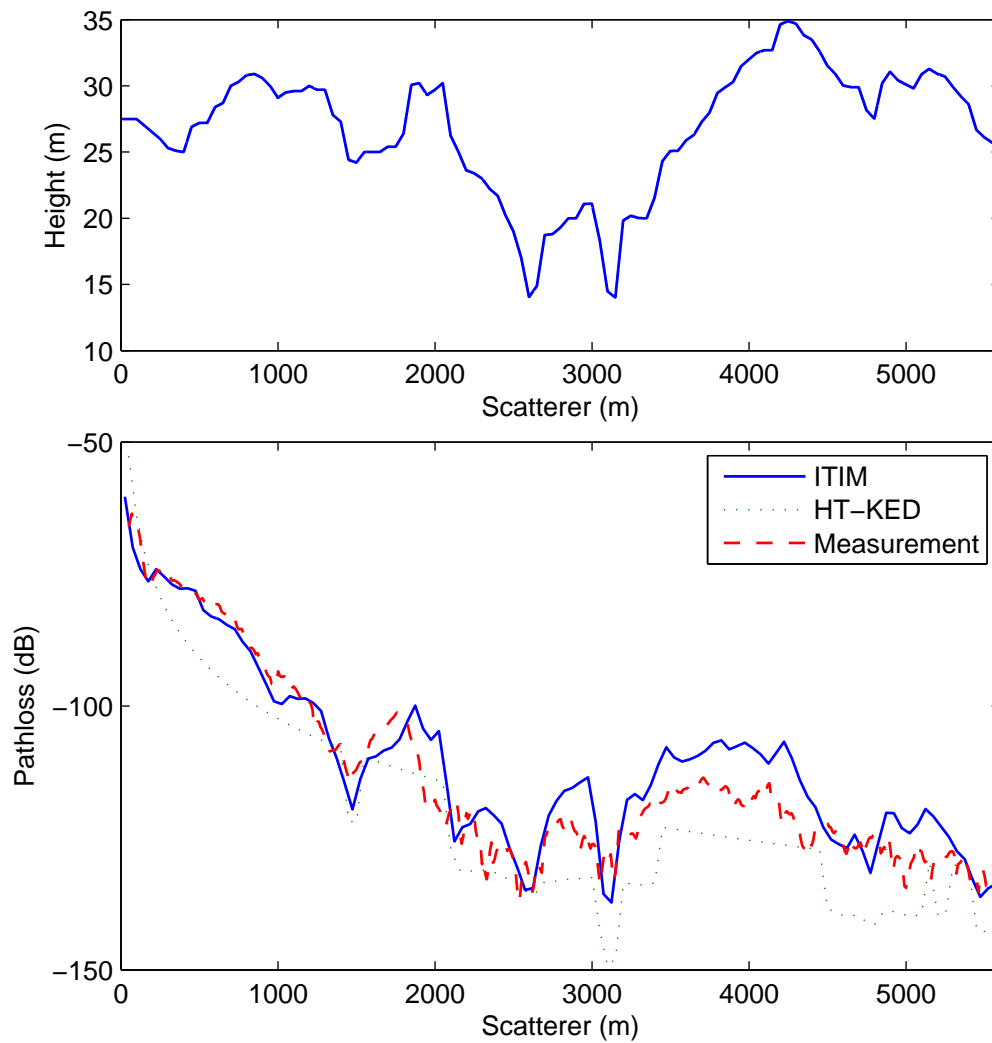


Figure C-3: Pathloss generated by ITIM, Hata Okumura model with multiple knife edge diffraction and measured data over Jerslev terrain profile. (a) Jerslev terrain profile, (b) Pathloss at 970MHz with TM^z Polarization.

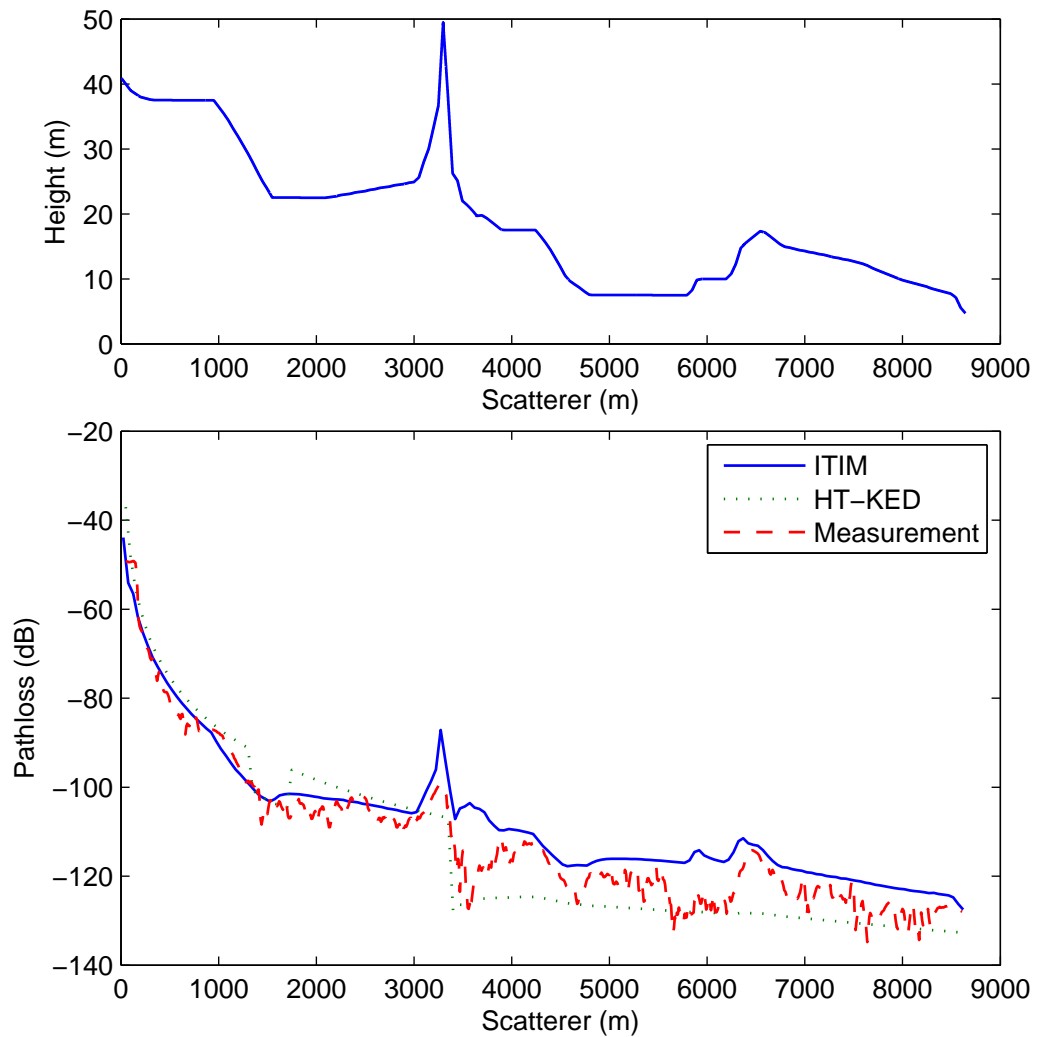


Figure C-4: Pathloss generated by ITIM, Hata Okumura model with multiple knife edge diffraction and measured data over Ravnstru terrain profile. (a) Ravnstru terrain profile, (b) Pathloss at 144MHz with TM^z Polarization.

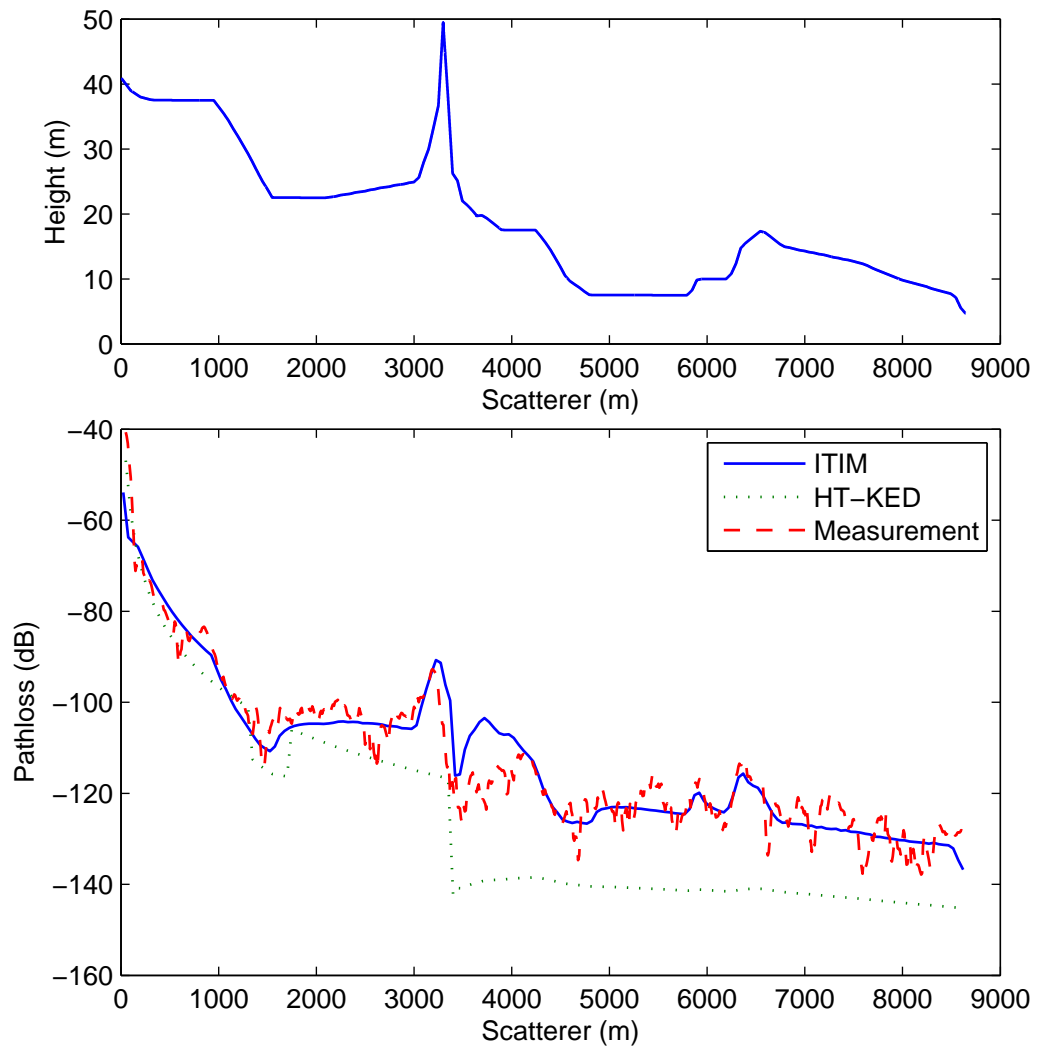


Figure C-5: Pathloss generated by ITIM, Hata Okumura model with multiple knife edge diffraction and measured data over Ravnstru terrain profile. (a) Ravnstru terrain profile, (b) Pathloss at 435MHz with TM^z Polarization.

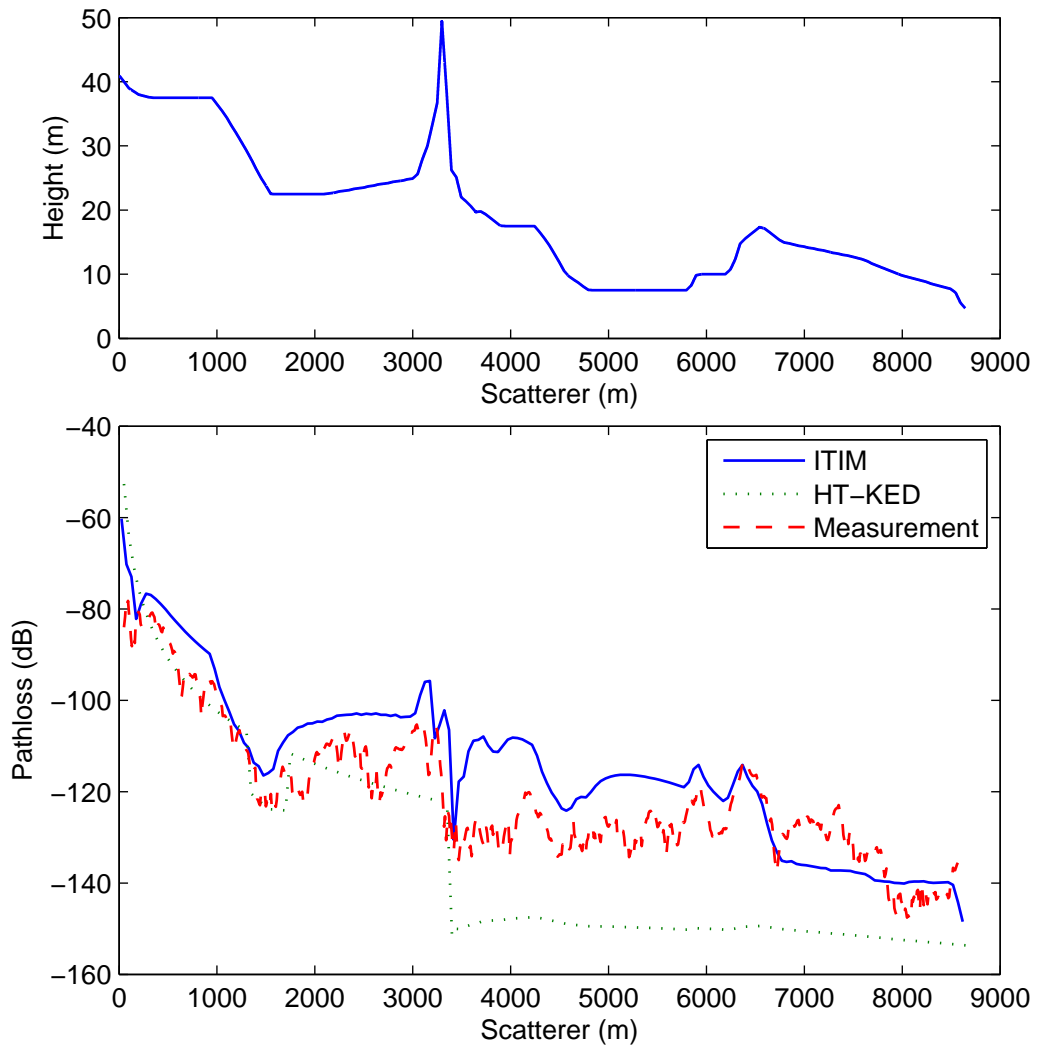


Figure C-6: Pathloss generated by ITIM, Hata Okumura model with multiple knife edge diffraction and measured data over Ravnstru terrain profile. (a) Ravnstru terrain profile, (b) Pathloss at $970MHz$ with TM^z Polarization.

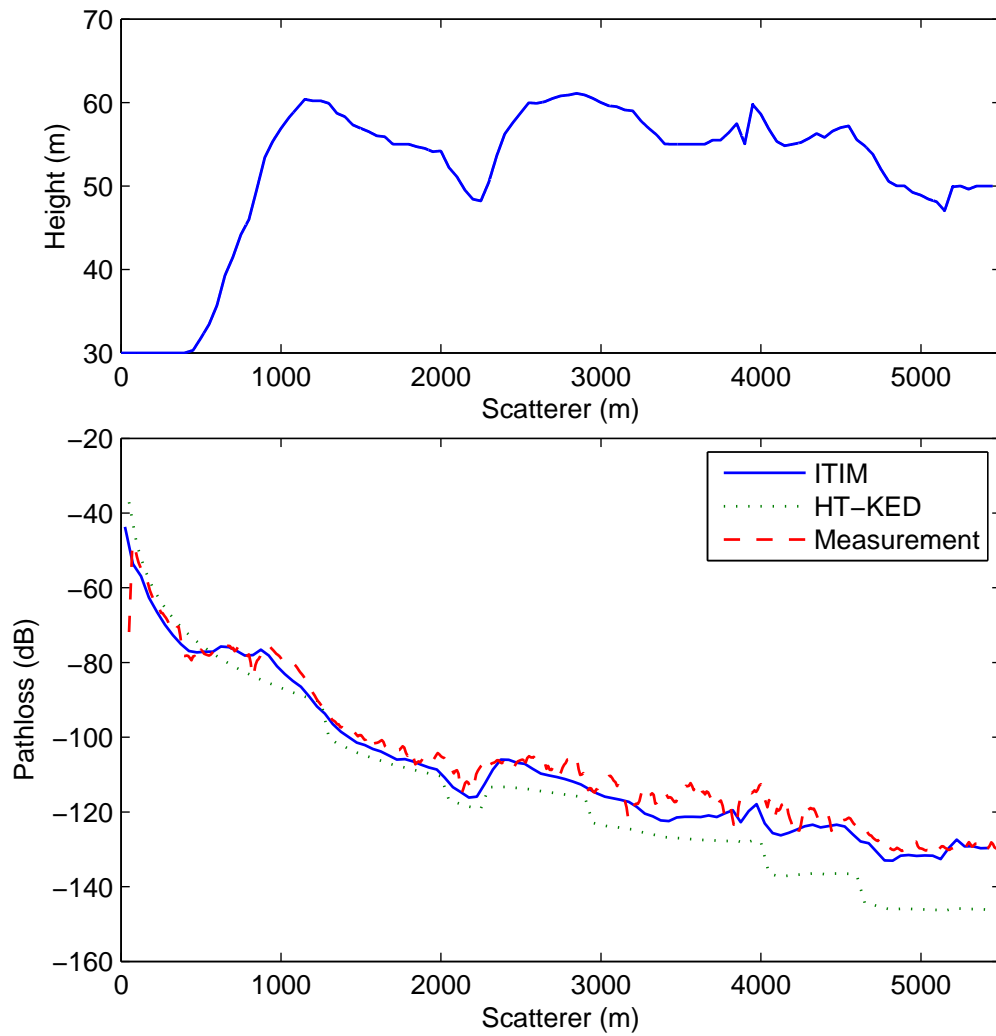


Figure C-7: Pathloss generated by ITIM, Hata Okumura model with multiple knife edge diffraction and measured data over Mjels terrain profile. (a) Mjels terrain profile, (b) Pathloss at 144MHz with TM^z Polarization.

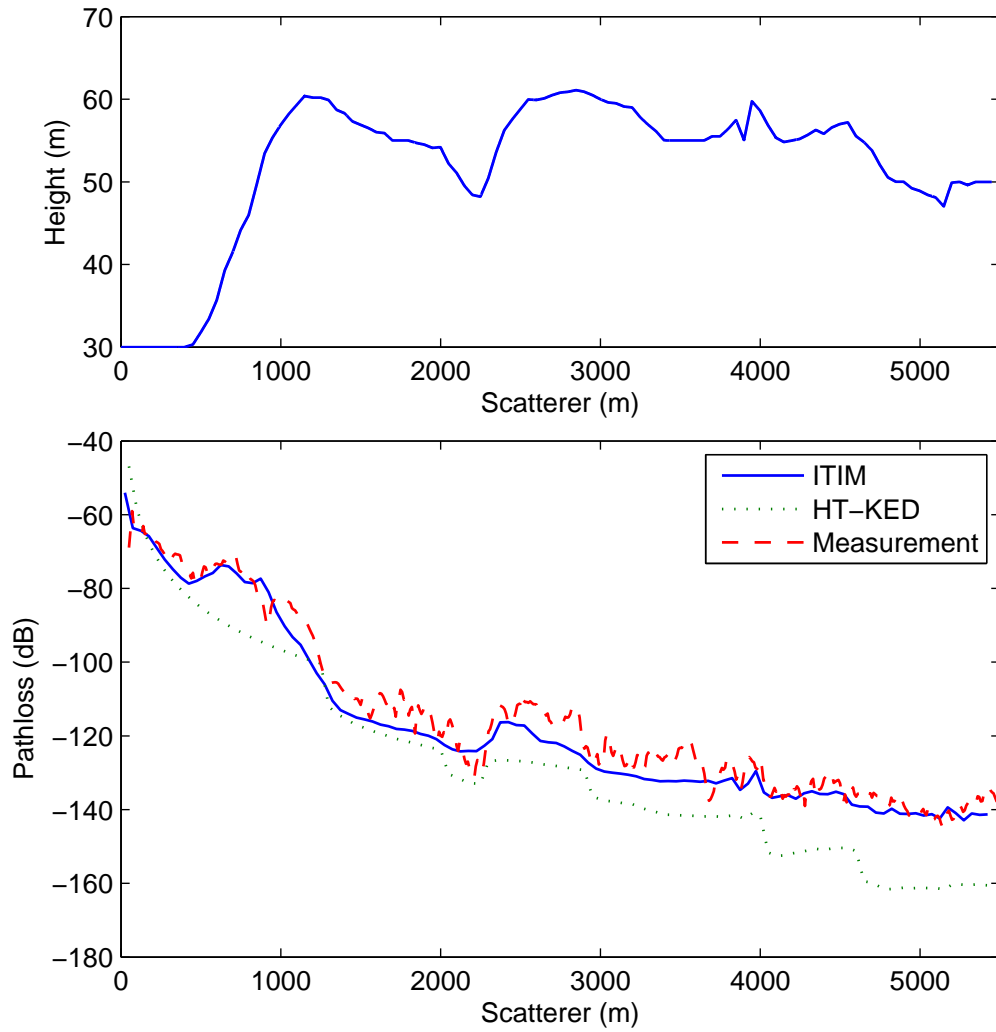


Figure C-8: Pathloss generated by ITIM, Hata Okumura model with multiple knife edge diffraction and measured data over Mjels terrain profile. (a) Mjels terrain profile, (b) Pathloss at 435MHz with TM^z Polarization.

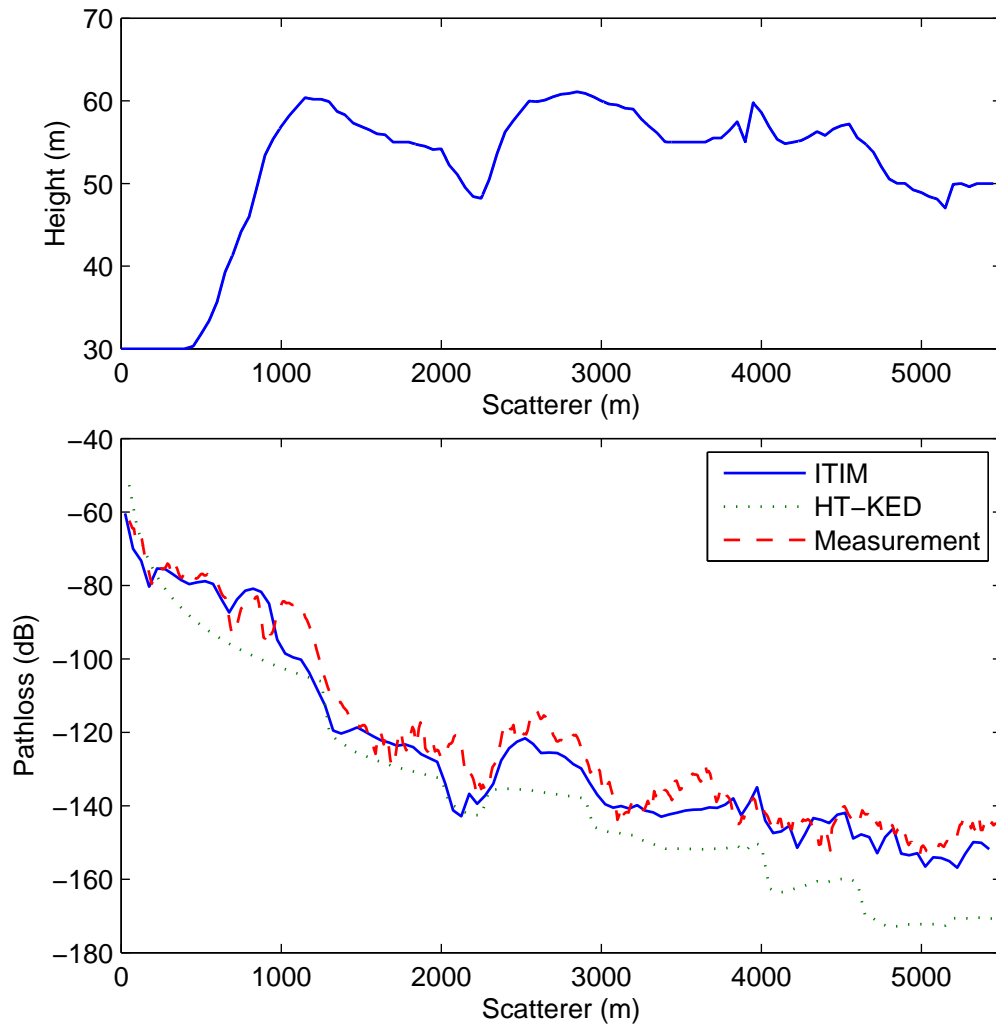


Figure C-9: Pathloss generated by ITIM, Hata Okumura model with multiple knife edge diffraction and measured data over Mjels terrain profile. (a) Mjels terrain profile, (b) Pathloss at 970MHz with TM^z Polarization.

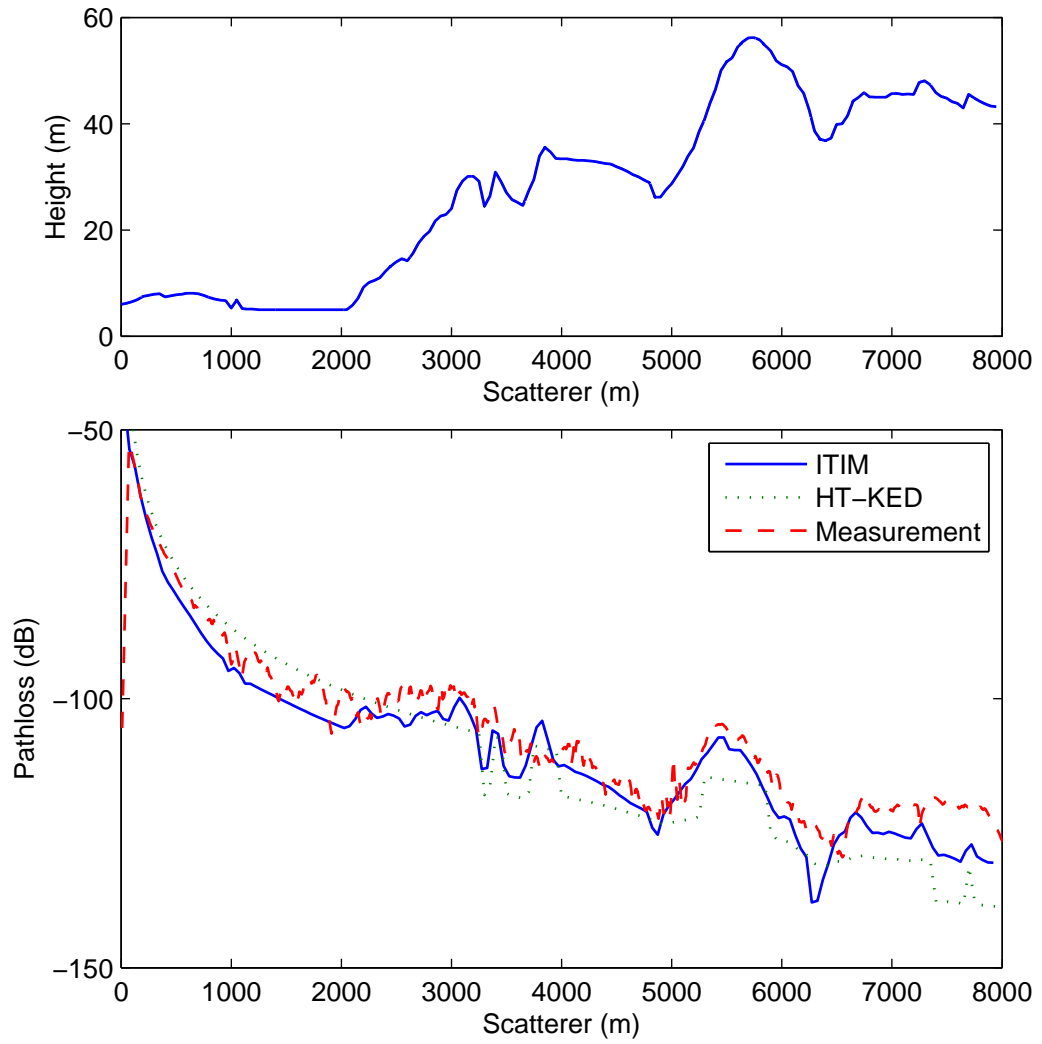


Figure C-10: Pathloss generated by ITIM, Hata Okumura model with multiple knife edge diffraction and measured data over Hadsund terrain profile. (a) Hadsund terrain profile, (b) Pathloss at $144MHz$ with TM^z Polarization.

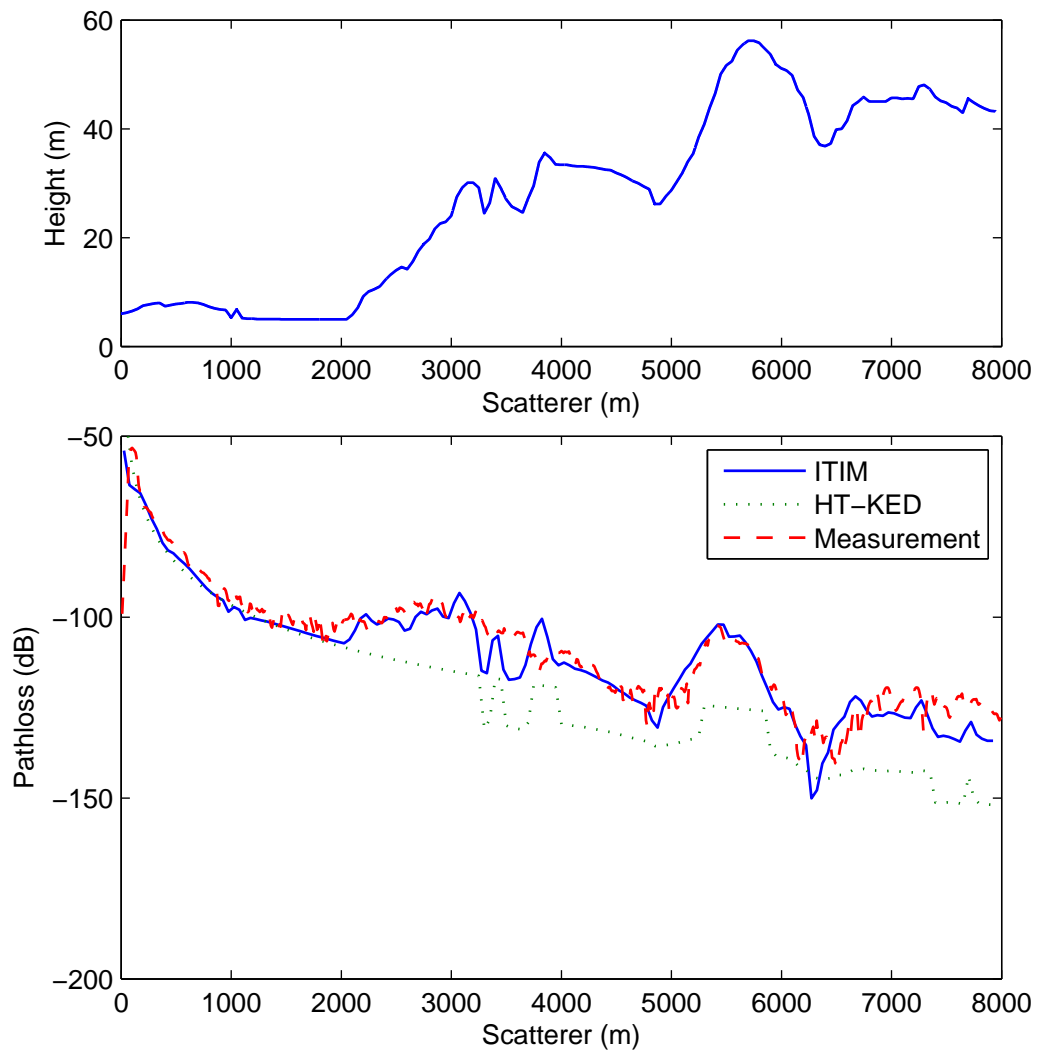


Figure C-11: Pathloss generated by ITIM, Hata Okumura model with multiple knife edge diffraction and measured data over Hadsund terrain profile. (a) Hadsund terrain profile, (b) Pathloss at 435MHz with TM^z Polarization.

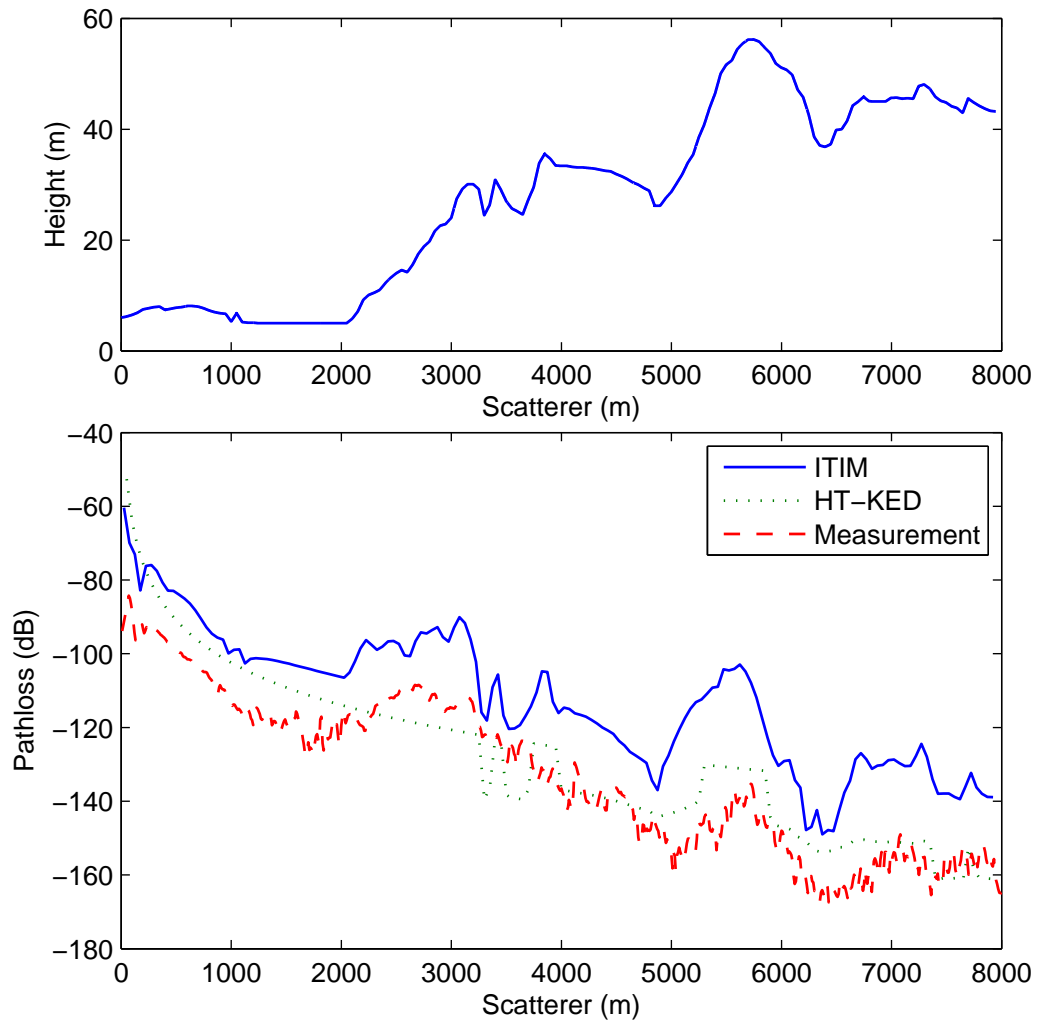


Figure C-12: Pathloss generated by ITIM, Hata Okumura model with multiple knife edge diffraction and measured data over Hadsund terrain profile. (a) Hadsund terrain profile, (b) Pathloss at 970MHz with TM^z Polarization.

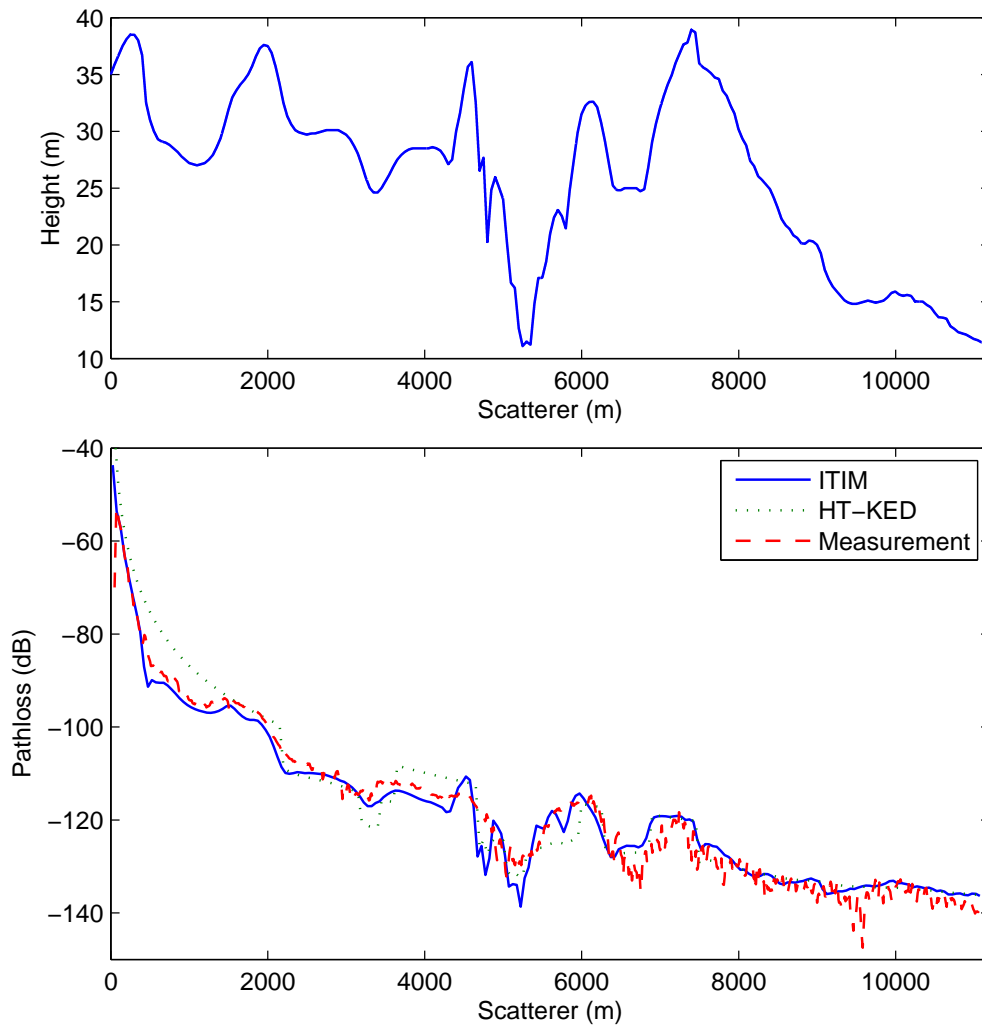


Figure C-13: Pathloss generated by ITIM, Hata Okumura model with multiple knife edge diffraction and measured data over Hjorringvej terrain profile. (a) Hjorringvej terrain profile, (b) Pathloss at 144MHz with TM^z Polarization.

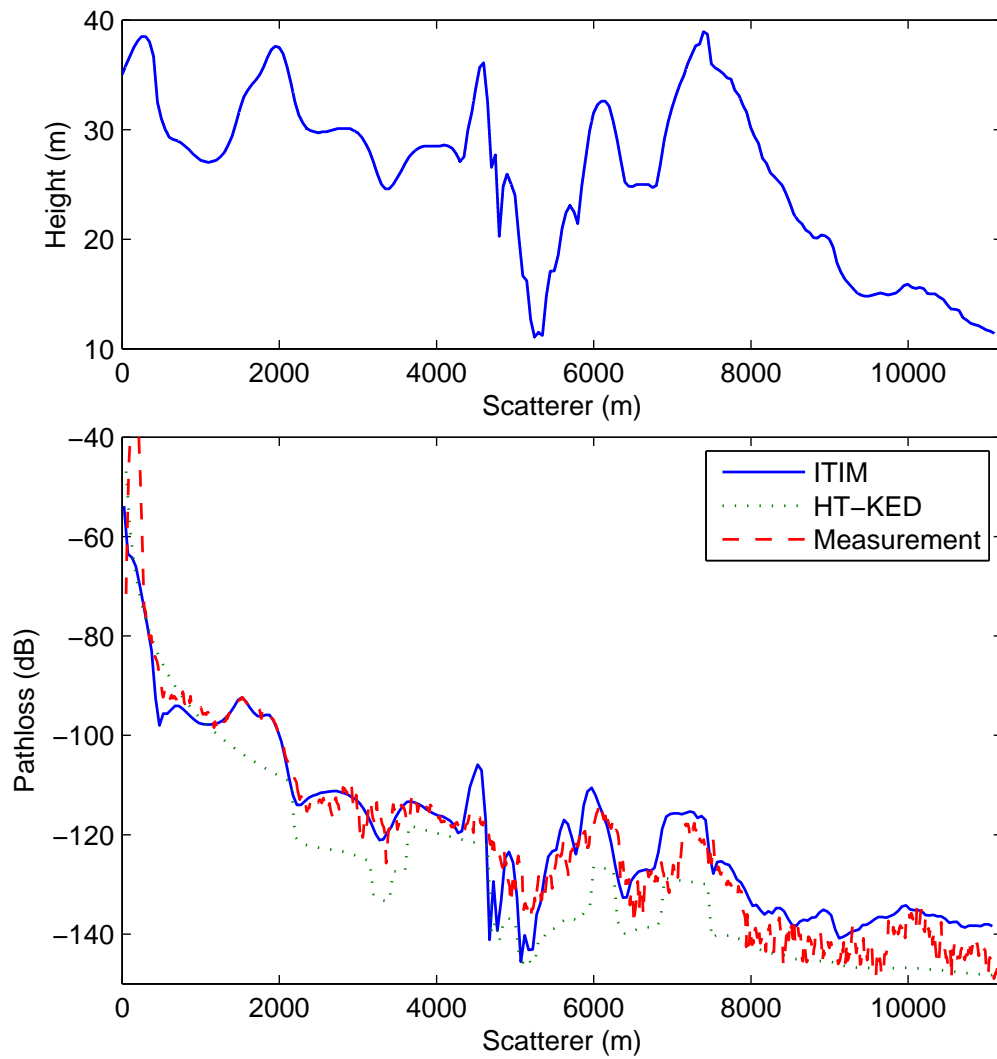


Figure C-14: Pathloss generated by ITIM, Hata Okumura model with multiple knife edge diffraction and measured data over Hjørringvej terrain profile. (a) Hjørringvej terrain profile, (b) Pathloss at 435MHz with TM^z Polarization.

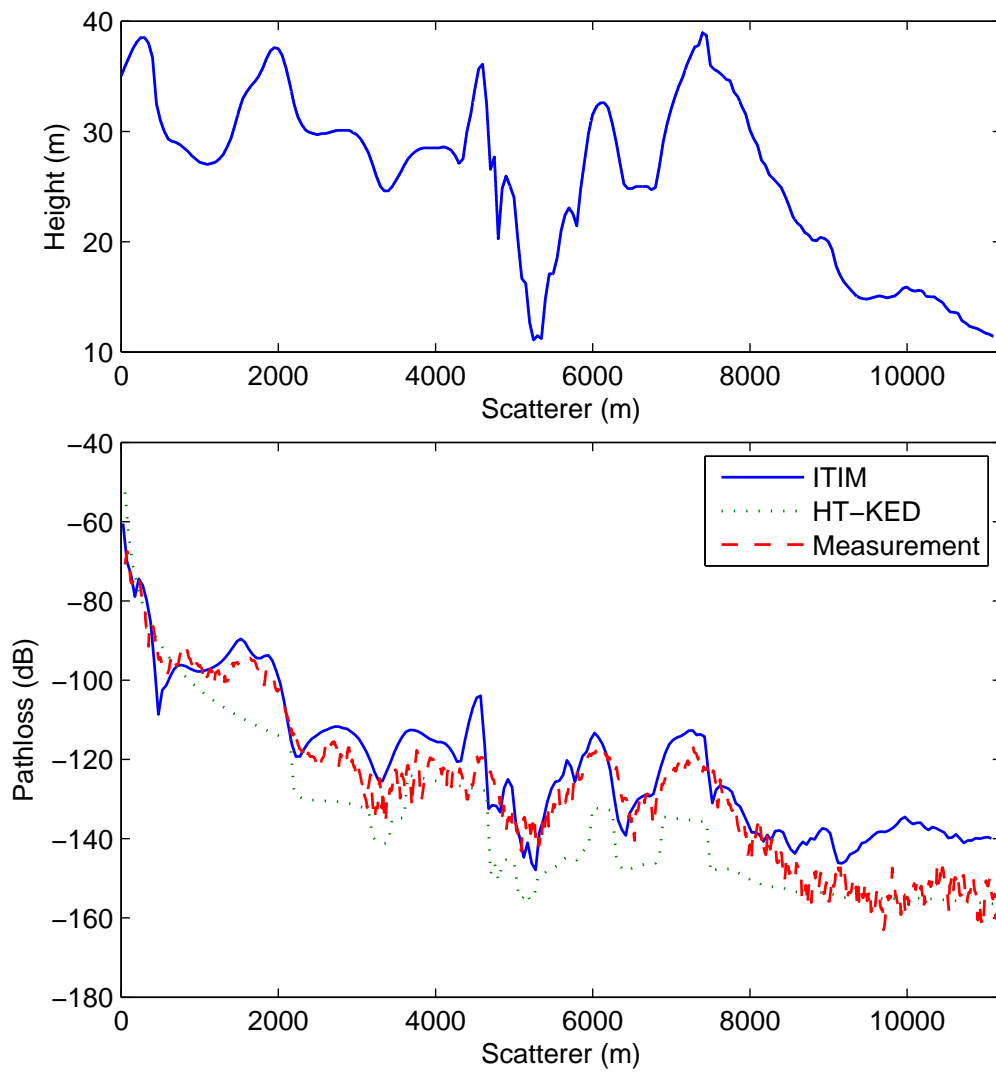


Figure C-15: Pathloss generated by ITIM, Hata Okumura model with multiple knife edge diffraction and measured data over Hjørringvej terrain profile. (a) Hjørringvej terrain profile, (b) Pathloss at 970MHz with TM^z Polarization.

Appendix D - Acronyms

| | |
|-----------------|--|
| BFBM | Block Forward Backward Method |
| BFBM-SA | Block Forward Backward Method with Spectral Acceleration |
| BMIA/CAG | Banded Matrix Iterative Approach with Canonical Grid |
| CBF | Characteristic Basis Function |
| CBFM | Characteristic Basis Function Method |
| CG | Conjugate Gradient |
| EFIE | Electric Field Integral Equation |
| EM | Electromagnetic |
| FAFFA | Fast Far Field Approximation |
| FBM | Forward Backward Method |
| FBM-SA | Forward Backward Method with Spectral Acceleration |
| FFT | Fast Fourier Transform |
| FMM | Fast Multipole Method |
| GFBM | Generalized Forward Backward Method |
| GMRES | Generalized Minimal Residual |
| HFBM | Hybrid Forward Backward Method |
| IE | Integral Equation |
| ITIM | Improved Tabulated Interaction Method |
| KED | Knife Edge Diffraction |
| MFIE | Magnetic Field Integral Equation |
| MoM | Method of Moments |

| | |
|----------------|---|
| NBSC | Normalized Bistatic Scattering Coefficient |
| PBTG | Physics-Based Two Grid |
| PBF | Primary Basis Function |
| PEC | Perfectly Conducting |
| RCS | Radar Cross Section |
| RRSS | Random Rough Surface Scattering |
| RWG | Rao-Wilton-Glisson |
| SA | Spectral Acceleration |
| SBF | Secondary Basis Function |
| SMCG | Sparse Matrix Canonical Grid |
| SSOR | Symmetric Successive Over Relaxation |
| TE | Transverse Electric |
| TIM | Tabulated Interaction Method |
| TL-ITIM | Two Level Improved Tabulated Interaction Method |
| TM | Transverse Magnetic |

Publications

1 Journals

- [1] 2014 D. Trinh, C. Brennan: Block Forward Backward Method with Spectral Acceleration for Scattering from Two Dimensional Dielectric Random Rough Surfaces. To be submitted to : IEEE Transactions on Antennas and Propagation.
- [2] 2014 C. Brennan, D. Trinh, R. Mittra: Improved tabulated interaction method for electromagnetic scattering from lossy irregular terrain profiles. Accepted for publication subject to revision: IEEE Transactions on Antennas and Propagation.
- [3] 2013 D. Trinh, C. Brennan, M. Mullen, P. Bradley and M. Condon: Improved forward backward method with spectral acceleration for scattering from randomly rough lossy surfaces. In: IEEE Transactions on Antennas and Propagation 61, No. 7, pp. 3922–3926.
- [4] 2012 D. Trinh, P. Bradley and C. Brennan: Fast Fourier transform based iterative method for electromagnetic scattering from 1d flat surfaces. In: IEEE Transactions on Antennas and Propagation 60, No. 11, pp. 5464–5467.

2 Proceedings

- [5] April 2014 C. Brennan, D. Trinh: Fullwave Computation of Path Loss in Urban Areas. Accepted for publication in Proceedings of 2014 European Conference on Antennas and Propagation (EUCAP).
- [6] May 2013 D. Trinh, R. Mittra and C. Brennan: Full wave analysis of EM wave propagation over terrain using the improved tabulated interaction method. In: Proceedings of 2013 URSI International Symposium on Electromagnetic Theory (EMTS), pp. 143–146.
- [7] April 2013 D. Trinh, C. Brennan: Comparison of improved forward backward method and symmetric successive over relaxation for computing the scattering from randomly rough lossy surfaces. In: IET International Conference on Information and Communications Technologies (IETICT 2013).
- [8] November 2012 D. Trinh, C. Brennan: Improved forward backward method with spectral acceleration for scattering from exponentially correlated rough lossy surfaces. In: Loughborough Antennas and Propagation Conference (LAPC), 2012.

- [9] September 2012 Vinh Pham-Xuan, D. Trinh, I. de Koster, K. Van Dongen, M. Condon and C. Brennan): Solution of large-scale wideband em wave scattering problems using fast fourier transform and the asymptotic waveform evaluation technique. In: 2012 International Conference on Electromagnetics in Advanced Applications (ICEAA), pp. 1133–1136.
- [10] March 2012 D. Trinh, C. Brennan : Tabulated interaction method for electromagnetic scattering from lossy irregular terrain profiles. In: 2012 6th European Conference on Antennas and Propagation (EUCAP), pp. 35–38.
- [11] March 2012 D. Trinh, C. Brennan: Tabulated interaction method for electromagnetic wave propagation in rural areas. In: 2012 Research Colloquium Communications and Radio Science into the 21st Century.
- [12] September 2012 D. Trinh, C. Brennan: Tabulated interaction method for electromagnetic wave propagation prediction in rural and mountainous areas. In: 2012 International Conference on Electromagnetics in Advanced Applications (ICEAA), pp. 1137–1140.
- [13] September 2011 D. Trinh, C. Brennan, M. Mullen and P. Bradley: Accelerated forward backward iterative solution for scattering from randomly rough lossy surfaces. In: 2011 International Conference on Electromagnetics in Advanced Applications (ICEAA), pp. 1290–1293.
- [14] September 2011 D. Trinh, C. Brennan, M. Mullen and P. Bradley: Extension of fast far field algorithm to propagation over lossy dielectric terrain and buildings. In: 2011 IEEE-APS Topical Conference on Antennas and Propagation in Wireless Communications (APWC), pp. 1249–1252.

3 COST papers

- [15] September 2013 C. Brennan, D. Trinh: Application of fullwave method in computation of scattering problem in urban areas. In: COST IC1004.
- [16] February. 2012 C. Brennan, D. Trinh: Application of ray tracing and accelerated fullwave method in computation of scattering problem over terrain and building profiles. In: COST IC1004.
- [17] October 2011 C. Brennan, D. Trinh and J. Diskin: Recent advances in full-wave and asymptotic propagation modeling. In: COST IC1004.

Bibliography

- [1] L. Tsang and J.A. Kong. *Scattering of Electromagnetic Waves: Numerical Simulation*. New York: Wiley, 2001.
- [2] Te-Kao Wu and Leonard L. Tsai. Scattering by arbitrarily cross-sectioned layered lossy dielectric cylinders. *IEEE Transactions on Antennas and Propagation*, 25(4):518–524, 1977.
- [3] D. Entekhabi, E.G. Njoku, P.E. O’Neill, K.H. Kellogg, W.T. Crow, W.N. Edelstein, J.K. Entin, S.D. Goodman, T.J. Jackson, J. Johnson, J. Kimball, J.R. Piepmeier, R.D. Koster, N. Martin, K.C. McDonald, M. Moghaddam, S. Moran, R. Reichle, J.-C. Shi, M.W. Spencer, S.W. Thurman, Leung Tsang, and J. Van Zyl. The soil moisture active passive (SMAP) mission. *Proceedings of the IEEE*, 98(5):704–716, May 2010.
- [4] M. Hata. Empirical formula for propagation loss in land mobile radio services. *IEEE Transactions on Vehicular Technology*, 29(3):317–325, 1980.
- [5] Y. Okumura. Field strength and its variability in vhf and uhf land-mobile radio service. *Rev. Elec. Comm. Lab*, 16(9-10):825–873, 1968.
- [6] Cost 231 final report, digital mobile radio: Cost 231 view on the evolution towards 3rd generation systems, commission of the european communities and cost telecommunications, Brussel. 1998.
- [7] S.R. Saunders. *Antenna and Propagation for Wireless Communication Systems*. Wiley, 2007.
- [8] K. Bullington. Radio propagation for vehicular communications. *IEEE Transactions on Vehicular Technology*, 26(4):295–308, 1977.
- [9] Jess Epstein and D.W. Peterson. An experimental study of wave propagation at 850 MC. *Proceedings of the IRE*, 41(5):595–611, 1953.
- [10] J. Deygout. Multiple knife-edge diffraction of microwaves. *IEEE Transactions on Antennas and Propagation*, 14(4):480–489, 1966.
- [11] C.L. Giovaneli. An analysis of simplified solutions for multiple knife-edge diffraction. *IEEE Transactions on Antennas and Propagation*, 32(3):297–301, 1984.

- [12] V. Erceg, S.J. Fortune, J. Ling, A.J. Rustako, and R.A. Valenzuela. Comparisons of a computer-based propagation prediction tool with experimental data collected in urban microcellular environments. *IEEE Journal on Selected Areas in Communications*, 15(4):677–684, 1997.
- [13] D.N. Schettino, F.J.S. Moreira, and C.G. Rego. Efficient ray tracing for radio channel characterization of urban scenarios. *IEEE Transactions on Magnetics*, 43(4):1305–1308, 2007.
- [14] R.A. Valenzuela. A ray tracing approach to predicting indoor wireless transmission. In *Vehicular Technology Conference, 1993., 43rd IEEE*, pages 214–218, 1993.
- [15] K. Rizk, J. Wagen, and F. Gardiol. Two-dimensional ray-tracing modeling for propagation prediction in microcellular environments. *IEEE Transactions on Vehicular Technology*, 46(2):508–518, May 1997.
- [16] K. Rizk, R. Valenzuela, S. Fortune, D. Chizhik, and F. Gardiol. Lateral, full-3d and vertical plane propagation in microcells and small cells. In *1998. VTC 98. 48th IEEE Vehicular Technology Conference*, volume 2, pages 998–1003 vol.2, 1998.
- [17] Shiun-Chi Jan and Shyh-Kang Jeng. A novel propagation modeling for microcellular communications in urban environments. *IEEE Transactions on Vehicular Technology*, 46(4):1021–1026, Nov. 1997.
- [18] Zhengqing Yun, Zhijun Zhang, and M.F. Iskander. A ray-tracing method based on the triangular grid approach and application to propagation prediction in urban environments. *IEEE Transactions on Antennas and Propagation*, 50(5):750–758, 2002.
- [19] Y. Corre and Y. Lostanlen. Three-dimensional urban EM wave propagation model for radio network planning and optimization over large areas. *IEEE Transactions on Vehicular Technology*, 58(7):3112–3123, 2009.
- [20] Seong-Cheol Kim, Jr. Guarino, B.J., III Willis, T., V. Erceg, S.J. Fortune, R.A. Valenzuela, L.W. Thomas, J. Ling, and J.D. Moore. Radio propagation measurements and prediction using three-dimensional ray tracing in urban environments at 908 MHz and 1.9 GHz. *IEEE Transactions on Vehicular Technology*, 48(3):931–946, 1999.
- [21] G.E. Athanasiadou and A.R. Nix. Investigation into the sensitivity of the power predictions of a microcellular ray tracing propagation model. *IEEE Transactions on Vehicular Technology*, 49(4):1140–1151, Jul 2000.
- [22] F. Mani and C. Oestges. A ray based method to evaluate scattering by vegetation elements. *IEEE Transactions on Antennas and Propagation*, 60(8):4006–4009, Aug. 2012.
- [23] Y. L C De Jong and M. H A J Herben. A tree-scattering model for improved propagation prediction in urban microcells. *IEEE Transactions on Vehicular Technology*, 53(2):503–513, March 2004.

- [24] F.A. Agelet, A. Formella, J.M. Hernando Rabanos, F.I. de Vicente, and F.P. Fontan. Efficient ray-tracing acceleration techniques for radio propagation modeling. *IEEE Transactions on Vehicular Technology*, 49(6):2089–2104, Nov. 2000.
- [25] J.T. Hviid, J.B. Andersen, J. Toftgard, and J. Bojer. Terrain-based propagation model for rural area—an integral equation approach. *IEEE Transactions on Antennas and Propagation*, 43(1):41–46, 1995.
- [26] S. Ray A. Peterson and R. Mittra. *Parabolic equation methods for electromagnetic wave propagation*. The Institution of Electrical Engineers, 2000.
- [27] M.F. Levy. Parabolic equation modelling of propagation over irregular terrain. In *1991. ICAP 91., Seventh International Conference on Antennas and Propagation*, pages 816–819 vol.2, Apr 1991.
- [28] M.F. Levy. Diffraction studies in urban environment with wide-angle parabolic equation method. *Electronics Letters*, 28(16):1491–1492, July 1992.
- [29] M.F. Levy. Diffraction studies in urban environment with wide-angle parabolic equation method. *Electronics Letters*, 28(16):1491–1492, July 1992.
- [30] A.A. Zaporozhets and M.F. Levy. Modelling of radiowave propagation in urban environment with parabolic equation method. *Electronics Letters*, 32(17):1615–1616, Aug. 1996.
- [31] A.A. Zaporozhets. Application of vector parabolic equation method to urban radiowave propagation problems. *IEE Proceedings on Microwaves, Antennas and Propagation*, 146(4):253–256, Aug. 1999.
- [32] C.F. Smith, A.F. Peterson, and R. Mittra. The biconjugate gradient method for electromagnetic scattering. *IEEE Transactions on Antennas and Propagation*, 38(6):938–940, June 1990.
- [33] J.C. West and J.M. Sturm. On iterative approaches for electromagnetic rough-surface scattering problems. *IEEE Transactions on Antennas and Propagation*, 47(8):1281–1288, Aug. 1999.
- [34] D. Holliday, L. L. DeRaad, and G. J. St-Cyr. Forward-backward: a new method for computing low-grazing angle scattering. *IEEE Transactions on Antennas and Propagation*, 44(1):722, May 1996.
- [35] M. Rodriguez Pino, L. Landesa, J.L. Rodriguez, F. Obelleiro, and R.J. Burkholder. The generalized forward-backward method for analyzing the scattering from targets on ocean-like rough surfaces. *IEEE Transactions on Antennas and Propagation*, 47(6):961–969, June 1999.
- [36] Hsi-Tseng Chou and Joel T. Johnson. A novel acceleration algorithm for the computation of scattering from rough surfaces with the forward-backward method. *Radio Science*, 33:1277–1287, 1998.

- [37] Hsi-Tseng Chou and J.T. Johnson. Formulation of forward-backward method using novel spectral acceleration for the modeling of scattering from impedance rough surfaces. *IEEE Transactions on Geoscience and Remote Sensing*, 38(1):605–607, Jan. 2000.
- [38] J.A. López, M.R. Pino, F. Obelleiro, and J.L. Rodríguez. Application of the spectral acceleration forward-backward method to coverage analysis over terrain profiles. *Journal of Electromagnetic Waves and Applications*, 15(8):1049–1074, 2001.
- [39] C. Brennan and P.J. Cullen. *IEEE Transactions on Antennas and Propagation*, 46(6):881–890, June 1998.
- [40] C. Brennan and P.J. Cullen. Tabulated interaction method for UHF terrain propagation problems. *IEEE Transactions on Antennas and Propagation*, 46(5):738–739, 1998.
- [41] C. Brennan and P.J. Cullen. Multilevel tabulated interaction method applied to UHF propagation over irregular terrain. *IEEE Transactions on Antennas and Propagation*, 47(10):1574–1578, 1999.
- [42] C. Brennan, P.J. Cullen, and L. Rossi. An MFIE-based tabulated interaction method for uhf terrain propagation problems. *IEEE Transactions on Antennas and Propagation*, 48(6):1003–1005, 2000.
- [43] V. V. S. Prakash and Raj Mittra. Characteristic basis function method: A new technique for efficient solution of method of moments matrix equations. *Microwave and Optical Technology Letters*, 36:95–100, 2003.
- [44] A. Yagbasan, C.A. Tunc, V.B. Erturk, A. Altintas, and R. Mittra. Characteristic basis function method for solving electromagnetic scattering problems over rough terrain profiles. *IEEE Transactions on Antennas and Propagation*, 58(5):1579–1589, May 2010.
- [45] Y.H. Kerr. Soil moisture from space: Where are we? *Hydrogeology Journal*, 15(1):117–120, Feb. 2007.
- [46] A. Merzouki, H. McNairn, and A. Pacheco. Mapping soil moisture using radarsat-2 data and local autocorrelation statistics. *IEEE Journal of Selected Topics in Applied Earth Observations and Remote Sensing*, 4(1):128–137, March 2011.
- [47] H.M.J. Barre, B. Duesmann, and Y.H. Kerr. SMOS: The mission and the system. *IEEE Transactions on Geoscience and Remote Sensing*, 46(3):587–593, March 2008.
- [48] Y.H. Kerr, P. Waldteufel, J.-P. Wigneron, J. Martinuzzi, J. Font, and M. Berger. Soil moisture retrieval from space: the soil moisture and ocean salinity (SMOS) mission. *IEEE Transactions on Geoscience and Remote Sensing*, 39(8):1729–1735, Aug. 2001.
- [49] L. Tsang and J.A. Kong. *Scattering of Electromagnetic Waves: Theories and Applications*. New York: Wiley, 2001.

- [50] A. Ishimaru. *Wave Propagation and Scattering in Random Media*. NY: Academic, 1978.
- [51] J.A. Kong. *Electromagnetic Wave Theory*. New York: Wiley, 1986.
- [52] W.C. Chew V. Jandhyala. A fast algorithm for the analysis of scattering by dielectric rough surface. *Journal of the Optical Society of America A*, pages 1877–1885, 1998.
- [53] V Rokhlin. Rapid solution of integral equations of scattering theory in two dimensions. *Journal of Computational Physics*, 86(2):414 – 439, 1990.
- [54] R. Coifman, V. Rokhlin, and S. Wandzura. The fast multipole method for the wave equation: a pedestrian prescription. *IEEE Antennas and Propagation Magazine*, 35(3):7–12, 1993.
- [55] V. Jandhyala, E. Michielssen, S. Balasubramaniam, and Weng Cho Chew. A combined steepest descent-fast multipole algorithm for the fast analysis of three-dimensional scattering by rough surfaces. *IEEE Transactions on Geoscience and Remote Sensing*, 36(3):738–748, 1998.
- [56] K. Pak P. Phu L. Tsang, C.H. Chan. A banded matrix iterative approach to monte carlo simulations of large-scale random rough surface scattering: TE case. *Journal of Electromagnetic Waves and Applications*, 7(9):1185–1200, 1993.
- [57] K. Pak P. Phu L. Tsang, C.H. Chan. Monte carlo simulations of large-scale composite random rough surface scattering based on the banded-matrix iterative method. *Journal of the Optical Society of America A*, 11(2):691–696, 1994.
- [58] Leung Tsang, C.H. Chan, K. Pak, and H. Sangani. Monte-carlo simulations of large-scale problems of random rough surface scattering and applications to grazing incidence with the BMIA/canonical grid method. *IEEE Transactions on Antennas and Propagation*, 43(8):851–859, 1995.
- [59] Qin Li, Chi-Hou Chan, and Leung Tsang. Monte carlo simulations of wave scattering from lossy dielectric random rough surfaces using the physics-based two-grid method and the canonical-grid method. *IEEE Transactions on Antennas and Propagation*, 47(4):752–763, 1999.
- [60] Qin Li, Chi-Hou Chan, Leung Tsang, and Guifu Zhang. Wave scattering from a lossy dielectric rough surface using PBTG-BMIA/CAG and applications to passive remote sensing. In *1998 IEEE International Geoscience and Remote Sensing Symposium Proceedings, 1998. IGARSS '98.*, volume 3, pages 1469–1471 vol.3, 1998.
- [61] C.D. Moss, Tomasz M. Grzegorzcyk, H.C. Han, and Jin Au Kong. Forward-backward method with spectral acceleration for scattering from layered rough surfaces. *IEEE Transactions on Antennas and Propagation*, 54(3):1006–1016, 2006.

- [62] Bin Liu, Zengyuan Li, and Yang Du. A fast numerical method for electromagnetic scattering from dielectric rough surfaces. *IEEE Transactions on Antennas and Propagation*, 59(1):180–188, Jan. 2011.
- [63] Lin Zhou, Leung Tsang, V. Jandhyala, Qin Li, and C.H. Chan. Emissivity simulations in passive microwave remote sensing with 3-d numerical solutions of maxwell equations. *IEEE Transactions on Geoscience and Remote Sensing*, 42(8):1739–1748, 2004.
- [64] Shaowu Huang, Leung Tsang, E.G. Njoku, and Kuan Shan Chan. Backscattering coefficients, coherent reflectivities, and emissivities of randomly rough soil surfaces at L-Band for SMAP applications based on numerical solutions of maxwell equations in three-dimensional simulations. *IEEE Transactions on Geoscience and Remote Sensing*, 48(6):2557–2568, 2010.
- [65] C. H. Chan and L. Tsang. A sparse-matrix canonical-grid method for scattering by many scatterers. *Microwave and Optical Technology Letters*, 8(2):114–118, 1995.
- [66] L. Tsang K.S. Pak and J. Johnson. Numerical simulations and backscattering enhancement of electromagnetic waves from two-dimensional dielectric random rough surfaces with the sparse-matrix canonical grid method. *Journal of the Optical Society of America A*, 14(7):1515–1529, 1997.
- [67] Qin Li, Leung Tsang, Jiancheng Shi, and Chi-Hou Chan. Application of physics-based two-grid method and sparse matrix canonical grid method for numerical simulations of emissivities of soils with rough surfaces at microwave frequencies. *IEEE Transactions on Geoscience and Remote Sensing*, 38(4):1635–1643, 2000.
- [68] P. Xu Q. Li L. Tsang, D. Chen and V. Jandhyala. Wave scattering with UV multi-level partitioning method part I: 2D problem of pec surface scattering. *Radio Science*, 39, 2004.
- [69] P. Xu Q. Li L. Tsang, D. Chen and V. Jandhyala. Wave scattering with UV multi-level partitioning method part II: 3D problem of NON-penetrable surface scattering. *Radio Science*, 39, 2004.
- [70] D. Torrungrueng, Hsi-Tseng Chou, and J.T. Johnson. A novel acceleration algorithm for the computation of scattering from two-dimensional large-scale perfectly conducting random rough surfaces with the forward-backward method. *IEEE Transactions on Geoscience and Remote Sensing*, 38(4):1656–1668, 2000.
- [71] D. Torrungrueng and Joel T. Johnson. The forward backward method with a novel spectral acceleration algorithm (FB-NSA) for the computation of scattering from two-dimensional large-scale impedance random rough surfaces. *Microwave and Optical Technology Letters*, 29(4):232–236, 2001.

- [72] T. Sarkar, E. Arvas, and S. Rao. Application of FFT and the conjugate gradient method for the solution of electromagnetic radiation from electrically large and small conducting bodies. *IEEE Transactions on Antennas and Propagation*, 34(5):635 – 640, May 1986.
- [73] M. Mullen, C. Brennan, and T. Downes. A hybridized forward backward method applied to electromagnetic wave scattering problems. *IEEE Transactions on Antennas and Propagation*, 57(6):1846 –1850, June 2009.
- [74] S. Ray A. Peterson and R. Mittra. *Computational methods for Electromagnetics*. IEEE Press Series on Electromagnetic Wave Theory, 1998.
- [75] R.F. Harrington. *Field Computation by Moment Methods*. Malabar,FL:Krieger, 1982.
- [76] C.A. Balanis. *Advanced Engineering Electromagnetics*. New York: Wiley, 1989.
- [77] S.M. Rao, D. Wilton, and A.W. Glisson. Electromagnetic scattering by surfaces of arbitrary shape. *IEEE Transactions on Antennas and Propagation*, 30(3):409–418, May 1982.
- [78] K. S H Lee, L. Marin, and J.P. Castillo. Limitations of wire-grid modeling of a closed surface. *IEEE Transactions on Electromagnetic Compatibility*, EMC-18(3):123–129, Aug. 1976.
- [79] R.D. Graglia, D.R. Wilton, and A.F. Peterson. Higher order interpolatory vector bases for computational electromagnetics. *IEEE Transactions on Antennas and Propagation*, 45(3):329–342, Mar 1997.
- [80] Li Ping Zha, Yun Qin Hu, and Ting Su. Efficient surface integral equation using hierarchical vector bases for complex EM scattering problems. *IEEE Transactions on Antennas and Propagation*, 60(2):952–957, Feb. 2012.
- [81] E.M. Klopff, N.J. Sekeljic, M.M. Ilic, and B.M. Notaros. Optimal modeling parameters for higher order MoM-SIE and FEM-MoM electromagnetic simulations. *IEEE Transactions on Antennas and Propagation*, 60(6):2790–2801, June 2012.
- [82] M. Shafieipour, I. Jeffrey, J. Aronsson, and V.I. Okhmatovski. On the equivalence of RWG method of moments and the locally corrected nystrom method for solving the electric field integral equation. *IEEE Transactions on Antennas and Propagation*, 62(2):772–782, Feb. 2014.
- [83] G. Kang, Jiming Song, Weng Cho Chew, K.C. Donepudi, and Jian-Ming Jin. A novel grid-robust higher order vector basis function for the method of moments. *IEEE Transactions on Antennas and Propagation*, 49(6):908–915, June 2001.
- [84] J. Shaeffer. Direct solve of electrically large integral equations for problem sizes to 1 M unknowns. *IEEE Transactions on Antennas and Propagation*, 56(8):2306 –2313, Aug. 2008.

- [85] R. Maaskant C. Craeye, J. Laviada and R. Mittra. Macro basis function framework for solving maxwell equations in Surface-Integral-Equation form. *Forum for Electromagnetic Research Methods and Application Technologies (FERMAT)*, March 2014.
- [86] Eric Suter and Juan R. Mosig. A subdomain multilevel approach for the efficient MoM analysis of large planar antennas. *Microwave and Optical Technology Letters*, 26(4):270–277, 2000.
- [87] Dung Trinh-Xuan and C. Brennan. Tabulated interaction method for electromagnetic scattering from lossy irregular terrain profiles. In *2012 6th European Conference on Antennas and Propagation (EUCAP)*, pages 35 –38, March 2012.
- [88] J. Song, Cai-Cheng Lu, and Weng Cho Chew. Multilevel fast multipole algorithm for electromagnetic scattering by large complex objects. *IEEE Transactions on Antennas and Propagation*, 45(10):1488 –1493, Oct. 1997.
- [89] J.B. Andersen. UTD multiple-edge transition zone diffraction. *IEEE Transactions on Antennas and Propagation*, 45(7):1093–1097, 1997.
- [90] M.R. Pino, R.J. Burkholder, and F. Obelleiro. Spectral acceleration of the generalized forward-backward method. *IEEE Transactions on Antennas and Propagation*, 50(6):785 –797, June 2002.
- [91] Chi Hou Chan, L. Tsang, and Q. Li. Monte carlo simulations of large-scale one-dimensional random rough-surface scattering at near-grazing incidence: Penetrable case. *IEEE Transactions on Antennas and Propagation*, 46:142 –149, Jan. 1998.
- [92] P. Xu and L. Tsang. Bistatic scattering and emissivities of lossy dielectric surfaces with exponential correlation functions. *IEEE Transactions on Geoscience and Remote Sensing*, 45(1):62 –72, Jan. 2007.
- [93] Richard W. Newton and John W. Rouse. Microwave radiometer measurements of soil moisture content. *IEEE Transactions on Antennas and Propagation*, 28(5):680–686, 1980.
- [94] Yisok Oh, K. Sarabandi, and F.T. Ulaby. An empirical model and an inversion technique for radar scattering from bare soil surfaces. *IEEE Transactions on Geoscience and Remote Sensing*, 30(2):370–381, 1992.
- [95] Z.-X. Li. Bistatic scattering from three-dimensional conducting rough surface with UV multilevel partitioning method. *Progress In Electromagnetics Research*, 76:381–395, 2007.
- [96] Peng Xu and Leung Tsang. Scattering by rough surface using a hybrid technique combining the multilevel UV method with the sparse matrix canonical grid method. *Radio Science*, 40(4):n/a–n/a, 2005.

- [97] Shaowu Huang and Leung Tsang. Electromagnetic scattering of randomly rough soil surfaces based on numerical solutions of maxwell equations in three-dimensional simulations using a hybrid UV/PBTG/SMCG method. *IEEE Transactions on Geoscience and Remote Sensing*, 50(10):4025–4035, Oct. 2012.